NUMERICAL SIMULATION OF FOAMING IN METAL PROCESSING WITH POPULATION BALANCE MODELING

A DISSERTATION SUBMITTED FOR THE DEGREE OF DOCTOR OF PHILOSOPHY

BY

MD. ABDUS SATTAR

FACULTY OF SCIENCE, ENGINEERING AND TECHNOLOGY

SWINBURNE UNIVERSITY OF TECHNOLOGY

MELBOURNE, AUSTRALIA

2014

DECLARATION

The candidate does solemnly and sincerely declare that the work in this thesis is solely done by the candidate. The work is original and has not been submitted in part or whole for any other academic award. Any use of my work in which copyright exists was done by way of fair dealing and for permitted purposes and any excerpt or extract from, or reference to or reproduction of any copyright work has been disclosed expressly and sufficiently and the title of the work and its authorship have been acknowledged in this work. I do not have any actual knowledge nor do I ought reasonably to know that the making of this work constitutes an infringement of any copyright work.

……..

Md. Abdus Sattar

Certification

This is to certify that the above statement made by the candidate is correct to the best of our knowledge.

Associate Professor Jamal Naser

Professor Geoffrey Brooks

ABSTRACT

In this study computational fluid dynamic (CFD) model has been developed and numerical simulation has been carried out to predict the formation of foam, the number density of different bubble class, thermo-chemical reaction and multiphase flow phenomena. A new approach for the numerical simulation of foaming has been proposed and used in the present study. Numerical simulation of multiphase flow with bubble break-up and bubble coalescence model available in the open literature has also been incorporated in the CFD model. An anomaly was identified in the model of daughter bubble distribution available in the literature and rectified in the present study. Population balance modelling was used to track the number density of different bubble class. The decarburisation reaction with heat generation due to exothermic reaction was considered in the present study. The numerical prediction was based on Eulerian-Eulerian approach where the liquid phase was treated as a continuum and the gas phase (bubbles) was considered as a dispersed phase. A user subroutine was written in FORTRAN programming language to incorporate foam formation and destruction, bubble interactions and decarburisation into the main CFD software. The simulated results from the CFD models were validated against the experimental data available in the open literature.

At the initial stage of the present study, a CFD model of bubble column reactor which is similar to the experimental model of Laari and Turunen (2003) was developed for the simulation of multiphase flow. The CFD model was used to predict the bubble number density of different bubble class and multiphase flow phenomena by incorporating bubble break-up and bubble coalescence model. Different bubble class was considered and their number density was tracked using population balance technique incorporating the rectified model of daughter bubble distribution. Results from this CFD model were validated against the experimental data available in the open literature. The results from the CFD model are found to be in reasonable agreement with the experimental data.

In the next stage of the study, a CFD model which is similar to the analytical model of Narsimhan (2010) has been developed for the simulation of creaming and formation of foam in aerated liquid using a new approach of foaming. The CFD model has been used

to predict the foam formation, the number density of different bubble class and the fluid flow phenomena in the system. The population balance method was used in this model to track the number density of different bubble class incorporating the rectified model of daughter bubble distribution. The results from the CFD model were validated against the analytical data from Narsimhan (2010) and found in a reasonable agreement.

In the next stage of the study a CFD model of a laboratory scale crucible which is similar to the experimental model of Jiang and Fruehan (1991) has been developed for the simulation of slag foaming on bath smelting slag ($CaO\text{-}SiO\text{-}Al_2O_3\text{-}FeO$). This CFD model was used to predict the foaming height of slag, number density of different class and the multiphase flow phenomena. This CFD model incorporated the new approach of foaming applied in the previous model. The population balance method was used to track the number density of different bubble class using the rectified model of daughter bubble distribution. The foaming index was evaluated and dimensionless analysis was performed based on the model available in the literature to correlate the foaming index with the physical properties of the slag. The results from this model were validated against the experimental data available in the literature and found reasonable agreement with the experimental data.

In the final stage of the study, a CFD model of 6 tonne Basic oxygen steel (BOS) converter which is similar to the pilot plant model of Millman et al. (2011) has been developed. This CFD model was used to predict the foam height, the number density of different bubble class, decarburisation, heat generation and velocity of different phases in the process. The model incorporated a new approach of foaming and bubble break-up and bubble coalescence event during the blowing process. The model incorporated the population balance method to track the number density of different bubble class using the rectified model of daughter bubble distribution. The decarburisation reaction with heat generation was also integrated into the process. The results from this CFD model were validated against the pilot plant data available in the literature and found to be in a reasonable agreement with the plant data.

ACKNOWLEDGEMENTS

I would like to express my praise to Almighty Allah Subhanawatala for giving me opportunity to finish the thesis successfully.

I would like to express my gratitude and profound respect to my supervisor Dr. Jamal Naser. I am very grateful for his supervision with amicable behaviour. His guidance and inspiration make my research work success. He guided me with appropriate direction and provided technical support. His depth know how of the pertinent field ease my understanding of the research problem through discussion with him in the meeting.

I am also grateful to my second supervisor Professor Geoffrey Brooks. He is very supportive as well as helpful. Throughout my research his delightful attitude and supervision make my research time enjoyable. His critical comments and revision of my research manuscript help improving my understanding of the research goal and increase my writing skill.

I would like to acknowledge the assistance of each high temperature processing (HTP) member especially Dr. Nazmul Huda and Dr. Morshed Alam who helped me a lot from the beginning of my PhD. In the HTP meeting, HTP member provided valuable suggestion and critical comments which improved my understanding and thinking.

I am also thankful to FEIS staff whose assistance accelerated my research work. Their assistance in terms of procurement of research items and supportive research equipment are highly appreciable. They are very helpful and amicable.

I am gratefully remembering the privileges and opportunities offered by Swinburne University of Technology, Australia. The University provided full scholarship and without this assistance it would be out of my ability to carry out my research work smoothly. The research facilities and research materials provided by the University are highly appreciable. I am also expressing my gratitude to the staff of this university who helped directly or indirectly to carry out my research work.

I am very delighted to acknowledge the contribution of my wife Suraiya Akter Laboni toward the completion of this thesis. She took all the household and family responsibility on her shoulder which made me relieved and helped me to concentrate on my research work. Her inspiration relieved all the distress and accelerated my research work. She is always caring and at the same time adamant in inspiration and nudge me to finish my research in time.

I also acknowledge the affection of my parents who continuously provides mental support which strengthens my ability to finish the research work. I am happy to acknowledge the contributions of my siblings who help me in different way throughout the journey of finishing the thesis.

At the end I would like to thank all of my friends and well-wisher here at the Faculty of Engineering and Industrial Science, Swinburne University of Technology, Australia, as well as in the community where I stay for their cooperation and hospitability. They provided support when needed and their company make living here enjoyable and pleasant.

Table of contents

List of Figures

List of Tables

Nomenclature

A	interfacial area, m^{-1}
B_B	birth of bubble by breakage,$m^{-3}s^{-1}$
B_C	birth of bubble by coalescence,$m^{-3}s^{-1}$
C_D	drag coefficient, dimensionless
C_f	increase coefficient of surface area
D_B	death of bubble by breakage,$m^{-3}s^{-1}$
D_C	death of bubble by breakage,$m^{-3}s^{-1}$
D_{SMD}	Sauter mean bubble diameter, m
D_g	diffusion coefficient, dimensionless
D_T	diameter of container, m
d	diameter of bubble, m
f_{BV}	break up fraction, dimensionless
f	body force vector
g	gravitation acceleration, ms^{-2}
h_0	initial thickness of air water, m
h_f	final thickness of air water, m
I	unit tensor

M	momentum interfacial exchange, Nm^{-3}
N	number of bubble class
n	number density of bubble, m^{-3}
P_B	probability of break up, dimensionless
P_C	coalescence efficiency, dimensionless
P	pressure,Nm^{-2}
r_B	radius of bubble, m
R_T	radius of container, m
$U_{l,max}$	liquid circulation velocity,ms^{-1}
S	source of transport equation, $kgm^{-3}s^{-1}$
T	Reynold stress, Nm^{-2}
t	time, s
$\overline{u_\lambda}$	mean turbulent velocity, ms^{-1}
v	average velocity of phases, ms^{-1}
V	velocity,ms^{-1}
V_i	volume of bubble class i, m^3
$X_{i,j}$	parameter, dimensionless

$X_{i,k}$ parameter, dimensionless

Greek letters

β constant, 2.046

ε turbulent energy dissipation rate, m^2s^{-3}

Ø volume fraction of bubble, dimensionless

α volume fraction, dimensionless

σ surface tension, Nm^{-1}

ρ density, kgm^{-3}

τ shear stress, Nm^{-2}

μ viscosity, $kgm^{-1}s^{-1}$

$\tau_{i,j}$ contact time, s

υ volume of bubble, m^3

μ_k molecular viscosity, $kgm^{-1}s^{-1}$

ξ size ratio, dimensionless

λ eddy size, m

Ω_B bubble break up rate,$m^{-3}s^{-1}$

Ω_C bubble coalescence rate,$m^{-3}s^{-1}$

$\theta_{i,j}$ collision rate,$m^{-3}s^{-1}$

$\theta_{i,j}^{T}$ turbulent collision rate,$m^{-3}s^{-1}$

$\theta_{i,j}^{LS}$ laminar shear collision rate,$m^{-3}s^{-1}$

$\bar{\gamma}$ mean shear, s^{-1}

χ_c critical energy

Subscript

B break up

C coalescence

b bubble

i ,j bubble class

k Phase or bubble class

l liquid

g gas

r relative

SMD Sauter mean diameter

λ eddy

CHAPTER 1

INTORDUCTION

1 Introduction

Steel is the most used metal in the world. The production of steel has surpassed any other materials in the world. Different processes and techniques are used to produce steel from pig iron. There has been huge improvement and changes in the method and technique for the production of steel to meet the demand and the quality of steel. Among various techniques, the oxygen steelmaking is the most widely used method to produce steel. In this process, a supersonic jet of oxygen is injected into the molten iron which is called blowing to remove dissolve carbon as well as impurities. The blowing process generate heat and produces large amount of gas because of the reaction of carbon with oxygen. Foam, a complex system, is observed in many industrial processes such as froth floatation, foam in aerated liquid and oxygen steelmaking. The gas produced from the reaction during the blowing as well as the free gas from the nozzle causes slag foam in oxygen steelmaking. Many researches were carried out to understand the slag foaming in a model of laboratory scale. Numerical simulation on oxygen steelmaking was also carried out to understand the thermo-chemical phenomena in the metallurgical process.

The bubble break-up and bubble coalescence are indispensable part of many industrial processes such as bubble column reactor and oxygen steelmaking. The oxygen steelmaking is very complex in nature. In this intense flow environment, gas bubbles break and also coalesce and this event causes the change of their number density. The number density of bubble is important because the interfacial area between the gas bubbles and liquid is vital for mass, momentum interfacial exchange as well as chemical reaction between gas and liquid phases. Simulation which is considered as a cheap alternative of experiment is a promising method to investigate the multiphase flow as well as thermo-chemical phenomena. CFD technique, a branch of simulation, has been used for many years in the field of engineering and metallurgical process to predict the multiphase flow phenomena. Most of the simulations were carried out based on two phase model. In the two phase flow involving gas and liquid, bubble coalesces due to film rupture and liquid drains out from the lamellae and Plateau border channel in foam are difficult to incorporate. At the same time it is hard to keep the foam on the liquid surface because the gas diffuses into the atmosphere.

1.1 Research background and motivation

Oxygen steelmaking process is widely used in the world to produce steel from pig iron. Pig iron contains typically 3.5-4.5% carbon. In the process, pure oxygen is injected into the molten metal mainly for the decarburisation and oxidation of impurities such as P, Si, S, and Mn. The process is very complex in nature because it involves multiphase flow phenomena at high temperature, exothermic chemical reactions, heat and mass transfer between phases and formation of slag foam. Slag foaming phenomena are observed during the blowing of oxygen into the hot metal in Basic Oxygen Steelmaking (BOS) process. Slag foam in basic oxygen steelmaking process facilitates to remove impurities from the hot metal during blowing of oxygen. Slag foam layer also acts as an insulator to protect heat from escaping from the bath. Slag foaming is also observed in Electric arc furnace (EAF) during decarburisation. Slag foaming in electric arc furnace steelmaking is critical for high productivity (Matsuura and Fruehan, 2009). The slag foam protects the refractory from the high intensity arc allowing for high power input. Control of slag foaming in these intense metallurgical processes is critical because if the slag foam suddenly becomes unstable in an EAF process, the height of the foam will suddenly decrease, and this can result in increased dust generation, destabilisation of the direct current (DC) arc, increased anode consumption, and heat loss from the vessel due to radiation. A worst case scenario can occur in the BOS process, where the foamy slag can deviate from an ideal steady state height, and begin ejecting violently from the furnace. This phenomenon is called as slopping (Nexhip et al., 2004).

Foam is formed by numerous gas bubble separated by thin film of liquid or solid which is called lamellae (Bhakta and Ruckenstein, 1997). The foam is a complex phenomenon where bubble coalesces due to film rupture and liquid drain out from the lamellae and Plateau border channel. The life of foam is dominated by the bursting of bubbles at the top and internal bubble coalescence which causes the coarsening (rearrangement of bubbles size) of foam and escape of gases as well as the drainage of liquid through the lamellae and Plateau border channel (Drenckhan and Langevin, 2010, Bhakta and Ruckenstein, 1997, Vardar-Sukan, 1998, Pugh, 1996). In foam, internal bubbles coalesce and burst at the top surface mainly because of lamellae break-up and the lamellae break-up is dictated by the drainage of liquid. In the gas-liquid two phases

flow, bubble coalesces due to film rupture and liquid drains out from the lamellae and Plateau border channel are difficult to incorporate in the foam. Therefore, in the present research, foam was considered as separate phase comprised of a mixture of gas and liquid to overcome the above drawback.

In multi-phase flow, where gas is dispersed into liquid such as injecting oxygen into liquid iron, bubble break-up and coalescence is indispensable event to occur. The bubble break-up in the gas liquid dispersion causes the larger bubbles to split into smaller bubble which ultimately changes their number density. The collision of bubbles with eddies are considered the main reason of bubble break-up (Liao and Lucas, 2009). The coalescence of bubbles also occurs in the gas liquid dispersion. In the coalescence event, bubbles collide with each other and agglomerate to grow bigger. Turbulent velocity of bubble and laminar shear is considered as the main reason of bubble coalescence. It is important to incorporate bubble break-up and coalescence event in gas liquid dispersion as well as in foam. Accurate prediction of bubble number density is important because the interfacial surface area of bubble depend on the number density of individual bubble class. The mass and heat transfer as well as the chemical reaction in the system depends on the interfacial area between gas and liquid phases (Bhole et al., 2008). Population balance equation (PBE) sometimes refers as population balance modelling (PBM) is used to track the number density of different bubbles class in the present research. An anomaly was identified in the model of daughter bubble distribution available in the literature (Hagesaether et al., 2002). The model of daughter bubble distribution was rectified and used in the present study.

Understanding of the foaming and bubble-bubble interactions is important for the oxygen steelmaking. It is challenging to investigate the above mentioned phenomena experimentally. Numerous researches were concentrated on the understanding of slag foaming in a laboratory scale model. Experiment was also carried out on pilot plant to investigate physio-chemical phenomena in the oxygen steelmaking. Though experiment gives the real scenario of the process but the cost involved in the experiment as well as the lack of technique to investigate in the bulk liquid during the process make it difficult to carry out. Computational fluid dynamic is a promising branch of numerical technique to understand the multiphase flow phenomena at high temperature incorporating

exothermic chemical reactions heat and mass transfer between phases and the formation of slag foam. In the present research numerical technique has been adopted to incorporate the above phenomena for the prediction of foam height, bubble number density and decarburisation in the process. Computational fluid dynamic (CFD) simulations of multiphase flow started many years ago and since then the technique has been used in many fields of engineering as well as metallurgical process involving multiphase flow phenomena. Numerous CFD model of multiphase flow have been developed, and numerical data has been validated through comparison against experimental data. There are two main approaches for the simulation of multiphase flow, namely the Euler–Lagrange method which considers the bubbles as individual entities and tracked the bubbles using trajectory equations, and the Euler–Euler method which is based on two-fluid model and this approach assumes the gas and liquid phases to be interpenetrating continua. Euler–Lagrange approach is better than Euler–Euler approach in some cases but the time and the cost involved in the simulation in Euler–Lagrange approach limits its application. Therefore, from the computational considerations, the Euler–Euler approach is more economical and commonly used in the field of engineering. So in the present research, the simulation was carried out based on Euler-Euler approach. In the present study different computation fluid dynamic models were developed and user subroutine has been written in FORTRAN programming language to incorporate bubble-bubble interaction, the comprehensive foaming phenomena and decarburisation reaction in the model.

A CFD model of bubble column reactor similar to the experimental model available in the literature was developed to incorporate bubble break-up and bubble coalescence model. Bubble break-up and coalescence model available in the literature were used to calculate the bubble break-up and coalescence rate. Then bubble break-up and coalescence rate was incorporated into the population balance equation to track the number density of different bubble class in the system. The model of daughter bubble distribution from Hagesaether et al. (2002) was rectified and used in the CFD model to predict the number density of different bubble class. The results from the model were validated against the experimental data of Laari and Turunen (2003), Laari and Turunen (2005) and Sha et al. (2006). Then a comprehensive foam model was proposed where foam was considered as a separate phase which is comprised of a mixture of gas and

liquid and used to predict the foam height with time in another CFD model. This new approach has been incorporated into a CFD model for the simulation of creaming and formation of foam in aerated liquid similar to the analytical model available in the literature. In this model only bubble coalescence due to film rupture were used and their number density was tracked using PBE with rectified model of daughter bubble distribution from the previous model. The results from the model were validated against the analytical data from Narsimhan (2010) model. Once the comprehensive foam model was applied and validated against analytical data, another CFD model which is similar to the experimental model available in the literature was developed and the comprehensive foam approach was incorporated into the model. The bubble break-up and coalescence was integrated into the model and the population balance equation was also included in the system as well as the rectified source term model. The results from the model were validated against the experimental data from Jiang and Fruehan (1991).

Finally a CFD model similar to the pilot plant model of BOS converter with capacity of 6 tonne was developed for the numerical simulation. A thin slice of the model instead of full model was considered to reduce computational time. The model also incorporated the bubble break-up and bubble coalescence closure available in the literature to calculate the bubble break-up and coalescence rate. The bubble break-up and coalescence rate was incorporated into the population balance equation to track the number density of different bubble class in the system. The rectified model of daughter bubble distribution from the previous model was used to estimate the birth and death of bubble due to break-up and coalescence. The comprehensive foam model applied in the previous model also used in this model to predict the foam height with time. Decarburisation reaction with heat generation was also considered into the system. The results from the model were validated against the pilot plant data from Millman et al. (2011).

The simulation was carried out by commercial CFD software AVL-FIRE 2009.2 and user subroutine was written in FORTRAN to incorporate bubble break-up and bubble coalescence rate, foam model, and decarburisation into the main software as well as the interfacial exchange of mass and momentum. The multiphase flow equation were based on Euler-Euler approach and presented in the respective chapter for the respective

model. The mathematical model for bubble-bubble interaction, foam model, decarburisation used for the respective model is presented in the respective chapter. The bubble break-up model of Luo and Svendsen (1996) and the coalescence model of Prince and Blanch (1990) was used in gas liquid dispersion. The coalescence model of Tong et al. (2011) was used in foam.

1.2 Research objectives

The main objective of this research is to perform a numerical simulation to understand slag foaming phenomena by incorporating population balance modelling which includes bubble break-up and coalescence as well as decarburisation in a comprehensive modelling of foaming. The objectives of the present research are:

1. Develop different CFD models.
   i. A 3D CFD model of a bubble column which is similar to the experimental model of Laari and Turunen (2003).
   ii. A 3D CFD model of a container of aerated liquid which is similar to the analytical model of Narsimhan (2010).
   iii. A 3D CFD model of a laboratory scale crucible which is similar to the experimental model of Jiang and Fruehan (1991).
   iv. A 3D CFD model of 6 tonne BOS steelmaking converter which is similar to the pilot plant model of Millman et al. (2011).
2. Carry out numerical simulation on different CFD models to predict bubble number density, the foam height and multiphase flow phenomena.
3. Analyse the predicted results obtained from the CFD models.
4. Validate the results from the CFD models against the results available from the open literature.

1.3 Thesis outline

Chapter 2 summarized the pertinent literature review of the present work. Different process available for the production of steel is highlighted and their chronological development is presented. The fundamentals of BOS steelmaking is presented in brief. The slag foaming in oxygen steelmaking is also presented. Then the fundamental of

foaming and foam rheology is presented and elaborated. Different types of foam together with the foam parameter are discussed. Different approach available for the simulation of multiphase flow in CFD are highlighted and discussed. The discussion on population balance modelling is presented in this chapter. Different numerical techniques for solving the population balance are highlighted and presented in this chapter. Different types of bubble break-up and coalescence mechanism are discussed and presented in this chapter. Finally the mechanism of daughter bubble distribution is discussed.

In Chapter 3, numerical simulation of two phase flow in a bubble column reactor with population balance modelling is presented. The research methodology and the modelling of the geometry of the 3D mesh used for the numerical simulation of bubble column reactor are presented in this chapter. The detailed description and dimension of the model and the boundary conditions assigned for the model is discussed and presented in this chapter. The chapter presents the detailed rectification of the source term model available in the literature. The governing equation for fluid flow, interfacial phenomena, and the equation for bubble break-up and coalescence closure are presented in this chapter. Bubble break-up and bubble coalescence closure term applied in the modelling of bubble column reactor is presented in this chapter. Population balance equation used for the modelling of bubble column reactor is also presented in this chapter. The results obtained from the simulation are presented at the end of this chapter. Chapter 3 presents the comparison of distribution of bubble number density of different bubble class from the predicted results with that of the experimental data available in the literature. Chapter 3 also presents the evaluated Sauter mean diameter at the different height of the column from the predicted results with the Sauter mean diameter evaluated from experimental data available. The comparison of time average liquid axial velocity and gas hold up from the predicted results with the experimental data available is also presented in Chapter 3.

In Chapter 4, numerical simulation of formation of foam and creaming in aerated liquid is presented. The model predicts the formation of foam in a container of aerated liquid similar to the analytical model available in the literature. The research methodology and the modelling for the numerical simulation of formation of foam and creaming in

aerated liquid are presented in this chapter. The detailed description and dimension of the model and the boundary conditions assigned for the model is discussed and presented in this chapter. The governing equation for fluid flow, interfacial phenomena, the equation for bubble break-up and coalescence, and the equation for foaming are presented in this chapter. The chapter discusses the phase diagram in details. The results obtained from the simulation of foam formation and creaming in aerated liquid are presented at the end of the Chapter 4. Chapter 4 presents the plotted phase diagram with different air volume fraction of the model and compared with the data available in the literature. The chapter also presents the bubble class distribution in the gas liquid dispersion and foam. The volumetric fraction of gas, liquid and foam with different time were also presented in this chapter. The Sauter mean diameter evaluated from the CFD results is presented in the phase diagram. The results from the CFD model were compared with the data available in the literature and discussed.

In Chapter 5, the CFD model of slag foaming in a bath smelting slag is presented. The research methodology and the numerical technique for the simulation of formation of foam in a bath smelting slag are presented in this chapter. The detailed description and dimension of the model and the boundary conditions assigned in this model has been discussed in this chapter. The governing equation for fluid flow, interfacial phenomena, the equation for bubble break-up and coalescence, and the equation for foaming are presented in this chapter. The foam height with different velocity and FeO content was presented in term of volumetric fraction of gas, liquid slag and foam. The foaming index of the slag is evaluated and presented and compared with the data available in the literature. Dimensionless analysis was performed and the results were compared with the data available in the literature. The distribution of different bubble class was presented and the Sauter mean diameter was calculated and presented.

In Chapter 6, the CFD model of BOS steelmaking converter with capacity of 6 tonne was presented. The research methodology and the modelling for the numerical simulation of foam formation on a 6 tonne BOS steelmaking converter are presented in this chapter. The detailed description and dimension of the model and the boundary conditions assigned for this model is discussed and presented in this chapter. The governing equation for fluid flow, interfacial phenomena, the equation for bubble break-

up and coalescence, and the equation for foaming are presented in this chapter. The mathematical model used for the decarburisation reaction in the present model is also presented in this chapter. The chapter presents the foaming height of the model with different time. The model also presents the Sauter mean diameter of bubbles and the distribution of individual bubble class in the model. The model incorporated the decarburisation reaction and the prediction results are also presented and compared with the pilot plant data available in the literature. Results from the present CFD model and the experimental data available in the literature are compared and discussed in this chapter.

In Chapter 7, the conclusions and remarks on the present research is presented. Then recommendations for further research are highlighted and discussed.

1.4 Publication from the present study

Journal Papers

1. **Sattar, M.A.**, Naser, J., Brooks, G., Numerical simulation of slag foaming on bath smelting slag (CaO-SiO_2-Al_2O_3-FeO) with population balance modeling. Chemical Engineering Science. 107, (2014) 165-180.

2. **Sattar, M.A.,** Naser, J., Brooks, G., Numerical simulation of creaming and foam formation in aerated liquid with population balance modeling. Chemical Engineering Science. 94, (2013) 69-78.

3. **Sattar, M.A.,** Naser, J., Brooks, G., Numerical Simulation of Two-Phase Flow with Bubble Break-up and Coalescence Coupled with Population Balance Modeling. Chemical Engineering and Processing: Process Intensification. 70, (2013) 66-76.

4. **Sattar, M.A.,** Naser, J., Brooks, G., Numerical Simulation of Slag Foaming in High Temperature Molten Metal with Population Balance Modeling. Procedia Engineering, 56, (2013), 421–428.

Conference Papers

1. **Md Abdus Sattar**, Jamal Naser, Geoffrey Brooks, Numerical Simulation of Slag Foaming in BOS Converter Steelmaking with Population Balance Modeling. 4th International Symposium on High-Temperature Metallurgical Processing, 2013.

2. **M.A.Sattar**, J.Naser, G.Brooks. Numerical Simulation of Slag Foaming in High Temperature Molten Metal with Population Balance Modeling. 5th BSME International Conference on Thermal Engineering. Procedia Engineering, Sciverse Science direct, 2012.

3. **Md. Abdus Sattar**, Jamal Naser, Geoffrey Brooks. A comprehensive approach for CFD Modeling of Slag Foaming with Population Balance Modeling. Proceedings of the 5th High Temperature Processing Symposium (HTPS 2013), Hawthorn, Victoria, Australia, 4-5 February 2013. pp. 91-92, FEIS, Swinburne University of Technology.

4. **Md. Abdus Sattar**, Jamal Naser, Geoffrey Brooks. Modeling of slag foaming coupled with decarburisation. TMS 2014.

5. **Md. Abdus Sattar**, Jamal Naser, Geoffrey Brooks. Numerical simulation of decarburisation in oxygen steelmaking with population balance modelling. ICME December, 2013.

CHAPTER 2

LITERATURE REVIEW

2 Literature review

In this chapter, recent developments for different process in the production of steel are summarized. The sequence of operation in BOS converter is highlighted and detailed thermo-chemical phenomena in the blowing process is presented. The slag foaming in oxygen steelmaking is also presented. Then the fundamental of foaming, their classification and foam rheology is presented and elaborated. Different types of foam together with the foam parameters are discussed. Population balance modelling is also presented in this chapter. Different types of numerical techniques for solving the population balance are highlighted in this chapter. Different types of bubble break-up and coalescence mechanisms available in the literature are summarized and presented in detail.

2.1 Steelmaking

Steelmaking is generally considered as the second step in producing steel from iron ore. In the earliest time of producing steel people used bloomery. Bloomery is one type of furnace which was widely used for smelting of iron from its oxide in the early days of steelmaking. The application and the demand for better quality of steel have increased rapidly. The method and technique used in the production of steel in the beginning of steel production did not meet the growing demand and quality. Therefore, there have been tremendous improvements in the technique as well as the process used to produce steel due to the rapid growth of demand and the quality of steel.

Steel is produced from pig iron. Pig iron contains high carbon (approximately 3.5-4.5%). The carbon is reduced from the pig iron to make steel. Other impurities such as Silicon (Si), Manganese (Mn), Phosphor (P), and Sulphur (S), are also removed from the pig iron depending on the quality of steel needed. The dissolve carbon as well as the impurities is removed from the pig iron by oxidation. Oxidation is done by injecting oxygen into the molten pig iron. Different techniques are applied for better mixing of gas and liquid and hence the oxidation reaction in the process. At the beginning of steelmaking, air is used for the oxidation reaction. Air is blown from the bottom of the vessel through the molten pig iron. The process is called bottom blown process. William Kelly of Eddyville, Kentucky and Henry Bessemer of England independently developed

the bottom-blown process. Bessemer patented the process in 1856 and the process is called Bessemer process. They used acid refractories liner for the protection of the vessel and the process is known as bottom-blown acid process. Sidney Gilchrist Thomas in England in 1871 developed bottom blown basic process and this was patented in 1879. In this process, instead of acid refractories liner basic refractories liner was used for the protection of the vessel and hence the process is known as bottom-blown basic process. The process is also called as Thomas, Thomas-Gilchrist or basic Bessemer process. Karl Wilhelm Siemens developed different technique. In his technique, instead of blowing air from the bottom, the burning fuel is allowed to pass over the top surface of liquid pig iron. The heat of the burning fuel initiates the chemical reaction for the purification. Karl Wilhelm Siemens developed the process in 1868 and the process is called as open hearth process (Fruehan, 1998, Dogan, 2011).

The idea of using pure oxygen instead of air for the refining of pig iron was proposed by many scientists. This idea drew much attention to numerous investigators and it was not until the late 1940s when the Swiss engineer Robert Durrer began experimenting with blowing pure oxygen against the metal bath. The process is called oxygen steelmaking because gaseous oxygen rather than air is used for refining molten pig iron and scrap mixture. The oxygen steelmaking process has dominated the steel production from molten pig iron of blast furnace or mixture of pig iron and scrap steel. The top blown oxygen process was first used in two plants at Linz and Donawitz in Austria and hence the process is acronym as “LD” process (Fruehan, 1998). The top blown oxygen process is called the basic oxygen steelmaking process or basic oxygen process. A successful bottom blown oxygen steelmaking process was developed in 1970s. In this process, removable tuyeres are mounted at the bottom of the furnace. A combination of top and bottom blown process are also in use in the steelmaking process. The various oxygen steelmaking processes used in the steelmaking industry is shown in Figure 2.1 (Miller et al., 1998).

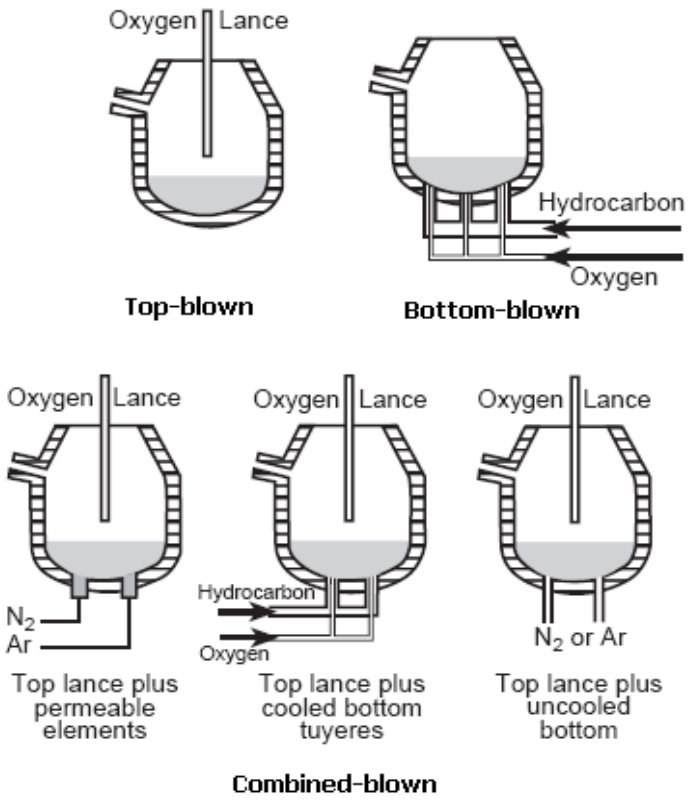

Figure 2.1. Different types of blowing in oxygen steelmaking (Miller et al., 1998).

Later, the amount of used or scrap steel is cheaply available and the use of the scrap steel together with the pig iron for refining has increased. The scrap steel is used with pig iron for refining to reduce the environmental impact. Therefore, significant growth of Electric Arc Furnace (EAF) has been observed in the last twenty years due to the availability of excess scrap steel at low cost. The discovery of the carbon arc by Sir Humphrey Davy in 1800 led to the use of arc-type furnaces. The practical application began with the work of Sir William Siemens, who in 1878 constructed, operated and patented furnaces operating on both the direct arc and indirect arc principles. The cost and availability of electric power as well as the lack of carbon electrode quality retard the rapid expansion of electric arc furnace at the beginning. The first successful commercial EAF was a direct arc steelmaking furnace which was placed in operation by Heroult in 1899 (Fruehan, 1998). A different type of EAF was used for the production of steel. Halcomb Steel Company of New York in the United States was installed in 1906 on a single phase, two electrode, and rectangular furnace with a capacity of 3.6 tonnes. Then Firth-Sterling Steel Company of Pennsylvania was installed in 1909 in the

south Works of the Illinois Steel company with three phase furnace. From 1910 to 1980 almost all steelmaking EAFs were built on three phase alternative current (AC). Later a large percentage of the new EAFs were built with DC system because of some advantage of DC over AC. The induction furnace was patented by Ferranti in Italy in 1877. The first large scale installation was made in 1914 at a plant of American Iron and Steel Company in Lebanon, Pennsylvania but was not successful because of low frequency (Fruehan, 1998). The coreless high frequency induction furnace was installed on a commercial scale at Sheffield, England. Electric arc furnace has improved significantly in term of reduce tap to tap time and reduction of energy consumption. Electric Arc furnace of other types are also in use such as vacuum arc remelting furnace (VAR), iron smelting furnace and on an experimental basis plasma type melting and reheating furnace (Fruehan, 1998). The present study is concerned with Basic Oxygen steel converter. Therefore, in the subsequent sections details of the BOS converter is presented.

2.2 Fundamentals of Basic Oxygen Steelmaking (BOS)

Basic oxygen steelmaking process is the most widely used process in the world to produce steel owing to it's shorter production time and lower production cost. The total steel production in the world in 2008 is 67.1% via BOS process (Brämming, 2010). Generally in this process, steel is produced from molten pig iron (sometimes referred as hot metal) and scrap steel. This pig iron or hot metal is produced from iron ore called oxide pellet in a blast furnace by adding coke (charcoal) in the blast furnace. Typical pig iron produced from the blast furnace contains about 3.5-4.5% carbon. In BOS converter, the carbon in the pig iron from the blast furnace is reduced by the oxidation of carbon with oxygen and the process is called as decarburisation reaction. The process is called Basic oxygen steelmaking because pure oxygen instead of air is used for the removal of carbon, in a vessel which has a basic protective inner lining. The oxygen can be supplied through bottom tuyeres and or via a top-lance blowing against the metal surface or in combination of both and the details of the configuration is presented in the previous section and can be seen in Figure 2.1 (Brämming, 2010). In the top blown process, oxygen is impinged into the hot metal through water cooled lanced in a supersonic jet and the process is termed as blowing. The sequence of operation from

filling of scrap steel and charging of hot metal to taping of liquid steel and pouring off slag is shown in Figure 2.2. Initially, scrap steel is filled in the vessel (Figure 2.2(a)) then a predetermined amount of hot metal is poured into the vessel (Figure 2.2 (b)). The purposes of using scrap steel is to recycle of used steel and to absorb heat during blowing of oxygen which help protect the vessel from overheating and keep the temperature of hot metal in working condition. Once the charging is completed and the vessel is positioned upright a lance equipped with nozzle at the end is lowered inside the vessel in a predetermined height from the liquid surface (See Figure 2.2 (c)). The lance supplies oxygen with supersonic jet and oxygen impinges into the liquid and rapid oxidation starts (Dogan, 2011). The reaction of oxygen with impurities such as C, Si, Mn, P and S takes place. These reactions are exothermic reaction which generates heat and therefore the temperature of the bulk liquid increases. The heat generated during the blowing helps melting the scrap as well as refining reactions. Flux, which is mixture of calcium and dolomite, is added in the process to remove the impurities and form a slag that can be separated from the steel and poured off from the furnace as a liquid. It also helps reduce the wear of furnace refractory.

The mass fraction of Silicon, Manganese, Phosphor and Sulphur is much less than that of carbon in the bulk liquid. Typical value of C=4-5%, Si=0.47%, P=0.08%, Mn=0.45% and S=0.04% is found in the literature (Millman et al., 2011). Carbon is removed from the bulk liquid as CO and CO_2 gas and it was estimated that 90% is CO gas (Brämming, 2010, Dogan, 2011). The blowing time is approximately 20 minutes (Dogan, 2011). Once the blowing is done the furnace is tilted to pour the steel from taphole which is located at the side of the vessel into a ladle and the process is termed as tapping (See Figure 2.2 (d)). The process generate large amount of gases during blowing of oxygen (Figure 2.2 (c)) mainly due to reaction of oxygen with carbon to produce carbon monoxide and thus causes the slag foaming. Slag foaming is important for post combustion and it also facilitate multiphase reaction leading to improved process kinetics, heat transfer and energy efficiency (Nexhip et al., 2004, Jiang and Fruehan, 1991). On the other hand if the process generates excessive slag foam then the slag foam overflows the vessel. This phenomenon is termed “slopping” in oxygen steelmaking. Slopping reduces productivity and increases operating cost and in some worst cases damages the vessel. It is important to understand the fundamental features

of the slag foaming in the pyrometallurgical process. When tapping is done, the slag remained on the surface of hot metal is poured off (See Figure 2.2(e)).

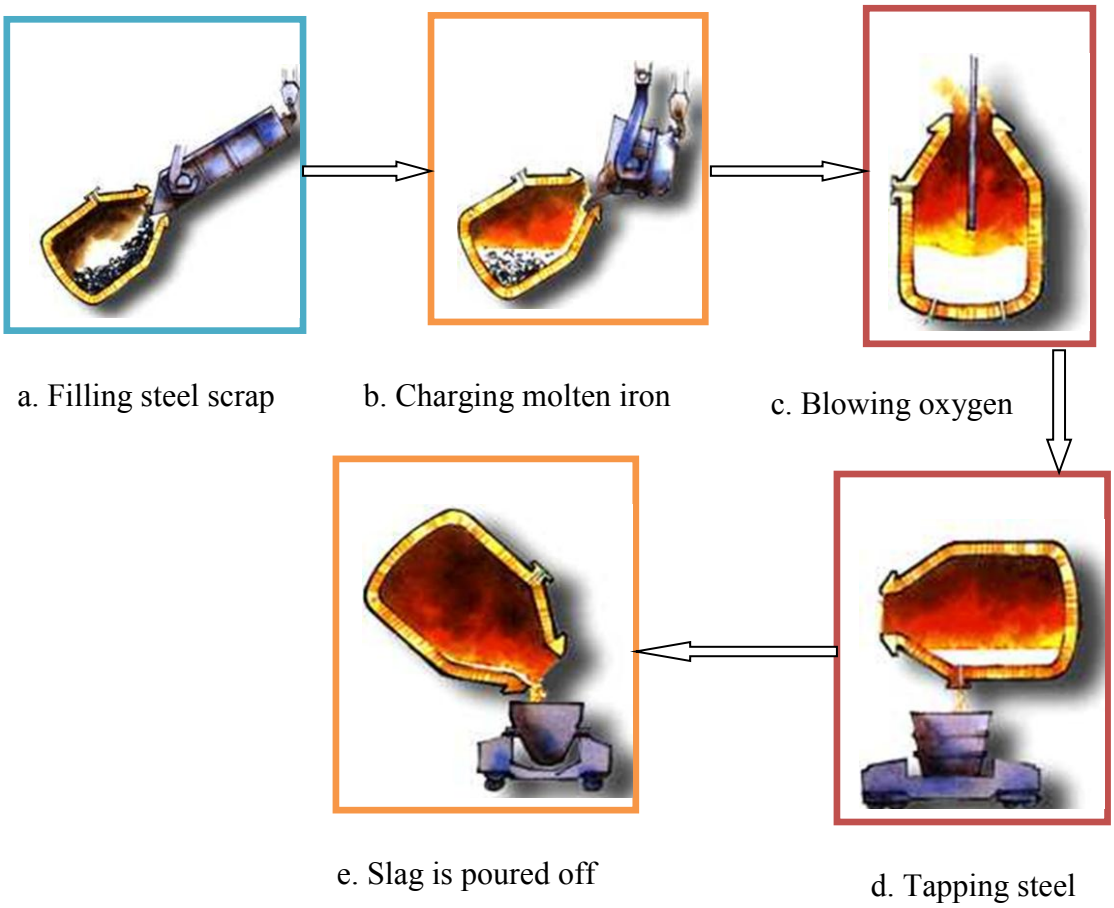

Figure 2.2. Sequence of operation in oxygen steelmaking (Bluescopesteel, 2011).

During the blowing of supersonic jet of oxygen, the blown oxygen penetrates into the liquid metal causing cavity below the nozzle (See Figure 2.3). The main purpose of blowing is to oxidize the carbon dissolved in the hot metal as well as impurities. Oxygen reacts with dissolve carbon in the interface between liquid and gas in the cavity of penetration. Swarm of gas bubbles travel toward top surface of liquid in the vessel which causes the formation of foam consisting of liquid slag, metal droplet, and solid particle. Slag foam is formed at the top of liquid surface due to gas bubble generation from the decarburisation reaction. The slag foam facilitates the multiphase reaction and removal of oxides of impurities and also acts as insulator to keep heat escaping from liquid. But excessive foam has detrimental effect on the production. Decarburisation

reaction also takes place in foam. The Figure 2.3 shows a top blown oxygen steelmaking process showing different regions in the system.

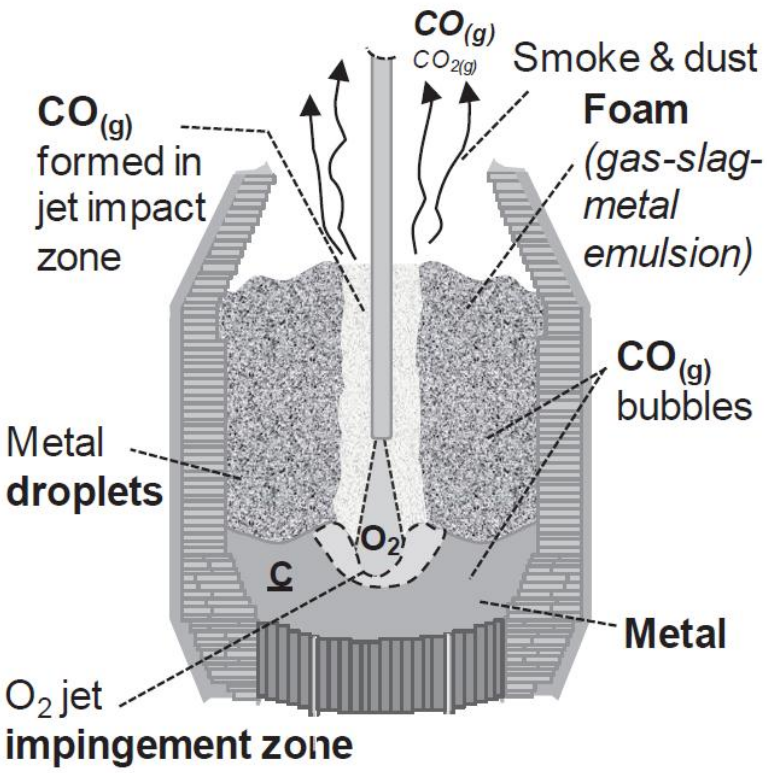

Figure 2.3. Blowing of oxygen in hot metal and scrap (Brämming, 2010).

Oxygen also reacts with liquid Fe to form FeO. Most of the reactions are exothermic which produces heat during the reaction. The oxidation reactions of different element and heat of enthalpy during the blowing are presented in Table 2.1.

Table 2.1. Heat of reaction (Dogan, 2011).

Oxidation Reactions	Heats of Reaction	
	Kilojoule	per mole of
C + 1⁄2O2 = CO	4173	C
C + O2 = CO2	14884	C
CO + 1⁄2O2 = CO2	4593	CO
Si + O2 = SiO2	13927	Si
Fe + 1⁄2O2 = FeO	2198	Fe
Mn + 1⁄2O2 = MnO	3326	Mn

Numerous experiments were carried out on oxygen steelmaking to understand the physio-chemical phenomena in the system. Cuthill (1981) studied different methods for the controlling of slopping in the Steel Company of Canada's Hiltonne Works in basic oxygen furnace installation. The author established link between slopping and various operational conditions based on the experience of the furnace operators and data from the process. Brämming (2010) carried out a trials on industrial scale BOS vessels of type LD using Fast Fourier transfer (FFT) spectrum analysis to find the frequency band with best correlation to an estimated foam height. He found that there is a correlation between vessel vibration and foam height which can be used for dynamic foam level and slopping control. Evestedt and Medvedev (2009) developed a model for slopping warning and mitigation based on the sound signal from a microphone located in the off-gas funnel to obtain an estimate of the slag level in the converter. Stroomer-Kattenbelt (2008) developed a dynamic control strategy for basic oxygen steelmaking which both

reduces the occurrence of slopping and increases the production capacity by reducing the batch time.

Numerous experiments in the laboratory were also carried out to understand the slag foaming phenomena of oxygen steelmaking. Air water models have also been used to model the foaming phenomena (Guthrie, 2009, Guo et al., 2002). Birk et al. (2003) presented an improved foam level estimation methodology from a microphone signal and its automatic calibration representing the LD converter process to a water model. Millman et al. (2011) studied the refining performance of BOS steel converter. They developed a fully automated sampling system in a 6 tonne converter to retrieve simultaneously representative of bulk metal bath and slag/metal emulsion samples from seven specified positions for every 2 min from start of blow. Different composition was used in the bulk metal and the lance height was kept fixed. They analysed oxidation of impurities such as C, Si, P, Mn and they measured the height of foam during the blowing of oxygen.

Numerical simulation was also carried out to understand the physio-chemical phenomena in the oxygen steelmaking. Panjkovic et al. (2002) studied the performance of an iron-bath reactor using a comprehensive numerical model that combines a computational fluid dynamics approach for the gas phase and a heat and mass balance model for the bath. They considered the reaction in the process and heat and mass transfer of phases in the system. Matsuura et al. (2008) developed a model to predict decarburisation and slag formation for the Electric Arc Furnace. The formation of foam and bubble-bubble interaction is important in oxygen steelmaking process. The foam formed in the process behaves differently than the liquid and gas and many phenomena in the foam such as drainage and bubble busting are necessary to incorporate into the modelling. The liquid drainage and bubble bursting is difficult to incorporate into the two phase flow simulation. In the gas and liquid metal dispersion, the bubble breaks into smaller one due to collision with turbulent eddies and aggregate into bigger bubble due to collision with other bubbles. The bubble inside foam also coalesces due to lamellae break-up. These phenomena are necessary to incorporate in the modelling of oxygen steelmaking process.

In the present research, a CFD model of 6 tonne BOS steel converter has been developed to predict the slag foaming in the process by incorporating the decarburisation reaction in the system. In the model bubble break-up and bubble coalescence was considered and their number density was tracked. Population balance modelling was applied to track the number density of different bubble class. Foam was considered as separate phase which is a mixture of gas and liquid. The liquid drainage in the foam as well as the bursting of bubble in the foam was incorporated into the CFD model. Only the decarburisation reaction was considered in the present model. The results from the present CFD model was compared with the pilot plant results of Millman et al. (2011) and presented in Chapter 6 at Section 6.4.

2.2.1 Slag foaming in oxygen steelmaking

Slag foaming is observed in oxygen steelmaking during the blowing of oxygen into the hot metal (Nexhip et al., 2004). The pyrometallurgical processes generate large quantity of gas which causes the slag foam. Foaming slags are important for post combustion reactions but excessive slag foam formation has detrimental effect on the process (Nexhip et al., 2004, Jiang and Fruehan, 1991). A picture of slopping in a steelmaking vessel is shown in Figure 2.4.

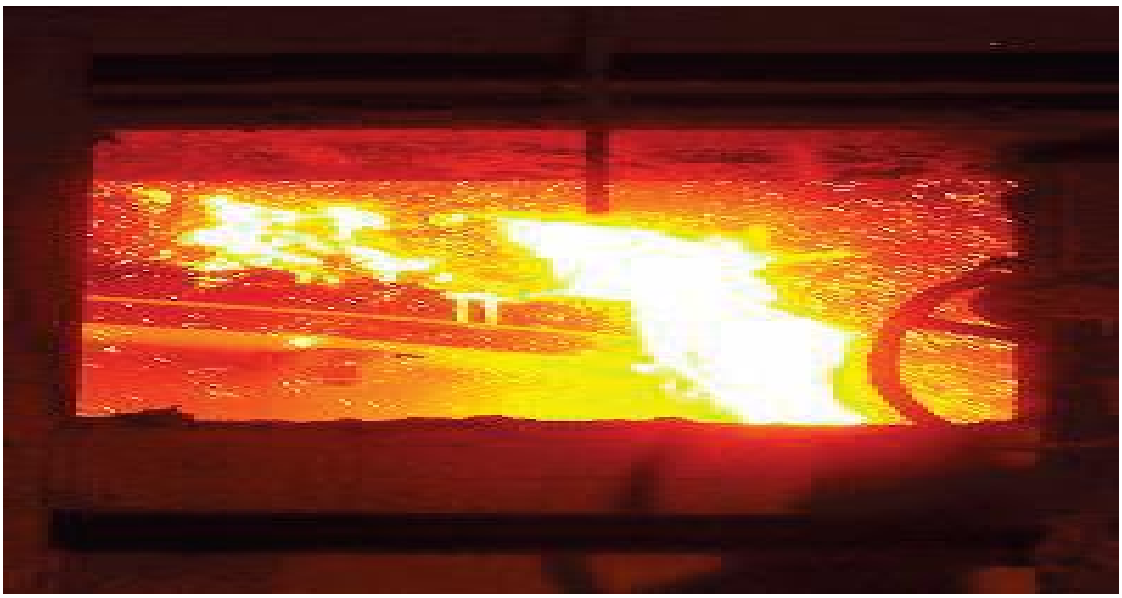

Figure 2.4. Sloping in steelmaking (Brämming, 2010).

Slopping reduces productivity and increases operating cost and in some cases damages the vessel. Therefore, it is important to understand the fundamental features of slag foaming in pyrometallurgical processes. Several studies have considered the modelling and prediction of slag foam height, where foaming is described in terms of a foam index or the gas void fraction or hold-up (Stadler et al., 2007). Foaming index and foam life are two main parameters to understand the features of slag foaming. The foaming index, which correlates foam height with superficial gas velocity was proposed by (Bikerman, 1953, Akers, 1976) for aqueous system. Considerable research activity has been directed toward understanding the foaming behaviour of slag over the past two decades, the major contributions coming from Fruehan and his group. Ito and Fruehan (1989) expressed the foaming index in term of foam layer thickness and actual gas velocity. The foaming index has empirically been related to physical properties of the slag such as the surface tension, viscosity, and density of the liquid and the size of the bubbles. Empirical models of foaming index were modeled by different researchers for different slag system (Roth et al., 1993, Morales et al., 1995, Jiang and Fruehan, 1991, Kim et al., 2001b). In these empirical studies the effect of bubble size was disregarded. Several studies have explicitly accounted for bubble size on the foam (Zhang and Fruehan, 1995, Ozturk and Fruehan, 1995, Lahiri and Seetharaman, 2002, Lin and Guthrie, 1995). Ito and Fruehan (1989) studied the foaming index and foam life of various slags. They found that slag foaming increase with increasing viscosity and decreasing surface tension. At the same time they have found that suspended second particle stabilize the foam life and had a larger effect than that of viscosity and surface tension. Kitchener and Cooper (1959) studied the foaming of $CaO\text{-}SiO_2$ slag at different temperatures. They measured the foam life and found that the foam life increased with decreasing temperature and decreasing basicity. Hara and Ogino (1992) measured the foam life and foam height and found a good correlation between the foam life, foam height, and surface tension of the slag.

Slag foam is formed by the entrapment of many gaseous bubbles in a liquid or solid. Slag foam is normally a complex system consisting of polydispersed gas bubbles separated by draining films which is called lamellae and the lamellae are joined in a chanel called Plateau border. The liquid is drained out from the lamellae through the Plateau border. The lamellae ruptures when the drainage casuses the film to reach a

critical limit. When the bubbles coalesce the number density of the bubble class changes which ultimately changes the number of individual bubble classes. In two phase flow (gas bubble and liquid) the above phenomena is difficult to incorporate into the model but most of the simulation is done on two phase flow. If the foam is considered as a sperate phase composed of gas and liquid then the life of the foam can be modeled by considering both foam formation due to phase transformation from gas and liquid, and foam destruction due to phase transformation from foam to gas and liquid. Bubbles also break and coalesce in the liquid before forming foam at the top. Monodisperse (same bubble size) foam suffers from film rupture (coalescence) and gas exchange (coarsening) between adjacent bubbles, both processes leading ultimately to polydispersity in bubble size (Drenckhan and Langevin, 2010). In the following section, the fundamentals of foaming and foam rheology are presented.

2.3 Fundamental of foaming and foam rheology

Foam is a substance that is formed by trapping many gaseous bubbles in a liquid or solid phase. The foam is extremely complex system consisting of poly dispersed gas bubbles separated by draining films. Anything that is analogous to such a phenomenon may be called as foam, such as quantum foam, polyurethane foam. Figure 2.5 shows soap foam.

Figure 2.5. Soap foam.

There is great practical interest about foam because of their widespread occurrence and important properties. Foam is desirable in fire-extinguisher, froth flotation for mineral processing, slag foaming in BOS an EAF converter and undesirable such as industrial distillation tower (Laurier and Fred, 1994). There is no satisfactory explanation of why certain liquids foam strongly, other feebly, and many not at all. A very wide range of foam persistence (Foam life) is observed with different materials from a fraction of second to years. However, despite chemical differences, there must be certain basic mechanical characteristics common to all strongly foaming liquids and differentiating them from non-foaming liquids. The onset of foaming on addition of a solute is hard to define experimentally and in fact little reliable evidence can be found in the literature about such borderline systems (Kitchener and Cooper, 1959). Most foam owes their existence to the surfactant. A surfactant is a constituent which is surface active. These surfactants are concentrated at the surface. Generally they reduce the surface energy or tension associated with the surface.

In foam, gas bubbles are dispersed, that is why gas is generally called dispersed phase, into either liquid or solid, which is called continuous phase, whereas in emulsion two or more immiscible (unblendable) liquids mixes. Both foam and emulsion fall in the general class of colloidal science. A colloid is a substance microscopically dispersed evenly throughout another substance. A colloidal system consists of two separate phases: a dispersed phase (or internal phase) and a continuous phase (or dispersion medium). Emulsions are part of a more general class of two-phase systems of matter called colloids. Although the terms colloid and emulsion are sometimes used interchangeably, emulsion tends to imply that both the dispersed and the continuous phase are liquid. In an emulsion, one liquid (the dispersed phase) is dispersed in the other (the continuous phase). Kozakevitch (1969) distinguished the foam and emulsion as the system consisting of small liquid droplets or gas bubbles imbedded in a liquid medium may be called emulsion when the distances separating the neighbouring droplets (gas/liquid emulsions) are large enough to allow (at least in principle) the independent movement of the liquid drops or bubbles. When the volume of the liquid medium in a gas/liquid emulsion is small as compared with the (total) volume of the gas bubbles, the medium will be present only in the form of thin films separating the adjacent bubbles; these cannot move freely, and the whole system is then called foam.

Hunter et al. (2008) discussed the similarities and differences of foam and emulsion by considering the size and deformability of dispersed phase, main forms of instability (foam instability due to thin film drainage, coalescence and rupture, Emulsion instability due to creaming and sedimentation), Effects of diffusion (gas diffusion leading to coarsening of bubble size, Ostwald Ripening which is controlled by molecular solubility for emulsion), Non-ionic surfactant effect, Hamaker constants, and Particle stabilized systems. In the present research, the dispersed phase (gas bubbles) separated by thin film of liquid will be termed as foam. The present research is concerned with the formation of foam and therefore in the subsequent section details of the foam rheology has been presented and discussed.

2.3.1 Types of foam

Different types of foam is observed and it is hard to classify all type of foam based on single criteria or parameter. Foam can be classified based on different parameter. Different types of parameter and based on the parameter different types of foam was found in the literature. Classification of foam based different parameter found in the literature is presented in Figure 2.6.

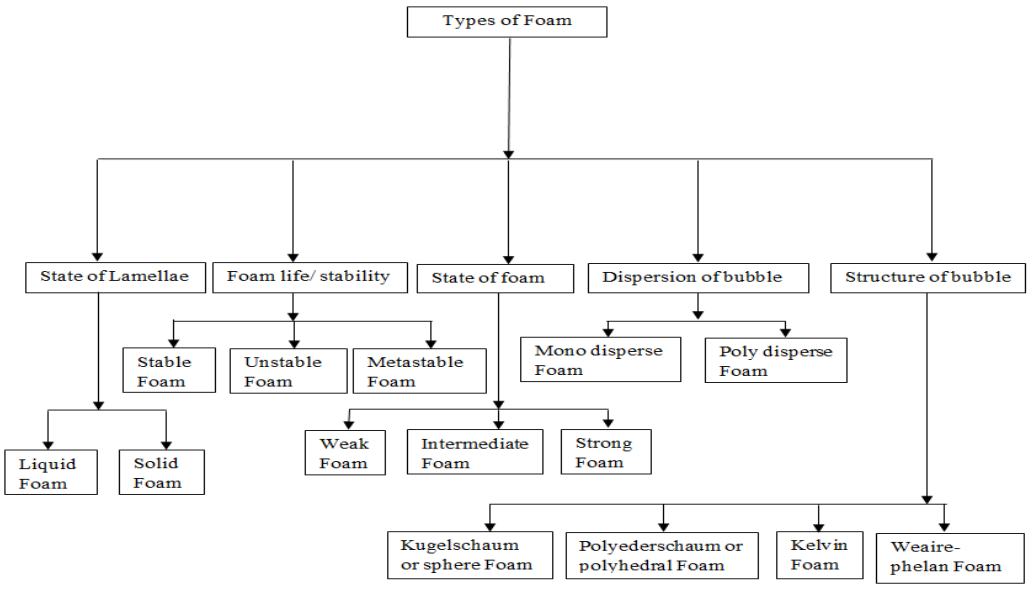

Figure 2.6. Classification of foam.

Based on the type of disperse and continuous phase or the state of lamellae, the foam can be classified as liquid foam and solid foam. If the continuous medium is liquid and the dispersed phase is gas then it is called liquid foam. Here the lamellae separating the gas bubble are liquid. This type of foam is also called as wet foam. Foam created by shaving cream, soap foam and the formation of foam in oxygen steelmaking falls in this category. If the continuous medium is solid and the dispersed phase is gas then it is called solid foam. Here the lamellae separating the gas bubble are solid. These types of foam are termed as dry foam. Foam made of metals like aluminium, steel or even non-metals like solid carbon is solid foam. Figure 2.7 presents liquid foam made of gas liquid and solid foam made from Aluminium. The shape and volume of solid foam normally does not change unless otherwise external force is applied and there is no liquid drainage and bubble bursting in it but the liquid foam is unstable due to liquid drainage and bubble bursting at the top surface of foam.

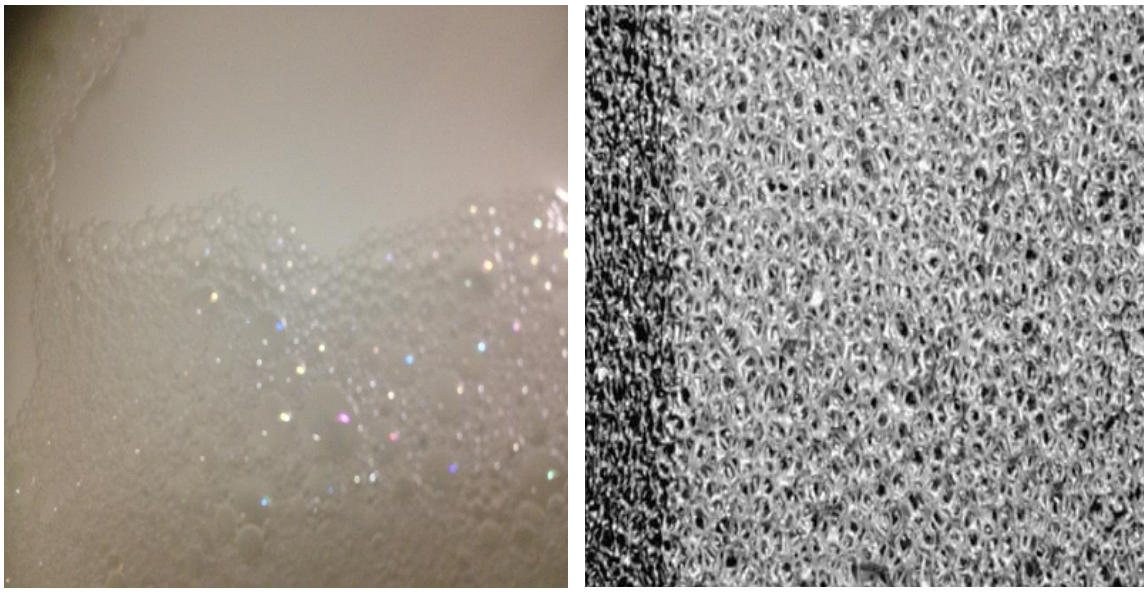

(a) (b)

Figure 2.7. (a) Liquid foam (b) Solid foam (Zhao et al., 2004).

Based on the stability, foam can be classified as stable, unstable, and metastable. All foams are thermodynamically unstable, due to their high interfacial free energy. Pugh (1996) classified foam based on stability into two extreme types, unstable or transient

and metastable. The lifetime of unstable or transient foams is several seconds. Mild surfactants such as short chain alcohols (ethyl, propyl, isobutyl, etc.) aniline, phenol, pine oil and short chain undissociated fatty acids (formic, propionic) belong to this group of weak frothers. Metastable or so-called permanent foams have lifetime as long as days. These foams usually have a lifetime ranging from about ten minutes to several hours. Neethling et al. (2005) classified foam as stable foam and unstable foam. According to their definition stable foams are those foams that neither undergo internal coalescence, nor do they burst at the top surface. Unstable foams are those foams where the bubble collapses at the top down with no internal coalescence. Many types of foam, especially those that are reasonably stable, exhibit this type of behaviour. Based on the characteristics of foam,Vardar-Sukan (1998) classified foams as unstable, metastable, transient or persistent. Unstable foam gradually approaches toward the equilibrium state, constantly breaks down the lamellae as the liquid dries between the bubbles. The lifetime of unstable foam depends on the concentration of the solution. Metastable foam is characterized by the fact that the drying of the liquid between bubbles can stop and the foam can persist indefinitely, if protected from disturbing influences such as vibration, draughts, evaporation, radiant heat, temperature differences, dust and other impurities. Metastability may be conferred on the foam by the presence of a solute that is positively adsorbed at the surface and requires work to remove it from there to the bulk liquid. The life of foam is determined by time of foam formed until all bubble burst. The present study is not concerned for the determination of foam life. The present study is concerned with the dynamic modelling of foam.

Kam (2008) classified three different states of foam termed as weak-foam, intermediate, and strong-foam The terms, weak and strong foams, have been used in the literature to describe the degree of gas-phase mobility reduction: strong foam is referred to as a state at which foam is fine textured with a significant reduction in gas mobility (or a significant increase in pressure gradient, with relatively low saturation), whereas weak foam is referred to as a state at which foam is sparsely textured with a slight reduction in gas mobility (or a slight increase in pressure gradient with relatively high saturation). Based on the dispersion of bubbles, foam can be classified as Mono-disperse foam and Poly-disperse foam. Mono-disperse foam has same size and shape of bubble but poly-disperse foam has an inconsistent size and shape of bubble. The structures of foam

changes continuously with increasing liquid fraction, both geometrically (swelling of Plateau borders and their junctions) and topologically (Weaire and Hutzler, 1999). The schematic of mono-disperse foam in 1D, 2D and 3D and poly disperse foam is presented in Figure 2.8.

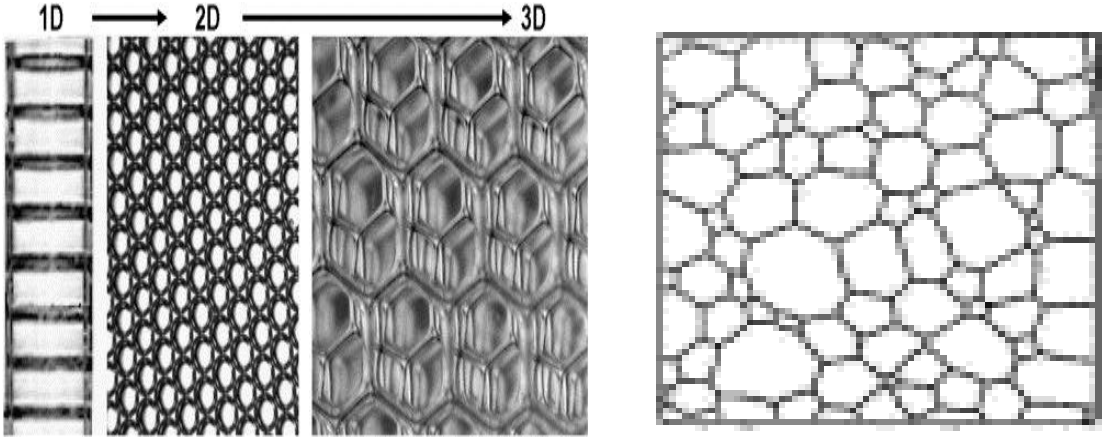

(a) (b)

Figure 2.8. (a) Mono-disperse (b) Poly-disperse foam (Drenckhan and Langevin, 2010).

In foam, bubble coalescence occurs due to rupture of lamellae and gas diffusion. The volume of the gas bubble changes continuously due to coalescence and gas diffusion. Mono-disperse foam turns into poly-disperse foam due to coalescence of bubble and diffusion of gas in bubbles. Present study considered foam as poly-dispersed foam consisting of different bubble size. Ten types of bubble class were considered in the present study.

Based on the structure of bubbles, foam can be classified as Kelvin structure, and Weaire-Phelan structure. Foam with spherical bubble shape is called Kugelschaum and polyhedral shape as polyederschaum (Pugh, 1996) as can be seen in Figure 2.9. Foam consists of packed bubble separated by thin film of liquid. Generally bubbles are in different shape and size in foam. The shape of bubble in foam is normally found as spherical where the liquid fraction is more than 20 percent. On the other hand the shape of bubble is normally found as polyhedral in a foam where the liquid fraction is less than 10 percent (Pugh, 1996).

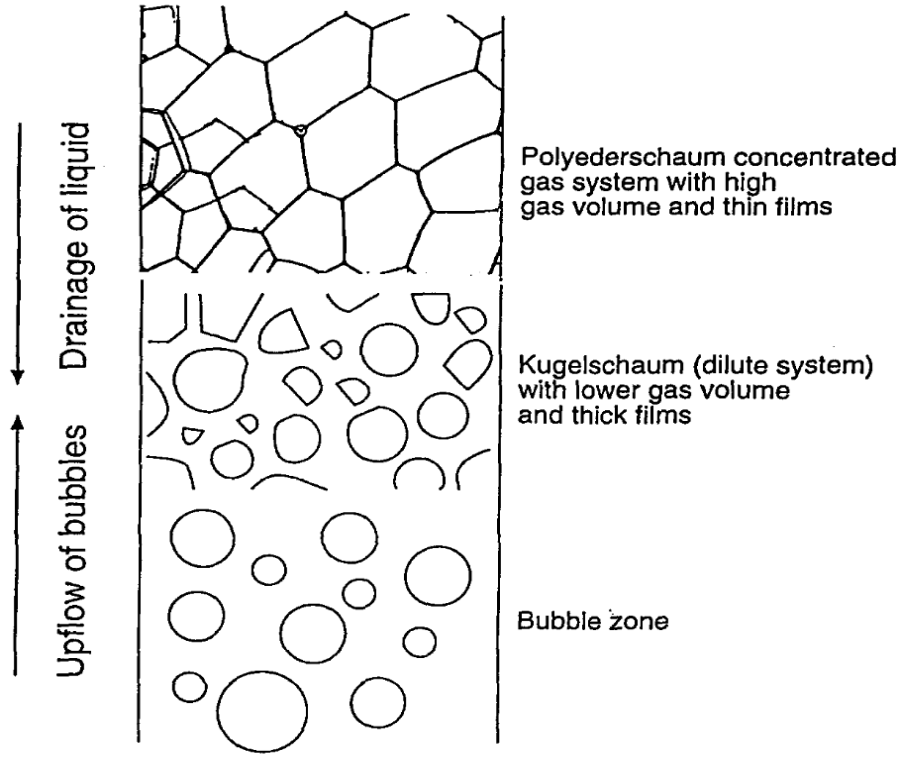

Figure 2.9. Kugelschaum and Polyederschaum foam structure (Pugh, 1996).

Present study considered foam bubble as polyhedral shape. Therefore, in the following section the structure of foam based on polyhedral shape has been presented.

2.3.2 Structure of foams

The building block of foam is gas bubbles separated by liquid or solid phase and the size and shape of bubbles in foam varies. The bubble is either a simple sphere where bubbles are loosely packed or polyhedral in shape where bubbles are closely packed. Even among bubbles having the same volume, there is a variation in the number of faces and the number of edges per face (Bhakta and Ruckenstein, 1997). Foam structures are often represented by unit cells which is gas bubbles of different shape (Gergely and Clyne, 2004). In the present study, polygon foam bubble has been considered. The schematic of a 3D polygon foam bubble showing the vertex, cell face and Plateau border is shown in Figure 2.10(a). The schematic of a 2D polygon foam bubble showing Plateau border with neighbouring bubble is shown in Figure 2.10(b).

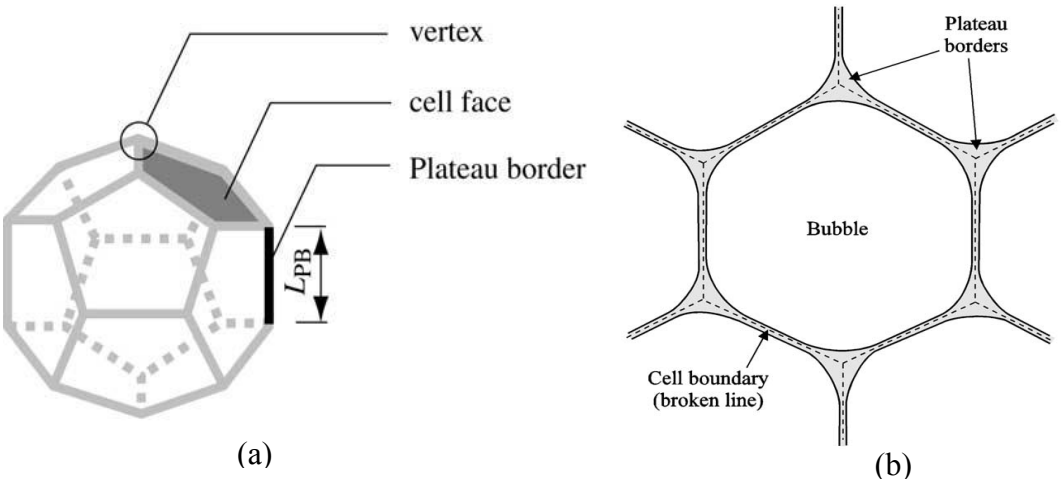

Figure 2.10. Schematic of foam Cell (a) 3D (Gergely and Clyne, 2004) and (b) 2D (Ireland, 2009).

Joseph Plateau, a Belgian physicist, formulated rules for foam which is known as Plateau's rules. This rule states that:

Three and only three films meet at an edge at an angle of 120.

Four and only four edges (Plateau border channels) meet at a point at an angle of 109.

The surface of the cell (bubbles) is a thin film of liquid called lamellae as can be seen in Figure 2.10. Figure 2.11 shows the pentagonal faces of two bubbles are attached with each other and separated by thin film of liquid. Three edges of lamellae from three bubbles are joined and make a channel and the channel is called Plateau border channel. Only three lamellae are connected and radiate 120° outward from the connection point. Figure 2.11 shows the Plateau border channel where the edges of lamellae of three bubbles are connected. In the present study, the bubbles were considered as the pentagonal dodecahedron shape.

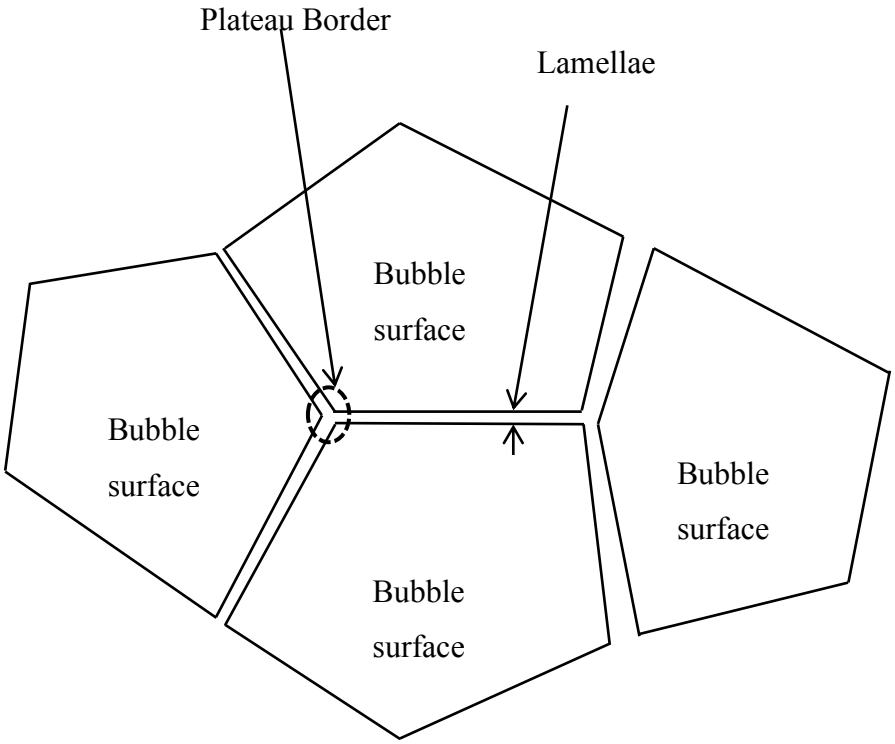

Figure 2.11. Schematic of Lamellae between two bubbles and Plateau border channel.

The liquid drainage occurs through the Plateau border channel due to gravity and capillary force. The mathematic model of liquid drainage is presented in Chapter 4 at Section 4.2.

2.3.3 Kelvin and Weaire–Phelan structure

Lord Kelvin in 1887 asked how space could be partitioned into cells of equal volume with the least area of surface between them, or what was the most efficient bubble foam? Then he proposed foam, based on the bitruncated cubic honeycomb, which is called the Kelvin structure. This is a convex uniform honeycomb formed by the truncated octahedron, which is a 14-sided space-filling polyhedron (a tetradecahedron), with 6 square faces and 8 hexagonal faces. To conform to Plateau's laws governing the structures of foams, the hexagonal faces of Kelvin's variant are slightly curved. The Figure 2.12 shows the Kelvin cell (Weaire et al., 2007). The Kelvin structure was

considered as the least surface area until 1994, when Weaire and Phelan (1994) published the first counter-example to the conjecture that the Kelvin structure has lowest surface area.

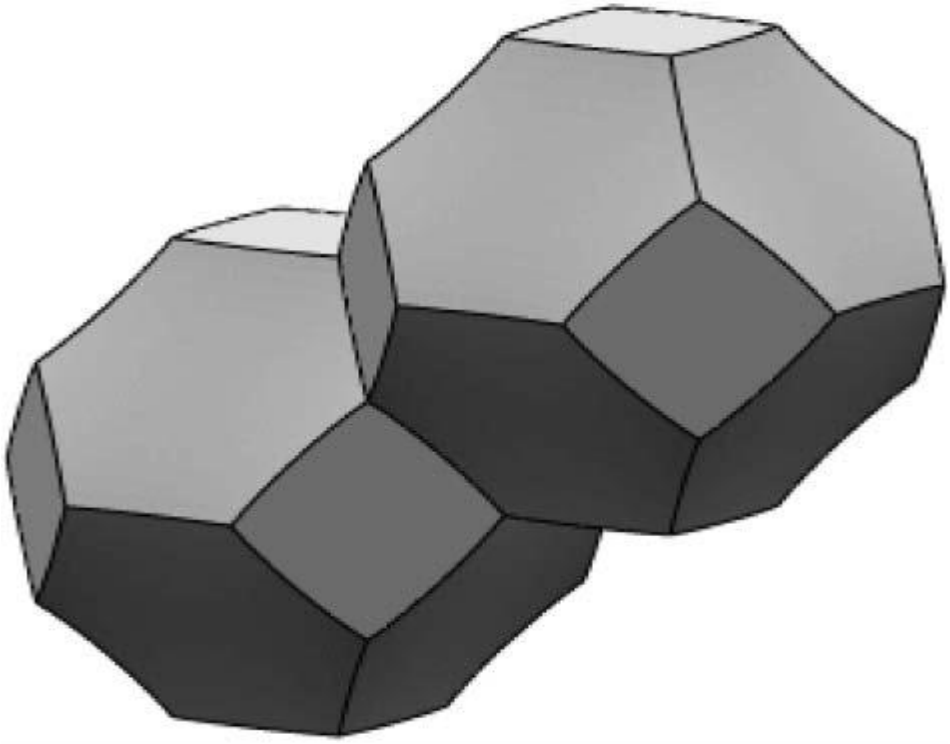

Figure 2.12. The Kelvin Cell, or tetrakaidecahedron, consists of six flat quadrilateral and eight hexagonal faces (Weaire et al., 2007).

In 1993 Denis Weaire and Robert Phelan, two physicists based at Trinity College Dublin, found that in computer simulations of foam a structure with 0.3% less surface area than Kelvin's structure. This structure was a better solution of the best-known Kelvin structure. The Figure 2.13 Shows the Weaire-Phelan structure of bubble. The Weaire-Phelan structure is based on clathrates a class of chemical compounds. This chemical is found in liquid crystals. Real-life foams are typically disordered and have a variety of bubble sizes and shapes. In geometry, the Weaire–Phelan structure is a complex 3-dimensional structure representing idealized foam of equal-sized bubbles. The Weaire–Phelan structure differs from Kelvin's in that it uses two kinds of cells, though they both have equal volume. One is an irregular dodecahedron with pentagonal faces, possessing tetrahedral symmetry. The second is a tetrakaidecahedron with two hexagonal and twelve pentagonal faces possessing antiprismatic symmetry. Like the

hexagons in the Kelvin structure, the pentagons in both types of cells are slightly curved. The surface area of the Weaire–Phelan structure is 0.3% less than that of the Kelvin structure. The Weaire–Phelan structure is considered as the optimal structure as no better structure has been found until now.

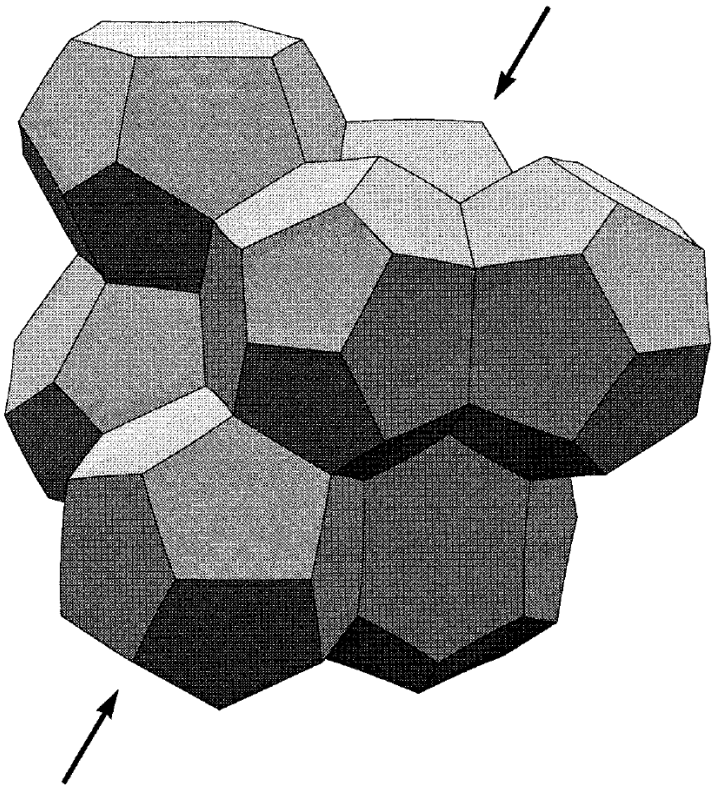

Figure 2.13. Weaire–Phelan structure (Kraynik and Reinelt, 1996).

In the present study, regular pentagonal dodecahedron has been considered for the simplification of numerical procedure of calculating drainage and bursting of bubble due to lamellae break-up. A regular pentagonal dodecahedron bubble is the most acceptable and idealized shape of bubble in real foam. There are 12 pentagonal faces with three meeting at each vertex. It has 20 vertices and 30 edges. The surface of the pentagon, a thin film of liquid termed as lamellae, is shared by adjacent bubble as described before. Three edges of lamellae from three pentagonal dodecahedron bubbles are joined and formed a Plateau border channel. Plateau border channel is curvature at 120° outward from the connection point. Liquid is drained out through the Plateau border channel which eventually causes the rupture of lamellae and thus causes the

coalescence of bubble in foam and bursting at the top. A pentagonal dodecahedron bubble is shown in Figure 2.14. In the present study, the shape of bubble is considered as regular pentagonal dodecahedron. The equation of drainage was calculated based on the regular pentagonal dodecahedron and presented Chapter 4 at Section 4.2.

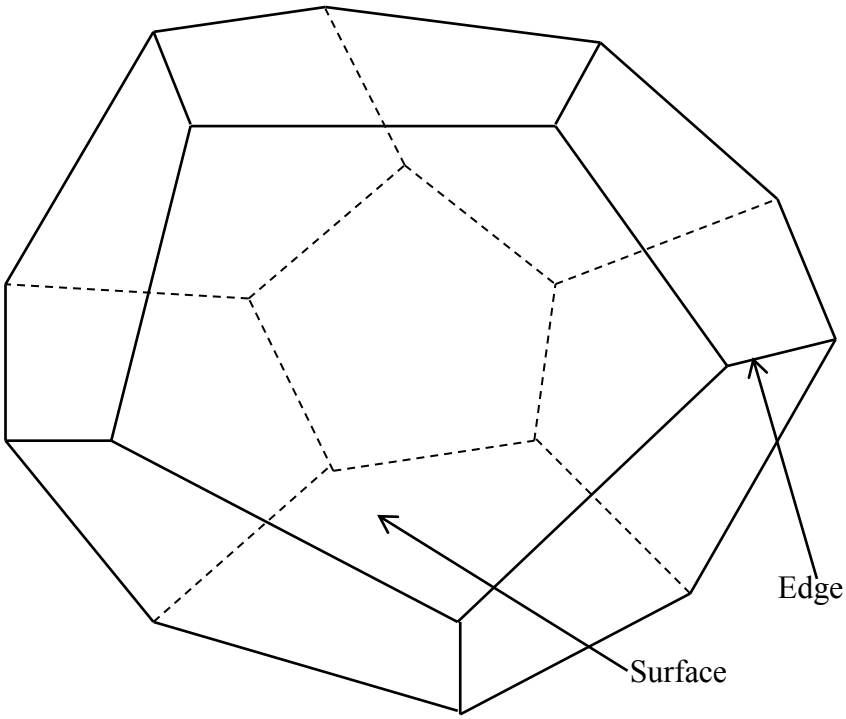

Figure 2.14. Schematic of the pentagonal dodecahedron foam.

2.3.4 Foam stability and parameter

Weaire and Hutzler (1999) has considered phenomena affecting foams classed into the following categories: structure, rheology, drainage and rupture/collapse. The stability of liquid foam is dictated by three main processes: Drainage, Coarsening and Film rupture. Foam drainage plays an important part in the formation and evolution of liquid foams. Freshly formed foam is not in equilibrium under gravity, and liquid drains out of it until such equilibrium is attained. This process is called free drainage. On the other hand, forced drainage is the steady flow through static foam, which can be produced by continuous addition of liquid at the top. The present model considered free drainage due to gravity. The drainage mechanism between bubbles is shown in Figure 2.15.

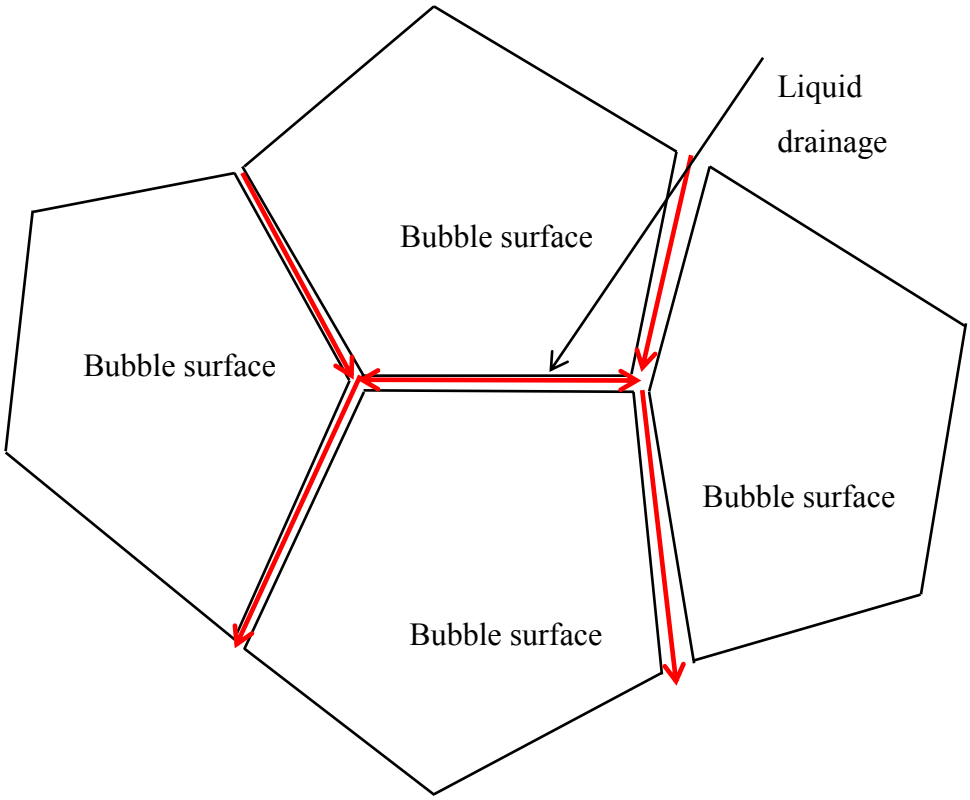

Figure 2.15. Simple drainage mechanism of liquid between bubbles.

Drainage causes the thinning of films between bubbles which eventually causes the coalescence of bubble due to film rupture when a critical film thickness is reached. Drainage can be slowed down by using viscous foaming solutions or by gelification/solidification (Drenckhan and Langevin, 2010). Neethling et al. (2005) derived the standard drainage equation which is based on the work of Leonard and Lemlich (1965) and Verbist et al. (1996), and relates the liquid velocity within a foam, to the cross-sectional of Plateau border area. The drainage equation is extended to include the impact of gas velocity, on liquid drainage. Initially the liquid will drain out due to gravity and will flow downward through the network. However, as a general rule, the drainage rate of foams may be decreased by increasing the bulk viscosity of the liquid from which the foam is prepared. An alternative method to decrease the foam drainage kinetics is by increasing the surface viscosity and surface elasticity. Generally, the surface viscosity and elasticity can be increased by packing a high concentration of

surfactant or particles in the surface causing high adhesive or cohesive bonding (Pugh, 1996).

Coarsening occurs due to gas diffusion between bubbles-some grow while others shrink and disappear. The net result of this process is that the average bubble size grows in time. Coarsening can be slowed down by using gases of poor solubility in water such as fluorinated gases; this simultaneously slows down drainage, since drainage is faster when bubbles are larger. Monodisperse foam with identical bubble topologies (such as the honeycomb or the Kelvin structure) would never coarsen since all bubbles are at the same pressure. But real monodisperse foams always contain topological defects and therefore sooner or later follow the same fate as their polydisperse cousins in that they head to a now well-accepted scaling state, in which only the average bubble size changes, whilst the normalised size distribution remains unchanged (Drenckhan and Langevin, 2010). Rupture will happen if a foam film gets too thin and weak. Eventually the foam will collapse and vanish. Film rupture due to evaporation also occurs if foams are left in the open atmosphere. Film rupture occurs more easily for larger bubbles, the probability of rupture being proportional to the film area, and decreasing with increasing surface compression elastic modulus of the surface layers. The mechanism of stabilization has been summarized by Pugh (1996). Stabilization of foam can be done by surfactant and liquid crystals (Drenckhan and Langevin, 2010).

Swisher and McCabe (1964) conducted an experimental study to understand the possible mechanisms for foam stability in the system of CaO-SiO_2-Cr_2O_3 where Cr_2O_3 is the foaming agent. They found that the Marangoni elasticity effect is probably the largest single contributor to foam stability, although the high viscosity of silicate melts makes some contribution in controlling the rate of drainage of liquid from bubble lamellae. The Marangoni effect (also called the Gibbs-Marangoni effect) is the mass transfer along an interface between two fluids due to surface tension gradient. Drainage affects coarsening since the process of liquid draining along channels (and out of the foam) exposes increasingly large areas of lamellae to coarsening. Meanwhile coarsening affects drainage, as it concentrates the available liquid in fewer (and consequently thicker and faster draining) channels (Grassia et al., 2006). To help stabilise foams or emulsions of pure components, it is normally necessary to add an additional third

component, a foaming/emulsifying agent. Foamers/emulsifiers are classically molecular surfactants.

Surface tension is a property of the surface of a liquid that allows it to resist an external force. Surfactant is a surface-active substance that lowers the surface tension of a liquid, allowing easier spreading, and lowering of the interfacial tension between two liquids, or between a liquid and a solid. Molecular surfactants generally contain a polar (hydrophilic) head group and a non-polar (hydrophobic) chain tail. Surfactants therefore preferentially adsorb to the air/oil–water interface. This reduces the free energy involved with producing a high surface area interface, and as a result, reduces the interfacial surface tension (Hunter et al., 2008). Polymers and proteins cause stability largely through electric and steric repulsion, controlled by the extent of unfolding (or 'denaturing' as unfolded proteins are known) and conformational layer structure on droplets. 'Semi-dilute' polymers and larger 'globular' proteins, which do not denature to the same extent, can further cause stability through changes to the rheological properties of the dispersion medium (namely through increase in viscosity). This may also be achieved through addition of agents such as glycerine. Of course, many naturally occurring emulsions and foams will contain a variety of types of agents, leading to potentially very complex interactions giving overall characteristics (Hunter et al., 2008, Pugh, 1996). The present study considers the coarsening of foam due to drainage of liquid. The effect of gas diffusion on coarsening was disregarded in the present study.

Kitchener and Cooper (1959) studied the foaming of CaO-SiO2 slag at different temperatures. They measured the foam life and found that the foam life increased with decreasing temperature and decreasing basicity. Hara et al. (1983) measured the foam life and foam height and found a good correlation between the foam life, foam height, and surface tension of the slag. In the present study, foaming index was considered. Whilst, there is some objection to the applicability of foaming index (Nexhip et al., 2004, Lin and Guthrie, 1995, Kapilashrami et al., 2006), the foaming index works well for the data set by Ito and Fruehan (1989). Therefore, this approach was used in the modelling of slag foaming in laboratory scale bath smelting slag and presented in Chapter 5 at Section 5.3.

2.3.5 Computational fluid dynamic modeling

Experiments are costly and the only cheap alternative of experiment is simulation. Most large scale simulation provides more insight than experiment. Although simulations would seem to be more advantageous experiments is also important because they provide 'reality-check' during the development of new products. Simulation is used by engineers and physicists to forecast or reconstruct the behaviour of an engineering product or physical situation under assumed or measured boundary conditions (geometry, initial states, loads, etc.). Computational fluid dynamic (CFD) is part of computational mechanics, which in turn is part of simulation techniques (Löhner, 2008). CFD is the analysis of systems involving fluid flow, heat transfer, and mass transfer and associated phenomena such as chemical reaction and bubble-bubble interaction by means of computer-based simulation (Versteeg and Malalasekera, 2007, Löhner, 2008).

The CFD technique has been used in many areas of industrial and non-industrial application. CFD has been used in many engineering field involving multiphase flow. The aerospace industry has integrated CFD technique into the design, research and development, and manufacture of aircraft and jet engines. CFD has also been used in the design of internal combustion engines (Versteeg and Malalasekera, 2007). CFD technique has been used in the chemical engineering process to understand the multiphase flow phenomena as well as mass and momentum interfacial exchange and the chemical reaction in the process. The metallurgical process such as oxygen steelmaking, which is very complex in terms of chemical reaction, mass and momentum transfer between phases, has adopted the CFD technique to understand the multiphase flow and associated phenomena in the system.

Fluid flow phenomena of a system are represented by Navier-Stokes equations. The Navier-Stokes equations are a system of non-linear second order equations in four independent variables. Navier-Stokes equations are based on the conservation laws of physics. Which states that mass, momentum and energy of a system is conserved. The solution of these equations is almost impossible analytically. Therefore, a discretization method is used to get the approximate solution. In this approximation the differential equation is approximated into a system of algebraic equation. A computer is used to

solve the system of algebraic equation iteratively (Versteeg and Malalasekera, 2007, Löhner, 2008).

There are many methods for the discretization of the differential equation. The main methods for discretization are: finite difference (FD), finite volume (FV) and finite element (FE) methods. Other methods such as spectral schemes, boundary element methods, and cellular automata are also used in CFD for special classes of problems. The discussion on finite difference (FD), finite volume (FV) and finite element (FE) methods is presented as follows:

The finite difference (FD) is believed to have been introduced by Euler in the 18th century. The starting point is the conservation equation in differential form. The solution domain is covered by a grid. At each grid point, the differential equation is approximated by replacing the partial derivatives by approximations in terms of the nodal values of the functions. The result is one algebraic equation per grid node in which the variable value at a certain number of neighbour nodes appear as unknowns. Taylor series expansion or polynomial fitting is used to obtain approximations to the first and second derivatives of the variables with respect to the coordinates (Versteeg and Malalasekera, 2007, Löhner, 2008).

The FE method is used to solve complex elasticity and structural analysis problems in solid geometry. In this method the domain is broken into a set of finite elements and each element is represented by element equations of the original problem. Then all set of element equations are recombined into a global system of equations for the final calculation. In the FE methods the equations are multiplied by a weight function. Then they are integrated over the domain. In this method the solution is approximated by a linear shape function for each element to guarantee continuity of the solution across element boundaries. The function can be constructed from the values at the corners of the elements. This approximation is then substituted into the weighted integral of the conservation law. The weighted integral with respect to each nodal value are set to zero. The result is a set of non-linear algebraic equations. An important advantage of finite element methods is the ability to deal with arbitrary geometries. The principal drawback, which is shared by any method that uses unstructured grids, is that the

matrices of the linearized equations are not as well structured as those for regular grids making it more difficult to find efficient solution methods (Versteeg and Malalasekera, 2007, Löhner, 2008).

The domain in FV method is divided into a finite number of volumes called control volume (CV). The FV method uses the integral form of the conservation equations for mass momentum and energy for the control volume. The computational node is located at the centroid of the control volume. The values of the variable are calculated each node of the control volume. Interpolation is used to express variable values at the CV surface in terms of the nodal values. Surface and volume integrals are approximated using suitable quadrature formulae. As a result, one obtains an algebraic equation for each CV, in which a number of neighbour nodal values appear. The FV method can accommodate any type of grid, so it is suitable for complex geometries. The grid defines only the control volume boundaries and need not be related to a coordinate system. The method is conservative by construction, so long as surface integrals (which represent convective and diffusive fluxes) are the same for the CVs sharing the boundary. The FV approach is perhaps the simplest to understand and to program. All terms that need be approximated have physical meaning which is why it is popular with engineers. Most of the CFD software is based on FV method such as FLUENT, PHOENICS, STAR-CD, and AVL-FIRE. Hence in the present study, AVL-FIRE software was used for the numerical simulation of multiphase flow phenomena (Versteeg and Malalasekera, 2007, Löhner, 2008).

2.3.6 Multiphase flow model

Multiphase flow is referred to the flow where more than one phase is present. A phase is a state of matter (gas, liquid and solid). The term multiphase flow is used to refer to any fluid flow consisting of more than one phase or component. A definition of phases by Wallis (1969) states: “A phase is simply one of the states of matter and can be either a gas, a liquid or a solid (AVL-FIRE, 2008). Two general topologies of multiphase flow can be usefully identified at the outset, namely disperse flows and separated flows. Disperse flows mean the distribution of finite particles, drops or bubbles (the disperse phase) in a connected volume of the continuous phase. On the other hand separated

flows consist of two or more continuous streams of different fluids separated by interfaces. Multiphase flow is a ubiquitous event in our environment such as raining, snowing, fog, dusty winds, and water flowing from a faucet, avalanches, mud slides, sediment transport, debris flows, and numerous other natural phenomena. Two phase flow is the simplest of its kinds. Sometime single-phase flow is assumed to avoid complexities provided the other phase have negligible effect on the flow. However, there are many phenomena, where this assumption is wrong such as cavitation, boiling, and slurry flows etc. The details behaviour of multiphase flow and their phenomenon they manifest can be explored in different ways. This can be visualized by experimental set up with appropriate instrument. Applying mathematical model and equation multiphase flow properties can be theoretically determined. The model and the prediction of details of multiphase flow and their phenomena can be achieved computationally by using the powerful computers to address the complexity of the flow (Brennen, 2005).

With the advent of high speed computing system the prediction of multiphase flow behaviour computationally is common now a day. In the present study, multiphase flow phenomena were predicted computationally using computer. There are two main approaches for the simulation of multiphase flow: Euler-Euler approach and Euler-Lagrangian approach. Euler-Euler and Euler-Lagrangian approach for the simulation of multiphase flow phenomena is presented in the following section.

2.3.7 Eulerian and Lagrangian approach

The two main approaches used for the simulation of multiphase flow are Euler-Euler approach and Euler-Lagrangian approach. In the Euler–Euler approach both the continuous and dispersed phases are considered to be interpenetrating continua. Eulerian–Lagrangian approach uses discrete bubble model (DBM) or model-free direct numerical simulations (DNS) where all the particle or bubble in the gas phase is tracked individually (Bannari et al., 2008, Bhole et al., 2008). The distinction between the Eulerian and Lagrangian method is the reference of observation. The distinction between the Eulerian and Lagrangian method is elucidated by the Figure 2.16. In the figure the domain is subdivided into a small volume which is called control volume and

presented by solid line. The fluid flow is represented by the velocity vector (arrow) and the material volume is represented by dotted line. The arrow represents the flow pattern of material volume. The control volume is fixed in space and the material volume enters into and exit from the control volume. The fluid flow can be observed either by observing the trajectory of material volume containing fluid or by observing fluid properties at a location fixed in the space.

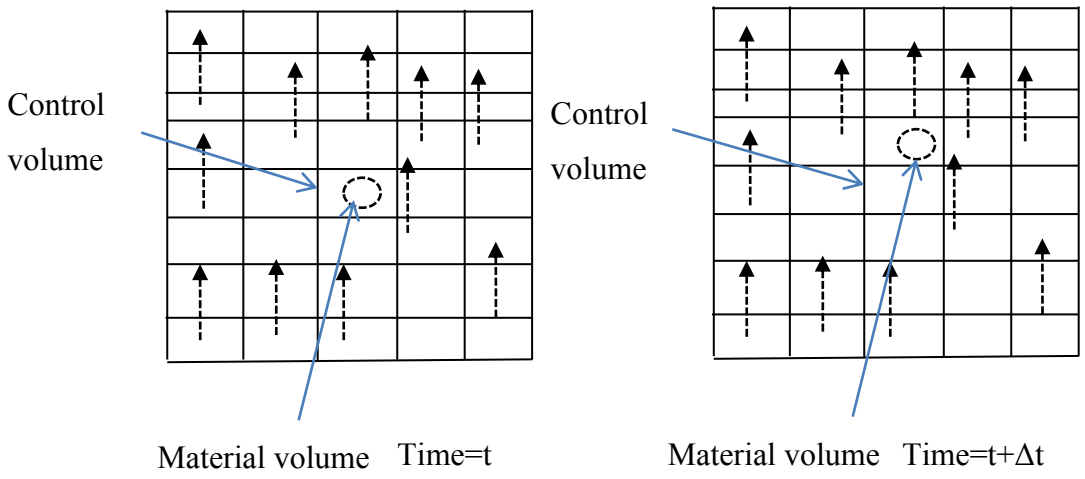

Figure 2.16. Schematic presentation of fluid flow with time.

In Lagrangian representation the position, pressure, and other properties of material volumes is sought and described. In Eulerian representation, the fluid properties inside control volumes is sought and described. The most natural way to observe a fluid flow is to observe the trajectories of discrete material volumes or parcels. In Eulerian method the control volume is fixed in space and the fluid flow in and out of the control volume is observed whereas in Lagrangian method the material volume flow in space is observed.

The Eulerian–Lagrangian has also been used in the field of gas–liquid bubble columns (Lapin and Lübbert, 1994, Sokolichin et al., 1997, Delnoij et al., 1997, Druzhinin and Elghobashi, 1998, Bunner and Tryggvason, 1999, Bokkers et al., 2006). The computation time and cost in Eulerian–Lagrangian approach is higher than in Euler–

Euler approach. Therefore, the Euler–Euler approach is more economical and commonly used (Bhole et al., 2008). The mathematical model of multiphase flow phenomena in Euler–Euler approach is well established. The present study used AVL-FIRE 2009.2 simulation software which is based on the Euler–Euler approach. The software allows the following model in Euler–Euler approach (AVL-FIRE, 2008):

• Homogeneous (Equilibrium) Model

• Multifluid Model

• Volume-of-Fluid (VOF) Free-Surface Model

In Euler-Euler approach, the homogeneous model is considered as the least accurate multiphase model. In this model, volume fraction equation is calculated for each phase but only a single momentum equation is calculated for the phases in momentum equilibrium. In the multifluid model, all conservation equations are solved for each phase. The Volume-of-fluid model is very similar to the homogeneous model from the numerical perspective. A single momentum equation is calculated for all phases that interact using the VOF model. However, the calculation of volume fraction equations using VOF model is considerably more accurate allowing the sharp resolution of the interfaces. One of the common defects of the VOF calculation can occur when the interface is not resolved sharply despite the use of the high-order discretization techniques for the volume fraction equation and in that case the VOF model degenerates into the homogeneous model. This is quite common in many practical calculations. It happens due to very high-resolution requirements of the VOF model that can be often hard to fulfil. Since the multifluid model requires by default the calculation of the complete set of the conservation equations for each phase, it represents the basis for the Euler-Euler schemes in the FIRE Eulerian Multiphase Module (AVL-FIRE, 2008).

The present research was carried out by using the commercial CFD package AVL FIRE (Version 2009.2). The FIRE Eulerian Multiphase Module with Multifluid Model based on the Euler-Euler approach was used. In Euler-Euler approach the disperse phase was divided into different bubble class and population balance equation was applied to track

their number density. The detailed descriptions of the population balance modelling are presented in the following section.

2.4 Population balance modeling, bubble break-up and coalescence

This section presents the overview of the population balance modelling for the prediction of bubble class in dispersed flow. Different types of population balance modelling and the method for their solution is highlighted. The source term of population balance equation is the death and birth of bubbles. So the different mechanism of bubble break-up and bubble coalescence is also discussed and presented and the model used for the present study is clarified.

2.4.1 Population balance model

Population balance modelling is a method to track individual entities by considering specific properties with time. Integro-partial differential equations which are called population balance equation (PBE) are used to calculate the number of individual entities with time. PBEs have been used in many branch of science including engineering especially in the field that deals with particle, bubbles. Population balances were used to model biological populations in the early 1960s and were first formulated for chemical engineering purposes by Hulburt and Katz (1964). The population balance equation (PBE) arises in numerous systems involving dispersed phases, for example, colloids, polymers, powders, or emulsions (Lin et al., 2002). Numerous CFD simulations of bubble columns have incorporated PBE to track the number density of different bubble class in the dispersed phase under Euler-Euler approach (Bannari et al., 2008, Bhole et al., 2008, Martín et al., 2007, Martín-Valdepeñas et al., 2007, Chen et al., 2005, Díaz et al., 2008). In some applications breakage and agglomeration, or coalescence, is an indispensable part of dispersion of two fluid phases. Then accurate prediction of mass transfer area through population balances requires modelling of breakage as well as coalescence of bubbles or droplets (Alopaeus et al., 2006). Present study deals with multiphase flow incorporating bubble break-up and bubble coalescence in the process. Therefore, the present study has incorporated the population balance equation to track the number density of different bubble class by taking into account the

bubble break-up and coalescence. The mathematical model of the population balance equation is presented in Chapter 3 at Section 3.2.3.3.

Population balances can be one-dimensional and multi-dimensional balances. In the one-dimensional population balance model only one property of bubble/particle such as size is modelled. It is possible to include measured properties such as liquid saturation (Darelius et al., 2005) in the kernel, but only granule size can be modelled in a one-dimensional population balance simulation (Iveson, 2002). In multi-dimensional PBM more than one property is considered. By using a multi-dimensional balance, granule size, liquid saturation and porosity can be modelled. It has been found that liquid saturation and granule porosity both influence the probability for coalescence in some cases (Annapragada and Neilly, 1996). The property measured of the particle size such as particle volume, mass or an equivalent diameter/radius, but other properties may also be of relevance: e.g. a distribution of surface area or particle velocity when inertial effects are important (Rigopoulos, 2010). Kostoglou and Konstandopoulos (2001) have solved the general multi-dimensional population balance equation by using Monte Carlo simulation and Biggs et al. (2003) have used an approach where the multi-dimensional population balance is replaced by multiple coupled one-dimensional population balances that are solved simultaneously. Verkoeijen et al. (2002) have proposed another framework for solving the general population balance equation presented by Randolph and Larson (1988). Applications where multi-dimensional population balances can be used have been described recently, but numerical techniques for solving the equations are still under development, as the equations are computationally demanding to solve. The present study is concentrated only on the volume of bubbles; therefore in the present study one-dimensional population balance equation has been used.

The population balance equations are a set of Integro-partial differential equations which gives the behavior of a population of particles from the analysis of behavior of single particle in local conditions (Ramkrishna, 2000). The literature on methods available for the solution of the PBE is quite extensive and is reviewed in a recent book by Ramkrishna (2000). There are many numerical techniques to solve the PBE. Among the various techniques, the method of successive approximations, the method of Laplace transform, the method of moments, weighted residuals, sectional methods, the finite

volume methods and Monte Carlo simulation methods are commonly used. The sectional methods are well known in process engineering because they are simple to implement and produce exact numerical results of some selected properties. On the other hand the finite volume schemes are well suited for solving conservation laws. The number density based PBE can easily be transformed to a conservation law of mass. Then the finite volume schemes can be implemented efficiently (Kumar, 2006). In the present study the PBE used is based on the finite volume approach. The population balance equation is discretized by fixed pivot or moving pivot technique (Kumar and Ramkrishna, 1996a, Kumar and Ramkrishna, 1996b). The source term in the PBE is the birth and death of bubble due to break-up and coalescence. Hagesaether et al. (2002) developed the model for the distribution of daughter bubble due to break-up and coalescence. The model proposed by Hagesaether et al. (2002) is most suitable for the implementation in CFD. However a small error was found in their model and in the present study, the error found in the model proposed by Hagesaether et al. (2002) has been rectified and used in this study. The details rectification is presented in Chapter 3 at Section 3.2.3.4.

The volume of bubble can change due to several reasons. The most common reasons are breakage, coalescence, gas diffusion, nucleation and growth (Kumar, 2006). In the present study, bubble breakage and coalescence was considered as the main reasons for the change of bubble volume. In the subsequent section, detailed review of the bubble break-up and coalescence mechanism is presented.

2.4.2 Bubble break-up model

In the last decades, analysing and modeling of the bubble break-up in the multiphase flow process has received considerable effort and a great number of models for the break-up frequency and daughter size distribution were published. The breakage of bubble causes the changes of bubble number density of different bubble classes in the system. The breakage of bubble is introduced as a source term in the population balance equation. Bubble break-up refers to the fragmentation of parents bubble (bubble that breaks) to its daughter bubble (bubble formed after breakage). There are different mechanisms by which bubble can break into its lower counterpart. The main

mechanisms found in the literature are turbulent fluctuation, viscous shear stress, shearing-off process and interfacial instability. The different mechanism of bubble break-up is shown in Figure 2.17.

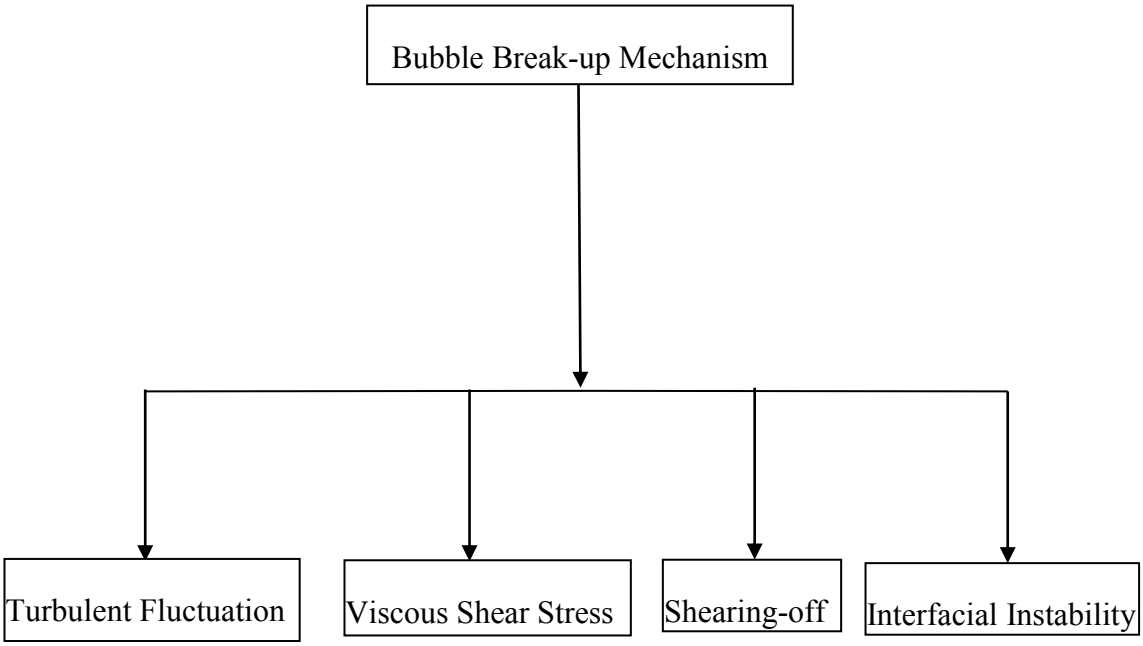

Figure 2.17. Different types of bubble break-up mechanisms.

2.4.2.1 Turbulent fluctuation and collision of eddy

In the turbulent case, the break-up of bubble is mainly caused by turbulent pressure fluctuations along the surface, or by bubble-eddy collisions. The bubble can be assumed to modify its spherical form with the fluctuation of the surrounding fluid or due to collisions with eddies. When the amplitude of the oscillation is close to that required to make the bubble surface unstable, it starts to deform and stretch in one direction leading to a neck that contracts further and fragments finally into two or more daughter bubbles (Liao and Lucas, 2009). Kolmogorov (1949) and Hinze (1955) developed a theory for bubble or drop break-up in turbulent flows. They suggested that a bubble breaks as a result of interactions with turbulent eddies that are of approximately the same size as the bubble. They assumed that the bubble size was in the inertial sub-range of turbulence length scales so that Kolmogorov's universal energy spectrum could be used to estimate the strength of eddies having sizes comparable to the bubble. The process of bubble

break-up due to surface instability which causes the necking and finally fragments into two or more daughter bubbles is shown in Figure 2.18.

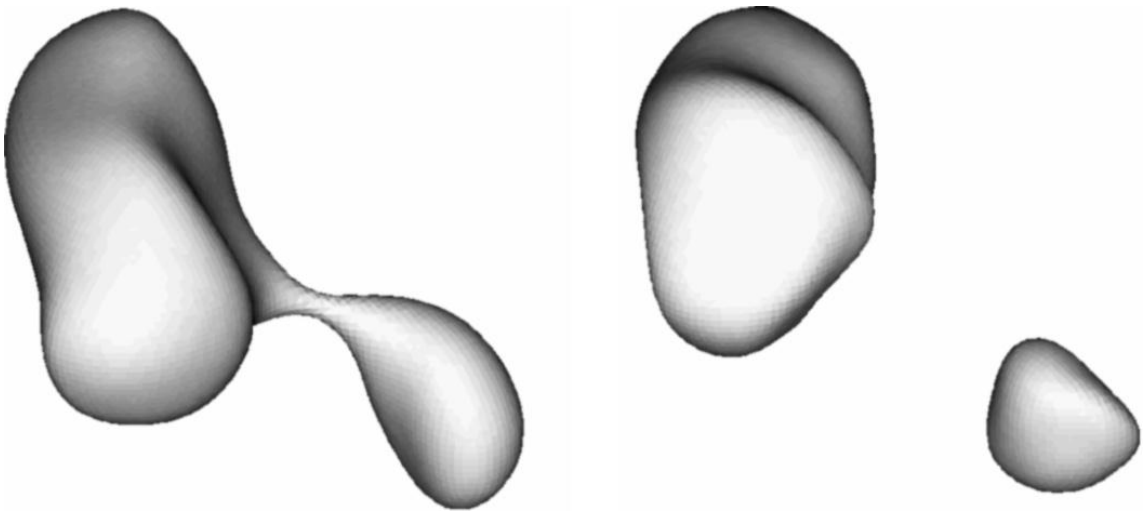

Figure 2.18. Break-up of bubble due to turbulent pressure fluctuation (Qian et al., 2006).

The break-up of a bubble in a turbulent flow field is also caused by the bombarding of eddies with characteristic size equal to or smaller than the bubble onto the surface of the bubbles. Eddies larger than the bubble merely carry the bubbles (Zhao and Ge, 2007). The Figure 2.19 shows the fragmentation of bubble due to the bombardment of eddy.

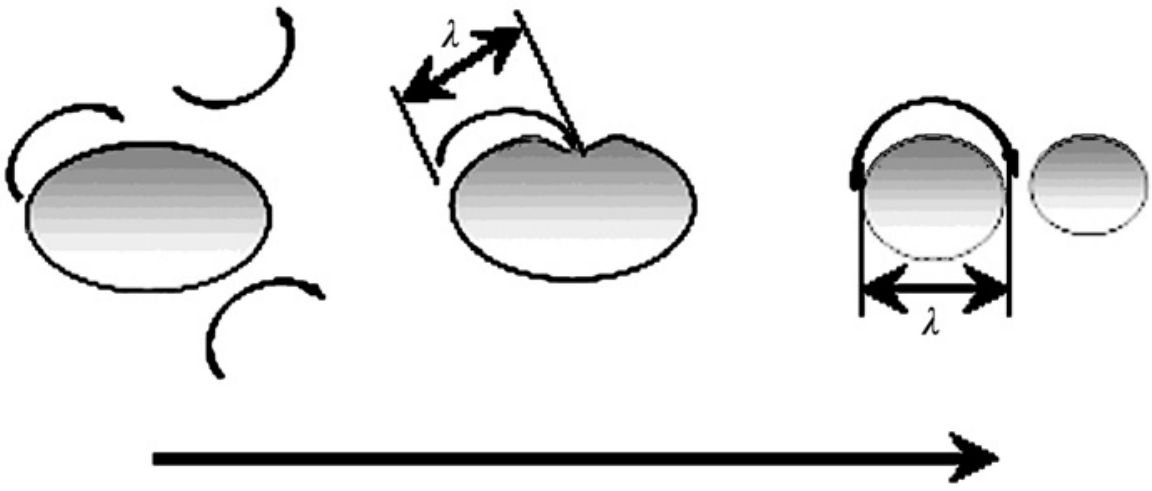

Figure 2.19. Bubble break-up due to eddy bombarding (Zhao and Ge, 2007).

The bubble break-up model developed by researcher due to turbulent fluctuation and collision of eddy is based on the critical energy. The definition of critical energy is defined arbitrarily and presented by Liao and Lucas (2009) in their review paper on bubble break-up mechanism as surface energy of the parent particle (Lee et al., 1987, Prince and Blanch, 1990, Martínez-Bazán et al., 1999a, Martínez-Bazán et al., 1999b) or the increase in the surface energy before and after break-up (Luo and Svendsen, 1996, Wang et al., 2003a, Zhao and Ge, 2007), or the mean value of the surface energy increase for breakage into two equal-size daughters and into a smallest and a biggest one (Tsouris and Tavlarides, 1994). For break-ups caused by this mechanism, five different criteria were used. The first criteria is based on the turbulent kinetic energy of the particle greater than a critical value (Coulaloglou and Tavlarides, 1977, Chatzi and Lee, 1987). The second criteria are based on the velocity fluctuation around the particle surface greater than a critical value (Alopaeus et al., 2002, Narsimhan et al., 1979). The third criteria is based on turbulent kinetic energy of the hitting eddy greater than a critical value (Lee et al., 1987, Luo and Svendsen, 1996, Prince and Blanch, 1990, Tsouris and Tavlarides, 1994, Martínez-Bazán et al., 1999a, Martínez-Bazán et al., 1999b). The fourth criteria is based on the inertial force of the hitting eddy greater than the interfacial force of the smallest daughter particle (Lehr et al., 2002). The fifth criteria is based on the combination of third and fourth the criterion (Wang et al., 2003b, Zhao and Ge, 2007).

There are also other researchers who consider Weber number as a criteria for bubble break-up. The Weber number, a dimensionless number, is the ratio between the inertial force and the surface tension force. Hinze (1955) pointed out a criterion for break-up based on a force balance and mentioned that a bubble would deform and break when the surface tension was unable to balance the random pressure fluctuations that cause deformation. He suggested that a bubble will break only when the Weber number exceeded a critical value and he estimated that the critical Weber number for drop break-up based on the experimental results and found 1.18. Levich (1962) developed a criterion for bubble break-up similar to that of Kolmogorov (1949) and Hinze (1955) except that Levich (1962) considered the density of the bubble as well as the liquid. Shinnar (1961) used Taylor (1934) analysis of break-up due to viscous stresses to develop a criterion for bubble break-up based on the assumption that the bubble sizes

are on the order of the Kolmogorov scale or smaller. Finally, Baldyga and Bourne (1993) generalized the above results to account for turbulent intermittency using a multi-fractal approach. The multi-fractal method accounts for the (often large) deviations of the local energy dissipation rate from the mean value. Many investigators have studied bubble or drop size distributions in turbulent flows theoretically and experimentally (Coulaloglou and Tavlarides, 1977, Prince and Blanch, 1990, Walter and Blanch, 1986, Bouaifi and Roustan, 1998). Although most researchers used the Kolmogorov-Hinze theory, many formulas were proposed to predict the maximum stable bubble or drop size, and a wide range of critical Weber numbers was obtained based on different assumptions and experiments. Sevik and Park (1972) predicted a critical Weber number equal to 2.6 by observing the splitting of air bubbles penetrating a water jet. They performed experiments with bubbles in the size range 4.0 to 5.8 mm. They postulated a resonance mechanism involving a bubble dynamics and turbulent fluctuations in addition to the force balance. According to their criterion, the threshold Weber number for break-up is determined by the condition that two characteristic frequencies are equal (Lamb, 1932). The other frequency is the characteristic frequency of turbulence fluctuations for eddies that are of the same size as the bubble.

Numerous applications of the bubble break-up model based on the turbulent collision are in the literature. Bannari et al. (2008) developed a CFD model to investigate the Coalescence and break-up in gas–liquid dispersion are represented using the CM of PBE. The models are implemented in the open source package Open-FOAM. Bannari et al. (2008) used the bubble break-up model developed by Luo and Svendsen (1996) in the CFD modelling of bubbly flow in a rectangular bubble column. Bordel et al. (2006) used the break-up model of Wang et al. (2003a) in the CFD modelling of bubbly flow. Martín-Valdepeñas et al. (2007) carried out a CFD comparative study of different bubble break-up models (Luo and Svendsen, 1996, Tsouris and Tavlarides, 1994, Martínez-Bazán et al., 1999a) in a turbulent multiphase jet. Chen et al. (2005) used the break-up model of Luo and Svendsen (1996) and the break-up model of Martínez-Bazán et al. (1999a) for the prediction of bubble break-up rate in the bubble column flow. Diaz et al. (2008) carried out a numerical simulation of the gas–liquid flow in a laboratory scale bubble column and the break-up of bubble were predicted using the model of Luo and Svendsen (1996) model. Mohanarangam et al. (2009) also carried out a numerical

simulation of the gas–liquid flow and the break-up of bubble were predicted using the model of Luo and Svendsen (1996) model. Montante et al. (2008) investigated the turbulent two-phase flow and the bubble size distribution in aerated stirred tanks by experiments and computational fluid dynamics modelling. In their modelling they used the break-up model of Luo and Svendsen (1996). Olmos et al. (2001) investigated the operation of a cylindrical bubble column to evaluate bubble sizes using the break-up model of Luo and Svendsen (1996). Bhole et al. (2008) also developed computational fluid dynamics code using finite volume method in Eulerian framework for the simulation of axisymmetric steady state flows in bubble columns. They incorporated the break-up model of Luo and Svendsen (1996) to predict the break-up rate of bubble.

Bannari et al. (2008) used the model of Luo and Svendsen (1996) for its simplicity. In Luo and Svendsen (1996) break-up model, a predefined daughter bubble size distribution is not needed to predict break-up rate for bubbles and thus avoids some of the problems of the original model. The daughter size distribution can be directly calculated from the model. At the same time the bubble break-up model of Luo and Svendsen (1996) assumes binary break-up and contains no adjustable parameters. Therefore, the break-up model of bubble based on turbulent kinetic energy of the hitting eddy greater than a critical value developed by Luo and Svendsen (1996) has been used in the present study. The details mathematical model of the bubble break-up rate is presented in Chapter 3 at Section 3.2.3.5.

2.4.2.2 Bubble break-up due to viscous shear stress

Viscous shear forces in the continuous phase will cause a velocity gradient around the interface and deform the fluid particle, leading to break-up. Shear stresses also appear due to the wake effect. If a trailing bubble or drop has its larger part outside a wake region, the shear stress across the wake boundary may split it as a result of elongation, bubble surface indentation and necking (Liao and Lucas, 2009). The pioneering work of Taylor (1934) demonstrated that the drop break-up occurs when the capillary number which expresses the ratio of the viscous stress acting on the drop surface and drop capillary pressure, exceeds some critical value, which depends on the ratio of the viscosities of the dispersed and continuous phases, called “viscosity ratio’. The bubble

break-up model based on viscous shear stress is available in the literature (Kocamustafaogullari and Ishii, 1995, Renardy and Cristini, 2001).

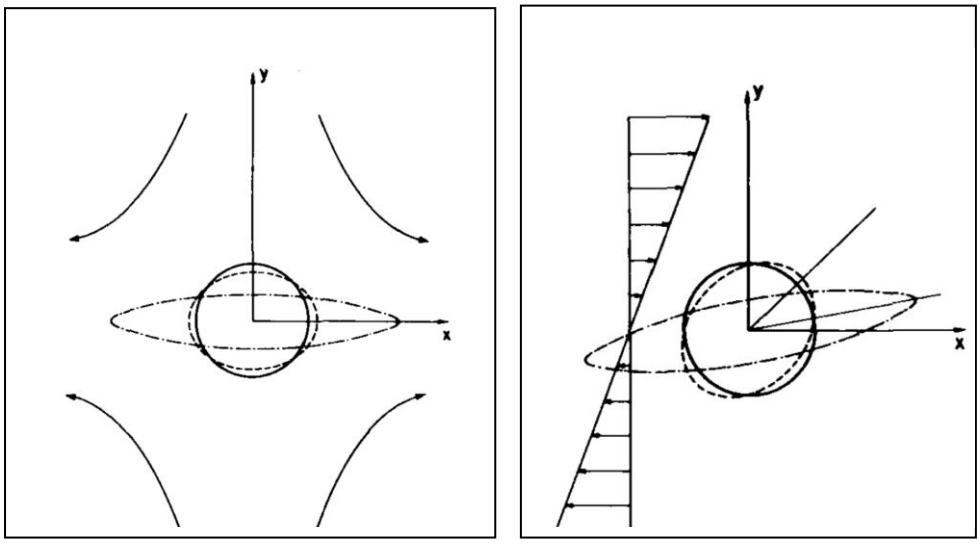

Figure 2.20. Successive deformation of bubble with increasing shear strength of a drop placed in (a) Simple shear flow and (b) Hyperbolic flow (Acrivos, 1983).

Vyakaranam and Kokini (2012) used FEM simulation method to predict air bubble dispersion in a viscous fluid in a twin-screw continuous mixer. They incorporated the break-up of bubble due viscous shear. Li and Renardy (2000) analysed deformation and break-up of a viscous drop in a Bingham liquid by placing a spherical drop between two moving parallel plates. This type of breakage is observed in highly viscous fluid. For the present study, the breakage of bubble due to viscous shear stress is not significant and therefore this mechanism of breakage is disregarded.

2.4.2.3 Bubble break-up due to shearing off

The shearing-off process is characterized by a number of small particles sheared-off from a large one, which is also called erosive breakage. In highly viscous flows, the shearing-off is determined by the balance between the viscous shear force and the surface tension at skirts of the cap/slug bubble. When the relative velocity is high enough, bubble skirt becomes unsteady and sheds from large bubbles with the generation of a large number of small bubbles at the rim. However, in the air–water

flow, the interfacial viscous shear force is shown to be negligible by both experimental and theoretical investigations due to the low viscosity of water. In this case, the shearing-off process is caused by the gas velocity profile inside the cap bubble. Gases inside the bubble move globally at the bubble terminal velocity, while the boundary near the air–water interface has a velocity equal to the annular liquid film surrounding the bubble.

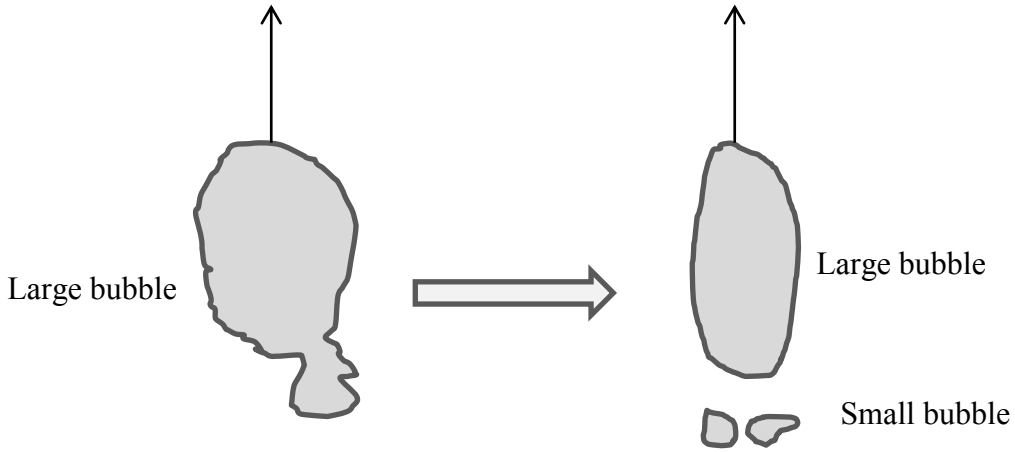

Figure 2.21. Schematic of shearing off small bubble from large bubble.

Lin and Sundararaj (2004) investigated sheet formation during drop deformation and break-up. The shearing of bubble is also investigated by (Smith et al., 2012) and (Jing and Xu, 2010). This type of breakage is also observed in highly viscous fluid therefore, in the present study, the breakage of bubble due to shearing off is disregarded.

2.4.2.4 Bubble break-up due to interfacial instability

Instability can occurs at the surface of bubble and eventually breaks the bubbles into parts. Most of the break-up mechanisms depend on the flow dynamic characteristics in the continuous phase. However, even in the absence of a net flow in the continuous phase as for example bubbles rise in a liquid and drops falling in a continuous gas or immiscible liquid, the break-up can be caused by interfacial instabilities. Interfacial instabilities in fluid systems are characterized by material interpenetration and mixing at molecular scales due to perturbations occurring at material interfaces. Rayleigh-Taylor,

Richtmyer-Meshkov, and Kelvin-Helmholtz instabilities are important hydrodynamic instabilities. Richtmyer-Meshkov instability is shock-induced and occurs due to the interaction between the shock wave and the perturbed material interface separating two fluids. Kelvin-Helmholtz instability is shear-induced and occurs in a continuous fluid system where velocity shear is present or between two fluids due to a sufficient velocity difference across the interface. The Schematic of bubble break-up mechanism due to interfacial instability is shown in Figure 2.22. In the process of the interfacial instabilities there are many stages involved, which are greatly affected by the parameters of the system.

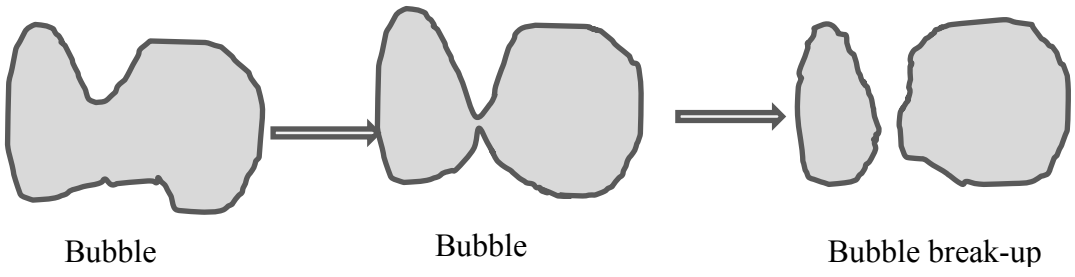

Figure 2.22. Schematic of bubble break-up due to interfacial instability.

All bubble break-up models are not significant for all conditions. In the present study, the continuous phase is in most cases turbulent flow and therefore the break-up frequency is focused on the turbulent flow. Furthermore, the turbulent fluctuation is assumed arbitrarily to be the dominant break-up mechanism and the effects of viscous force, relative velocity and interfacial instability on break-up phenomena are not significant for the present study.

2.4.3 Bubble coalescence model

The coalescence of bubble also causes the changes of number density of bubble classes in the system. In the population balance equation, the coalescence of bubbles is introduced as a source term in the main equation. The coalescence of bubble is reverse of bubble break which is the aggregation of bubble. A review on various mechanisms and available kernel models for the coalescence of fluid particles (bubbles and drops) is

available the recent paper by Liao and Lucas (2010). The most popular and acceptable theory of bubble coalescence is the film drainage model. Coalescence of bubbles occurs when two bubbles collide, trapping liquid between them and the liquid drains out until a critical thickness is reached and eventually the film ruptures. Generally, three theories or criteria have been proposed for the coalescence process. The most popular theory is the film drainage model. Shinnar and Church (1960) state that, after the collision bubbles the bubbles may cohere together and be prevented from coalescing by a thin film of liquid trapped between them. Attractive forces between them drive the film to drain out until it collapses, and coalescence follows. The whole coalescence event can be divided into three sub-processes: (1) two bubbles collide, trapping a small amount of liquid between them; (2) bubbles keep in contact till the liquid film drains out to a critical thickness; (3) the film ruptures resulting in coalescence. Bubble coalescence occurs when two bubbles come closer and collide; therefore the collision of bubble is the prerequisite of coalescence. There are different mechanisms by which bubbles come closer. From the literature reviews it is found that collision, a prerequisite to coalescence, may occur due to turbulence fluctuation, viscous shear stress, laminar shear, capture in turbulent eddies, buoyancy and wake interaction (Liao and Lucas, 2010, Prince and Blanch, 1990, Wang et al., 2005, Wu et al., 1998, Friedlander, 2000, Friedlander, 1977, Chesters, 1991). The main mechanisms found in the literature are shown in Figure 2.23.

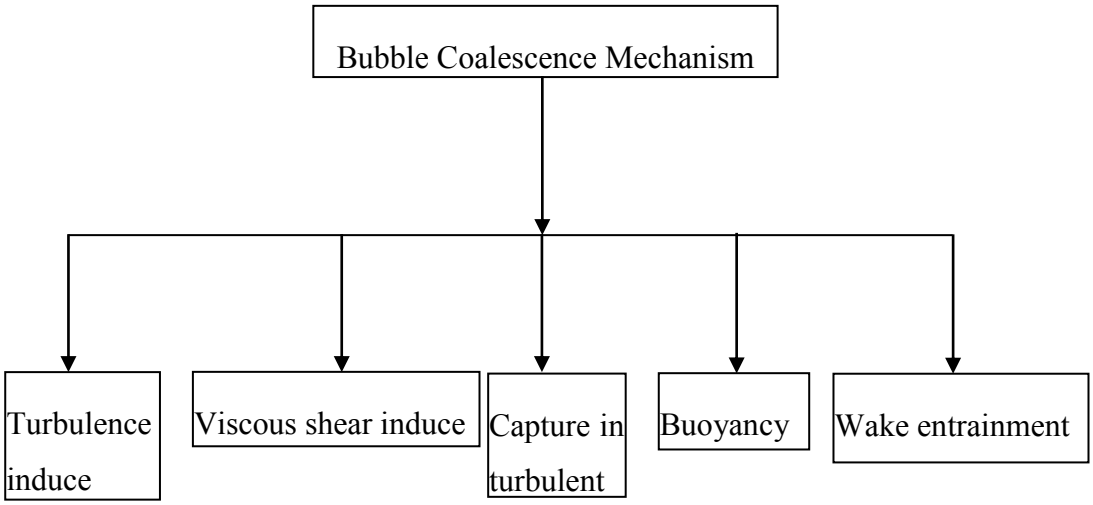

Figure 2.23. Different types of bubble coalescence mechanisms.

2.4.3.1 Turbulent induce collision

Coalescence of bubble may be caused by the collisions of bubbles and this collision may be caused by the fluctuating turbulent velocity of the surrounding liquid. The Figure shows the coalescence of two bubbles due to turbulent velocity. The sub-processes of (a) two bubbles collide, trapping a small amount of liquid between them; (b) bubbles keep in contact till the liquid film drains out to a critical thickness; (c) the film ruptures resulting in coalescence is shown in the Figure 2.24.

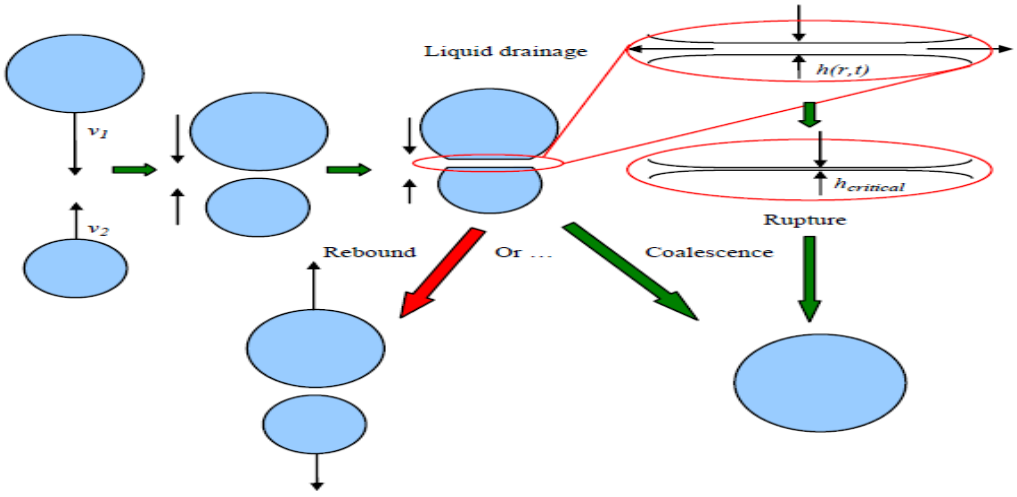

Figure 2.24. Schematic of turbulent induce collision (Chen et al., 2005).

The model of coalescence of bubble due to turbulent fluctuation is available in the literature (Prince and Blanch, 1990, Wu et al., 1998, Lehr et al., 2002, Wang et al., 2005). The difference among the model is mainly the calculation of collision frequency and coalescence efficiency. Numerous application of this model is in the literature. Bordel et al. (2006) used the coalescence model of Lehr et al. (2002) in the CFD modelling of bubbly flow. Mohanarangam et al. (2009) used coalescence model of Prince and Blanch (1990) based on turbulent fluctuation to predict the coalescence rate. Olmos et al. (2001) investigated the operation of a cylindrical bubble column to evaluate bubble sizes using the break-up model of Luo and Svendsen (1996) and the coalescence model from Prince and Blanch (1990) is used. Diaz et al. (2008) carried out a numerical simulation of the gas–liquid flow in a laboratory scale bubble column using

the coalescence model of Prince and Blanch (1990) due to turbulent induce collision. Present study has considered the coalescence model of Prince and Blanch (1990) to predict the coalescence rate of bubble based on turbulent fluctuation. The details of the mathematical model are presented in Chapter 3 at section 3.2.3.6.

2.4.3.2 Viscous shear induce collision

Swarm of bubble often undergoes shear flow, which causes the dispersed particles to collide with each other. The Figure 2.25 shows the movement of bubble under shear flow. Friedlander (1977) pointed out that particles in a uniform, laminar shear flow may collide with each other because of velocity gradients which prevail also in the bulk of a turbulent flow (Liao and Lucas, 2010). Friedlander (1977) and Tavlarides and Stamatoudis (1981) presented the model of frequency of shear-induced collisions in the uniform laminar flow. The model based on laminar shear is developed by Prince and Blanch (1990).

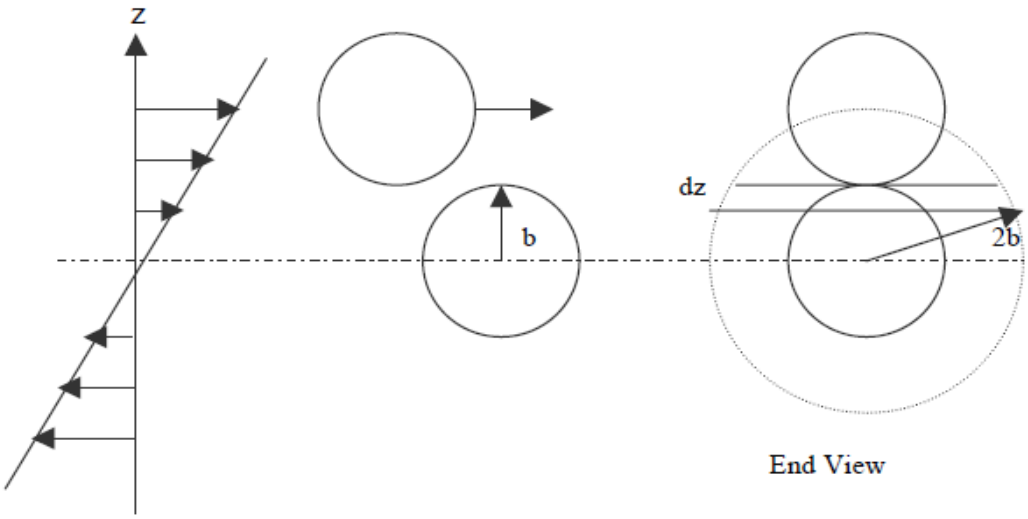

Figure 2.25. Shear induce flow of bubbles (Agarwal, 2002).

2.4.3.3 Capture in turbulent eddies

In this mechanism bubble is captured by the turbulent eddies. Then the velocity of bubble is dominated by the velocity of eddies. This happens when the size of eddies are larger than the size of bubbles. The Figure 2.26 shows the mechanism of bubble coalescence due to capture in turbulent eddies schematically. Chesters (1991) states the when the drop size is much smaller than the size of the energy dissipating eddies found in a turbulent flow, the force governing the collision will be predominantly viscous. In other words, the bubble velocities will be very close to the velocity of the continuous phase flow field. It is the same case when the density difference is negligible (Kocamustafaogullari and Ishii, 1995). Under this condition, the collision frequency will be determined only by local shear of the flow in turbulent eddies. In contrast to the laminar shear, the turbulent shear rate is used in the capture in turbulent eddies.

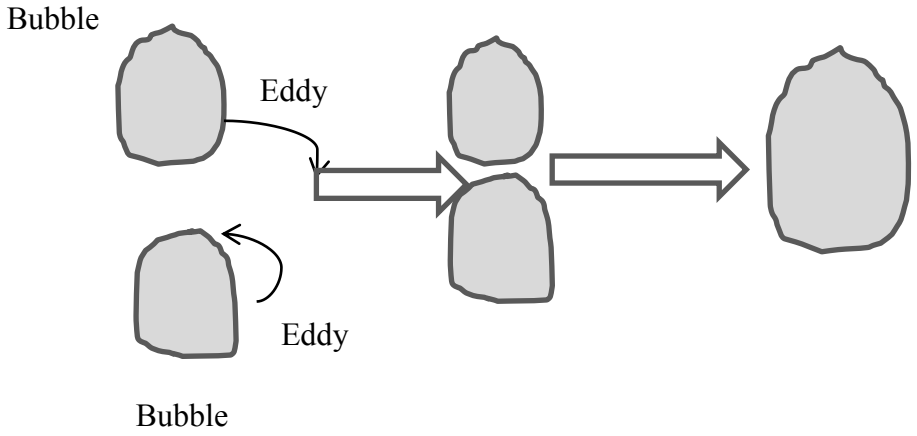

Figure 2.26. Schematic of bubble coalescence due to capture in turbulent eddies.

2.4.3.4 Buoyancy induce collision

The bubble in a liquid rises with different velocity due their difference size. Because of the relative velocity between bubbles they collide on their way to top surface of liquid. The bubble coalescence mechanism due to buoyancy induced collision is shown in Figure 2.27. According to Prince and Blanch (1990), bubble collisions may result from the difference in rise velocities of bubbles having different sizes. Laari and Turunen

(2005) used the model of Prince and Blanch (1990) to predict the coalescence of bubble in a gas-liquid reactor. Bordel et al. (2006) used the buoyancy driven collision model of Prince and Blanch (1990) in the CFD modelling of bubbly flow.

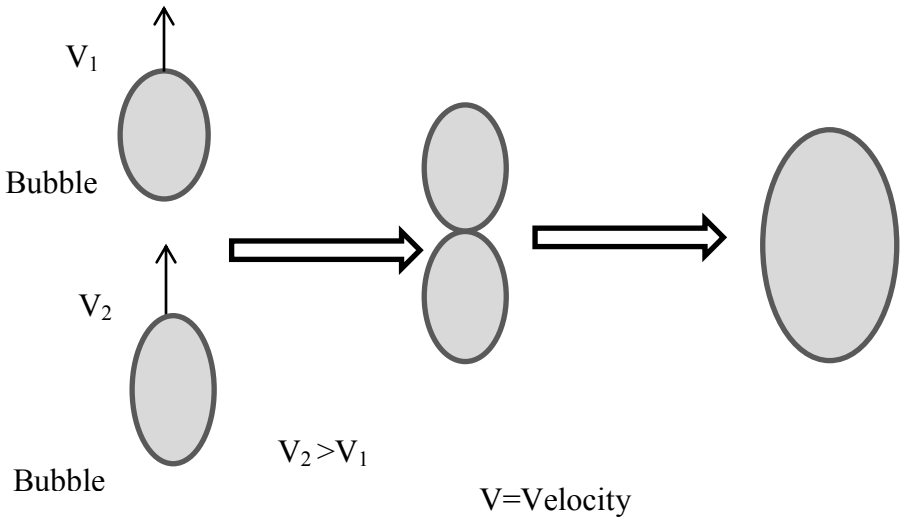

Figure 2.27. Schematic of bubble coalescence due to buoyancy induce collision.

In the present study, the Euler-Euler approach was incorporated in the modelling of bubble-bubble interaction of the system. In the Euler-Euler approach, the velocity of bubble is same as the velocity of gas phase. Therefore, all bubbles rise with the same velocity and hence there is no relative velocity between bubbles. But the relative velocity is the primary cause of this type of coalescence. For this reason the coalescence of bubble based on the buoyancy driven collision was disregarded in the present study.

2.4.3.5 Wake entrainment collision

During the free-rise of gas bubbles through a liquid an amount of liquid is inevitably carried up and accelerated behind the bubbles, which is known as the wake. The wake entrainment is a phenomena where the trailing bubble accelerates and coalescences with the leading one when the bubble enters the wake region of a leading large bubble as shown in Figure 2.28. When the leading bubble is large, a circular wake is formed

behind the large leading bubble. This wake is considered as a mixing region with a high level of turbulence.

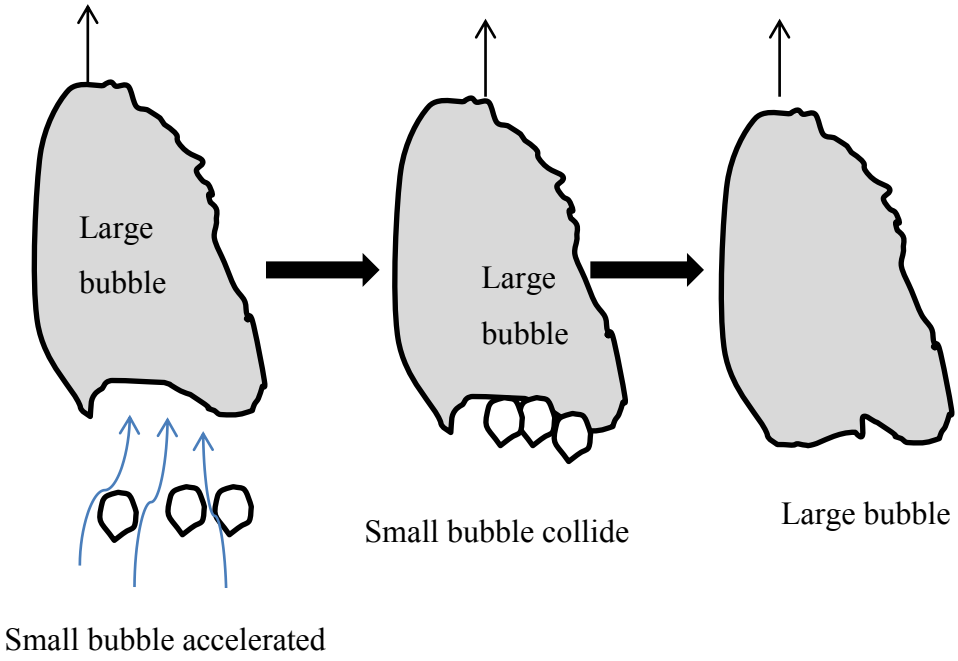

Figure 2.28. Schematic of bubble coalescence due to wake entrainment.

In the last few decades it has been realized that the wakes play a significant role in the interaction between bubbles (Komasawa et al., 1980). When bubbles enter the wake region of a leading bubble, they will accelerate and may collide with the preceding one (Bilicki and Kestin, 1987). In the experiment of Stewart (1995), the wake was observed to be the driving force and sole mechanism for bubble interaction. Wake-induced collisions result in coalescence primarily between pairs of large cap bubbles in fluids sufficiently viscous to keep their wakes laminar. Different model of collision frequency due to wake entrainment is available in the literature (Wu et al., 1998, Hibiki et al., 2001, Kalkach-Navarro et al., 1994). The mechanism of Wake entrainment is the dominant interaction mechanism of cap bubbles and accounts for the transition from bubbly to slug flow (Liao and Lucas, 2010). The relative velocity between the leading and following bubbles is important in the wake entrainment but in the present model bubbles were assumed to move with same velocity irrespective of their size.

There are numerous model for bubble break-up and bubble coalescence available in the open literature. All models are not applicable for all conditions and at the same time incorporation of all the models is out of the scope of the present study. Therefore, in the present study the break-up model of Luo and Svendsen (1996) due to turbulence and the coalescence model of Prince and Blanch (1990) in the gas liquid dispersion was considered. The coalescence model of Tong et al. (2011) was used in foam. The mathematical model of bubble break-up and bubble coalescence mechanism used in this study is presented in Chapter 3-4.

2.4.4 Daughter bubble distribution

When parent bubble (bubble which breaks/coalesces) undergoes break-up or coalescence event it generates a daughter bubble (bubble form after break-up or coalescence). The daughter bubbles it produces may not match exactly to the bubble class considered in the present study. Therefore, the daughter bubbles need to distribute among the predefined bubble class after break-up and coalescence. If the volume of daughter bubble falls between predefined bubble classes then the daughter bubble is distributed using the model developed by Hagesaether et al. (2002). The distribution of daughter bubbles into parents bubble due to break-up and coalescence is modelled by Hagesaether et al. (2002). The model has been used by many researchers (Laari and Turunen, 2003, Laari and Turunen, 2005, Sha et al., 2006). The model is suitable for CFD model of bubble break-up and coalescence. But an anomaly was found in the equation of birth and death term due to break-up and coalescence. Therefore, the model of Hagesaether et al. (2002) has been rectified and used in the present study. The detailed rectification is discussed and presented in Chapter 3 at Section 3.2. In the present study bubble was divided into finite number of class. Division was done based on the volume of bubble. Each class has exact volume. In this study, the method of class (CM) (Ramkrishna, 2000, Kumar and Ramkrishna, 1996a, Kumar and Ramkrishna, 1996b) was used to divide the bubble. The application of CM can be found in the literature (Bannari et al., 2008). In the division of bubble class, the volume of upper bubble class was considered as twice of its lower counterpart and bubbles are considered as sphere.

CHAPTER 3

MODELING OF BUBBLE COLUMN REACTOR WITH POPULATION BALANCE

3 Modeling of bubble column reactor with population balance

This chapter presents a numerical simulation of a bubble column reactor for the prediction of number density of different bubbles class in turbulent dispersed flow. A computational fluid dynamic (CFD) model was developed for the numerical simulation of multiphase flow coupling with bubble break-up and bubble coalescence. The daughter bubble distribution source term model of Hagesaether et al. (2002) has been rectified and used for the numerical simulation of the present model. The details of the rectification of this model has been explained and presented in this chapter. The numerical prediction was based on two fluid models, using the Eulerian-Eulerian approach where the liquid phase was treated as a continuum and the gas phase (bubbles) was considered as a dispersed phase. Bubble-bubble interactions, such as breakage due to turbulence and coalescence due to the combined effect of turbulence and laminar shear were considered. A user subroutine has been written in FORTRAN programming language to incorporate bubble break-up and bubble coalescence into the main CFD software. The number density of different bubble class was determined at different height of the bubble column and Sauter mean diameter of the bubbles class was calculated. The result shows that the radial distributions of number densities of lower bubble classes are more than its higher counterpart. The result also shows that the Sauter mean diameter increases with the increase of height up to 1m and then become steady. The predicted results from the CFD model were validated against experimental data available in open literature. Simulated results are found to be in reasonable agreement with the experimental data available in the literature.

3.1 Introduction

Many industrial processes use bubble column reactor such as Fischer-Tropsch synthesis, coal liquefaction, and fermentation processes due to high interfacial area, high mass and heat transfer (Chen et al., 2005). Accurate prediction of individual bubble are important for the design of a system as the change of the number of bubbles change the interfacial area which affects the heat and mass transfer between phases. Various mechanisms of bubble break-up have been investigated over time. The main mechanisms found in the literature are turbulence fluctuation, viscous shear stress, shearing-off process and interfacial instability (Liao and Lucas, 2009, Zhao and Ge, 2007, Müller-Fischer et al., 2008, Taylor, 1934, Qian et al., 2006, Wang et al., 2005). For the coalescence mechanisms five types are found in the literature, namely, turbulent induced coalescence, viscous shear induced coalescence, capture in turbulent eddies, buoyancy driven coalescence, and wake-entrainment (Luo and Svendsen, 1996, Prince and Blanch, 1990, Friedlander, 1977, Wu et al., 1998, Chesters, 1991). All mechanisms of bubble break-up and coalescence are not significant in all conditions. Bubble break-up due to turbulence and bubble coalescence due to turbulence and laminar shear are the focus of this study.

Hulburt and Katz (1964) used population balances to model demographic population in the early 1960s and were first implemented in chemical engineering purposes (Verkoeijen et al., 2002). The population balance equation (PBE) arises in numerous systems involving dispersed phases, for example, colloids, polymers, powders, and emulsions (Lin et al., 2002). The literature on methods available for the solution of the PBE is quite extensive and is reviewed in the recent book by Ramkrishna (2000). Population balances are of two types: one-dimensional and multi-dimensional balances. In one-dimensional balance, only one property, such as size is modeled whereas in multi-dimensional balance, more than one property such as size, liquid saturation and porosity are modelled (Ramachandran and Barton, 2010, Darelius et al., 2005, Iveson, 2002). There are different numerical techniques to solve the PBE: the method of successive approximations, the method of Laplace transforms, the method of moments, weighted residuals, sectional methods, the finite volume methods and Monte Carlo simulation methods (Kumar, 2006).

The gas bubbles in liquid can be modeled in three different approaches: Eulerian–Lagrangian approach, direct numerical simulations (DNS) and Euler–Euler approach. Eulerian–Lagrangian approach uses discrete bubble model (DBM) or model-free direct numerical simulations (DNS) where all the particle or bubble in the gas phase is tracked individually. This approach is limited by the computational cost and time of simulation (Lapin and Lübbert, 1994, Sokolichin et al., 1997, Delnoij et al., 1997, Druzhinin and Elghobashi, 1998). In the Euler–Euler approach both the continuous and dispersed phases are considered to be interpenetrating continua. The disperse phase is divided into different bubble classes and population balance equation is applied to track their number density. Lo (1996) developed the multiple size group (MUSIG) model where the author divided the bubbles in different size group with same velocity. Ramkrishna (2000) presented bubble distribution through a finite number of bubble classes called class of method (CM). In the CM, the PBEs are solved in terms of the volume fractions of each bubble class. The population balance equation is discretized by fixed pivot or moving pivot technique (Kumar and Ramkrishna, 1996a, Kumar and Ramkrishna, 1996b). The model proposed by Hagesaether et al. (2002) for turbulent binary break-up of dispersed fluid particles is most suitable for the implementation in CFD. However a small error was found in the source term of death and birth of bubbles due break-up and coalescence in the population balance equation. Gas-liquid flow involving bubbles are very important for many industrial processes including metal processing. CFD has been successfully used in metal processing involving gas-liquid flow (Alam et al., 2011, Alam et al., 2010a, Alam et al., 2010b, Alam et al., 2012, Huda et al., 2012, Laari and Turunen, 2003, Sha et al., 2006, AVL-FIRE, 2008).

In this study, the correction of an error found in the development of source term of death and birth of bubbles due to break-up and coalescence in the population balance equation proposed in Hagesaether et al. (2002) is presented. A 3D CFD model similar to the experimental model of Laari and Turunen (2003) was developed for the numerical simulation. The developed CFD model is used to predict the number density of different bubble class. The daughter bubble distribution source term in the model derived by Hagesaether et al. (2002) for PBE has been corrected and used to evaluate the number density of different bubble class. Then the Sauter mean diameter is calculated along the height of the model. The bubble break-up model of Luo and Svendsen (1996) and the

coalescence model of Prince and Blanch (1990) are used in the present study. Ten types of bubble classes are considered in the present study. The result obtained from the simulation is compared with the predicted and experimental result of Laari and Turunen (2003). The predicted data is also compared with that of Laari and Turunen (2005) and Sha et al. (2006).

3.2 Model geometry and methodology for bubble column reactor

The governing equations for the conservation of mass and momentum in Eulerian multiphase flow model and the numerical methods used for the modelling of bubble column reactor are presented in this section. Population balance equation and the equation for the closure term of bubble break-up and bubble coalescence are presented in this section. The details of the modification of the existing daughter bubble distribution source term of bubble break-up and bubble coalescence are explained and elaborated in this section. The details descriptions of the boundary conditions assigned for modelling of bubble column reactor is elaborated here. The details of the modelling techniques and its feature are discussed. Meshing procedure of the present model and the methodology used for the numerical simulation is also presented. Initial conditions of the model and the properties of the fluid used for the numerical simulation are also presented in this section.

3.2.1 Model geometry and features

Simulation was carried out in a cylindrical bubble column similar to the experimental model of Laari and Turunen (2003). The generated grid of the model is shown in Figure 3.1. The bubble column is 4.6m high with 0.078m internal diameter. The inlet diameter was 2.34×10^{-3}m which is equivalent to sparger of 382 holes with diameter 1.2×10^{-4} each. The surface mesh of the model was generated by the CAD software Rhinoceros 3.0 then the surface mesh was imported in CFD simulation software AVL FIRE 2009.2 to generate volume mesh of the model. The meshing was performed by using the Fame Advance Hybrid technique available in the simulation software. Special refinement was done on the inlet of the model. The volume mesh of the model was generated and numerical simulation was performed by commercial CFD package AVL

FIRE 2009.2. The simulation was run in an unsteady state with a time step of 10^{-1} second on Intel Xeon Quad Core Z400 Machine with 8.0 GB RAM with processor speed 2.66 GHz.

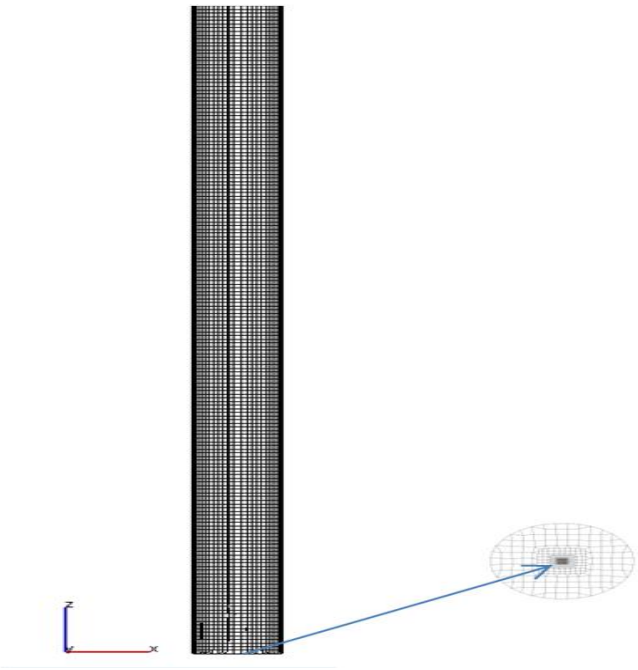

Figure 3.1. Grid generated for the numerical analysis of bubble column reactor.

In this model, an unsteady state solution for multiphase momentum and continuity were used and for turbulence, a standard $k-\varepsilon$ turbulence model was used. A cell centered finite volume approach was used to discretise the governing equations and the resulting discretised equations were solved iteratively. The Central Differencing Scheme (CDS) can generate numerical oscillations yielding unbounded and non-monotonic solutions. A well-known remedy is to adopt the (first-order-accurate) upwind differencing scheme (AVL-FIRE, 2008). The inaccuracy involved in turbulent modeling, foam modeling, chemical reaction etc. used in the present complex phenomena does not warrant the improvement which may have been achieved through the usage of higher order differential schemes. Therefore, for momentum and turbulence, first order upwind differencing scheme was used. The central differencing scheme with second order accuracy was used for the continuity equation. Walls were treated as nonslip boundaries with standard wall function. The modelling of bubble break-up and bubble coalescence

together with the population balance modelling was incorporated in the main CFD software as subroutine written by the author in FORTRAN programing language. Bubbles were divided into ten bubble classes where the volume of the upper bubble class was twice the volume of the lower countepart such that $v_i = 2v_{i-1}$. The diameters of the bubble classes tracked in this simulation are presented in Table 3.1.

Table 3.1 Bubble classes used in the simulation.

Bubble class index	1	2	3	4	5	6	7	8	9	10
Bubble diameter ($\times 10^{-3}m$)	1.57	1.98	2.49	3.14	3.96	4.98	6.27	7.91	9.97	12.56

3.2.2 Boundary conditions assigned for bubble column reactor

The following boundary conditions were applied in the computational domain for bubble column reactor.

3.2.2.1 Inlet

The inlet was considered at the centre of the bottom of the bubble column reactor as can be seen in Figure 3.1. At the inlet, velocity boundary condition were applied to match the experimental condition of Laari and Turunen (2003). Different superficial gas velocity was considered. The inlet velocities were 0.1m/s, 0.2m/s, and 0.6 m/s.

3.2.2.2 Outlet

The outlet boundary condition are applied at the region where fluid exit from the calculation domain. In this air water model, gas exits from the top surface of the bubble

column reactor and therefore the top surface was assigned as outlet. The diameter of the exit of the column was 78mm. Only gas phase was allowed to exit from the outlet. Static pressure boundary conditions were applied at the outlet of the model.

3.2.2.3 Wall

The wall boundary type is considered as solid wall. A non-slip condition was applied at all walls. A fixed temperature obtained from the experimental model of Laari and Turunen (2003) was assigned to the wall.

3.2.3 Governing equations for the modelling of bubble column reactor

The governing equation used for the simulation of bubble column reactor is presented in the following section. The equation includes the fundamental flow equation such as conservation of mass and momentum equation. The interfacial exchanges of momentum is also presented. The equation for the population balance modeling and the closure term of bubble break-up and bubble coalescence is presented.

3.2.3.1 Eulerian multiphase model and mass conservation equation

The CFD solver employed uses the finite volume discretization method which rests on integral conservation statements applied to a general control volume. The Eulerian multiphase flow model solves the conservation of mass, momentum, and energy of each phase in each cell. The exchange of mass, momentum, and energy are dealt with the interphase exchange term in the conservation equation. The governing equations in this approach can be derived by ensemble averaging the fundamental conservation equations for each phase to describe the motion of liquid and gas in a bubble column. Both the continuous and the dispersed phases are modelled in the Eulerian frame of reference as interpenetrating continua. The momentum equations of the phases interact with each other through inter-phase momentum exchange terms. The commercial CFD software AVL Fire 2009.2 was used in the present study. There is no phase transformation in the model. The mass conservation equation used in the present model as (AVL-FIRE, 2008):

$$\frac{\partial(\alpha_k \rho_k)}{\partial t} + \nabla . \alpha_k \rho_k v_k = 0, \qquad k = l, g \tag{3.1}$$

Where α_k is volume fraction of phase k, v_k is average velocity of phase k.

3.2.3.2 Momentum conservation equation

The momentum conservation equation for each phase in Eulerian- Eulerian approach on the finite volume method has been used. The momentum conservation equation used for the present model can be written as:

$$\frac{\partial(\alpha_k \rho_k v_k)}{\partial t} + \nabla . \alpha_k \rho_k v_k v_k = -\alpha_k \nabla \mathrm{p} + \nabla . \alpha_k (\tau_k + T_k^t) + \alpha_k \rho_k f + M_k \quad , k = 1 \ldots N \tag{3.2}$$

Where f is the body force vector which comprises of gravity and M_k is the momentum interfacial exchange between phases ($k = l, g$) and p is pressure.

Shear stress was calculated using the following equation.

$$\tau_k = \mu_k \left[(\nabla v_k + \nabla v_k^T) - \frac{2}{3} \nabla . v_k \right] \tag{3.3}$$

And Reynold stress was calculated using the following equation.

$$T_k^t = \mu_k^t \left[(\nabla v_k + \nabla v_k^T) - \frac{2}{3} \nabla . v_k I \right] - \frac{2}{3} \rho_k K_k I . \tag{3.4}$$

Here I is a unit tensor usually known as Kronecker delta.

The turbulent viscosity was calculated using the following equation:

$$\mu_k^t = C_\mu \rho_k \frac{K_k^2}{\varepsilon_k} . \tag{3.5}$$

Where K and ε are turbulent kinetic energy and its dissipation rate respectively.

3.2.3.2.1 Momentum interfacial exchange

The momentum interfacial exchange between bubbles and liquid due to bubble break-up and bubble coalescence is taken into account. The bubble induced drag force is considered in the present study. The momentum interfacial exchange between bubbles

(gas phase) and liquid is modeled by considering interfacial momentum source. The momentum interfacial exchange is calculated using the following equation (AVL-FIRE, 2008) by considering the drag force:

$$M_l = C_D \frac{1}{8} \rho_l A_i |V_r| V_r = -M_g \tag{3.6}$$

Where the relative velocity of phases was calculated using the equation:

$$V_r = V_g - V_l \tag{3.7}$$

And interfacial area density was calculated using the following equation

$$A_i = \frac{6\alpha_g}{D_{SMD}} \tag{3.8}$$

and the Sauter mean diameter was calculated using the following equation (Bannari et al., 2008).

$$D_{SMD} = \frac{1}{\sum_{i=1}^{n} \frac{\phi_i}{d_i}} \tag{3.9}$$

The drag coefficient C_D is a function of Reynolds number

$$Re_b = \frac{V_r D_{SMD}}{\nu_l} \tag{3.10}$$

The equation of drag coefficient is (Schlichting, 1979):

$$C_D = \begin{cases} \frac{24}{Re_b}\left(1 + 0.15 {Re_b}^{0.687}\right) & Re_b \leq 1000 \\ 0.438 & Re_b > 1000 \end{cases} \tag{3.11}$$

3.2.3.3 Population balance equation

To track the number density of different bubble classes PBE was used. In AVL Fire population balance equation is known as scalar transport equation and this equation was used to predict the number density of different bubble classes. The scalar transport equation solves the volume fraction of each bubble classes. The population balance equation can be expressed as:

$$\frac{\partial}{\partial t}(\alpha_g \rho_g \phi_i) + \nabla . \alpha_g \rho_g v_g \phi_i = \nabla . \alpha_g \rho_g \mathrm{D_{gi}} \nabla \phi_i + \mathrm{S_i} \quad (3.12)$$

Where, S_i is the source term of bubble class i due to break-up and coalescence and the source term was calculated using the equation (Bannari et al., 2008):

$$S_i = \rho_g (B_{B_i} - D_{B_i} + B_{C_i} - D_{C_i}) \quad (3.13)$$

Where B_{B_i}, B_{C_i}, B_{C_i}, and D_{C_i} are birth and death due to break-up and coalescence respectively. The daughter bubble distribution source term of Hagesaether et al. (2002) is corrected in this study. The details of this correction are presented in the next section. The volume fraction ϕ_i of bubble class i is related with the gas volume fraction which can be expressed as (Bannari et al., 2008):

$$\phi_i = \frac{\alpha_i}{\alpha_g V_c} \quad (3.14)$$

The total volume α_i of bubble class i is the product of the total number of bubble in class i and the volume of single bubble of that class and can be written as (Bannari et al., 2008):

$$\alpha_i = N_i V_i \quad (3.15)$$

3.2.3.4 Modification of source term for population balance equation

The equations (3.16) and (3.17) are for birth of bubble due to break-up of higher bubble classes and death of bubble which take part into break-up respectively. The equations (3.21) and (3.22) are for birth due to coalescence of lower bubble classes and death of that bubble taking part in coalescence. Bubbles are divided into finite number of classes therefore, it is assumed that no break-up of the smallest bubble class, (i=1), and no coalescence in the largest class, (i=N) (Hagesaether et al., 2002). The birth of bubble class i due to break-up from Hagesaether et al. (2002):

$$B_{B_i} = \sum_{k=i+1, i\neq N}^{N} {}_B(\vartheta_k, \vartheta_i) + \sum_{k=1, i\neq N}^{i} X_{i+1,k} \; {}_B(\vartheta_{i+1}, \vartheta_k) + \sum_{k=1, i\neq 1}^{i-1} \left(1 - X_{i,k}\right) \; {}_B(\vartheta_i, \vartheta_k), i = 1, \ldots, N, \quad (3.16)$$

The death of bubble class i due to break-up from Hagesaether et al. (2002):

$$D_{B_i} = \sum_{k=1}^{i-1} \Omega_B(\vartheta_i, \vartheta_k), i = 2, \dots\dots, N, \tag{3.17}$$

Bubbles are divided into finite number of classes. Each bubble class diameter is defined so as the volume of the class is twice the volume of the class below. Where $_B(\vartheta_i, \vartheta_k)$ is the break-up rate of bubble size v_i into v_k and the complementery fraction can be expressed as:

$$v_j = v_i - v_k \tag{3.18}$$

Each bubble class is of exact volume and if the break-up volume fraction v_j falls between classes, then it is distributed according to the following equation as:

$$v_j = x_{i,k} v_{i-1} + (1 - x_{i,k}) v_i \tag{3.19}$$

And the fraction of bubble distributed among classes based on the following equations.

$$x_{i,k} = 2^{1+k-i}, k < i \tag{3.20}$$

The birth of bubble class i due to coalescence from Hagesaether et al. (2002):

$$B_{C_i} = \sum_{j=1, i\neq N}^{i-1} X_{i,j} \;\; _C(\vartheta_i, \vartheta_j) + \sum_{j=1}^{i-1} (1 - X_{i-1,j}) \;\; _C(\vartheta_{i-1}, \vartheta_j), i = 2, \dots\dots, N, \tag{3.21}$$

The death of bubble class i due to coalescence from Hagesaether et al. (2002):

$$D_{C_i} = \sum_{j=1}^{N-1} \;\; _C(\vartheta_i, \vartheta_j) + \;\; _C(\vartheta_i, \vartheta_i), i = 1, \dots\dots, N-1, \tag{3.22}$$

Here the term $_C(\vartheta_i, \vartheta_j)$ is coalescence rate of bubble i and j and the coalescence product is distributed among the classes such that

$$v_i + v_j = x_{i,j} v_i + (1 - x_{i,j}) v_{i+1} \tag{3.23}$$

And the fraction of bubble distribution among the classes is calculated using the following equation.

$$x_{i,j} = 1 - 2^{j-i}, i \geq j \text{ ,} \tag{3.24}$$

For the sake of simplicity of presentation and ease of understanding it is assumed that there are 3 types of bubble classes. It is further assumed that the lowest class does not break and the highest class does not coalesce. The birth of bubble class 1 due to break-up death of bubble class 2 and 3 from equation (3.16) is:

$$B_{B_1} = [\ \ {}_B(\vartheta_2, \vartheta_1) + \ \ {}_B(\vartheta_3, \vartheta_1)] + \left[X_{2,1} \ \ {}_B(\vartheta_2, \vartheta_1)\right] \tag{3.25}$$

Similarly the birth of bubble class 2 due to break-up of bubble class 3 from equation (3.16) is:

$$B_{B_2} = [\ \ {}_B(\vartheta_3, \vartheta_2)] + \left[X_{3,1} \ \ {}_B(\vartheta_3, \vartheta_1) + X_{3,2} \ \ {}_B(\vartheta_3, \vartheta_2)\right] + (1 - X_{2,1}) \ \ {}_B(\vartheta_2, \vartheta_1) \tag{3.26}$$

There is no birth of bubble class 3 because it is the highest bubble class and there is no death of bubble class 1 because it is the lowest class. So the death of bubble class 2 due to birth of bubble class 1 from equation (3.25).

$$D_{B_2} = [\ \ {}_B(\vartheta_2, \vartheta_1)] + \left[X_{2,1} \ \ {}_B(\vartheta_2, \vartheta_1)\right] \tag{3.27}$$

And the death of bubble class 3 due to birth of bubble class 1 and 2 from equation (3.25) and (3.26)

$$D_{B_3} = [\ \ {}_B(\vartheta_3, \vartheta_1)] + \left[X_{3,1} \ \ {}_B(\vartheta_3, \vartheta_1) + X_{3,2} \ \ {}_B(\vartheta_3, \vartheta_2)\right] \tag{3.28}$$

The death of bubble class 2 due to break-up from equation (3.17) is:

$$D_{B_2} = \ \ {}_B(\vartheta_2, \vartheta_1) \tag{3.29}$$

The death of bubble class 3 due to break-up from equation (3.17) is:

$$D_{B_3} = \ \ {}_B(\vartheta_3, \vartheta_1) + \ \ {}_B(\vartheta_3, \vartheta_2) \tag{3.30}$$

To satisfy conservation it is obvious that the birth of any bubble class is to be balanced by the death of other bubble class. It is easily observed that the birth of bubble class 1 due to break-up of bubble class 2 in equation (3.27) is not equal to that of equation (3.29). Similarly the birth of bubble class 1 and 2 due to break-up of bubble class 3 in equation (3.28) is not equal to that of equation (3.30). From the population balance equation and numerical simulation point of view the birth of any bubble class due to

break-up of same bubble class is redundant. So the break-up birth of bubble class 2 ($(1-x_{2,1})\Omega_B(\vartheta_2,\vartheta_1)$) should be excluded in the birth of bubble class 2. Therefore, from the equation of birth of bubble due to break-up (Eqn.3.16) the term $\sum_{k=1,i\neq 1}^{i-1}(1-X_{i,k})\ \ {}_B(\vartheta_i,\vartheta_k)$ should be removed. The term $\sum_{k=1,i\neq N}^{i} X_{i,k}\ \ {}_B(\vartheta_i,\vartheta_k)$ should be added in the equation of death of bubble due to break-up (Eqn. 3.17). Now the closure term for break-up can be rearranged as:

$$B_{B_i} = \sum_{k=i+1,i\neq N}^{N}\ \ {}_B(\vartheta_k,\vartheta_i) + \sum_{k=1,i\neq N}^{i} X_{i+1,k}\ \ {}_B(\vartheta_{i+1},\vartheta_k), i = 1,\dots\dots,N, \tag{3.31}$$

$$D_{B_i} = \sum_{k=1}^{i-1}\ \ {}_B(\vartheta_i,\vartheta_k) + \sum_{k=1,i\neq N}^{i} X_{i,k}\ \ {}_B(\vartheta_i,\vartheta_k) i = 2,\dots\dots,N, \tag{3.32}$$

Similarly the inconsistency in the closure term for coalescence can be presented. There is no coalescence birth and death of the lowest class and the highest class respectively. So the birth of bubble class 2 due to coalescence from equation (3.21) is:

$$B_{C_2} =\ \ {}_C(\vartheta_1,\vartheta_1) + X_{2,1}\ \ {}_C(\vartheta_2,\vartheta_1) - X_{1,1}\ \ {}_C(\vartheta_1,\vartheta_1) \tag{3.33}$$

Similarly the birth of bubble class 3 due to coalescence from equation (3.21).

$$B_{C_3} = \left[(1-X_{2,1})\ \ {}_C(\vartheta_2,\vartheta_1) + (1-X_{2,2})\ \ {}_C(\vartheta_2,\vartheta_2)\right] \tag{3.34}$$

The death of bubble class 1 due to coalescence birth of 2 and 3 from equation (3.33) and (3.34) are:

$$D_{C_1} =\ \ {}_C(\vartheta_1,\vartheta_1) +\ \ {}_C(\vartheta_2,\vartheta_1) - X_{1,1}\ \ {}_C(\vartheta_1,\vartheta_1) \tag{3.35}$$

And the death of bubble class 2 due to coalescence birth of 3 from equation (3.34) is:

$$D_{C_2} =\ \ {}_C(\vartheta_2,\vartheta_1) +\ \ {}_C(\vartheta_2,\vartheta_2) - X_{2,1}\ \ {}_C(\vartheta_2,\vartheta_1) - X_{2,2}\ \ {}_C(\vartheta_2,\vartheta_2) \tag{3.36}$$

The death of bubble class 1 from equation (3.22) is:

$$D_{C_1} = [\ \ {}_C(\vartheta_1,\vartheta_1) +\ \ {}_c(\vartheta_1,\vartheta_2)] + [\ \ {}_C(\vartheta_1,\vartheta_1)] \tag{3.37}$$

The death of bubble class 2 from equation (3.22) is:

$$D_{C_2} = [\ \ {}_C(\vartheta_2,\vartheta_1) +\ \ {}_C(\vartheta_2,\vartheta_2)] + [\ \ {}_C(\vartheta_2,\vartheta_2)] \tag{3.38}$$

Now the death of bubble class 1 due to coalescence birth of 2 and 3 in equation (3.35) is not equal to the death of bubble class 1 from equation (3.22) presented in equation (3.37). Similarly the death of bubble class 2 due to coalescence birth of bubble class 3 in equation (3.36) is not equal to the death of bubble class 2 from equation (3.22) presented in equation (3.38).

Therefore, from the equation of death of bubble due coalescence (Eqn. 3.22) the term $_C(\vartheta_i, \vartheta_i)$ should be removed and new term $-\sum_{j=1}^{i} X_{i,j}$ $_C(\vartheta_i, \vartheta_j)$ should be added to satisfy the birth and death of bubble due to coalescence. Now the closure term for coalescence birth and death can be rearranged as:

$$B_{C_i} = \sum_{j=1, i\neq N}^{i-1} X_{i,j} \;\; {}_C(\vartheta_i, \vartheta_j) + \sum_{j=1}^{i-1}(1 - X_{i-1,j}) \;\; {}_C(\vartheta_{i-1}, \vartheta_j), i = 2, \dots\dots, N, \quad (3.39)$$

$$D_{C_i} = \sum_{j=1}^{N-1} \Omega_C(\vartheta_i, \vartheta_j) - \sum_{j=1}^{i} X_{i,j}\Omega_C(\vartheta_i, \vartheta_j), i = 1, \dots\dots, N-1, \quad (3.40)$$

3.2.3.5 Bubble break-up model and closure term

The bubble break-up is the consequence of a collision of bubble with turbulent eddy. The main parameter inducing a bubble break-up is the energy and size of the eddy (Huh et al., 2006). Eddies that are larger than the bubble merely carry the bubble and do not cause the bubble to break. Again it is assumed that eddies which are much smaller than the bubble do not have enough energy to break the bubble (Schlichting, 1979). Therefore, eddies that are smaller or equal to the bubble size causes the bubble to break-up due to collision. In the present study binary break-up model is considered. In binary break-up model, parent bubbles break-up into only two daughter bubbles. The break-up model of Luo and Svendsen (1996) was used in the present study. The rate of bubble break-up $_B$ is the product of collision frequency ω_B and the probability of bubble break-up P_B. The break-up rate of bubble class i into k colliding with the eddy size λ_j can be written as:

$$_B(\vartheta_i, \vartheta_k) = \omega_B(d_i, \lambda_j) \times P_B(d_i, \lambda_j, d_k) \quad (3.41)$$

Where $_B(\vartheta_i, \vartheta_k)$ is the break-up rate of bubble of volume v_i into daughter bubble of volume v_k with another daughter bubble of volume $v_i - v_k$ and $\omega_B(d_i, \lambda_j, d_k)$ is the

collision frequency of bubble class i with eddy λ_j and $P_B(d_i, \lambda_j, d_k)$ is the probability of breakage. The collision frequency of bubble class i and eddy size λ_j can be written as:

$$\omega_B(d_i, \lambda_j, d_k) = \frac{\pi}{4}(d_i + \lambda_j)^2 \overline{u_\lambda} \times n_\lambda \times n_{d_i} \tag{3.42}$$

The average turbulent velocity of eddy λ_j can be expressed as:

$$\overline{u_\lambda} = \beta^{1/2}(\varepsilon\lambda)^{1/3} \tag{3.43}$$

And the number density of eddy can be calculated as:

$$n_\lambda = \frac{0.822(1-\alpha_d)}{\lambda^4} \tag{3.44}$$

The number of bubble can be calculated as:

$$n_{d_i} = \frac{\alpha_i}{V_i} \tag{3.45}$$

The probability of break-up can be written as:

$$P_B(d_i, \lambda_j, d_k) = \exp(-\chi_c) \tag{3.46}$$

Where, χ_c is the critical dimensionless energy. The critical dimensionless energy can be calculated as:

$$\chi_c = \frac{12 C_f \sigma}{\beta \rho_c \varepsilon^{2/3} d_i^{5/3} \xi^{11/3}} \tag{3.47}$$

Here, C_f is the increase of coefficient of surface energy. The increase of coefficient of surface energy can be calculated as:

$$C_f = f_{BV}^{2/3} + (1 - f_{BV})^{2/3} - 1 \tag{3.48}$$

And $\xi = {}^{\lambda}/_{d}$ is the size ratio between eddy and bubble, and $f_{BV} = \frac{v_k}{v_i}$ is the volume fraction of parent bubble v_i that constitutes daughter bubble v_k.

3.2.3.6 Bubble coalescence model and closure term

The bubble coalescence occurs due to the collision of bubbles. The collision of bubble is induced by the turbulence of liquid, laminar shear, buoyancy and wake entrainment. The coalescence of two bubbles is induced when they collide. A small amount of liquid is trapped between the bubbles and the liquid drains gradually causing the liquid film between the bubbles to reach a critical thickness and a film rupture occurs resulting in coalescence (Huh et al., 2006). Based on this phenomena, Prince and Blanch (1990) derived the coalescence of bubbles. The coalescence model of Prince and Blanch (1990) has been used in the present study. The coalescence rate Ω_C can be written as the product of collision rate θ_{ij} and coalescence efficiency P_C as:

$$\Omega_C = \theta_{ij} \times P_C(d_i, d_j) \tag{3.49}$$

Prince and Blanch (1990) modelled a collision frequency based on the summation of the turbulent collision rate, buoyancy-driven collision rate and laminar shear collision rate. In the present study the turbulence and laminar shear collision rate is considered:

The turbulent collision rate can be written as (Prince and Blanch, 1990):

$$\theta_{ij}^{T} = 0.089 n_i n_j (d_i + d_j)^2 \varepsilon^{1/3} (d_i^{2/3} + d_j^{2/3})^{1/2} \tag{3.50}$$

The laminar shear collision rate can be written as (Prince and Blanch, 1990):

$$\theta_{ij}^{LS} = \frac{4}{3} n_i n_j \left(r_i + r_j\right)^3 \left(\frac{\overline{dU_l}}{dR}\right) \tag{3.51}$$

The mean shear rate is calculated as:

$$\bar{\gamma}(R) = 5.3 \frac{U_{l,max}}{R_T} \tag{3.52}$$

Where, R_T is the radius of the container. The centreline liquid circulation velocity can be calculated from the following equation:

$$U_{l,max} = \left(\frac{(1-0.75\alpha_g)}{1-\alpha_g}\right) \frac{\alpha_g g D_T^2}{48 \upsilon_t} \tag{3.53}$$

And the turbulent kinetic viscosity is calculated using the following equation.

$$v_t = 0.0536 \frac{D_T^{1.77}}{\rho_l} \tag{3.54}$$

Collision efficiency determines what fraction of bubble collisions lead to coalescence events. It is a function of the contact time between bubbles and the time required for bubbles to coalesce (Prince and Blanch, 1990). Prince and Blanch (1990) used the coalescence efficiency modeled by Coulaloglou and Tavlarides (1977). Present CFD model also used the same coalescence efficiency which can be written as:

$$P_C(r_i, r_j) = \exp\left(-{}^{t_{ij}}/_{\tau_{ij}}\right) = exp\left[-\frac{\left\{\frac{r_{ij}^3 \rho_l}{16\sigma}\right\}^{1/2} \varepsilon^{1/3} \ln\frac{h_0}{h_f}}{r_{ij}^{2/3}}\right] \tag{3.55}$$

Where the coalescence time can be calculated as:

$$t_{ij} = \left\{\frac{r_{ij}^3 \rho_l}{16\sigma}\right\}^{1/2} \ln\frac{h_0}{h_f} \tag{3.56}$$

The equivalent radius is calculated using the equation given below.

$$r_{ij} = \frac{1}{2}\left(\frac{1}{r_{bi}} + \frac{1}{r_{bj}}\right)^{-1} \tag{3.57}$$

And the contact time is calculated using the equation as:

$$\tau_{ij} = \frac{r_{ij}^{2/3}}{\varepsilon^{1/3}} \tag{3.58}$$

The initial and final thickness for air-water is 10^{-4}m and 10^{-8}m. The coalescence rate of bubble i and j is given by the total collision frequency Γ_{ij} multiplied by the coalescence efficiency.

$$\Gamma_{ij} = \left\{\theta_{ij}^T + \theta_{ij}^{LS}\right\} \times P_C(r_i, r_j) \tag{3.59}$$

3.2.4 Initial conditions of the model and properties of fluids

Initially the whole model was filled with liquid water and bubble was injected through the bottom of the column. Initially the bubbles of the lowest class (class 1) were assumed to enter the calculation domain through the inlet at the bottom of the column. The properties of the fluids used in this study are presented in Table 3.2.

Table 3.2. The properties of the fluids used for the simulation of bubble column.

Properties	Water	Air
Density (kg/m^3)	997.713	1.188
Viscosity (Ns/m^2)	1.002E-03	1.824E-05

3.2.5 Grid independency test

Two different grid of the model was generated with a control volume (number of cells) of 148,127 and 293,307. Simulation was performed on both grid using superficial gas velocity of 0.1m/s and it has been verified the convergence of the solution in both cases. Time averaged velocity at time t=300 second for 0.01m/s superficial gas velocity at the height of 0.1m is shown in Figure 3.2. No significant differences were observed in the results. Therefore, for all the subsequent simulations, the 148,127 control volumes numerical mesh was used.

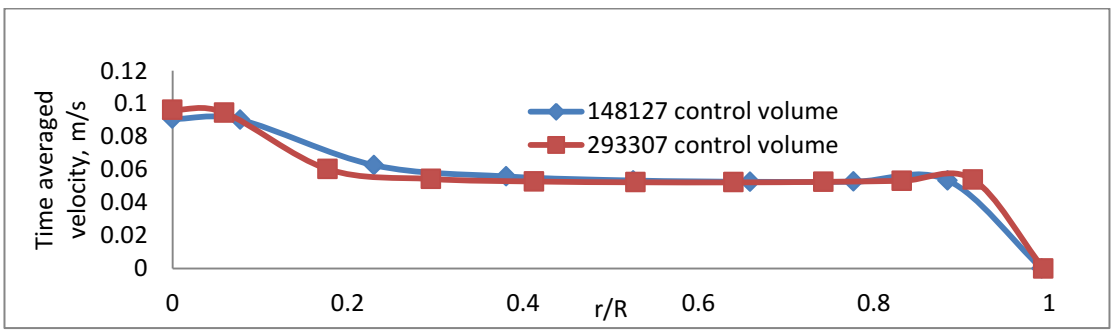

Figure 3.2. Gas velocity radial profile with different control volume.

3.3 Results and discussion

The superficial gas velocity and bubble diameters are specified at the inlet. Gas was feed through the inlet at the bottom of the column and the inlet area was equal to the inlet area of the total number of hole of the sparger. It is difficult to incorporate 382 inlets with diameter only 0.12mm in a perforated plate in the mesh. Therefore gas was introduced at the centre of the bottom of the bubble column. The total area of the inlet and the flow rate were similar to the experimental model. This approach for inlet was adopted to avoid unnecessary number of cells and the time of computing. Pressure reference cell were selected at the outlet of the column. Pressure boundary condition was applied and atmospheric pressure was specified at the outlet. The bubbles are assumed to enter the calculation domain with the initial diameter measured at z=0 plane in the experimental model of Laari and Turunen (2003). The bubble break-up and coalescence source term in the population balance equation corrected in the present study was used. The simulation was carried out for superficial gas velocity of U_g =0.01, 0.02, and 0.06m/s. The total run time of the simulation was 600s of real time.

The bubble enters into the system through the nozzle at the center of the bottom of the model. The bubble plume at the heights of 0.0m, 0.35 and 0.9m with superficial gas velocity 0.01m/s, 0.02m/s and 0.06m/s is shown in Figure 3.3, Figure 3.4 and Figure 3.5. The figures show that the bubble dispersion from the center increases with the increase of height. Gas bubbles dispersed in liquid due to diffusion and turbulent rise velocity. When bubble rises from the bottom, the drag force, viscous shear force and the buoyancy acting on the bubble causes it to rise with an oscillating motion (turbulent velocity). This turbulent velocity causes bubbles to collide with each other and radiate from the center. Some bubble coalesces while other deflects from each other. The deflection due to collision of bubbles and oscillation motion together with diffusion causes the bubble to disperse from the center. The bubble plume is higher when gas velocity is higher. When superficial gas velocity is higher the amount of gas in other word the bubble injected into the system is more than that of lower superficial gas velocity.

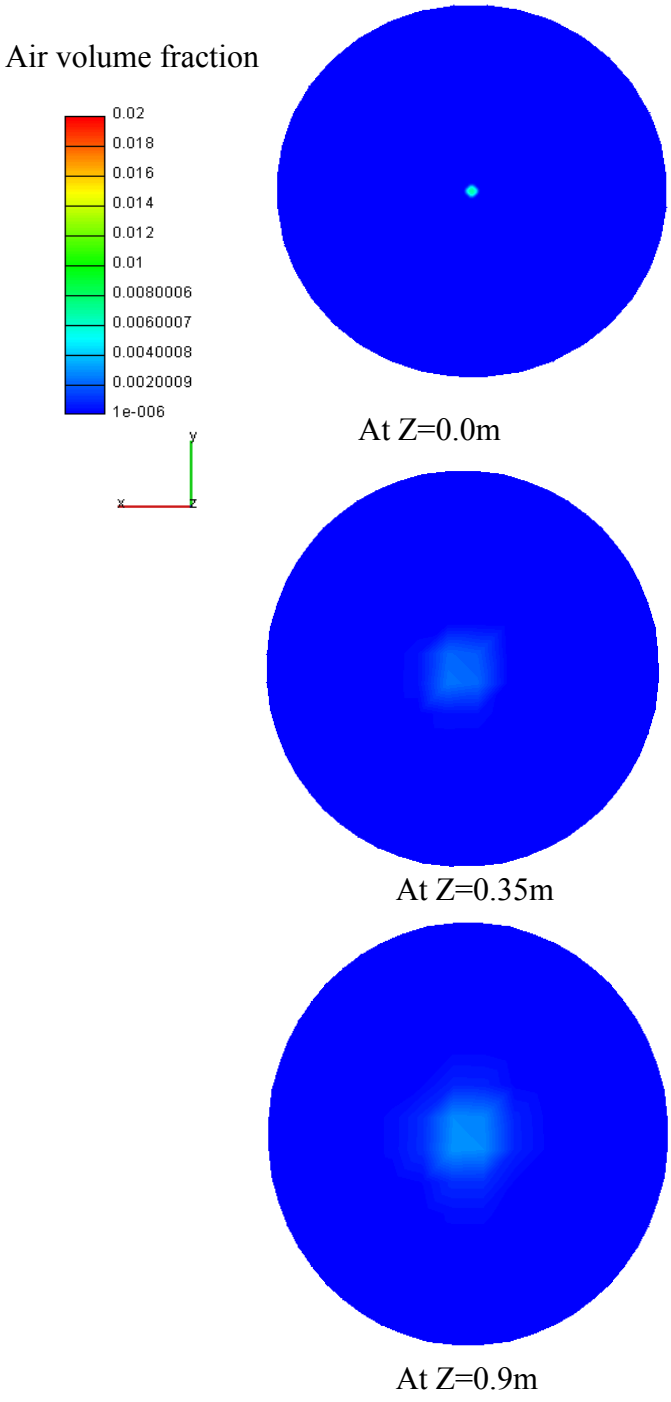

Figure 3.3. Bubble plume at different height with superficial gas velocity U_g =0.01m/s.

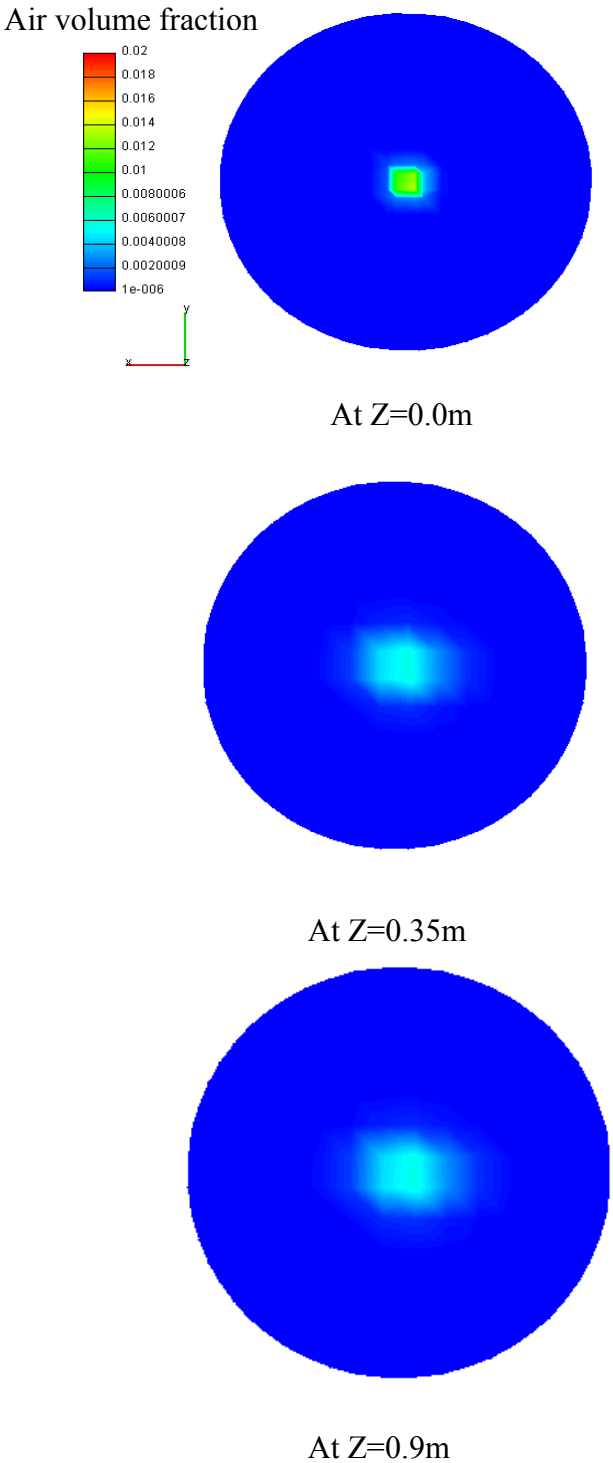

Figure 3.4. Bubble plume at different height with superficial gas velocity U_g =0.02m/s.

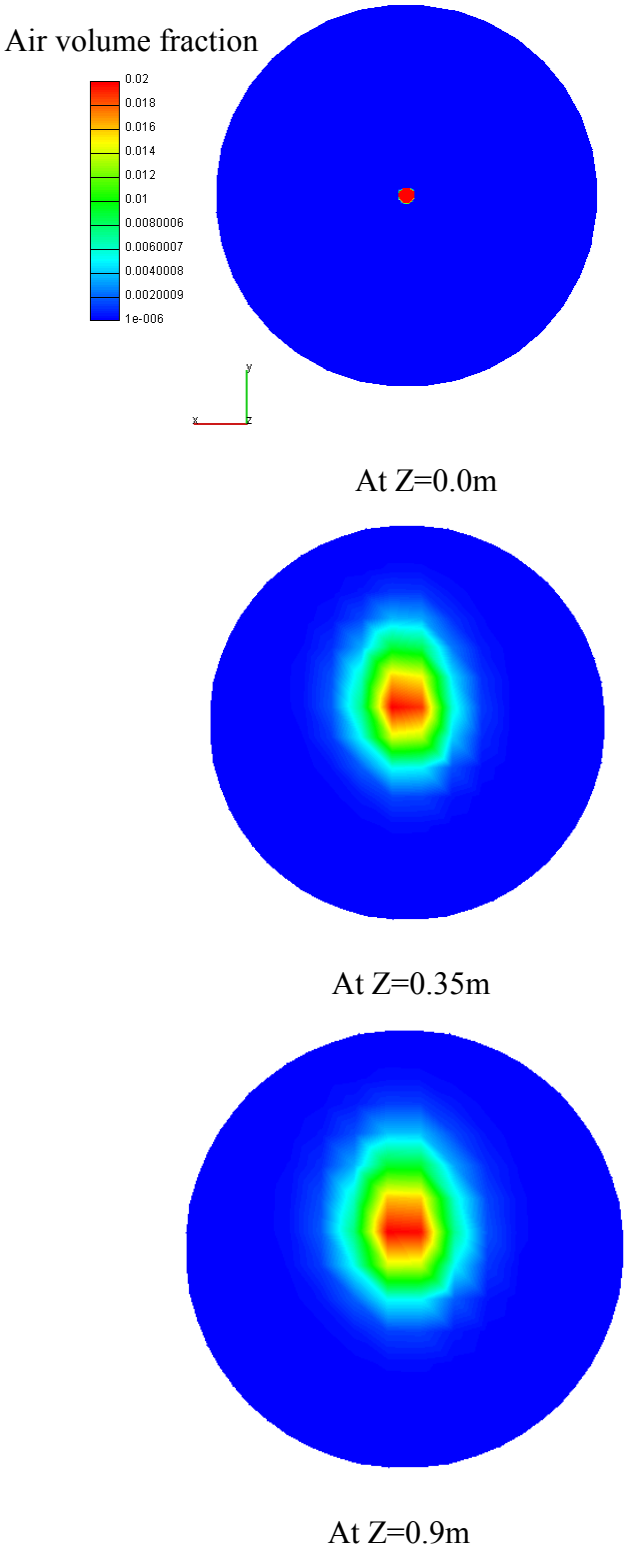

Figure 3.5. Bubble plume at different height with superficial gas velocity U_g =0.06m/s.

In the present study ten types of bubble classes were considered. The bubbles of the lowest class (class 1 measured at z=0 in the experimental model of Laari and Turunen (2003) were assumed to enter into the system. The radial distribution of different bubble classes at height of 0.35m with superficial gas velocity of 0.01m/s, 0.02m/s, and 0.06m/2 is shown in Figure 3.6, Figure 3.7 and Figure 3.8. The figure shows that the bubble of different classes are densely packed at the center and dispersed radially. The figure also shows that the number densities of lower bubble classes are more than its higher counterpart. In this model the bubble class 1 (the lowest class considered in this study) was assumed to enter into the bubble column through nozzle hence its number density is more at the inlet. As it moves upward the bubble coalescence causes the decreases of its number density. The birth of upper bubble classes results from the coalescence of lower bubble classes. As only class 1 bubble was considered to enter into the bubble column, the coalescence event results in the increase of lower classes. The number density shifted toward higher bubble classes with increase of height as can be seen in Figure 3.9-Figure 3.11. The break-up rate of upper bubble classes increases with increases of their population, which finally slows down the number density of upper bubble classes with height.

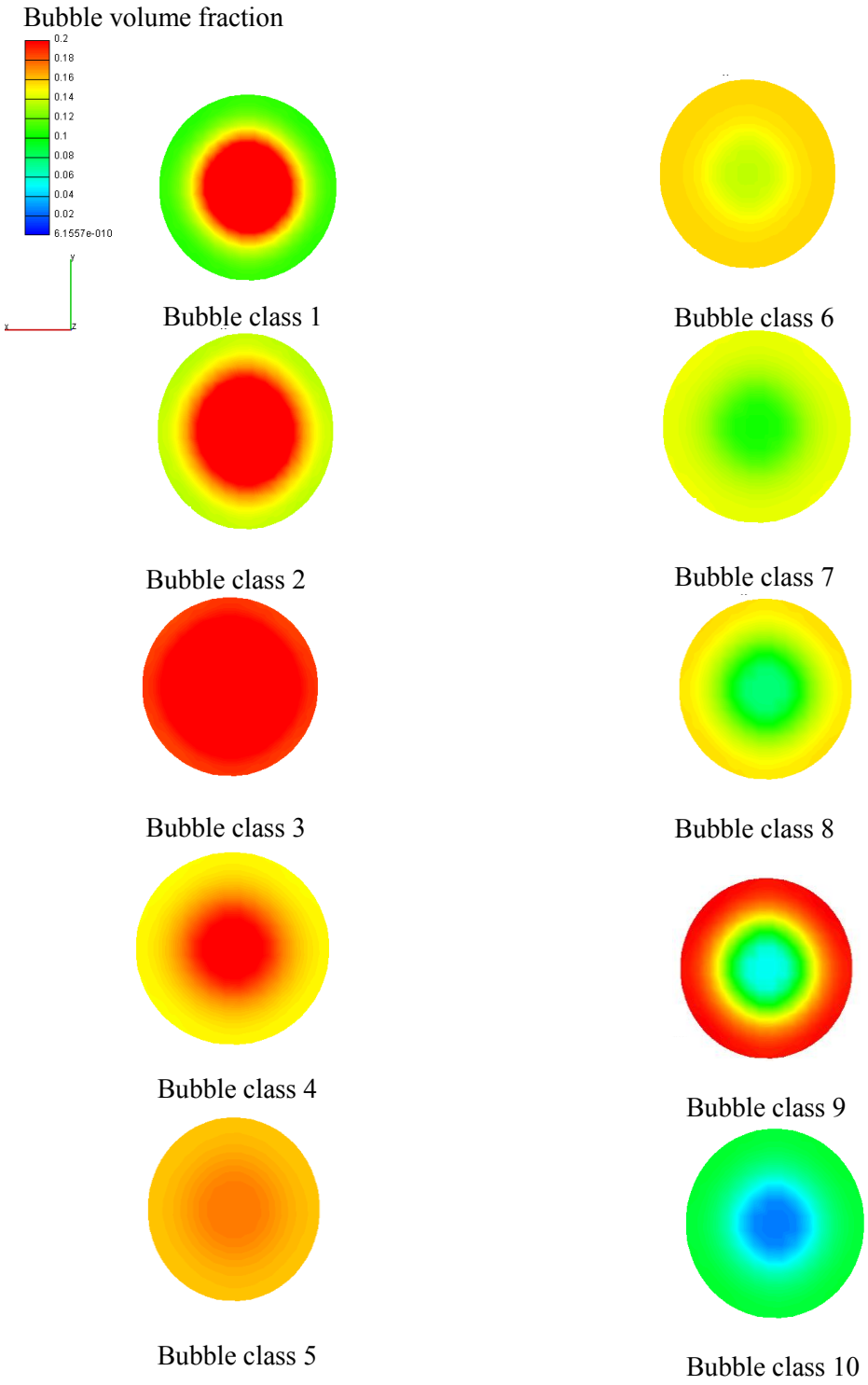

Figure 3.6. Radial distribution of different bubble classes at height 0.1m with superficial gas velocity U_g =0.01m/s.

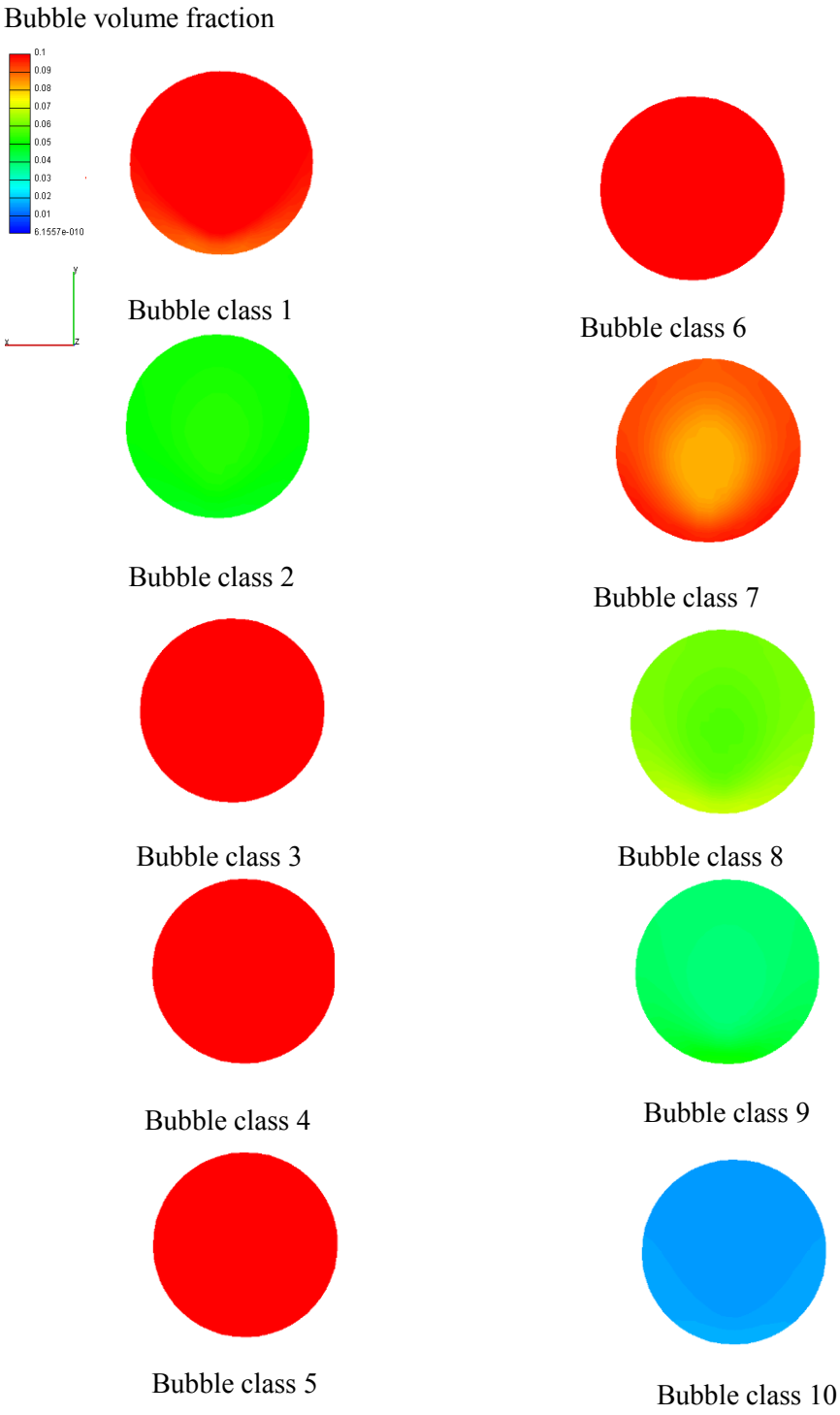

Figure 3.7. Radial distribution of different bubble classes at height 0.1m with superficial gas velocity U_g =0.02m/s.

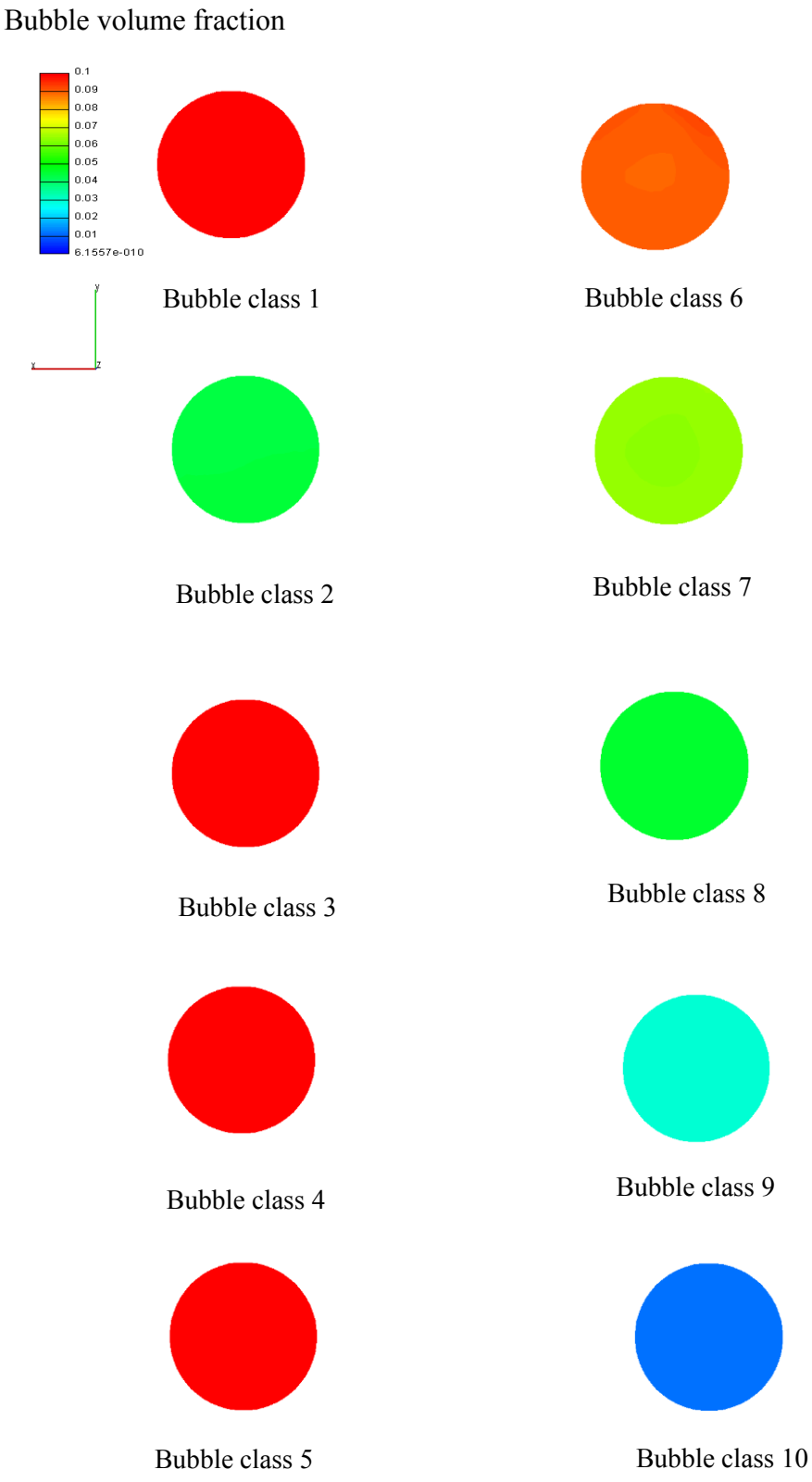

Figure 3.8. Radial distribution of different bubble classes at height 0.1m with superficial gas velocity U_g =0.06m/s.

The distribution of different bubble class in term of volumetric fraction of each bubble class along the length of the column in the Z-Y plane is presented in Figure 3.9, Figure 3.10 and Figure 3.11. The bubble number density of class 1, 2, 3 and 4 are closer to the inlet whereas, the number density of other bubble classes (Bubble class 5, 6, 7, 8, 9, and 10) increase with the increase of height. Initially bubble class 1 was injected into the calculation domain through the inlet of the nozzle and therefore their number density is higher near to the inlet. The bubble class 1 moves upward and collide with each other to form higher bubble classes, therefore, the number density of bubble class 2,3, and 4 increases with increase of height. The bubble class 1-4 move and collide with each other and these coalescence events cause the upper bubble to grow and therefore, the bubble class 6, 7, 8, 9, 10 increase with increases of height. At the same time bubble break-up events also occur and the bigger bubble breaks into smaller bubble. Birth and death of bubbles are due to break and coalescence. The birth of lower bubble class is due to the break-up of higher bubble class. Similarly the birth of higher bubble class is due to the coalescence of lower bubble classes. The bubble class 1 is the lowest bubble class which does not take part in breakage and bubble class 10 is the higher bubble class which does not take part in coalescence. In the lower part of the column the majority of the bubbles are smaller bubbles, whereas in the upper part the majority of bubbles are bigger bubble. The number density of each bubble classes is balanced by the birth and death of each bubble class and remains quasi-steady state in the system before it escapes atmosphere through the outlet of the column.

The lower bubble class is closer to the injection of gas. The higher bubble class increases with increases of height of the column. The number of bubble class 1 is closer to the inlet because only bubble class 1 is considered to enter into the calculation domain through the inlet. The bubble class 1 coalesces with its own kind and other bubble class available to form upper class due to turbulent coalescence near to the inlet. The turbulent kinetic energy close to the inlet is highest than other parts of the column. This turbulent energy causes coalescence of smaller bubble into bigger bubble at the same this turbulent energy increase the break-up of bigger bubble class. The break-up of bubble depends on many parameters. The number of bubble available for break-up, the number of eddy, the size of eddy and the energy of eddy are among them (see eqns. 3.41-3.48). The number of higher class bubbles near to the inlet is less than other parts

of the column. So when the number of upper bubble class is formed due to the turbulent coalescence of lower bubble classes this upper bubble class also breaks into lower bubble class in this region. The bubble break-up occurs only when the critical energy of eddy exceeds the energy needed to break-up the surface of bubble (see eqn. 3.47). At the inlet the energy of eddy is higher than other part of the column. Therefore larger bubbles are formed because of the coalescence of lower bubble class and sometimes the break-up of bigger bubble classes is closes to the inlet than other part of the column. The remaining larger bubbles which do not break and the small bubbles in that region move upward. The turbulent kinetic energy decreases due to dissipation and the number of eddies and the energy of eddies also decreases. The lower bubble class also coalesce in the other regions of the column to form higher bubble classes. The bigger bubble breaks up less in the upper region than the region around the inlet because of the changes of break-up parameter. That is why the higher bubble classes (bigger size bubbles) are more in the upper region of the column than in the lower region.

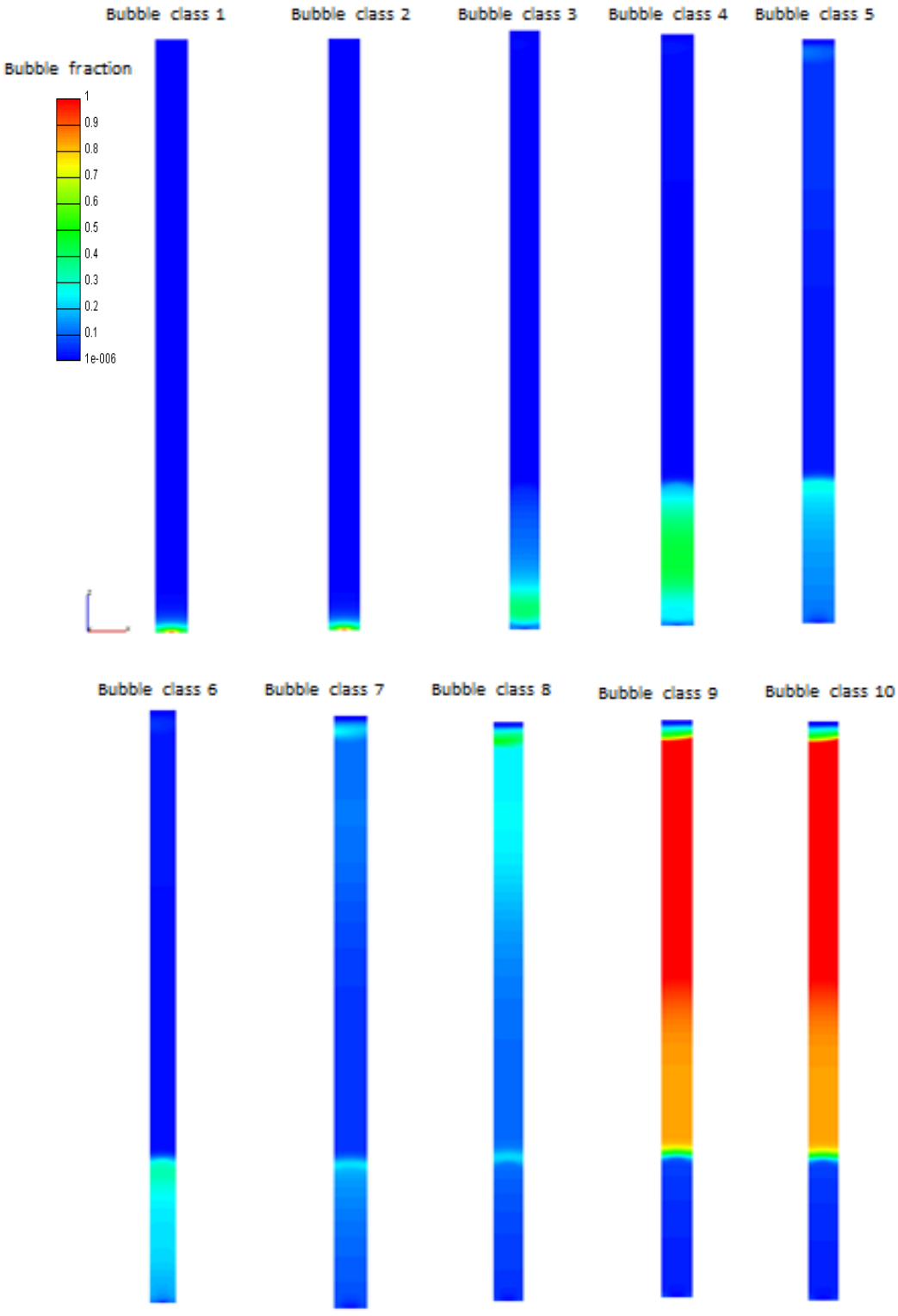

Figure 3.9. Different bubble classes along the length of the column with superficial gas velocity U_g =0.01m/s.

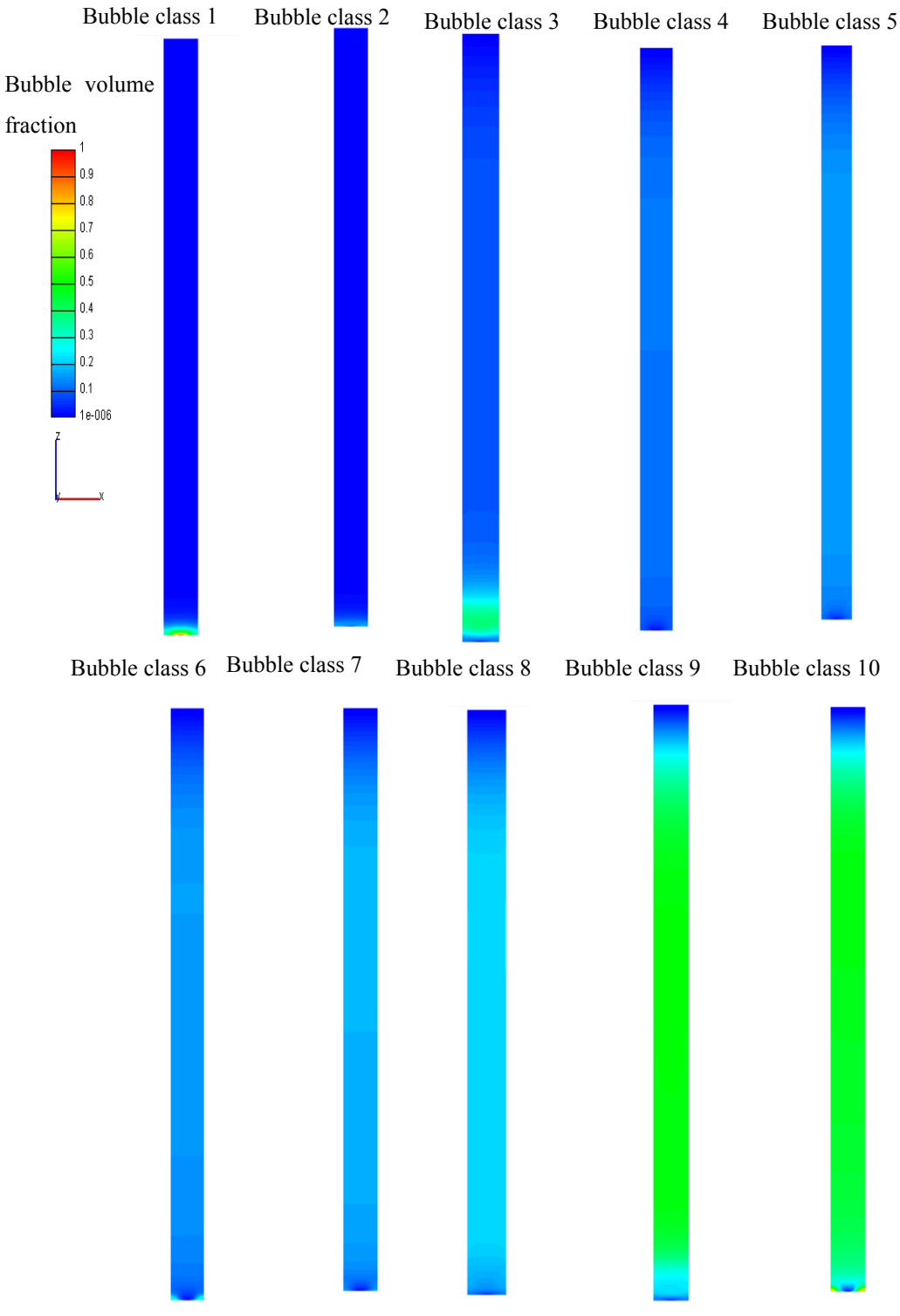

Figure 3.10. Different bubble classes along the length of the column with superficial gas velocity U_g =0.02m/s.

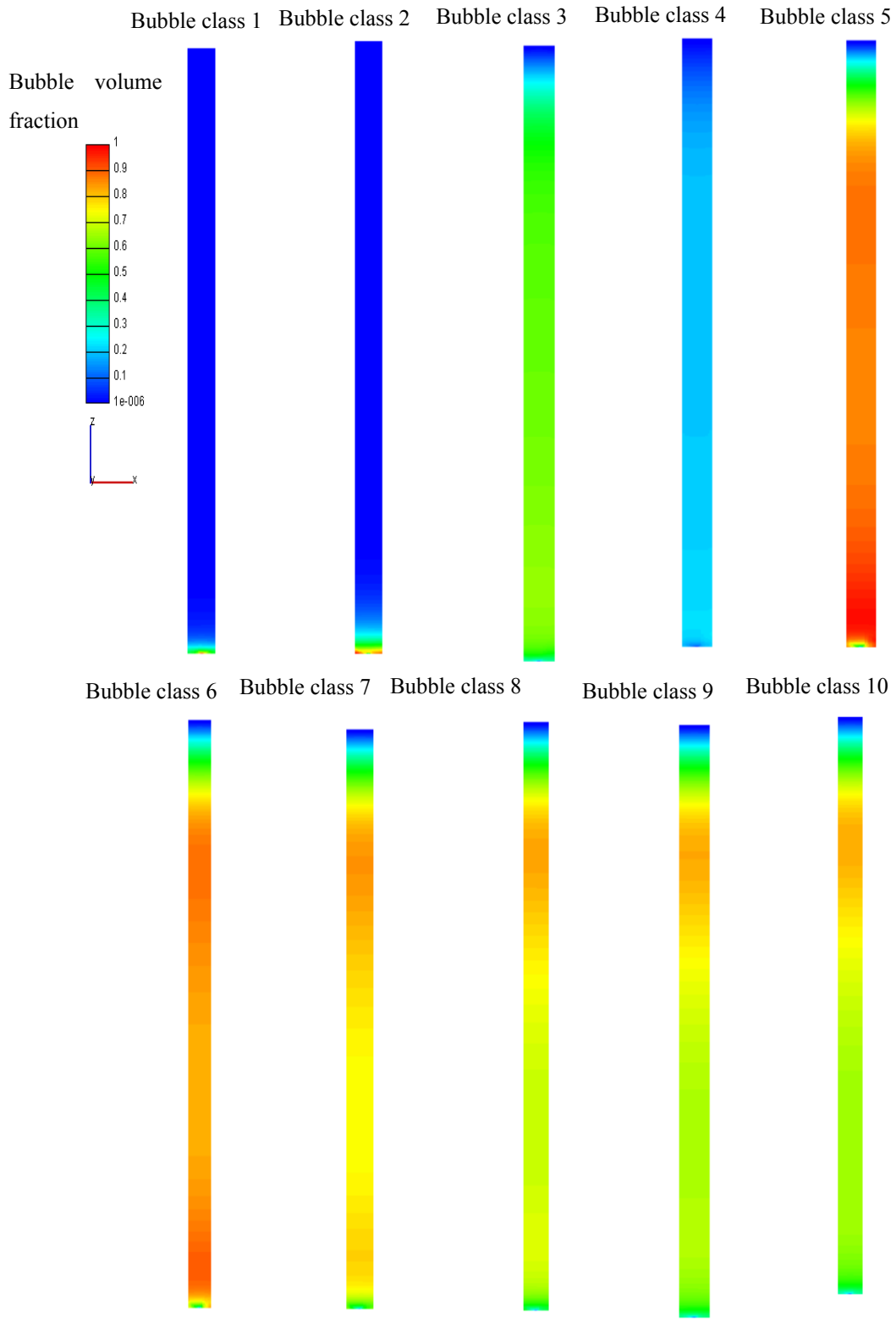

Figure 3.11. Different bubble classes along the length of the column with superficial gas velocity U_g =0.06m/s.

The averaged Sauter mean diameters of the bubbles from 500s to 600s at an interval of 10s were taken. The Sauter mean diameter of the bubbles at z=0. 0.35, 0.9, 1.65 and 2.4m from the bottom of the column similar to the height of Laari and Turunen (2003) experimental model has been evaluated. Figure 3.12, 3.13, and 3.14 shows the Sauter mean diameter of bubble along the height of the column when the superficial gas velocity is 0.01m/s, 0.02m/s, and 0.06m/s respectively. The Sauter mean diameter of the bubble increases with the increase of height. The rate of increase is higher up to 1 meter of height then diminishes with increase of height. This is due to the fact that the coalescence of bubbles increases with increasing height but at the same time the increases of upper bubble class increases their break-up rate which eventually reduces the rate of increase. The dispersion of bubble increases with the increase of height (See Figure 3.3-3.5 and Figure 3.6-3.8) so the overall coalescence rate decreases (See eqn. (3.49)-(3.59)) which slow down the increase of Sauter mean diameter and become steady after certain height.

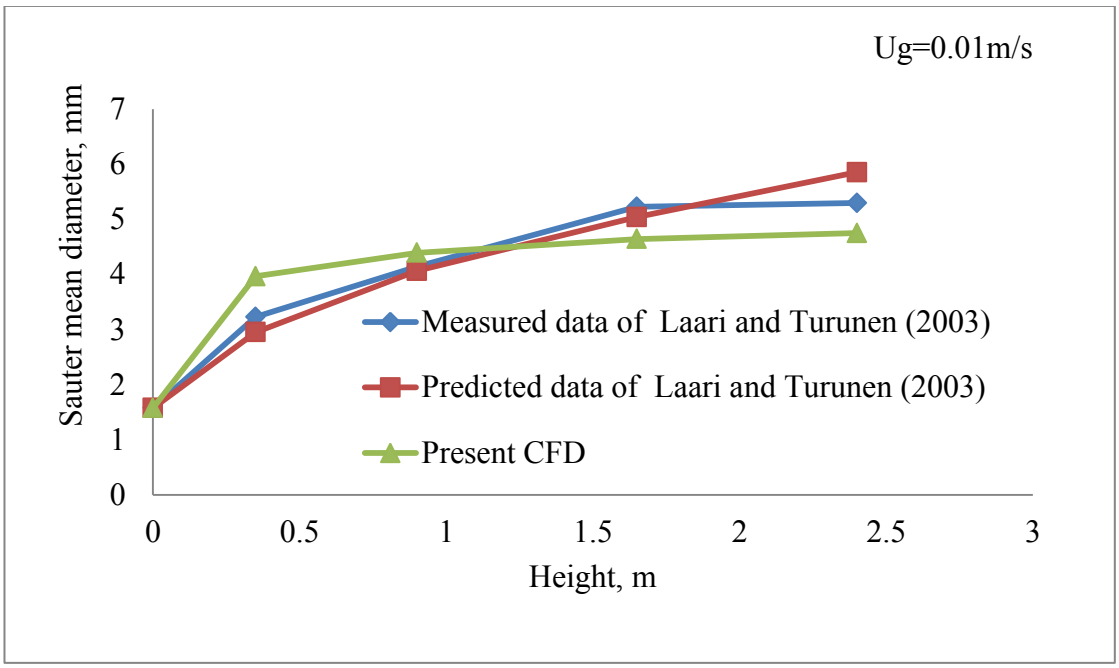

Figure 3.12. Sauter mean diameter at different height with gas superficial velocity 0.01m/s.

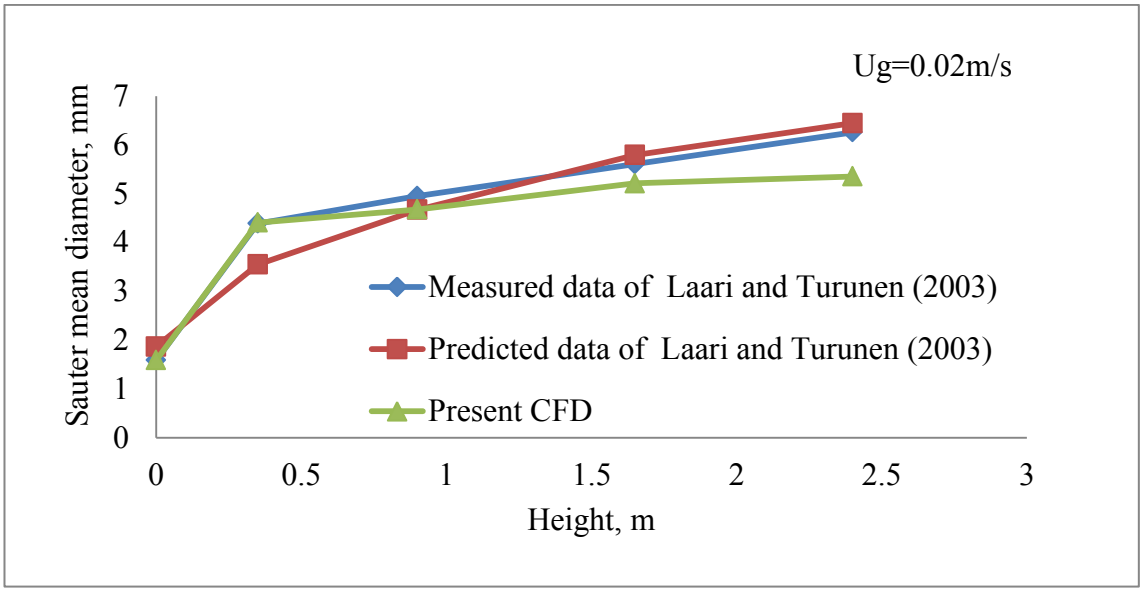

Figure 3.13. Sauter mean diameter at different height with gas superficial velocity 0.02m/s.

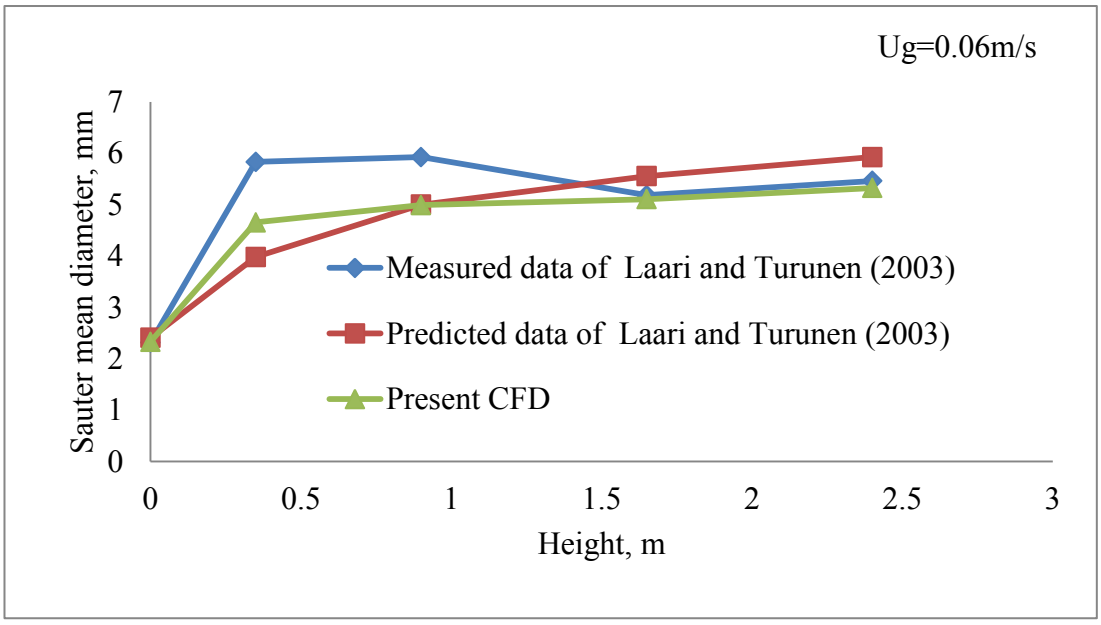

Figure 3.14. Sauter mean diameter at different height with gas superficial velocity 0.06m/s.

At superficial gas velocities U_g =0.02 and 0.06m/s the simulation results show good agreement with the experimental data but at U_g =0.01 the simulation over predicts the Sauter mean diameter at 0.5m. The results of the present CFD model and the predicted data of Laari and Turunen (2003) presented in Figure 3.12, 3.13 and 3.14 are not significantly different. This is due to the fact that the correction has little impact on the scalar transport equation. The gas flow rate for the present study was very low compared to the size of column. The mass flow rate of air was 4.7×10^{-8} kg/s, 9.5×10^{-8}kg/s, and 2.85×10^{-8}kg/s when the superficial gas velocity was 0.01m/s, 0.02m/s and 0.06m/s respectively. The number of bubble and the amount of gas enter into system is very little (See Figure 3.3-3.5 and Figure 3.6-3.8) compared to the size of the column. Therefore, the numbers of bubble breaking and coalescing is insignificant and have little impact on the calculation of their distribution into different bubble classes. Accurate prediction of the number of different bubble classes is important for the design of reactor. The interfacial area between gas bubble and liquid dictate the reaction, mass and momentum transfer between them. For a large complex reactor used in industry with more break-up and coalescence phenomena the rectification can have significant impact.

Laari and Turunen (2005) and Sha et al. (2006) used the population balance solution method presented by Hagesaether et al. (2002) to estimate the birth and death terms of coalescence and breakage for each bubble class. The present CFD model used the rectified model of Hagesaether et al. (2002) to estimate the birth and death terms of coalescence and breakage for each bubble class. The simulated Sauter mean diameter predicted in the present simulation and that of Sha et al. (2006) and Laari and Turunen (2005) are presented in Figure 3.15. The Figure shows that the Sauter mean diameter increases with the increases of height for all models and become steady after 1.5m for the present CFD results and that of Sha et al. (2006) and Laari and Turunen (2005) is not available after 1.5m. Although small difference in the Sauter mean diameter is visible in Figure 3.15, the general trend of the Sauter mean diameter with height is same. Sha et al. (2006) and Laari and Turunen (2005) used a rectangular column whereas the present model used cylindrical column similar to the experimental model of Laari and Turunen (2003). Though Laari and Turunen (2005) and Sha et al. (2006)used

rectangular column for the prediction of bubble classes there is small difference in the Sauter mean diameter evaluated. The Sauter mean diameter at 1.5m predicted by the model of Sha et al. (2006) is higher than that of Laari and Turunen (2005). The difference in the Sauter mean diameter between Laari and Turunen (2005)and Sha et al. (2006) can be attributed to the model parameter and different numerical technique used. The present model incorporated the coalescence model of Prince and Blanch (1990) due to turbulence and laminar shear and break-up model of Luo and Svendsen (1996). Laari and Turunen (2005) and Sha et al. (2006) incorporated coalescence model of Prince and Blanch (1990) due to turbulence and buoyancy and break-up model of Lehr et al. (2002). The Sauter mean diameter predicted by the present CFD model is higher than that of Sha et al. (2006). The difference in results between the present model and that of Laari and Turunen (2005) and Sha et al. (2006) can be attributed to the difference of bubble break-up model incorporated and the initial bubble size and their classes considered. The difference in results can also be attributed to the different superficial gas velocities employed in the simulation. At the same time the rectification of the source term of Hagesaether et al. (2002) also causes a difference in the prediction of results.

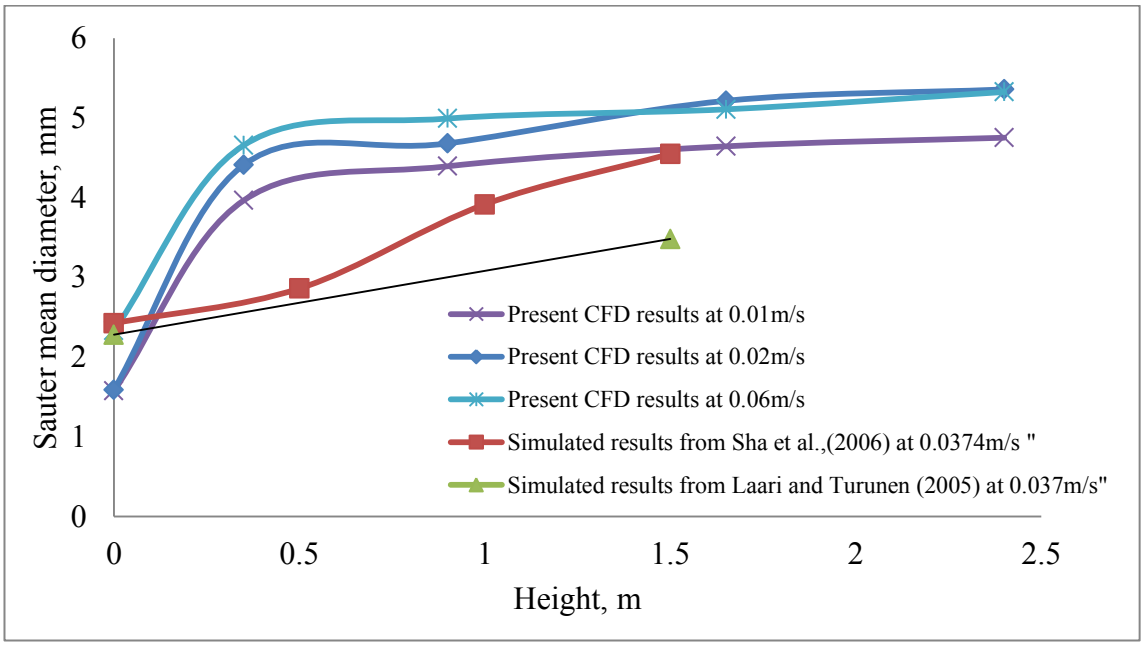

Figure 3.15. Comparison of simulated Sauter mean diameter at different height with different inlet velocity.

The time averaged axial liquid velocity and volume fraction at $\frac{z}{D} = 4.48$ is presented in Figure 3.16 and 3.17 though no experimental data of this model is available for comparison. Figure 3.16 shows that the liquid axial velocity at the centre is the highest in the upward direction and decreases as r increases and the liquid flow downward after certain value of r/R before going to zero at the wall of the column. Bubbles are densely packed at the center and scattered toward the wall of the column (See Figure 3.3-3.5 and Figure 3.6-3.8). Bubble rises toward the top surface of the liquid due to buoyancy. The liquid in vicinity of the surface of bubble moves upward along with the bubble due to drag force and skin friction between bubble surface and liquid. Velocity decreases with the increase of the distance between the contact surfaces. A vortex is created and the liquid flown upward is balanced by the liquid flown downward. The liquid in contact with the wall remain stagnant. Gas is injected at the centre of the bottom so the liquid volume fraction is less at the center and highest near the wall as seen in Figure 3.16. As expected the liquid volume fraction decrease with the increase of superficial gas velocity.

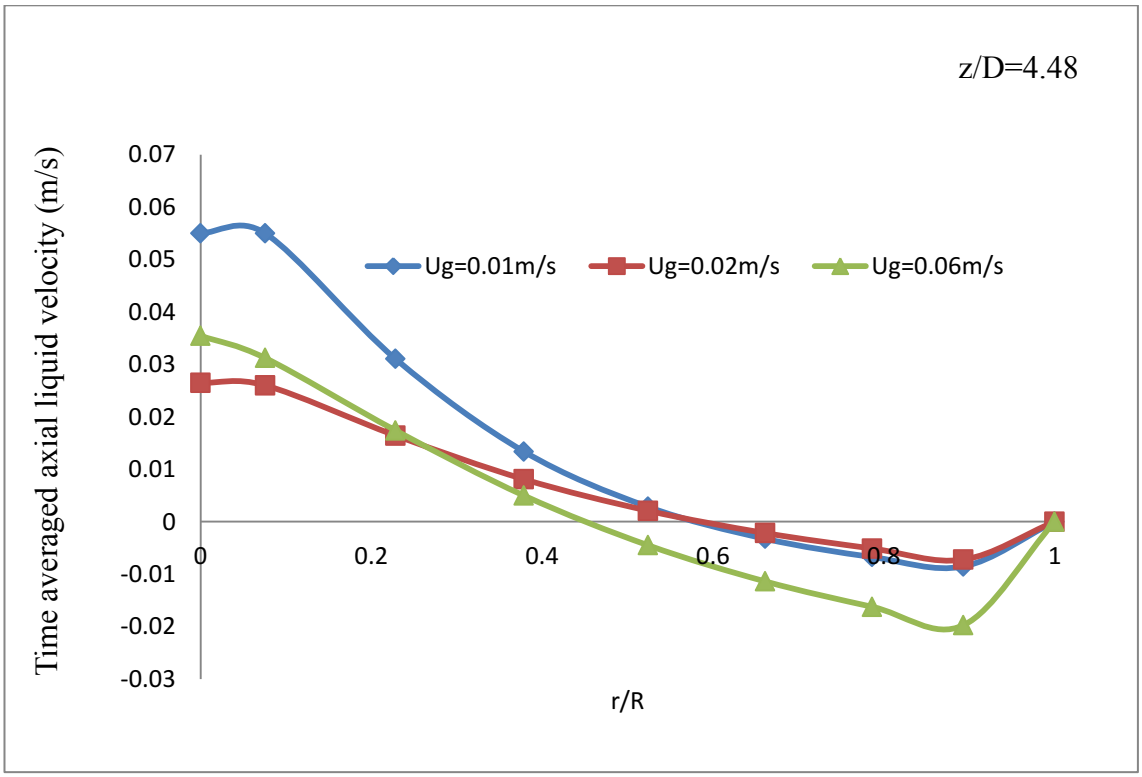

Figure 3.16. Time averaged axial liquid velocity.

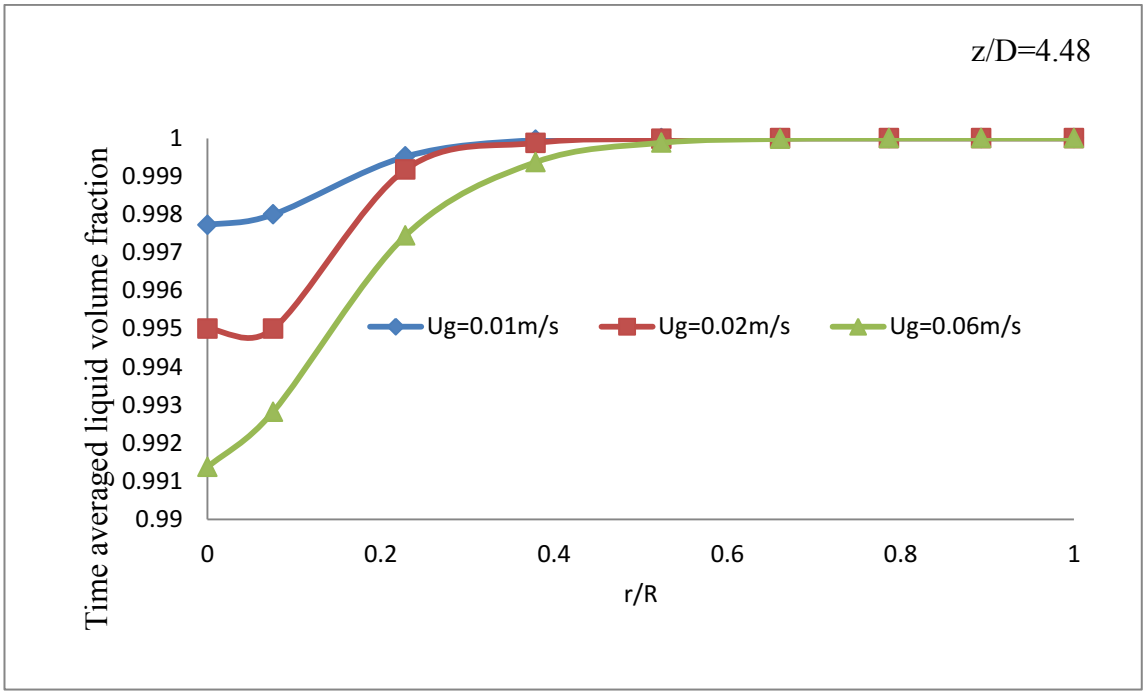

Figure 3.17. Time averaged axial liquid hold up.

The radial profile of velocity and liquid volume fraction of this model conforms that of Bhole et al. (2008) and Bannari et al. (2008). Bannari et al. (2008) carried out their simulation for a rectangular bubble column and Bhole et al. (2008) used a cylindrical column. A sensitivity analysis was performed by changing the cell size and the results showed to be independent of grid size. In this model only one inlet rather than 382 inlet of sparger was considered. The bubbles were assumed to enter into the calculation domain with diameter measured in the experiment (Laari and Turunen, 2003). Specific types of bubble break-up (Luo and Svendsen, 1996) and bubble coalescence (Prince and Blanch, 1990) were considered. However, there are other model (Müller-Fischer et al., 2008, Taylor, 1934, Wang et al., 2005, Wu et al., 1998, Chesters, 1991) available in the open literature but were not implemented in this study. The simulation results were compared when the number of control volumes was 148127 and 293307 for superficial gas velocity of 0.01m/s and the results found were independent of mesh (See Section 3.2.5).

The turbulent kinetic energy of gas phase at a height of 1.65m from the bottom of the column for superficial gas velocity of 0.01m/s, 0.02m/s and 0.06m/s are presented in

Figure 3.18. The gas volume fraction is concentrated near to the inlet of the nozzle (See Figure 3.3-3.5) and disperses with time along the length of the column. The turbulent kinetic energy is more at the centre than other part of the column. The turbulent kinetic energy increases with the increase of superficial gas velocity (See Figure 3.18). By increasing the superficial gas velocity the volumetric fraction of gas phase and their velocity in the column also increase therefore the turbulent kinetic energy is also increased. The gas bubble moves upward from the nozzle tip at the bottom and disperse toward the inner wall then collide with the wall and reflect back to the centre. The plume of bubble at the centre of the column moves upwards and escapes from the exit of the column.

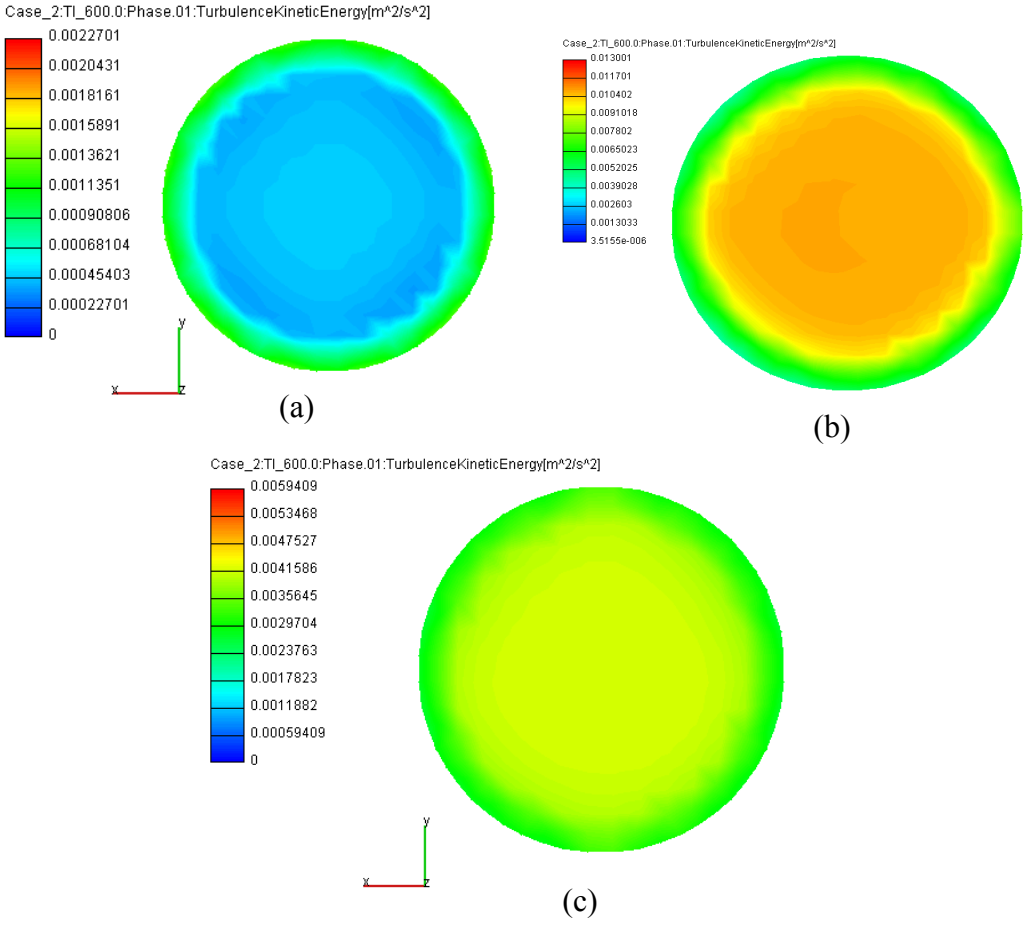

Figure 3.18. Turbulent kinetic energy with different superficial gas velocity (a) v=0.01m/s (b) v=0.02m/s (c) v=0.06m/s.

The velocity profiles in the column along the length in z-y plane for superficial gas velocity of 0.01m/s, 0.02m/s and 0.06m/s are presented in Figure 3.19. The gas enters into the system through the inlet of the nozzle with different superficial gas velocity. As the gas moves upward then it gradually disperse toward the wall of the column. At low superficial gas velocity the dispersion starts far from the inlet whereas when the superficial gas velocity is increased the gas dispersed immediately after the inlet.

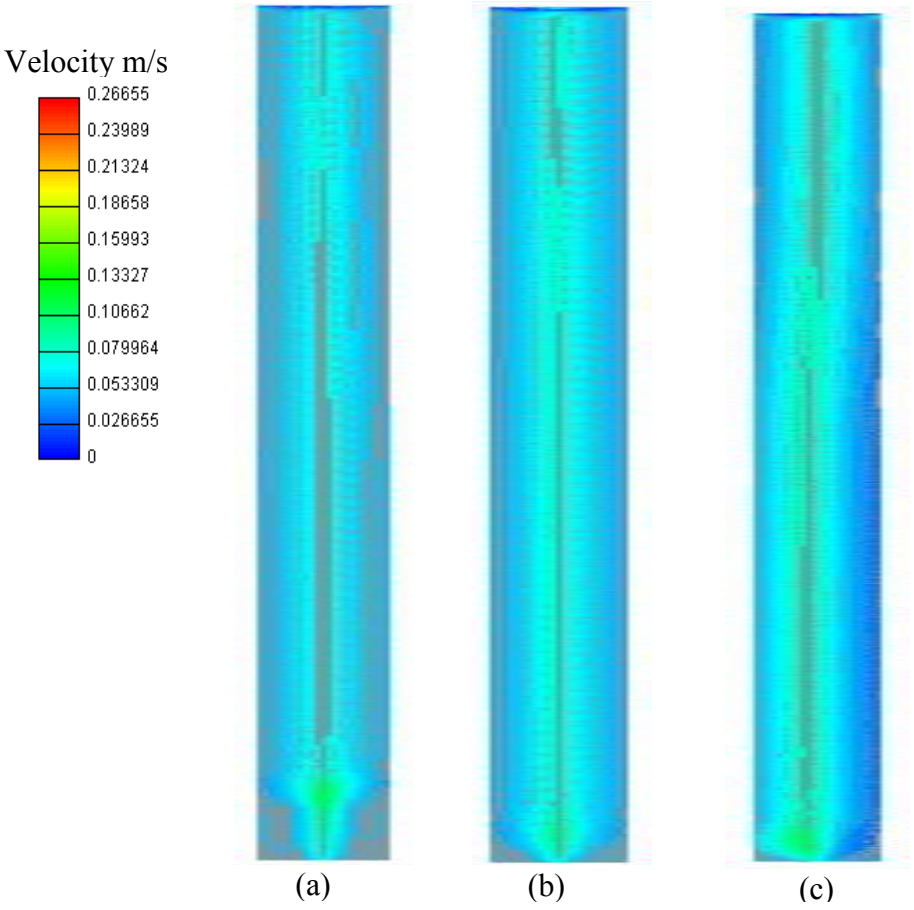

Figure 3.19. Velocity contour of gas at 600s for (a) v=0.01m/s, (b) v=0.02/s and (c) v=0.06m/s.

The gas enters into the system through the inlet of the bubble column. The gas enters into the liquid with the initial energy and velocity specified at the inlet. This inlet gas pushes the liquid near the inlet and move upward. The velocity and turbulent kinetic energy of gas around the inlet is higher than other part of the column due to initial velocity and energy. The liquid is stagnant at the beginning of the simulation therefore the momentum energy of the gas injected is higher than the liquid of the system. There

is significant exchange of momentum between gas and liquid. The exchange of momentum between gas and liquid in the present CFD model is dealt with the interfacial momentum exchange source term in the momentum equation (eqn. 3.2 and eqn.3.6). Gas moves upward with initial velocity and momentum energy and the significant amount of its momentum energy is transferred into the momentum energy of liquid. Therefore, velocity and turbulent kinetic energy of the gas decreases with increase of height of the bubble column. Gas also diffuses into the system and this diffusion causes the dissipation of turbulent kinetic energy. Therefore, at the inlet the turbulent kinetic energy and velocity is concentrated along the centre of the column and diffused and scattered as it moves upward.

The bubble plume for the present simulation shows that the bubble dispersion from the center increases with the increase of height. This was attributed to that fact that gas bubbles dispersed in liquid due to diffusion and turbulent rise velocity. The radial distribution of different bubble classes shows the number densities of lower bubble classes were more than its higher counterpart because of the consideration of the lowest class entering into the bubble column. The Sauter mean diameter calculated from the predicted number of different bubble classes increases with the increase of height up to 1m and then become steady. The coalescence of bubbles increases with increasing height but at the same time the increases of upper bubble class increases their break-up rate which eventually reduces the rate of increase. The dispersion of bubble increases with the increase of height so the overall coalescence rate decreases which slow down the increase of Sauter mean diameter and become steady after certain height. The result of this model using a modified source term was compared with the available result in the literature and found to conform (Laari and Turunen, 2003, Bhole et al., 2008, Bannari et al., 2008, Laari and Turunen, 2005, Sha et al., 2006). There were no significant difference between the result of the present CFD model and the predicted data of Laari and Turunen, (2003) because the gas flow rate for the present study was low compared to the size of column. The number of bubbles and the amount of gas entering the system is very little. Therefore, the number of bubble breaks and coalesces is insignificant and have little impact on the calculation of their distribution into different bubble classes. The rectification can have significant impact for a large complex reactor used in industry with more break-up and coalescence phenomena.

CHAPTER 4

MODELING OF FOAMING IN AERATED LIQUID WITH POPULATION BALANCE MODELING

4 Modeling of foaming in aerated liquid with population balance modeling

This chapter presents the numerical modeling of foaming in aerated liquid with population balance modelling. The model considered in the present simulation is similar to the analytical model of Narsimhan (2010). A new approach for the simulation of foam formation in aerated liquid is proposed. The details of the new approach has been explained and presented in this chapter. Foam is considered as a separate phase which is comprised of a mixture of air and liquid. A computational fluid dynamic (CFD) model has been developed for the simulation of creaming and formation of foam in aerated liquid using the proposed approach. The model has been used to predict foam formation, different bubble class and fluid flow with time. The model accounts for the formation of foam due to transformation of both air and liquid into foam and it's destruction due to liquid drainage and bursting of bubbles. Different types of bubble class were considered and their coalescence was taken into account. The coalescence model of Prince and Blanch (1990) was considered for air-liquid dispersion whereas for the foam layer, the bubble coalescence due to film rupture developed by Tong et al. (2011) was used for present model. A population balance method was used to track the number density of different bubble class and the fixed pivot method was used to discretize the population balance equation. The source term for coalescence in the scalar transport equation was updated using a rectified model of Hagesaether et al. (2002). User subroutine has been written in FORTRAN programming language to incorporate bubble coalescence as well as proposed approach of foaming into the main CFD software. The number density of different bubbles class was determined and the Sauter mean diameter of the bubble class was evaluated. A phase diagram was drawn for different initial air volume fraction. The results obtained from the simulation were compared with the data available in the literature. The results obtained are in reasonable agreement with the results of Narsimhan (2010). The discrepancies were mainly attributed to assumption of uniform size bubble in Narsimhan (2010).

4.1 Introduction

Computational fluid dynamic (CFD) simulations of gas–liquid two phase flows started more than two decades ago (Bhole et al., 2008). These have been used in many fields of engineering involving gas-liquid flow (Buwa and Ranade, 2002, Chen et al., 2005, Díaz et al., 2008, Alam et al., 2011, Alam et al., 2010a, Alam et al., 2010b, Alam et al., 2012, Huda et al., 2012). Numerous CFD model of multiphase flow have been developed, and numerical data has been validated through comparison with experimental data. There are two main approaches for the simulation of multiphase flow, namely the Euler–Lagrange method which considers the bubbles as individual entities tracked using trajectory equations, and the Euler–Euler method which is based on two-fluid model which assumes the gas and liquid phases to be interpenetrating continua (Bannari et al., 2008, Bhole et al., 2008). From computational considerations, the Euler–Euler approach is more economical and commonly used (Bhole et al., 2008).

In bubbly flow, the bubbles are accumulated at the top of liquid surface leading to the formation of foam if surface active agent is present and the bubble accumulation is faster than the decay (Vardar-Sukan, 1998). Foam is formed by the entrapment of many gaseous bubbles in a liquid or solid. Foam is normally a complex system consisting of poly-disperse gas bubbles separated by draining films. In aerated liquid, bubble creams at the top surface of liquid to form foam. Aerated products are commonly used and foaming has become one of the fastest growing processing operations for the development of new innovative products. Air is sometimes incorporated in the form of fine bubbles in order to render texture to these products. Air is incorporated into these products by a variety of different techniques such as fermentation, whipping, mixing, vacuum expansion, and gas injection (Narsimhan, 2010).

In foam, bubbles are separated by thin film which is called lamellae and the lamellae are joined in a channel called Plateau border. The liquid is drained out from the lamellae through the Plateau border. The lamellae rupture when the drainage casuses the film to reach a critical limit. When the bubbles coalesce the number density of the bubble class changes which ultimately changes the number of individual bubble classes. In the two phase flow (gas bubble and liquid) the above phenomena is difficult to incorporate but

most of the simulation is done on two phase flow. If the foam is cosidered as a sperate phase which is composed of gas and liquid then the life of the foam can be controlled by it's formation due to phase transformation from gas and liquid and destruction of foam due to phase transformation from foam to gas and liquid.

Monodisperse (same bubble size) foam suffers from film rupture (coalescence) and gas exchange (coarsening) between adjacent bubbles, both processes leading ultimately to poly-dispersity in bubble size (Drenckhan and Langevin, 2010). Narsimhan (2010) assumed that the bubble in the dispersion is uniform size and the bubble coalescence does not occur in the dispersion as well as in the foam layer. A review on various mechanisms and available kernel models for the coalescence of fluid particles (bubbles and drops) is available in the recent paper by Liao and Lucas (2010). The most popular and acceptable theory of bubble coalescence is the film drainage model. Coalescence of bubbles occurs when collision of two bubbles takes place, trapping liquid between them and the liquid drains out until a critical thickness is reached and eventually the film ruptures. Collision a prerequisite to coalescence that may occur due to turbulence fluctuation, viscous shear stress, laminar shear, capture in turbulent eddies, buoyancy and wake interaction (Liao and Lucas, 2010, Chesters, 1991, Friedlander, 1977, Prince and Blanch, 1990, Wang et al., 2005, Wu et al., 1998). The collision model of Prince and Blanch (1990) due to laminar shear is considered in the present model. The bubble coalescence model based on film rupture developed by Tong et al. (2011) has been used in the foam layer of the present model.

In this study a new approach has been used to simulate the foam formation in aerated liquid. This study assumed that the bubbles of uniform size was distributed homogeniusly and the event of coalescence of bubble occured in the dispersion as well as the foam layer. Bubbles were classified by classes of method (CM). Coalescence of bubbles due to laminar in gas-liquid dispersion and film rupture in foam is considered and their number density is evaluated. Population balance equation has been used to track the number density of different bubble class. A modfied source term has been used to update the source in the population balance equation. A phase diagram as a plot of dimensionless height versus the charctersitic time has been drawn for different intial air volume fraction and compared with the data available in open literature. The combined

Sautermean diameter of bubble in gas and foam phase has also been evaluated and ploted in the phase diagram.

4.2 Model geometry and methodology for foaming in aerated liquid

This section presents the mass and momentum conservation equations for the modelling of foaming in aerated liquid in Eulerian multiphase flow approach. The population balance equation and the equation for the closure term of bubble coalescence incorporated in the foaming model of aerated liquid are presented in this section. The details of the proposed approach for the foaming of gas liquid dispersion are explained and elaborated in this section. The boundary conditions of the model considered for the numerical simulation of foaming is also presented here. The modeling technique and the features of the model are discussed in this section. Meshing procedure of the present model and the methodology used for the numerical simulation is also presented. Initial conditions of the model and the properties of the fluid used for the numerical simulation are also presented in this section.

4.2.1 Model geometry and features

Numerical prediction of foaming in aerated liquid was done in a container of height 5×10^{-2}m and diameter of 2×10^{-2}mfollowing the condition of Narsimhan (2010) analytical model. The surface mesh of the model was generated using the CAD software Rhinoceros 3.0. The surface mesh was imported into CFD simulation software AVL FIRE 2009.2. The 3D volume mesh of the model has been generated using the Fame Advance Hybrid technique available in the simulation software AVL FIRE 2009.2. The generated grid for the numerical simulation of creaming and foam formation in aerated liquid is shown in Figure 4.1. The model was filled up with uniformly distributed air of volume fraction of 20% and 40% in a Newtonian fluid. The simulation was run in an unsteady state with a time step of 2.5^{-2} second on Intel Xeon Quad Core Z400 Machine with 8.0 GB RAM with processor speed 2.66 GHz.

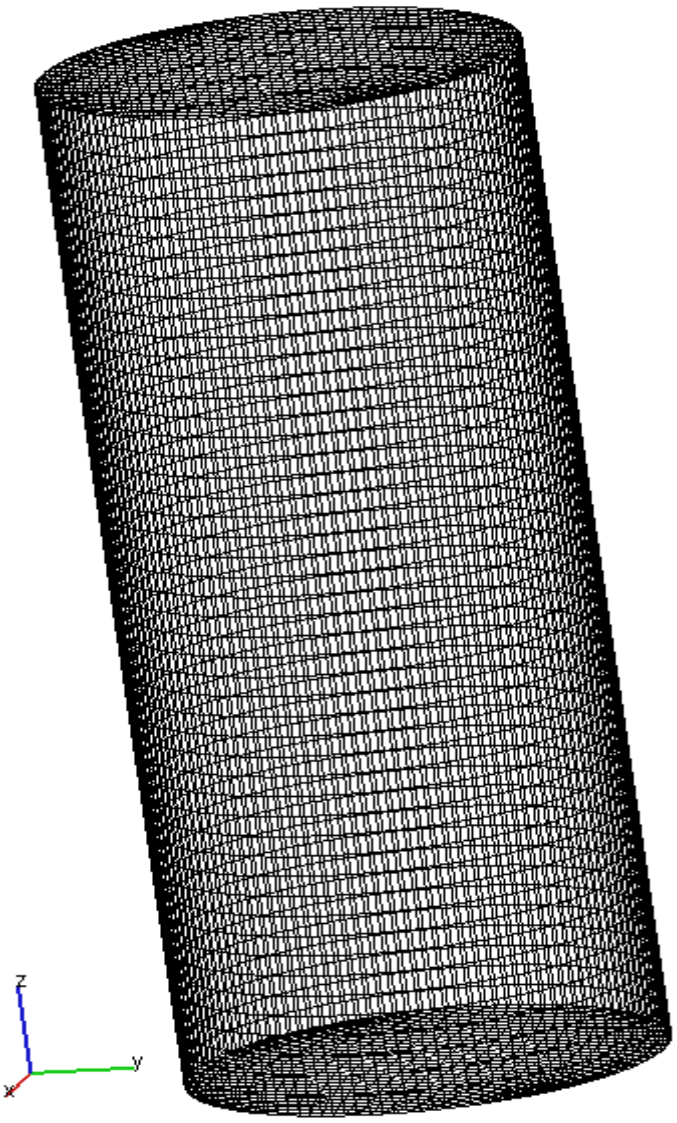

Figure 4.1. Grid generated for the numerical analysis of aerated liquid.

Numerical simulation was performed by commercial CFD package AVL FIRE 2009.2. The total number of cells was 45000 and there was no inlet and outlet flow. The bubbles are allowed to move upward and naturally the liquid flows downward due to gravity and density difference. The diameters of the bubble classes considered in this model are presented in Table 4.1. Ten types of bubble classes were considered in this model .The volume of the upper bubble class was considered as twice the volume of the lower countepart such that $v_i = 2v_{i-1}$. Initially the bubbles of the lowest class (class 1) were assumed to be uniformly distributed into the system.

Table 4.1. Bubble classes used in the simulation.

Bubble class index	1	2	3	4	5	6	7	8	9	10
Bubble diameter ($\times 10^{-3}m$)	0.5	0.63	0.794	1.00	1.26	1.59	2.00	2.52	3.18	4.00

An unsteady state multiphase solution for momentum and continuity were used and for turbulence, a low Reynolds number version of $k-\varepsilon$ turbulence model (Jones and Launder, 1972) was used for the gas and liquid phases and the foam phase was considered as laminar. A cell centered finite volume approach was used to discretize the governing equations and the resulting discretized equations were solved iteratively using segregated approach. For momentum and turbulence, first order upwind differencing scheme was used whereas for continuity equation a central differencing scheme with second order accuracy was used. Walls were treated as nonslip boundaries with standard wall function. The modelling of bubble coalescence and population balance modelling as well as foaming model was incorporated in the main CFD software as subroutine written by the author in FORTRAN programing language. The Capillary number was considered as 0.1 for the present modelling of creaming and foam formation. The capillary number refers to the ratio of capillary force and gravitational force. The viscosity and surface tension were obtained from the same capillary number and Peclet number used in the present study and Narsimhan (2010) model.

4.2.2 Boundary conditions assigned for the model

The following boundary conditions were considered for the modelling of creaming and formation of foam in aerated liquid.

4.2.2.1 Inlet

The model was filled up with uniformly distributed air of volume fraction of 20% and 40% in a Newtonian fluid. Then the mixture was kept undisturbed so that the liquid flows downward and the gas flow upward to settle at the top with time. Therefore no specified inlet was considered where the fluid will enter.

4.2.2.2 Outlet

The top surface of the model was specified as the outlet (see Figure 4.1). The diameter of the exit was 2×10^{-2}m following the condition of Narsimhan (2010) analytical model. Static pressure boundary conditions were applied at the outlet.

4.2.2.3 Wall

In this model the wall was considered as solid wall. A non-slip condition was applied at all walls. There was no movement of the mesh as well as no heat transfer between the wall and outside environment.

4.2.3 Governing equations for the modelling of foaming in aerated liquid

The governing equation used for the simulation of foaming in aerated liquid is discussed and presented in the following section. The equation includes the fundamental flow equation such as conservation of mass and momentum equation. The interfacial exchanges of mass and momentum is also presented. Bubble break-up and bubble coalescence as well as popluation balance equation is also presented and discussed. The euqations for the presentation and explanation of phase diagram is also discussed and presented in this section.

4.2.3.1 Mass conservation equation

The mass conservation equation used in the present study is based on the Eulerian-Eulerian multiphase approach. Gas, liquid and foam phases are treated as separate phases. The mass conservation equation used for the modelling of bubble column reactor presented in Chapter 3 is also used for the present model except a mass

interfacial exchange term is included in the mass conservation equation because in the present model there is exchange of mass between phases. For the modelling of creaming and formation of foam in aerated liquid, the mass conservation equation used can be written as:

$$\frac{\partial \alpha_k \rho_k}{\partial t} + \nabla . \alpha_k \rho_k V_k = \sum_{l=1, l \neq k}^{N} \Gamma_{kl} \ , \quad k=1,\ldots\ldots,N \tag{4.1}$$

Where α_k is the volume fraction of phase k, V_k is phase k velocity, and Γ_{kl} is the interfacial mass exchange between phases k and l.

4.2.3.1.1 Mass interfacial exchange

In the present model, gas and liquid transform into foam when in any cell there is more than 75 percent gas provided liquid is available in that cell. Similarly foam also transforms into liquid and gas due to liquid drainage and bubble bursting at the top. This mass transformation between phases was dealt with mass interfacial exchange term in the mass conservation equation (Eqn. 4.1). The mass transformation between gas and foam was calculated using the following equation:

$$\Gamma_f = \frac{\frac{\pi}{6} d_i^3 \left(\rho_g {}_{\sum_i^n N_{i_g}} - \rho_f {}_{\sum_i^n N_{i_f}} \right)}{dt} = -\Gamma_g \ , \qquad N_{i_g} \leq N_{i_{av}} \tag{4.2}$$

Where N_{i_g} is the number of bubble in gas phase transformed into foam phase, N_{i_f} is the number of bubble in foam transformed into gas phase, dt is time step and $N_{i_{av}}$is the number of gas bubble available in that cell. The number of gas bubble transformed into foam bubble was calculated from the equation.

$$N_{i_g} = \frac{\alpha_l v_c}{n_p a_p l_i}, \alpha_g \geq 0.75 \tag{4.3}$$

Where α_l is volume fraction of liquid in the cell and v_c is the volume of that cell. The number of foam bubble transformed into gas bubble is calculated from the equation:

$$N_{i_f} = \frac{q_{PB}}{n_p a_p l_i}, \alpha_f > 0 \tag{4.4}$$

Similarly the mass transformation between liquid and foam was calculated using the following equation:

$$\Gamma_f = \frac{n_p a_p l_i\left(\rho_l \Sigma_i^n N_{i_g} - \rho_f \Sigma_i^n N_{i_f}\right)}{dt} = -\Gamma_l\,, \qquad N_{i_g} \le N_{i_{av}} \tag{4.5}$$

4.2.3.2 Momentum conservation equation

The momentum conservation equation for each phase in Eulerian-Eulerian approach on the finite volume method has been used. The momentum conservation equation used for the present model is similar to that of the modelling of bubble column reactor which is presented in Chapter 3 at Section 3.2.3.2 (refer to Eqns. 3.2-3.5). In the previous model for turbulent a standard $k-\varepsilon$ model was used for the gas and liquid whereas for the present model a low Reynolds number version of $k-\varepsilon$ model (Jones and Launder, 1972) was used for the gas and liquid phases and the foam phase was considered as laminar. The turbulent viscosity was calculated using the following equation taken from Jones and Launder (1972) as:

$$\mu_k^t = C_\mu f_u \rho_k \frac{K_k^2}{\varepsilon_k}. \tag{4.6}$$

In the above equation f_u is added and its value was calculated from the following equation:

$$f_u = \exp\left[-2.5 \Big/ \left(1 + R/_{50}\right)\right] \tag{4.7}$$

Here R is Reynold number.

4.2.3.3 Momentum interfacial exchange

There is significant momentum exchange between phases. The momentum exchanges between phases were dealt with the momentum interfacial exchange term in the momentum conservation equation (Eqn. (3.2) in Chapter 3). The momentum interfacial exchange between phases due to bubble coalescence was taken into account. The bubble

induced drag force was considered in the present study. The momentum interfacial exchange between phases was modeled by considering interfacial momentum source. The momentum interfacial exchange between gas and liquid was calculated using the equation presented in Chapter 3 at Section 3.2.3.2.1 (refer to Eqns. 3.6-3.11).

4.2.3.4 Population balance equations

The number density of different bubble classes changes in the gas liquid dispersion as well as in the foam due to coalescence of bubble. The population balance equation was used to track the number density of individual bubble class. The population balance equation presented in Chapter 3 at Section 3.2.3.3 was also used for the present model (refer to Eqns. 3.12-3.15). This PBE is termed as scalar transport equation in the AVL Fire 2009.2 software. The source term of coalescence in the scalar transport equation has been updated using the source term model of Hagesaether et al. (2002) with rectification and presented in Chapter 3 at Section 3.2.3.4 (refer to Eqns. 3.31-3.32 and Eqns. 3.39-3.40).

4.2.3.5 Bubble coalescence in air-liquid dispersion

In the present model the container was filled up with uniformly distributed air of volume fraction of 20% or 40% in a Newtonian fluid. The container is then left undisturbed to let the liquid settle at the bottom with time and the air to rise on the top. A layer of foam is formed during this process of settlement. During the process of foam formation bubble comes closer to each other and they coalesce. The process is very slow and there is very low turbulence in the system. Therefore, there is no break-up of bubble due to bombardment of turbulent eddies. So for the present model only coalescence event was taken into account. The coalescence model of Prince and Blanch (1990) has been used in the present study. The coalescence model of Prince and Blanch (1990) based on the laminar shear collision was used for the present model. The laminar shear was calculated using equation which is presented in Chapter 3 at Section 3.2.3.6 (refer to Eqns.3.49, 3.51-3.54). The final form of the coalescence rate used for the present model is as:

$$\Gamma_{ij} = \left\{\theta_{ij}^{LS}\right\} \times P_C\left(r_i, r_j\right) \tag{4.8}$$

The efficiency of the coalescence was calculated using equation which is presented in Chapter 3 at Section 3.2.3.6 (refer to Eqns. 3.55-3.58).

4.2.3.6 Bubble coalescence in foam

Foam is formed at the top of the container and liquid settle at the bottom. There is gas liquid dispersion in between foam and liquid. In foam coalescence of bubble also takes place due to liquid drainage. The liquid drain out through the Plateau border channel and the lamellae reaches in a critical thickness and burst. This bursting of lamellae which separate the bubble causes them to coalesce. The coalescence of bubble inside foam was modelled by Tong et al. (2011). In the present model, the coalescence of bubble inside foam was calculated using the model of Tong et al. (2011). The coalescence rate $\Omega_{C_{i,j}}^{f}$ of a bubble of the ith group with bubbles of the jth group was calculated using the following equation:

$$\Omega_{C_{i,j}}^{f} = n_{p_i} P_{i,j} f_{i,j} \tag{4.9}$$

where n_{p_i} is the number of films per bubble of the ith group, $P_{i,j}$ is the failure rate of films separating bubbles of the ith and jth groups, $f_{i,j}$ is the probability of a bubble of the ith group sharing the same film with the bubbles of jth group in the foam.

Inside foam bubble is deformed as polyhedral shape with different size and shape. In the present simulation it was assumed that the bubbles are in pentagonal dodecahedron shape. Ten types of bubble classes with different diameter were considered in this model which is presented in Table 4.1. From the geometry of pentagonal dodecahedron, the number of film per bubble is $n_{p_i} = 6$. The probability of a bubble of the ith group sharing the same film with the bubbles of jth group can be calculated as

$$f_{i,j} = \frac{n_{p_j} n_j}{\sum_{k=1}^{M} n_{p_k} n_k} \tag{4.10}$$

Where n_j and n_k is the number of bubble of the jth and kth group respectively.

The frequency of the film failure is inversely proportional to the life time of the film as:

$$P_{i,j} = k\frac{1}{\tau} \tag{4.11}$$

The coefficient k in the equation depends on the fluid viscosity and surface chemistry. The coefficient also includes the hybrid effects of relevant physicochemical properties of the employed surfactant solution on the stability of films (Tong et al., 2011). Keeping operational parameter and the physiochemical properties of the fluid constant in the simulation the coefficient can be determined by adjusting its value in the simulation (Tong et al., 2011). In the present study the operational parameter such as input velocity as well as the composition of the molten metal was varied. The effect of the coefficient was disregarded ($k = 1$) in the present study.

Amount of liquid per bubble, $\emptyset_i/N_i$ so the time required to drain out this liquid is (Bhakta and Ruckenstein, 1997):

$$\tau = (\emptyset_i/N_i)/q_{PB} \tag{4.12}$$

4.2.3.7 Phase diagram

During creaming the aerated mixture can be separated into different region. A clear liquid region at the bottom and above it a region of same air volume fraction as the initial volume fraction, then a transition region of increasing air volume fraction and at the top a foam layer where the air bubbles are closely packed and deformed (see Figure 4.2) (Narsimhan, 2010). The dimensionless height Z^*can be calculated as:

$$Z^* = \frac{Z}{h} \tag{4.13}$$

Where z is the distance from the top and h is the total height of the container. The characteristic time t^* can be calculates as:

$$t^* = \frac{U_0 t}{h} \tag{4.14}$$

Where, t is the time and U_0 is the free creaming velocity of an isolated air bubble in the liquid. The dimensionless Peclet number Pe can be given by

$$Pe = \frac{U_0 h}{D_0} \tag{4.15}$$

$D_0 = \frac{kT}{6\pi\mu d}$ is the Stokes-Einstein equation for diffusion of spherical particle through liquid with low Reynolds number. Where k and T is the Boltzmann constant and absolute temperature respectively. The Peclet number Pe was considered as 6.25×10^{13} for the present study.

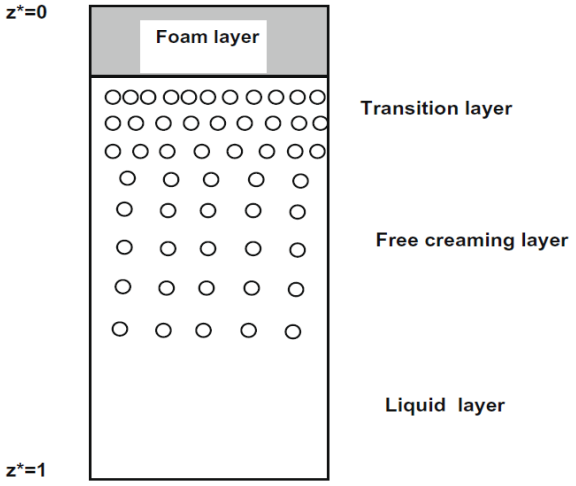

Figure 4.2. Different regions in an aerated liquid (Narsimhan, 2010).

The typical phase diagram is shown in Figure 4.3. The equation for a characteristic line is given by (Narsimhan, 2010):

$$Z^* = Z_0^* + V(\emptyset_{in})t^* \tag{4.16}$$

In phase diagram, the region bounded by the curve ABO is the initial air volume fraction and the region bounded by curve OBC is the transition region of increasing air volume fraction. The region below OC line is the foam layer and above the curve APBC is clear liquid. The details explanation of coordinate and equation for the different point and lines respectively in the phase diagram is available in Narsimhan (2010).

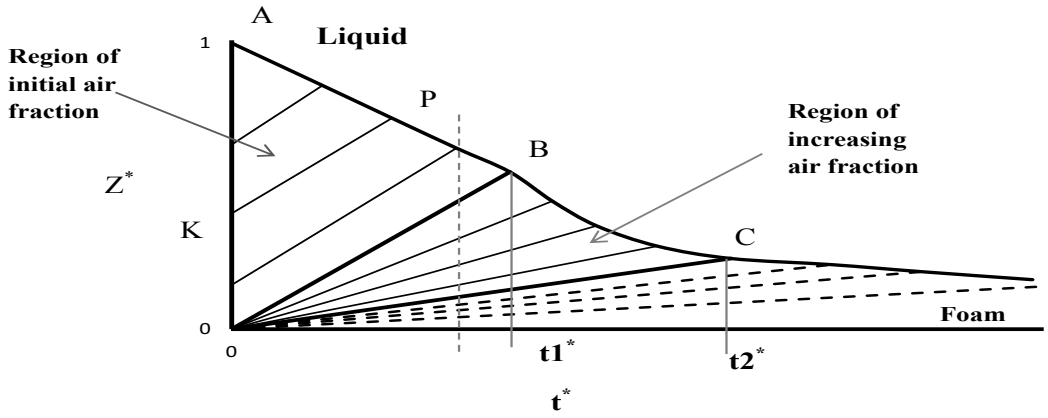

Figure 4.3. Typical phase diagram (Narsimhan, 2010).

4.2.3.8 The proposed comprehensive approach for simulation of foam

Foam is composed of many gaseous bubble separated by thin film called lamellae. The lamellae is inter connected by a channel called Plateau border (PB). In foam, bubble bursts at the top and coalesce due to film rupture caused by liquid drain-out through the Plateau border. It is difficult to incorporate these characteristics of foam in an ordinary two phase gas/liquid simulation approach. The foam is supposed to accumulate at the top, but in gas liquid two phase approach, the gas diffuses in the atmosphere and is difficult to hold at the top. The above drawback is eliminated by considering foam as a separate phase made up of gas and liquid. The foam is formed by the gas bubble and holding liquid in the lamellae and Plateau border channel. The destruction of foam is due to the bursting of bubbles at the top and coalescence inside foam. The new approach enables us to apply the characteristic of foam.

In wet foam the liquid volume fraction is typically between 10% and 20% and the bubbles are approximately spherical, while in dry foam the volume fraction of liquid is less than 10% and the bubbles are more polyhedral in shape (Breward, 1999). The liquid content in foam lies between 0.1-0.2 or lower (Pawlat et al., 2004, Guo et al., 2002, Schick, 2004). The development of onset of foam is found to form when the gas fraction is 0.74 by Pilon and Viskanta (2004). If the bubbles are mono-dispersed and randomly

packed, then the value of liquid fraction is about 0.36, while for close packed bubbles the value is about 0.26 (Narsimhan, 2010). Drenckhan and Langevin (2010) reported of liquid volume fraction of 0.24 to 0.36 in the foam for fcc (face-centred cubic) packing from sphere to random close packed bubble. Narsimhan (2010) also reported the formation of foam at the value of air volume fraction of 0.74 or more.

In the present study the gas liquid mixture is considered to be foam when the gas volume fraction is more than or equal to 0.75. However, in the absence of a proper surface active agent in the foam, the viscosity, density and surface tension properties of foam will be such that the bubble inside the foam will burst immediately and foam will return to liquid and gas phases. In this situation the bubbles are considered as closely packed with polyhedral shape. So when the gas volume fraction in any cell reaches 0.7 then gas bubble and the liquid is transformed into foam according to proportion.

A total of 21 scalars were assigned to track 10 bubble classes in gas and 10 bubble classes in foam separately and a liquid in the foam. The properties of foam were determined from the amount of gas and liquid present in the foam. The density and viscosity of foam is calculated by the following equation:

$$\rho_f = \rho_l \alpha_l + \rho_g (1 - \alpha_l) \tag{4.17}$$

$$\mu_f = \mu_l \alpha_l + \mu_g (1 - \alpha_l) \tag{4.18}$$

Where ρ is density, μ is viscosity $\emptyset$ is scalar fraction (liquid) in the foam and subscript f, g, l denote foam, gas and liquid respectively.

4.2.3.9 Liquid drainage in foam

The bubble is considered as pentagonal dodecahedron shape. There are 12 films and 30 channels in a pentagonal dodecahedron bubble. Each Film or lamellae is shared by two bubbles and each the Plateau border channel is shared by three bubbles. So, the number of film per bubble is $n_f = 6$ and the number of Plateau border channel is $n_p = 10$. The volume of a regular pentagonal dodecahedron with edge length l is

$$V = 7.7 l^3 \tag{4.19}$$

And the area of each pentagonal film

$$A = 1.72l^2 \tag{4.20}$$

According to the definition, the volume of pentagonal dodecahedron bubble with radius R is:

$V = \frac{4}{3}\pi R^3$ We get $l = 0.816R$ (4.21)

Liquid is trapped in film and Plateau border. So the total amount of liquid entrapped per bubble is the sum of the liquid in lamellae and the Plateau border. The total amount of liquid entrapped by the bubble class i is

$$\emptyset_i = N_i n_p a_p l_i + N_i n_f a_f x_f \tag{4.22}$$

Where $\emptyset_i$ is liquid content, N_i is the number of bubble, l_i is the length of Plateau border, a_p is the cross section of the Plateau border of bubble class i and x_f is the thickness of the film. The thickness of the film is much smaller, so neglecting the liquid in film the equation (4.22) becomes

$$\emptyset_i = N_i n_p a_p l_i \tag{4.23}$$

Total amount of liquid entrapped by all the bubbles in a bubble class is the sum of the liquid entrapped by each individual bubbles in the class.

$$\emptyset = \sum_i^N \emptyset_i \tag{4.24}$$

Once foam is formed many factors contribute to the stability and pattern of foam formation (Vardar-Sukan, 1998). The liquid drainage due to gravity through Plateau border derived by Bhakta and Ruckenstein (1997) is used in the present study and elaborated here. The flow rate of liquid in foam of horizontal plane is the sum of the flow rate through all Plateau border channels. Flow rate depend on the orientation of Plateau border and highest in a vertical position and lowest in horizontal position. Let us consider the Plateau border with cross section area a_p is inclined at an angle θ with vertical. The average velocity of liquid is:

$$u_\theta = \frac{c_v a_p}{20\sqrt{3}\,\mu}\left[\rho g \cos\theta + \sigma \frac{d}{d\left(\frac{z}{\cos\theta}\right)}\left(\frac{1}{r_p}\right)\right] \tag{4.25}$$

Average velocity of liquid in a vertical Plateau border can be calculated as:

$$u = \frac{c_v a_p}{20\sqrt{3}\mu}\left(\rho g + \frac{\delta}{\delta z}\left(\frac{\sigma}{r_p}\right)\right) \tag{4.26}$$

From equation (4.25) and (4.26) we get

$$u_\theta = \cos\theta \frac{c_v a_p}{20\sqrt{3}\,\mu}\left[\rho g + \sigma \frac{d}{dz}\left(\frac{1}{r_p}\right)\right] = u\cos\theta \tag{4.27}$$

Now the volumetric flow rate through the channel can be calculated as:

$$q_\theta = u_\theta a_p = u a_p \cos\theta \tag{4.28}$$

If the Plateau border is randomly oriented then the probability of orientation between θ and $\theta + d\theta$ is $\sin\theta\, d\theta$ and the average volumetric flow rate:

$$\bar{q} = \int_0^{\pi/2} q_\theta(\sin\theta) d\theta = \frac{u a_p}{2} \tag{4.29}$$

Total volumetric flow through the Plateau border (PB) channel across the plane is the product of PB channel per bubble intersected by the horizontal plane, number of bubbles intersected by horizontal plane per unit area and mean flow rate through PB. The number of Plateau border channels per bubble intersected by a horizontal plane is $n_p/5$. For the calculation of number of bubble intersected by the horizontal let us consider $F(R)dR$ the fractional number bubble with radii between R and $R + dR$. The number of bubble with centers at a distance between X and $X + dX$ from the plane is $2NAF(R)dRdX$, where N is the number of bubble per unit volume, A is the foam cross section area. Only the bubble whose center is at a distance smaller than their radii $X < R$ will intersect the plane. Therefore, the number of bubbles of radius R which intersect the plane is

$$\int_{X=0}^{X=R} 2NF(R)dRdX = 2NF(R)dR \tag{4.30}$$

Factor of 2 is due the fact that both side of the plane is considered. The total number of bubble intersected by the plane

$$\int_{R=0}^{R=\infty} 2NRF(R)dR = 2N\bar{R} \tag{4.31}$$

Now the flow of liquid due to gravity drainage through Plateau border channel is:

$$q_{PB} = 2N\bar{R}\left(\frac{n_p}{5}\right)\bar{q} = \frac{3}{15}NRn_p a_p u \tag{4.32}$$

If it is assumed that surface tension and the radius of curvature of Plateau border do not change with height then the velocity of drainage can written as:

$$u = \frac{c_v a_p \rho g}{20\sqrt{3}\mu} \tag{4.33}$$

The cross section area of the Plateau border channel from Leonard and Lemlich (1965) used by Bhakta and Ruckenstein (1997) is presented here. The cross section area of the Plateau border channel a_p is calculated from radius of curvature of the Plateau border wall $r_p$and the film thickness x_f. The cross section area can be written as:

$$a_p = \frac{\left(0.322r_p + 1.732x_f\right) - 2.721{x_f}^2}{0.644} \tag{4.34}$$

The thickness of the film is much smaller than the bubble diameter and the radius of curvature of Plateau border. Then the cross section of the Plateau border can be written as:

$$a_p = 0.161{r_p}^2 \tag{4.35}$$

All the model parameters used in the present study are presented in Table 4.2.

Table 4.2. Model parameters employed in the simulation.

Model parameter	Value
C_μ	0.09
k	1
c_v	1

4.2.4 Initial conditions of the model and the properties of fluids

In the analytical model the cylinder is initially filled up with a uniformly distributed volume fraction (20% and 40%) of air in Newtonian liquid. The analytical model accounts for the creaming and formation of foam layer. In the present study the simulation was carried out in a container of height 5×10^{-2} m and diameter of 2×10^{-2}m following the condition of Narsimhan (2010) analytical model. Similar to the analytical model of Narsimhan (2010), in the present study the container was filled with different initial air volume fraction. The two models simulated in the present study were with 20 percent and 40 percent air in a Newtonian liquid respectively. Initially the bubbles of the lowest class (class 1) were assumed to be uniformly distributed into the Newtonian liquid of the system. The properties of the fluids used in this study are presented in Table 4.3.

Table 4.3. Properties of the fluids used for the modelling of creaming and foam.

Properties	Air	Liquid
Density (kg/m^3)	1.188	1001.188
Viscosity (Ns/m^2)	1.824E-05	0.404

4.2.5 Grid independency test

Two different number of grid for the model was generated with a control volume (number of cell) of 45000 and 75000. Numerical simulation was carried out on both grid with initial air volume fraction of 20% and the convergent was verified in both cases. No significant differences were observed in the results. The height of foam at the top in term of volume fraction of foam at 90s for both meshes is presented in Figure 4.4. The length of foam formation for the both cases is almost similar. Therefore, for all the subsequent simulations and results, the 45000 control volumes numerical mesh was used.

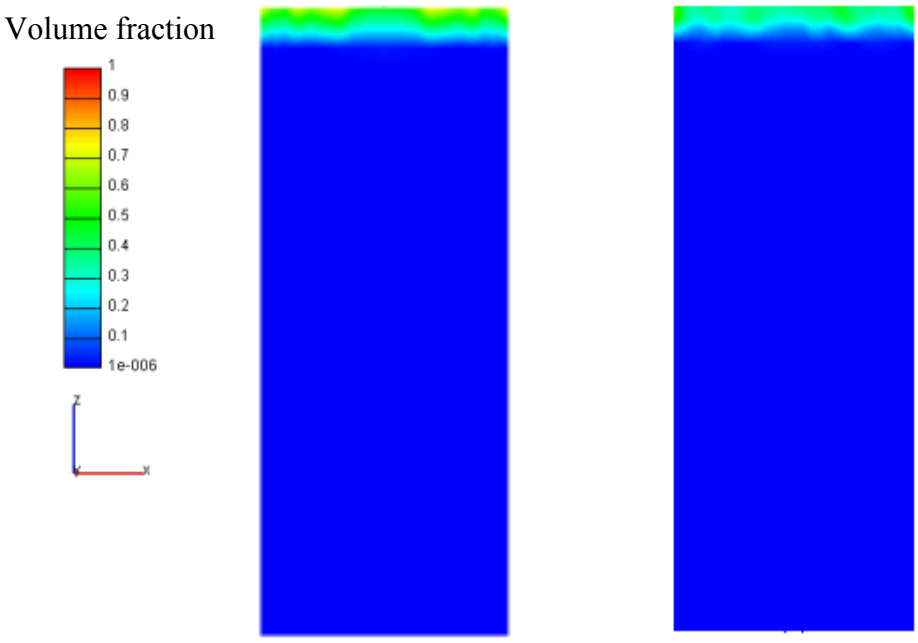

Figure 4.4. Formation of foam at 90s (a) 75000 cells (b) 45000 cells.

4.3 Results and discussions

4.3.1 Presentation of results obtained from simulation of Narsimhan (2010) analytical model

The simulation starts with a cylinder filled up with uniformly distributed air of volume fraction of 20% and 40% in a Newtonian fluid separately. The cylinder is then left undisturbed to let the liquid settle at the bottom with time and the air to rise on the top. A layer of foam is formed during this process of settlement. Results are presented in this section in the form of phase diagram (explained in section 4.2) and volume fraction of the air, liquid and foam.

The phase diagram from the present simulation and (Narsimhan, 2010) model for an initial air volume fraction of 0.4 is shown in Figure 4.5. In order to distinguish between the present simulation and the results of Narsimhan (2010) analytical model, Narsimhan (2010) results are presented with letters and numbers with prime ($'$). The present simulation results are presented in solid lines and the Narsimhan (2010) analytical data is presented in dotted lines. The figure shows the clear liquid region above the curve ABCD for the present simulation and above the curve $AB'C'D'$ for Narsimhan (2010) results. Initial air volume fraction, transition region of increasing air volume fraction and foam layer can be seen by the region bounded by the curve ABO, OBC and OCD for the present simulation and by the curve OAB', $OB'C'$ and $OC'D'$ for Narsimhan (2010) model. Initially the volume fraction of air was 0.4 and uniform throughout. As the time elapsed the clear liquid layer starts to settle at the bottom and the gas volume fraction decreases at the bottom. At the same time the air volume fraction increases at the top and foam starts to appear. At the longer time, the transition layer of increasing air volume fraction is formed above the creaming layer and the foam layer is formed at the top. These phenomena can also be seen in Figure 4.11 and Figure 4.12. In the present simulation, the transition to increasing air volume fraction and formation of foam layer occurs somewhat earlier than that of Narsimhan (2010) model. This can be attributed to the fact that the present simulation predicts the creaming velocity which is a little faster than the analytical model. This creaming velocity causes the dispersion to

settle faster and causes the formation of foam earlier as can be seen below the curve OCD and OC′D′ in Figure 4.5.

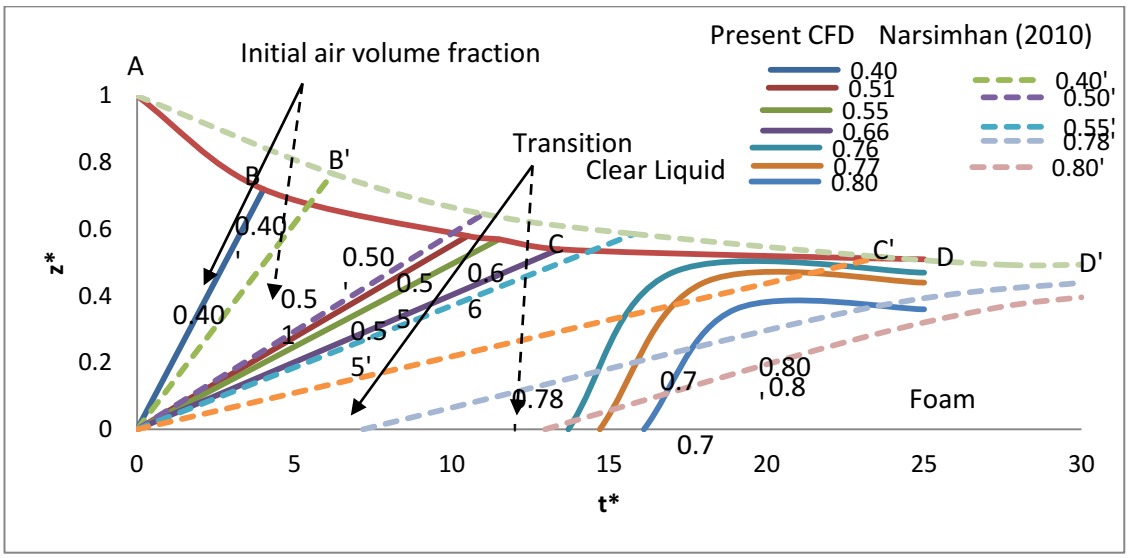

Figure 4.5. Phase diagram as plot of z^* vs.t^* for an initial air volume fraction of 0.4. Different regions are identified along with contours of constant volume fraction.

Phase diagram from the present simulation and Narsimhan (2010) model for the initial air volume fraction of 0.2 is shown in Figure 4.6. The figure clearly shows the liquid, foam layer, initial volume fraction and transition region of increasing air volume fraction. The figure indicates that the curve ABC is different from the curve AB′C′. The dimensionless height (z^*) and characteristic time (t^*) depends on the creaming velocity (refer Eqn. (4.11) and Eqn. (4.12)). The present CFD model predicts the creaming velocity slower than that of Narsimhan (2010). The number of bubble when initial air volume fraction of 0.2 is less than that of when initial air volume fraction of 0.4. The overall number of upper bubble class when initial air volume fraction of 0.2 is less than that of when initial air volume fraction of 0.4. The effect of larger bubble class resulting from coalescence on the creaming velocity is more when initial air volume fraction is 0.4 than that of when initial air volume fraction of 0.2. In the present model, when the gas volume fraction in any cell reaches 0.75 then the gas and liquid is transformed into foam based on the equation (4.2)-(4.5). The gas volume fraction at the top cell and subsequently below the top cell reaches 0.75 faster when initial air volume fraction is

0.4 than that of when initial air volume fraction is 0.2. Therefore, faster creaming is observed when initial air volume fraction is 0.4. The profile of the phase diagram for initial volume fraction of 0.2 is different from that of the initial volume fraction of 0.4. In both cases, same Newtonian fluid was used so the effect of variation of initial air volume fraction on the variation of time for transition to foam can be investigated. There is significant difference in the amount of foam formed at the top due to variation in the initial air volume fraction as can be seen in Figure 4.11 and Figure 4.12.

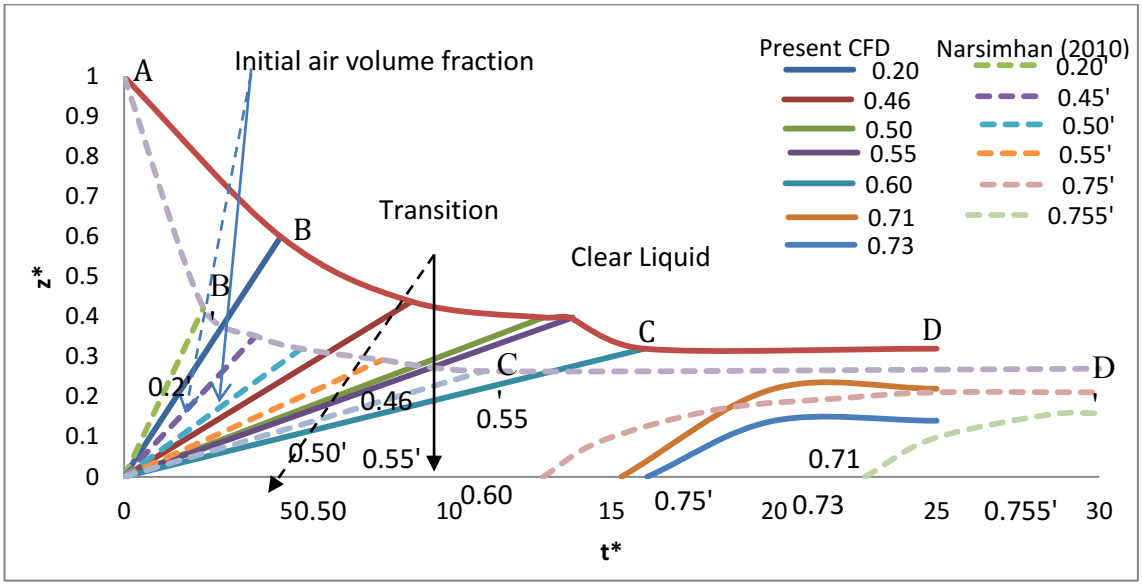

Figure 4.6. Phase diagram as plot of z^* vs.t^* for an initial air volume fraction of 0.2. Different regions are identified along with contours of constant volume fraction.

The radial distribution of different bubble classes at height of 0.048m (distance from the bottom of the container) with initial air volume fraction of 0.4 and 0.2 at 250s is shown in Figure 4.7 and Figure 4.8. The figure shows that the number densities of lower bubble classes (Bubble calss1-Bubble class5) are more than its higher counterpart. In this model the bubble class 1 (the lowest class considered in this study) was uniformly distributed into the system hence its number density is more. The birth of upper bubble classes results from the coalescence of lower bubble classes. As only class 1 bubble was uniformly distributed initially, the coalescence event results in the increase of lower classes. But as time elapses the bubble coalescence causes the increase of upper bubble class (not shown for brevity).

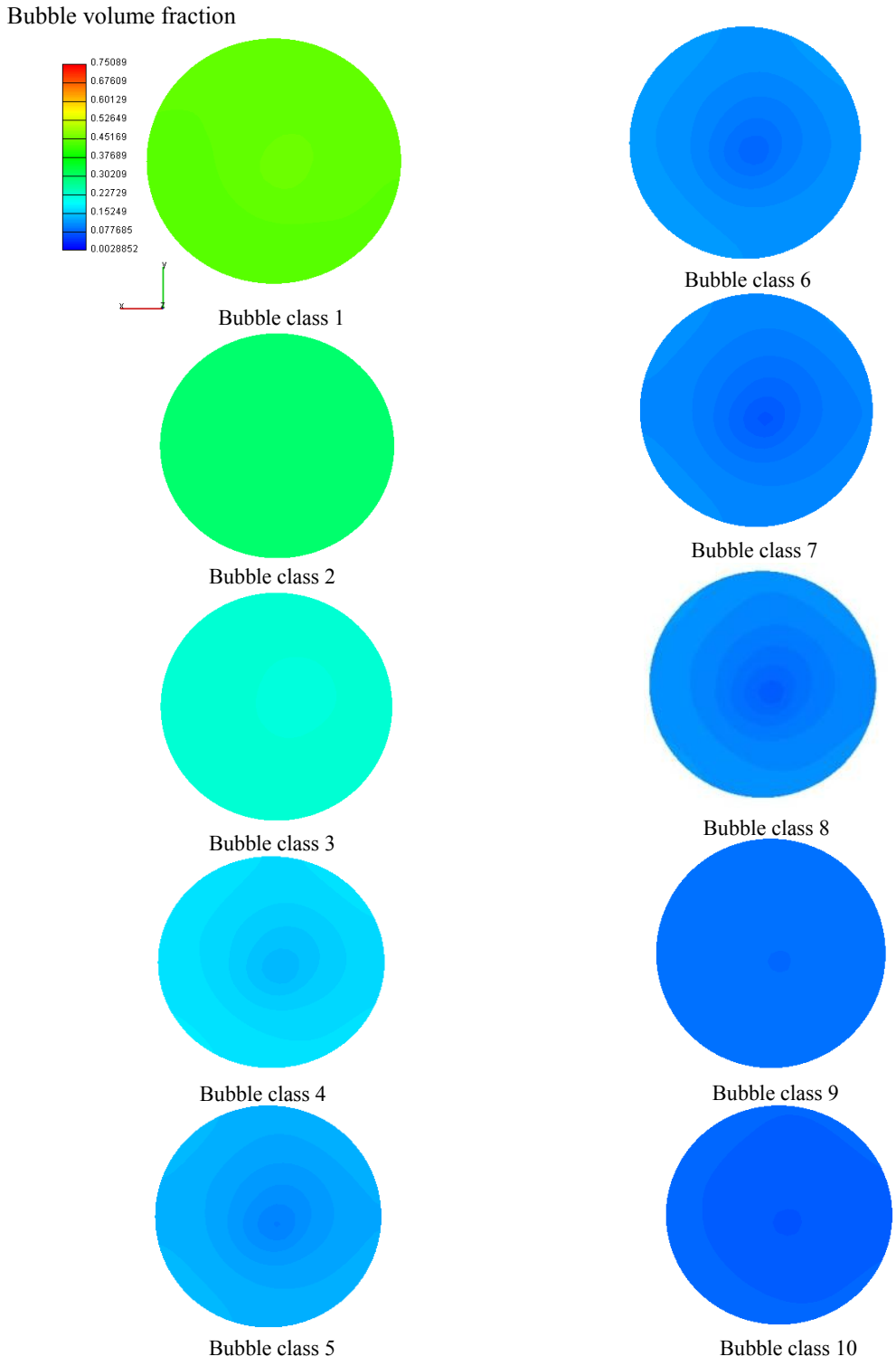

Figure 4.7. Radial distribution of different bubble classes at height 0.048m with initial air volume fraction of 0.4 at 250s.

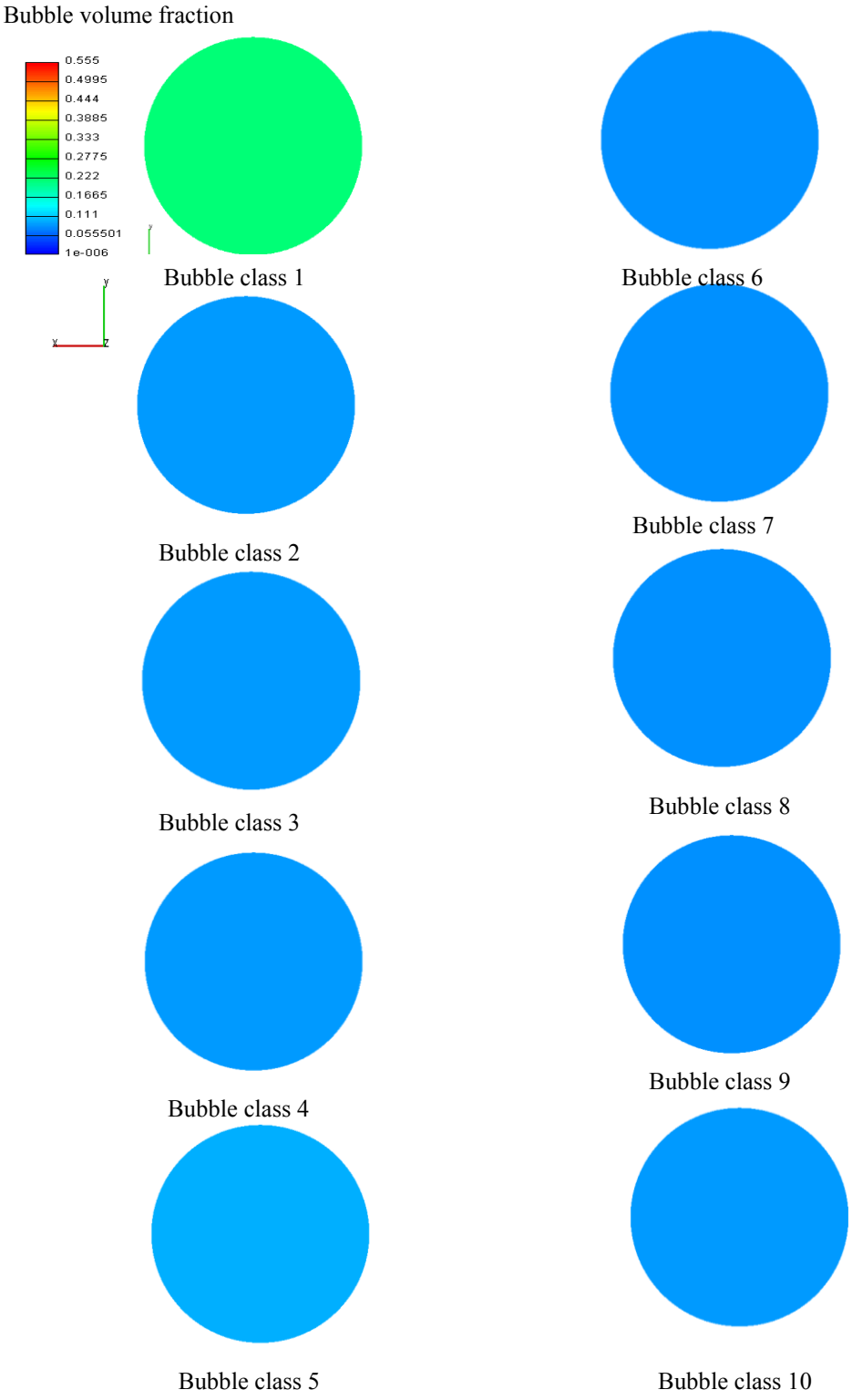

Figure 4.8. Radial distribution of different bubble classes at height 0.048m with initial air volume fraction of 0.2 at 250s.

The Sauter mean diameter of bubble is also calculated and plotted in the same phase diagram with dimensionless height and characteristic time. Initially the air bubbles of diameter 0.5 mm were uniformly distributed in the liquid. The figures show that the Sauter mean diameter of the bubble increases with time. The Sauter mean diameter is highest in the foam layer as can be seen in Figure 4.9 and Figure 4.10. This is mainly due to more film rupturing in the foam than that the dispersed phase. The Sauter mean diameter in the foam layer does not change significantly as can be seen in Figure 4.9 and Figure 4.10. This is because longer time is required for the film to rupture for further coalescence in the foam. In foam layer, the coalescence of bubble depend on the film rupture due to drainage of liquid entrapped by Plateau border channel whereas in creaming layer the coalescence is caused by laminar shear. Longer time required to drain out all liquid entrapped by bubble and therefore coalescence event in foam layer is slower than cream layer.

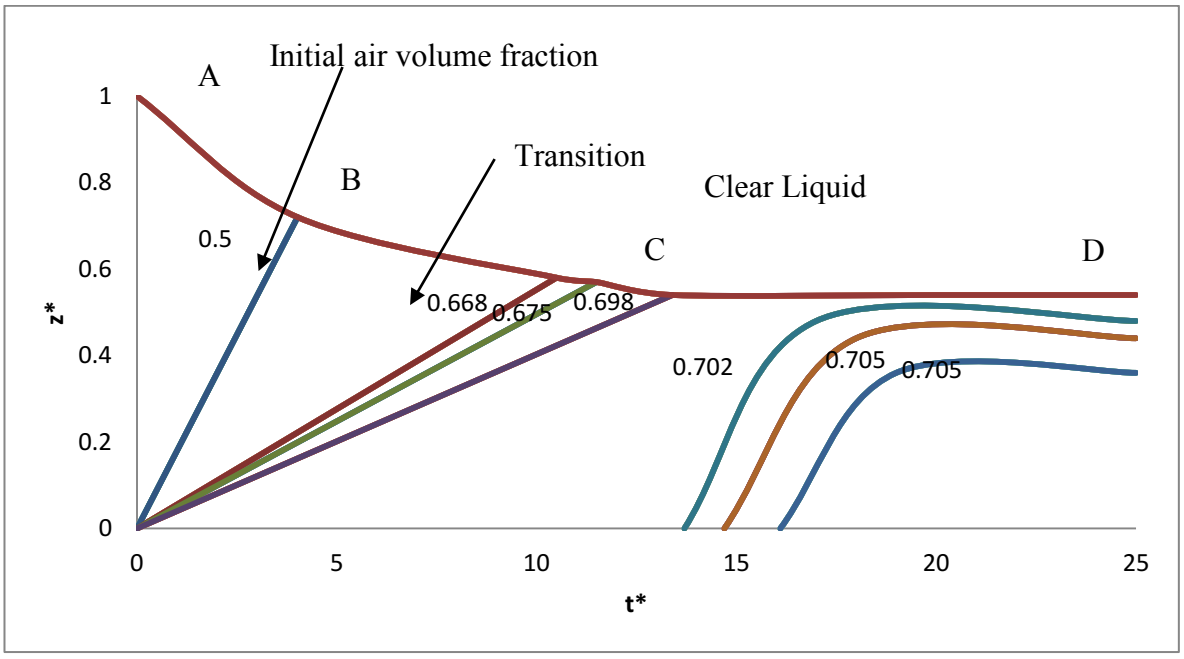

Figure 4.9. Sauter mean diameter in phase diagram for an initial air volume fraction of 0.4.

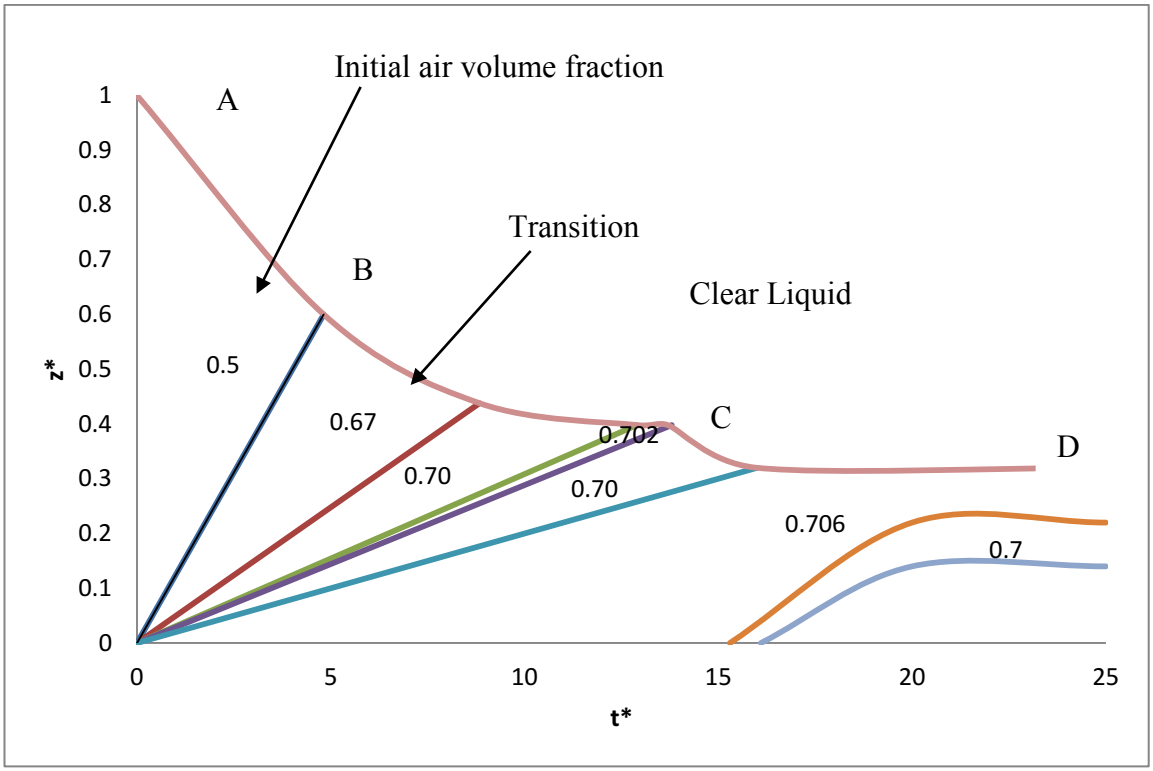

Figure 4.10. Sauter mean diameter in phase diagram for an initial air volume fraction of 0.2.

The volume fractions of air, liquid and foam at different time is presented in Figure 4.11 and Figure 4.12. Clear liquid, foam layer, initial volume fraction and transition region of increasing air volume fraction are visible in the figures. Clear liquid layer at the bottom can be seen at 60s and at the same time the air volume fraction increases at the top and foam starts to appear (Figure 4.11(a) and Figure 4.12(a)). The transition layer of increasing air volume fraction is formed above the creaming layer and the foam layer is formed at the top at time 150s (Figure 4.11(b) and Figure 4.12 (b)). At 600s the transition layer decreases and the foam layer increases as can be seen in Figure 4.11 (c) and Figure 4.12 (c). The above phenomena conforms that of Narsimhan (2010) findings. Figure 4.11and Figure 4.12 show significant influence of the initial air volume fraction. For the same liquid, the higher initial air volume caused more dispersion to form more foam than that with lower air volume fraction.

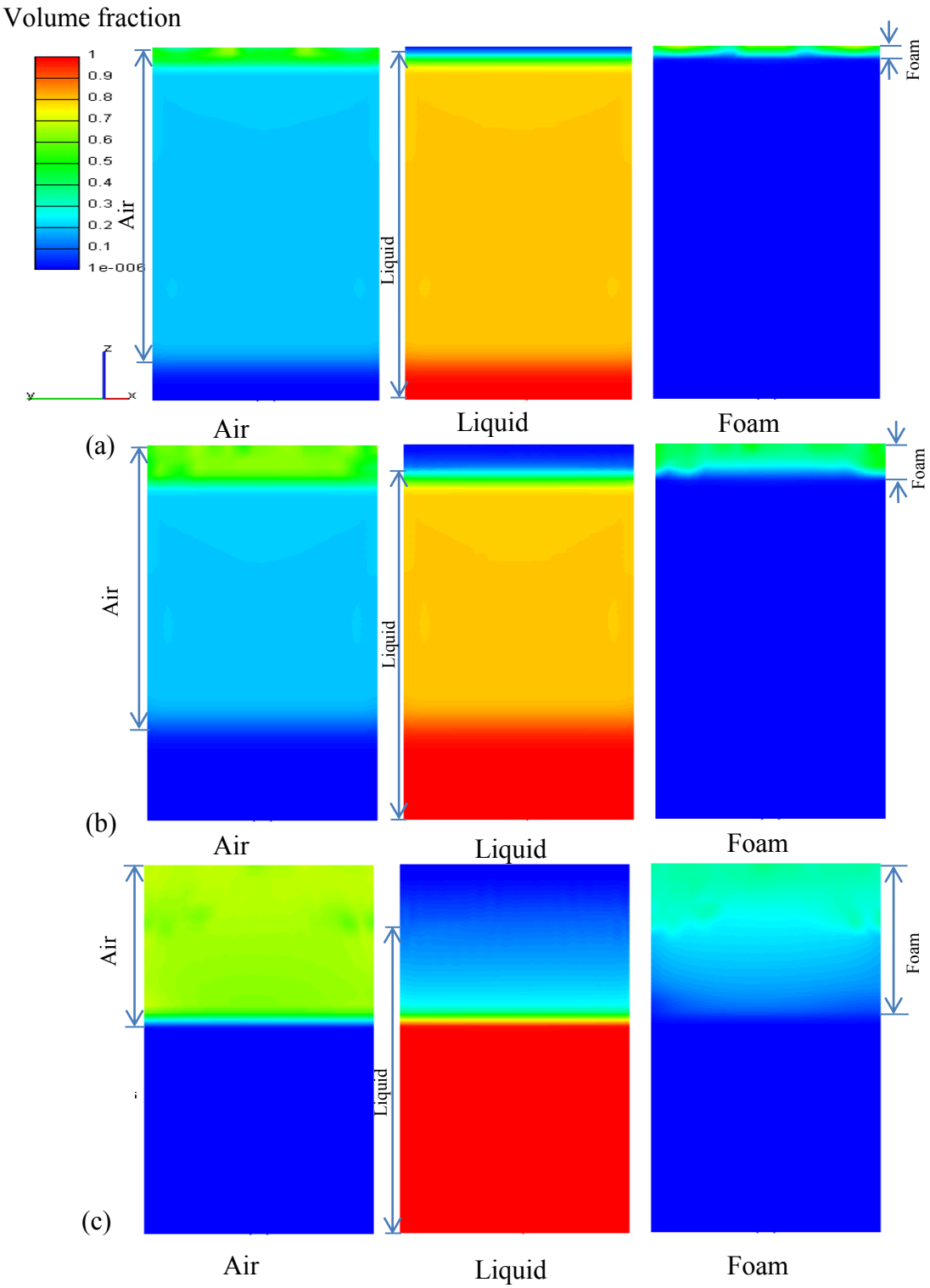

Figure 4.11. Transformation of air liquid dispersion into foam at initial air fraction 0.2. (a) at 60s. (b) at 150s. (c) at 600s.

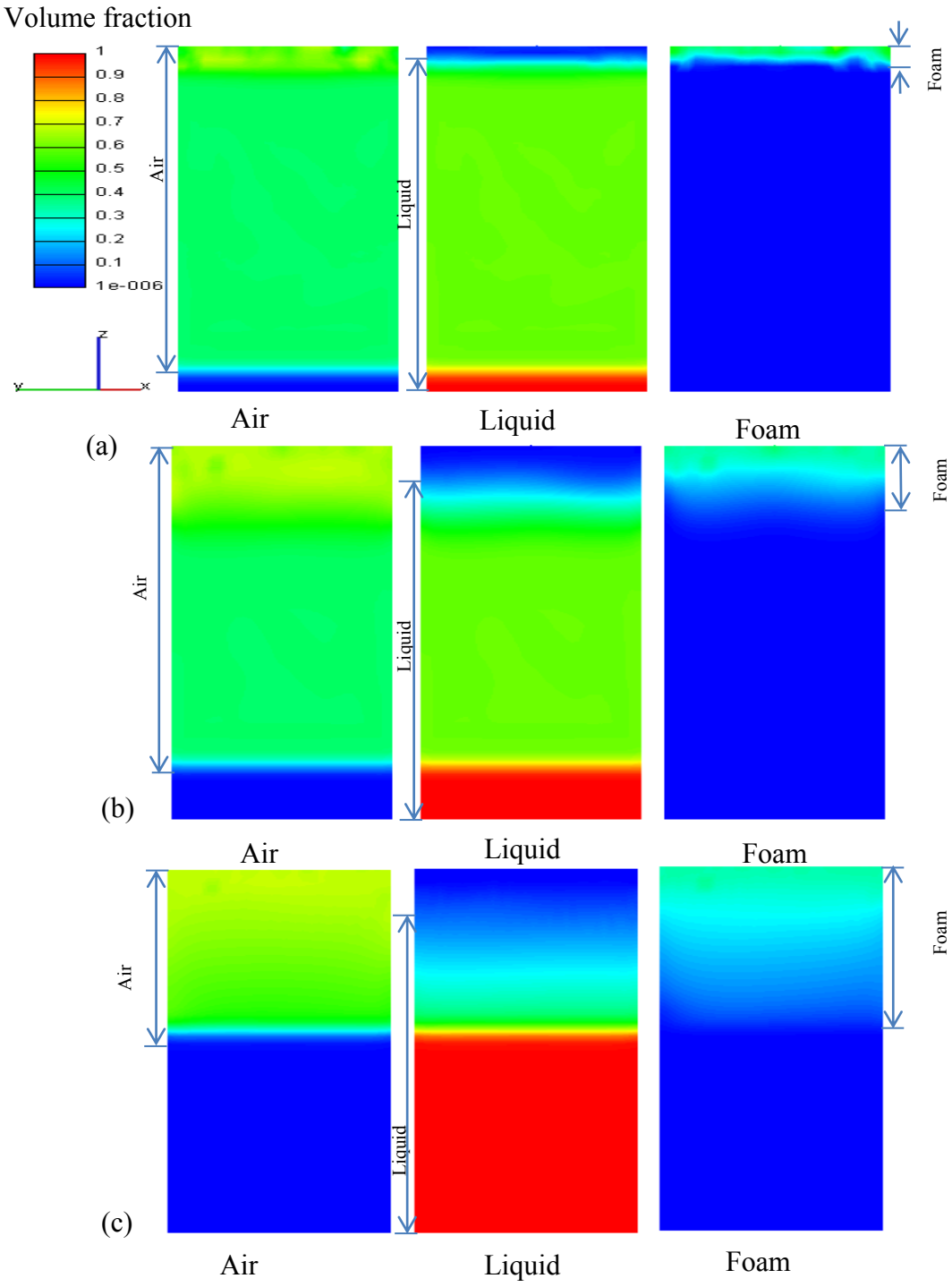

Figure 4.12. Transformation of air liquid dispersion into foam at initial air fraction 0.4. (a) 60s. (b) 150s. (c) 600s.

The velocity profile of different phases with initial air volume fraction of 0.2 and 0.4 is presented in Figure 4.13 and Figure 4.14 respectively. The figure shows that gas flows all regions inside the container at 60s whereas at 600s the flow of gas is visible near to the top surface of the container. Initially the container was filled up with a homogenous mixture of gas and liquid. Then the mixture in the container was left undisturbed and the liquid settles at the bottom but the gas moves upward due to density difference. Therefore, the gas moves upward and liquid flows downward from all region of the container at the beginning of the simulation. The liquid which settles at the bottom remains stagnant because there is no flow of fluid. At the same time foam is formed at the top surface of liquid and its height increases with time. Gas also flows inside the foam and escape into the atmosphere through the outlet of the container.

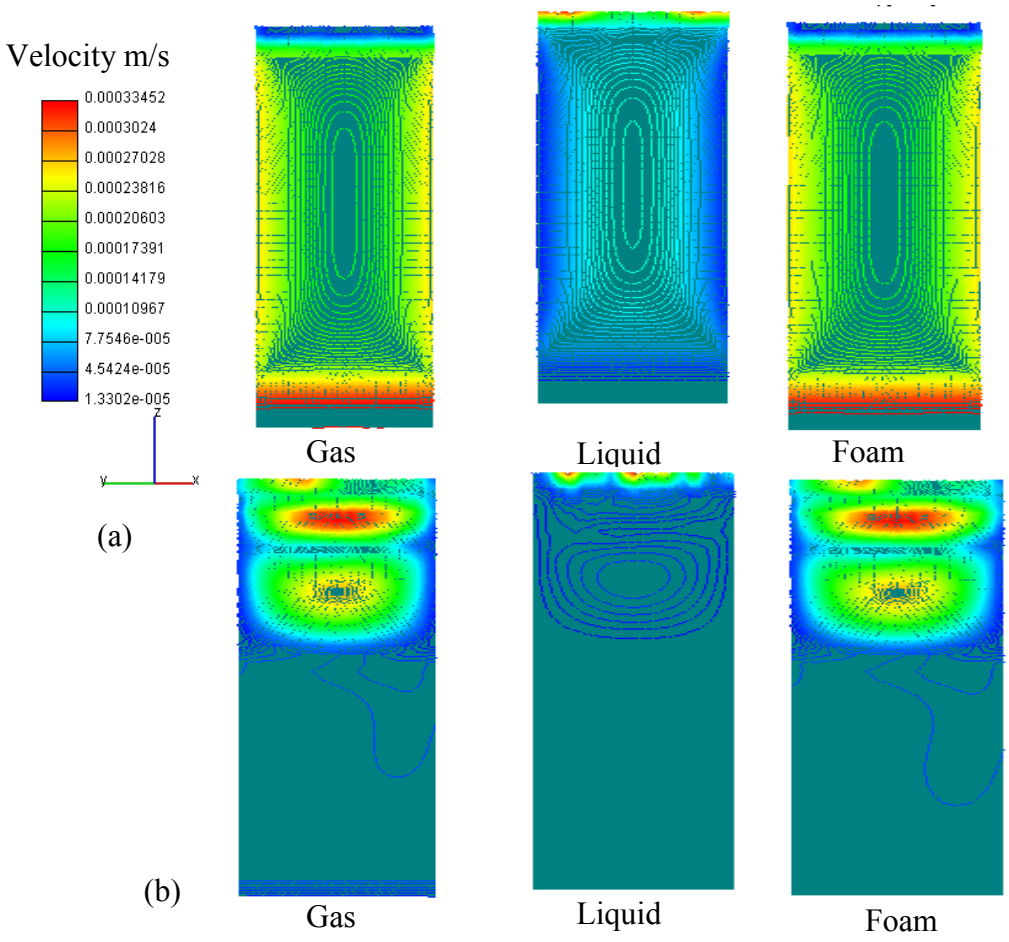

Figure 4.13. Velocity profile of different phases at initial air fraction 0.4 (a) 60s. (b) 600s.

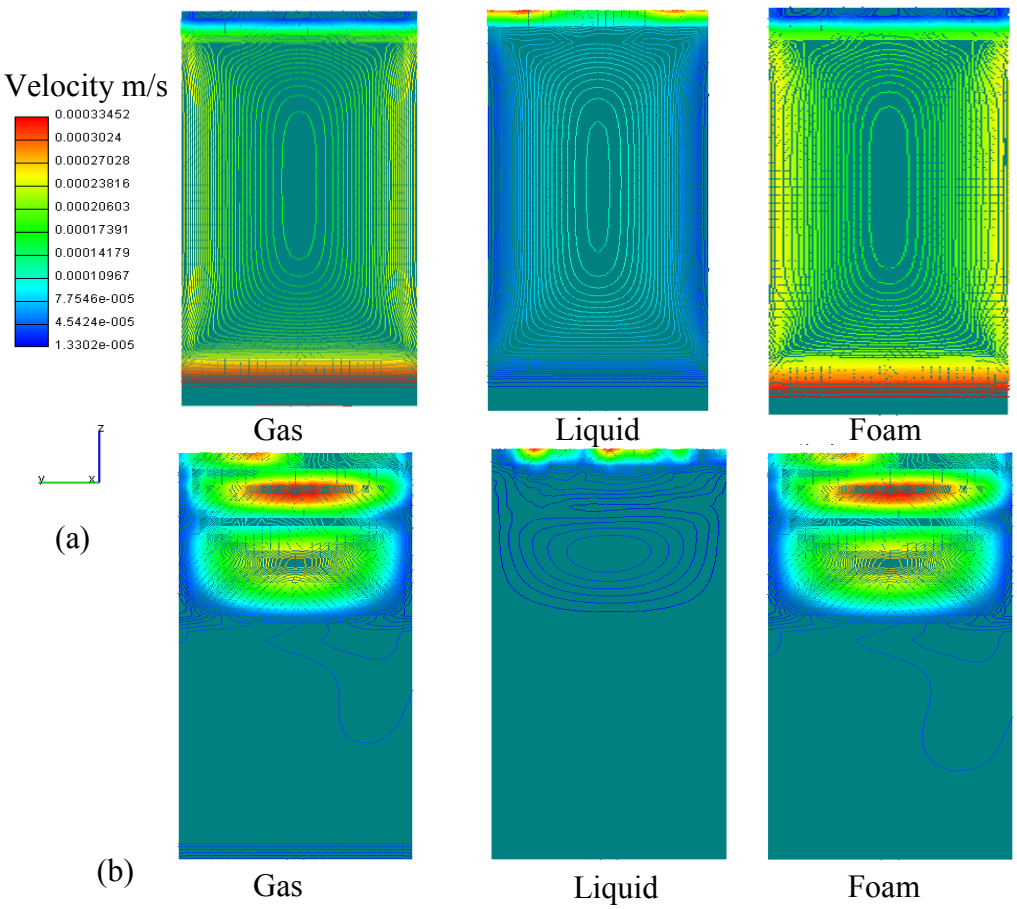

Figure 4.14. Velocity profile of different phases at initial air fraction 0.2 (a) 60s. (b) 600s.

The flow of gas toward the top surface of liquid continues until all liquid settle at the bottom and gas diffuses into the atmosphere. The formation of foam at the top surface of liquid and the clear liquid at the bottom of the container can be seen in Figure 4.11 and Figure 4.12. The gas and liquid mixture can be seen in between the foam at the top surface and clear liquid at the bottom (See Figure 4.11 and Figure 4.12) of the container. Due to flow of gas toward the top surface and liquid settle at the bottom because of density difference, the volume of gas-liquid mixture decreases with the increase of time. The present model predicted the transition to increasing air volume fraction and formation of foam layer somewhat earlier than that of Narsimhan (2010) for an initial air volume fraction of 0.4. It was also found in the phase diagram that the dimensionless height and time for the present CFD model was more than that of Narsimhan (2010) for an initial air volume fraction of 0.2. The event of coalescence was considered both in

the dispersed and the foam layer and population balance modeling was applied to track the number density of different bubble classes. The Sauter mean diameter of bubble were evaluated and plotted in the phase diagram. Monodisperse foam suffers from film rupture and gas exchange between adjacent bubbles, both processes leading ultimately to poly-dispersity in bubble size (Drenckhan and Langevin, 2010). Narsimhan (2010) assumed uniform size bubble in the dispersion and the bubble coalescence not to occur in the dispersion as well as in the foam layer. However, the bubbles were of poly-dispersed size in the present study and the coalescence of the poly-disperse bubbles were taking into account in the present study. This may have contributed to the difference in the results shown in Figure 4.5 and Figure 4.6. The viscosity and surface tension used in the present study were obtained from the capillary number and Peclet number used in the present study and Narsimhan (2010) model. As the value of viscosity and surface tension is not mentioned in their study reasonable values were assumed to arrive at the same capillary number and Peclet number to that of Narsimhan (2010). This difference in viscosity and surface tension may have contributed to the difference in the results shown in Figure 4.5 and Figure 4.6. The numerical inaccuracy associated with the numerical scheme used in the present study and the turbulence model used in the present study may also have contributed to the difference in the result shown in Figure 4.5 and Figure 4.6. The present CFD model assumes that the shape of bubbles during the formation of foam is pentagonal dodecahedron. In reality the bubble of different shapes exist in the foam. In this simulation it is also considered that the cross section of the Plateau border channel does not change with height of foam and the liquid in the lamellae is negligible. The life of foam depends on the concentration of surface active agent so the concentration gradient is important for the calculation of drainage and film rupture. More experiment results based on the above phenomena are necessary to incorporate this fact in the present CFD model for accurate prediction of the features of foam.

CHAPTER 5

MODELING OF FOAMING IN A LABORATORY SCALE BATH SMELTING SLAG

5 Modeling of foaming in a laboratory scale bath smelting slag

This chapter presents the numerical modelling of foaming in a laboratory scale bath smelting slag. The model presented in this chapter is same as the experimental model of Jiang and Fruehan (1991). The new approach of foaming explained and presented in the Chapter 4 is also used this model of foaming. A computational fluid dynamic (CFD) model has been developed for the simulation of slag foaming on bath smelting slag ($CaO\text{-}SiO_2\text{-}Al_2O_3\text{-}FeO$) by considering foam as a separate phase which is comprised of a mixture of gas and liquid. The model accounts for the formation of foam due to transformation of both gas and liquid into foam and it's destruction due to liquid drainage and bursting of bubble. The bubble break-up and coalescence was considered in gas-liquid dispersion whereas in the foam layer, the bubble coalescence due to film rupture was incorporated. Population balance modeling was used to track the number density of different bubble class and fixed pivot method was used to discretize the population balance equation. The source term model of Hagesaether et al. (2002) rectified and presented in Chapter 3 is also used in this model. A user subroutine has been written using FORTRAN programming language to incorporate bubble break-up and bubble coalescence as well as foaming of slag into the main CFD software. The model predicted the foam height of the slag system ($CaO\text{-}SiO_2\text{-}Al_2O_3\text{-}FeO$). The content of FeO was changed and its effect on the foaming index was observed. The results from the present model show that foaming index decreases with increase of FeO content in slag. The results from the CFD model also show that the foaming index of a slag with Al_2O_3 is higher than that of slag without Al_2O_3. Dimensionless analysis was performed based on the model available in the literature to correlate the foaming index with the physical properties of the slag and the coefficient of the foaming index was found to be 109 and 127. The predicted results from the present study are in reasonable agreement with the experimental data.

5.1 Introduction

Slag foaming phenomena are found in many ferrous and non-ferrous pyro-metallurgical processes, such as open hearth furnace, basic oxygen furnace (BOF), blast furnace, and copper-making (Nexhip et al., 2004). The pyro-metallurgical processes generate large quantity of gas which causes the slag to form foam. Foaming slags are important because it is the medium for post combustion and the large surface areas facilitate the multiphase reactions; leading to improved process kinetics, heat transfer and energy efficiency (Nexhip et al., 2004, Jiang and Fruehan, 1991). On the other hand excessive slag foam formation causes it to overflow the vessel and this phenomenon is termed as slopping in oxygen steelmaking. Slopping reduces productivity and increases operating cost and in some cases damages the vessel. Therefore, it is very important to understand the fundamental features of the slag foaming in the pyro-metallurgical process for the optimization of the system.

Slag foaming phenomena in metallurgical processes have been investigated to develop an innovative processes and to reduce energy consumption, particularly in the smelting reduction and steelmaking processes (Kim et al., 2001a). Recently, the smelting reduction process for the production of iron has received considerable attention due to lower capital cost, higher production rate, and the diversity of charging materials (Jiang and Fruehan, 1991). Several studies have considered the modeling and prediction of the slag foam height, where foaming is conveniently described in terms of a foam index or the gas void fraction or hold-up (Stadler et al., 2007). Foaming index and foam life are two main parameters to understand the features of the slag foam. The foaming index, which correlates the foam height with superficial gas velocity, used for aqueous foam proposed by Bikerman (1953) and Akers (1976). In the past decade research activity was concentrated toward understanding the foaming behavior of slag and the major contributions coming from Fruehan and his group. Ito and Fruehan (1989) expressed the foaming index in term of foam layer thickness and actual gas velocity. The foaming index has empirically been related to physical properties of the slag such as the surface tension, viscosity, and density of the liquid and the size of the bubbles. Empirical model of foaming index was modeled by different researcher for different slag foaming (Roth et al., 1993, Morales et al., 1995, Jiang and Fruehan, 1991). In the above empirical

model the effect of bubble size was disregarded. Several model explicitly accounted for the bubble size of the foam (Lin and Guthrie, 1995, Lahiri and Seetharaman, 2002, Zhang and Fruehan, 1995, Ozturk and Fruehan, 1995). Ito and Fruehan (1989) studied the foaming index and foam life to understand the effect of slag composition on foaming in iron and steelmaking process. They found that slag foaming increase with increasing viscosity and decreasing surface tension. At the same time they have found that suspended second particle stabilize the foam life and had a larger effect than that of viscosity and surface tension. Kitchener and Cooper (1959) studied the foaming of $CaO\text{-}SiO_2$ slag at different temperatures. They measured the foam life and found that the foam life increased with decreasing temperature and decreasing basicity. Hara and Ogino (1992) measured the foam life and foam height and found a good correlation between the foam life, foam height, and surface tension of the slag.

The advent of high speed computing machine facilitates the use of computational fluid dynamic model in many engineering fields. Numerous CFD model of multiphase flow have been developed, and numerical data has been validated through comparison with experimental data. It has been successfully used in metal processing involving gas-liquid flow (Buwa and Ranade, 2002, Chen et al., 2005, Díaz et al., 2008, Alam et al., 2011, Alam et al., 2010a, Alam et al., 2010b, Alam et al., 2012, Huda et al., 2012). There are two main approaches for the simulation of multiphase flow, namely the Euler–Lagrange method which considers the bubbles as individual entities tracked using trajectory equations, and the Euler–Euler method which is based on two-fluid model which assumes the gas and liquid phases to be interpenetrating continua(Bannari et al., 2008, Bhole et al., 2008). From computational considerations, the Euler–Euler approach is more economical and hence more popular (Bhole et al., 2008).

Slag foam is formed by the entrapment of many gaseous bubbles in a liquid slag. The slag foam is normally an extremely complex system consisting of poly-dispersed gas bubbles separated by draining liquid films of molten slag which is called lamellae and the lamellae are joined in a chanel called Plateau border (PB). The liquid is drained out from the lamellae through the Plateauborder chanel. The thin film of liquid (lamellae) reaches a critical limit due to liquid drainage and the bubbles separeated by this lamellae coalesces. It is difficult to incorporate these characteristics of foam in an ordinary two

phase gas/liquid simulation approach. The foam is normally accumulated at the top, but in gas liquid two phase approach, the gas diffuses in the atmosphere and is difficult to hold at the top. The above drawback is eliminated by considering foam as a separate phase made up of gas and liquid. The foam is formed by the gas bubble holding liquid in the lamellae and Plateau border channel. The destruction of foam is due to the bursting of bubbles at the top and coalescence inside foam. The new approach enables us to apply the characteristic of foam (Sattar et al., 2013). In wet foam the liquid volume fraction is typically between 10% and 30% and the bubbles are approximately spherical, while in dry foam the volume fraction of liquid is less than 10% and the bubbles are more polyhedral in shape (Pawlat et al., 2004, Guo et al., 2002, Schick, 2004, Pilon and Viskanta, 2004, Drenckhan and Langevin, 2010, Narsimhan, 2010). The coalescence bubbles the number density of the bubble class changes which ultimately changes the number of individual bubble classes. Bubble also breaks and coalesces in the liquid before forming foam at the top. Bubble break-up due to turbulence and bubble coalescence due to turbulence and laminar shear are considered in the present study. The bubble break-up model of Luo and Svendsen (1996) and the coalescence model of Prince and Blanch (1990) are used in the present study. The bubble coalescence model based on film rupture by Tong et al. (2011) has been used in the foam layer of the present study.

In this study a computational fluid dynamic model (CFD) model based on Euler–Euler approach has been developed to simulate slag foaming in bath smelting. The model predicts the foam height with different superficial gas velocity and iron oxide (FeO) content. The foam was considered as separate phase which is comprised of a mixture of gas and liquid. Different bubble classes were considered and the population balance modeling was incorporated to track the number density of different bubble classes. Bubble break and bubble coalescence were employed and their Sauter mean diameter were evaluated in the foam. Finally the foaming index for different FeO content was determined and elucidated. Dimensionless analysis was performed to correlate the foaming index with the physical properties of slag.

5.2 Model geometry and methodology for foaming in bath smelting slag

This section presents the mass and momentum conservation equations for the modelling of foaming in bath smelting slag in Eulerian multiphase flow approach. The population balance equation and the equation for the closure term of bubble coalescence incorporated in the foaming model of aerated liquid are discussed in this section. The proposed approach for the foaming in bath smelting slag is also discussed in this section. The boundary conditions of the model considered for the numerical simulation of foaming is also presented here. The modeling technique and the features of the model are discussed in this section. The meshing procedure of the present model and the methodology used for the numerical simulation are also presented. Initial conditions of the model and the properties of the fluid used for the numerical simulation are also presented in this section.

5.2.1 Model geometry and features

Numerical simulation of slag foaming was carried out in a container of height 12cm and the diameter of 4.5cm following the small scale experimental model of Jiang and Fruehan (1991). The generated grid for the present model showing the nozzle is presented in Figure 5.1. The depth of slag was 4.3cm from the bottom for a crucible of diameter of 4.5cm. The inlet of a nozzle with diameter of 1.6mm was placed 1cm above from the bottom of the crucible. The nozzle was placed at the center of the crucible. Argon gas was injected into the slag through the nozzle. The gas was assumed to enter the calculation domain as bubble of diameter of 0.5mm. The surface mesh of the model was generated by the CAD software Rhinoceros 3.0 then the surface mesh was imported in CFD simulation software AVL FIRE 2009.2 to generate volume mesh of the model. The meshing was performed by using the Fame Advance Hybrid technique available in the simulation software. Special refinement was done on the inlet of the model to achieve fine grid at inlet. Walls were treated as nonslip boundaries with standard wall function. The simulation was run in an unsteady state with a time step of 2.5^{-2} second on Intel Xeon Quad Core Z400 Machine with 8.0 GB RAM with processor speed 2.66 GHz.

The volume mesh of the model was generated and numerical simulation was performed by commercial CFD package AVL FIRE 2009.2. The modelling of bubble break-up, bubble coalescence and population balance modelling as well as foaming model was incorporated in the main CFD software as subroutine written by the author in FORTRAN programing language. In the present study ten types of bubble classes were considered. The volume of the upper bubble class was twice the volume of the lower countepart such that $v_i = 2v_{i-1}$. The diameters of the bubble classes tracked in this simulation are presented in Table 5.1. Initially the bubbles of the lowest class (class 1) were assumed to enter into the calculation domain through the inlet of the nozzle.

Table 5.1. Bubble classes used in the simulation.

Bubble class index	1	2	3	4	5	6	7	8	9	10
Bubble diameter ($\times 10^{-3}m$)	0.5	0.63	0.794	1.00	1.26	1.59	2.00	2.52	3.18	4.00

In this model, an unsteady state multiphase solution for momentum and continuity were used and for turbulence, a standard $k-\varepsilon$ turbulence model was used. A cell centered finite volume approach was used to discretize the governing equations and the resulting discretized equations were solved iteratively using segregated approach. For momentum and turbulence, first order upwind differencing scheme was used whereas central differencing scheme with second order accuracy was used for the continuity equation. All the model parameters used in the present study are presented in Table 5.2.

Table 5.2. Model parameters employed in the simulation.

Model parameter	Value
C_μ	0.09
k	1
c_v	1

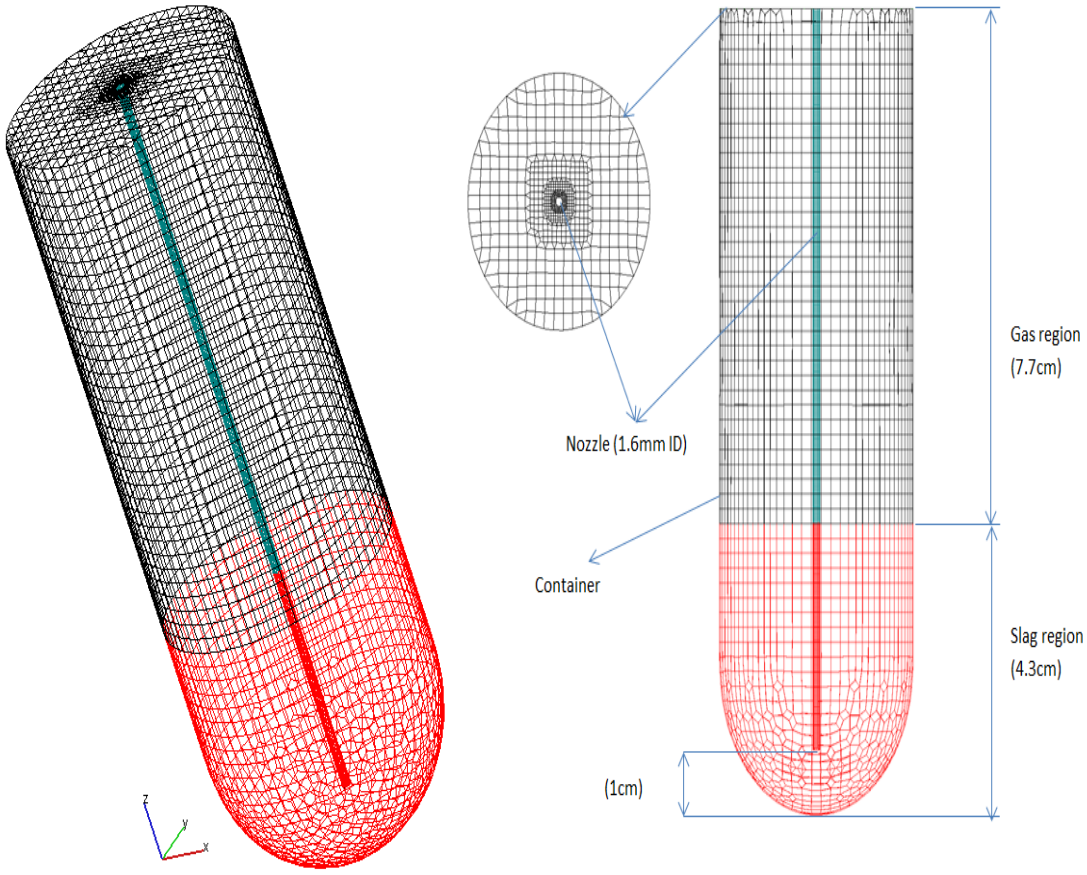

Figure 5.1. Grid generated for the simulation (a) 3D mesh (b) Outline.

5.2.2 Boundary conditions

The following conditions were assigned for the modelling of slag foaming.

5.2.2.1 Inlet

The inlet was specified at the nozzle tip of the computational domain (see Figure 5.1). Velocity boundary conditions were applied. The velocities were chosen to match with the experimental data of Jiang and Fruehan (1991). At the inlet, gas phase were injected which contains pure Argon (Ar) similar to the experimental model of Jiang and Fruehan (1991).

5.2.2.2 Outlet

The outlet was specified at the top surface of the mesh excluding the region occupied by the nozzle (See Figure 5.1). The diameter of the exit was 4.5cm. Static pressure boundary conditions were applied at the outlet.

5.2.2.3 Wall

The wall was considered as solid for this model. A non-slip condition was applied at all walls. The fixed temperature obtained from the pilot plant was assigned for the wall.

5.2.3 Governing equations for the modelling of foaming

The present study has considered gas, liquid and foam as separate phases for the purposes of modelling. Bubble classes were introduced as scalar of gas phase. Different regions can be identified in the domain of the model based on the presence of each of the three phases as shown in Figure 5.2. Liquid is at the bottom of the crucible. Foam remains at the top surface of liquid. The gas is above the top surface of foam. A mixture of gas and liquid (a gas liquid dispersion) remains around the outer surface of nozzle. However, due to transient dynamic nature of the three fluid phases in the domain, any phase may exist anywhere at any instant of time. To cater for the transient dynamic situation in the domain, the present model solves all the transport equation for all the three phases throughout the whole domain. The phase may also coexist anytime

anywhere in the domain. In this modelling, the bubble break-up and coalescence phenomena are applied in the gas liquid dispersion. The bubble coalescence due to film rupture is applied in the foam phase. The mathematical model used for the mass and momentum conservation equations for the modelling of foaming in bath smelting slag in Eulerian multiphase flow approach is presented in the following section. The population balance equation and the equation for the closure term of bubble break-up and bubble coalescence incorporated in the foaming model are also discussed and presented in the following section.

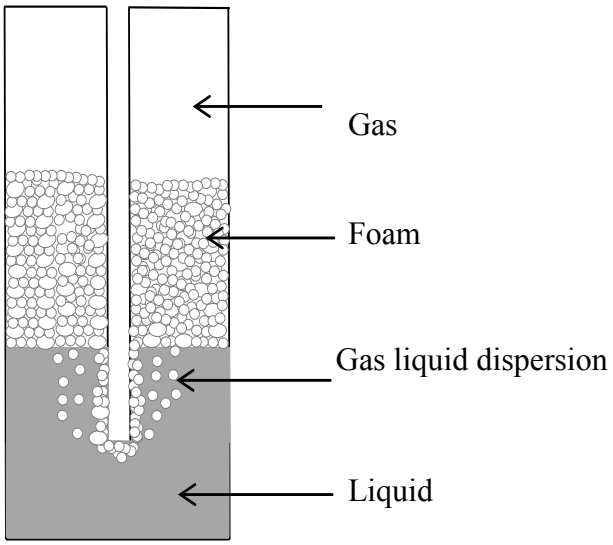

Figure 5.2. Schematic of different regions in the model.

5.2.3.1 Euler-Euler multiphase model and mass conservation equation

The governing equations used in the present study are based on the Eulerian-Eulerian multiphase approach. In Eulerian-Eulerian multiphase flow model gas, liquid slag and foam phases interact with each other and there is significant exchange of mass and momentum between phases. The model was developed by using commercial CFD package AVL FIRE 2009.2. Interfacial mass and momentum were modeled by using user-defined subroutines (UDF). The CFD solver employed uses the finite volume discretization method which rests on integral conservation statements applied to a general control volume. The Eulerian multiphase flow model solves the conservation of

mass and momentum of each phase in each cell. The exchange of mass and momentum are dealt with the interphase exchange term in the conservation equation. The governing equations in this approach can be derived by ensemble averaging the fundamental conservation equations for each phase to describe the motion of liquid slag, gas and foam. Both the continuous and the dispersed phases are modelled in the Eulerian frame of reference as interpenetrating continua. Gas, liquid and foam are treated as separate phases. The mass conversion equation used (AVL-FIRE, 2008) for the numerical prediction of foaming in aerated liquid is also used for the prediction of slag foaming in the current model. The mass conservation equation is presented in Chapter 4 at Section 4.2.3.1(refer to Eqn.4.1).

5.2.3.1.1 Mass interfacial exchanges

Similar to the model presented in Chapter 4 in the present model, gas and liquid transform into foam when in any cell there is more than 75 per cent gas provided liquid is available in that cell. At the same time foam also transforms into liquid and gas due to liquid drainage and bubble bursting at the top. This mass transformation between phases was dealt with mass interfacial exchange term in the mass conservation equation (Eqn. 4.1 in Chapter 4 Section 4.2). The mass transformation between gas and foam and between liquid and foam was calculated using the equation presented in Chapter 4 at Section 4.2.3.1 (Refer to Eqns. 4.2-4.5).

5.2.3.2 Momentum conservation equation

The momentum conservation equation for each phase in Eulerian-Eulerian approach on the finite volume method has been used. The momentum conservation equation used for the present model is similar to that of the modelling of bubble column reactor presented in Chapter 3 at Section 3.2.3.2 (refer to Eqns.3.2-3.5). For turbulent a standard $k-\varepsilon$ model was used for the gas and liquid whereas foam phase was considered as laminar.

5.2.3.2.1 Momentum interfacial exchanges

In the present model the momentum exchange between phases was taken into account. The momentum interfacial exchange between phases due to bubble break-up and

coalescence was considered. The bubble induced drag force is considered in the present study. The momentum interfacial exchange between phases was modeled by considering interfacial momentum source term in the momentum conservation equation presented in Chapter 3 at Section 3.2.3.2. The momentum interfacial exchange equation presented in Chapter 3 at Section 3.2.3.2.1 (refer to Eqns.3.6-3.11) was also used for the present model.

5.2.3.3 Population balance equations

In the present model bubble break-up and bubble coalescence was considered. Therefore the number density of individual bubble class is changed due to bubble break-up and bubble coalescence in the gas liquid dispersion as well as in the foam. The population balance equation was used to track the number density of individual bubble class. The population balance equation presented in Chapter 3 at Section 3.2.3.3 (refer to Eqns. 3.12-3.15) was also used for the present model. This PBE is known as scalar transport equation in the AVL Fire software. The source term of coalescence in the scalar transport equation has been updated using the source term model of Hagesaether et al. (2002), with rectification and the details of the rectification is presented in Chapter 3 at section 3.2.3.4 (refer to Eqns. 3.31-3.32 and Eqns. 3.39-3.40).

5.2.3.4 Bubble break-up model and closure term in gas liquid dispersion

In the present model bubble break-up due to turbulent collision of bubbles with eddies were considered in the gas liquid dispersion. This model also consider binary break-up model in which parent bubble break-up into only two daughter bubbles. The break-up model of Luo and Svendsen (1996) was incorporated in the present study. The details of the model and the equation for the bubble break rate are presented in Chapter 3 at Section 3.2.3.5 (refer to Eqns. 3.41-3.48).

5.2.3.5 Bubble coalescence model and closure term in gas liquid dispersion

The present model also considers bubble coalescence in the gas liquid dispersion. The bubble coalescence occurs due to the collision of bubbles. The collision of bubble is induced by the turbulent of liquid, laminar shear, buoyancy and wake entrainment. The

coalescence of two bubbles is induced when they collide. A small amount of liquid is trapped between the bubbles and the liquid drains gradually causing the liquid film between the bubbles to reach a critical thickness and a film rupture occurs resulting in coalescence (Huh et al., 2006). The bubble coalescence model by Prince and Blanch (1990) which is based on the Laminar shear collision and turbulent collision is also used for the present model. The details of the model and the equations used for the present model to calculate the coalescence rate is presented in Chapter 3 at section 3.2.3.6 (refer to Eqns. (3.49)-(3.59)).

5.2.3.6 Bubble coalescence model and closure term in foam

In the modelling of slag foaming in bath smelting slag the coalescence of foam due to lamellae rupture was considered. Foam is formed during the injection of argon into the molten metal. Once foam is formed there is liquid drainage in the Plateau border channel which causes the bubble coalescence due to lamellae break-up. In this model the coalescence of bubble inside foam developed by Tong et al. (2011) was incorporated. The details model of bubble coalescence in the foam due to film rupture is presented in Chapter 4 at Section 4.2.3.6 (refer to Eqns. (4.9)-(4.12)).

5.2.3.7 Liquid drainage

Liquid is trapped in the film which separates bubbles and Plateau border of foam cell. The liquid drainage due to gravity through the Plateau border channel derived by Bhakta and Ruckenstein (1997) was used in the modelling of slag foaming of the present model. The details of the model and pertinent equation are presented in Chapter 4 at section 4.2.3.9 (refer to Eqns. 4.19-4.35).

5.2.3.8 Foaming index and dimensionless analysis model

Ito and Fruehan (1989) defined the foaming index as the ratio of foam height to the superficial gas velocity. The foaming index was calculated using the equation from Ito and Fruehan (1989) as:

$$\sum = \frac{H_f}{U_g^s} \tag{5.1}$$

Where H_f is the foam height (cm) from the liquid surface and U_g^s is the superficial gas velocity (cm/s). To correlate the foaming index with the physical properties of slag Ito and Fruehan (1989) and Jiang and Fruehan (1991) derived dimensionless group. The equation for dimensionless parameter can be written as (Jiang and Fruehan, 1991, Ito and Fruehan, 1989):

$$\prod_1 = \frac{\sum g\mu}{\sigma} \tag{5.2}$$

$$\prod_2 = \frac{\rho\sigma^3}{\mu^4 g} \tag{5.3}$$

$$\prod_1' = \frac{\sigma^4\rho^{1/4}}{\mu g^{1/4}} \tag{5.4}$$

$$\prod_2' = \frac{\sum\rho^{1/4}g^{3/4}}{\sigma^{1/4}} \tag{5.5}$$

Where μ viscosity, ρ density, σ surface tension and g gravity.

5.2.4 Initial conditions of the model and properties of fluids

Initially the depth of slag was 4.3cm from the bottom of a crucible with diameter of 4.5cm. The temperature of liquid slag was 1773K. The inlet of a nozzle with diameter of 1.6mm was placed 1cm above from the bottom of the crucible. The nozzle was placed at the center of the crucible so that the foam is formed uniformly. Argon gas was injected into the slag through the nozzle. The gas was assumed to enter the calculation domain as bubble of diameter of 0.5mm. The properties of the fluids used in this study are presented in Table 5.3.

Table 5.3.The properties of the fluids used for the modelling of slag foam (Jiang and Fruehan, 1991).

Properties	Gas(Ar)	Liquid		
		CaO/SiO_2=1.25, Pct Al_2O_3=4		
		PctFeO =3.0	PctFeO =7.5	PctFeO =15
Density(kg/m^3)	0.2745	2733	2790	2889
Viscosity(Ns/m^2)	2.23E-05	0.381	0.353	0.314
Surface tension (mN/m)	-	477.2	483.6	494.6

5.2.5 Grid independency test

Two different grid of the model was generated with control volume of 207,705 and 150,103 cells. Simulation was performed on both grids using superficial gas velocity of 0.01m/s and it has been verified the convergence of the solution in both cases. No significant differences were observed in the results. Therefore, for all the subsequent simulations, the 150,103 control volumes numerical mesh was used. Time averaged gas velocities for the control volume of 207,705 and 150,103 are presented in Figure 5.3.

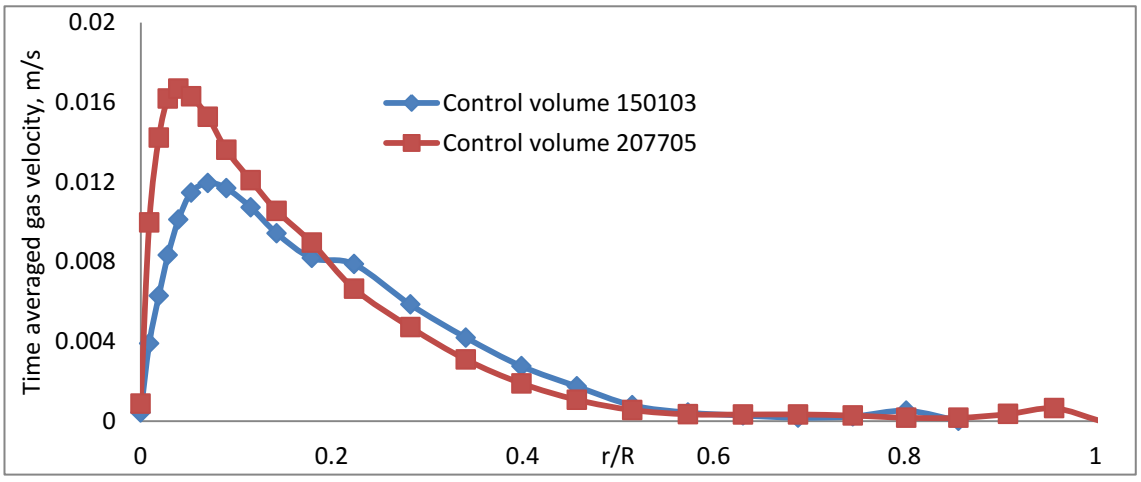

Figure 5.3. Time averaged gas velocity.

5.3 Results and discussion

The simulations were carried out in a crucible of height 12cm and diameter of 4.5cm. Initially the crucible was filled up to 4cm of slag from the bottom and 8.7cm of gas above the slag as shown in the Figure 5.1. Argon gas was injected through the nozzle into the slag. The nozzle was placed at the center of the crucible so that the foam formed at the top becomes uniformly distributed. The height of foam in this model is dynamically balanced by the formation of foam due to transformation of both gas and liquid into foam and it's destruction due to liquid drainage and bursting of bubble. When the foam height was reached in steady state the height of foam was measured. The height of foam was measured as the distance between the surface of the clear liquid (interface between the bottom surface of foam and the top surface of liquid) and the top surface of the foam (interface between the top surface of foam and the gas). Various gas flow rate was used to measure the height and the foaming index was measures from the slope of the line of foam height vs. superficial gas velocity plot.

The slag foam formation with time at 1773K for a slag CaO-SiO_2-Al_2O_3 with 3 per cent (pct), 7.5 percent and 15 percent of FeO is presented in Figure 5.4, Figure 5.5 and Figure 5.6. Figure 5.4(a) shows that the foam layer at the top starts to appear at 10 second. As the time elapsed the foam layer continues to increases (Figure 5.4(b)) and become steady state in a situation where the rate of foam growth is equal to the rate of bubble burst at the top and the liquid drainage as shown in Figure 5.4(c). This phenomenon was also observed when FeO content was changed and shown in Figure 5.5 and Figure 5.6.

At the beginning of injection of gas, foam starts to form around the nozzle tip in the gas liquid interface when it satisfy the foam formation condition and moves upward along the outer surface of the nozzle then it settle on the top surface of liquid (See Figure 5.4(a)). The free gas also moves upward and escapes into the top gas region in the container where the velocity and turbulent kinetic energy is more than other part of the container (See Figure 5.15-Figure 5.17(a) and Figure 5.18-Figure 5.20(a)). As time elapse the foam height increases (See Figure 5.4(b)) which obstructs the quick release of gas into the gas region of the container and therefore the velocity and turbulent kinetic

energy is reduced (See Figure 5.15-Figure 5.17(b) and Figure 5.18-Figure 5.20(b)). When the foam height reaches in a steady state condition then the bubble bursting and the free gas from the nozzle starts to escape through foam layer into the gas region of the container (See Figure 5.15-Figure 5.17(c) and Figure 5.18-Figure 5.20(c)). Similar phenomena were observed when FeO and velocity were changed.

The simulation was run for 300 second of real time. When the foam height reached almost steady state the height of the foam was measured. Due to transient flow behaviour, the foam height was in quasi steady state so the average foam heights from 250s to 300s were measured at an interval of 10s (see Table A.6 and Table A.7).

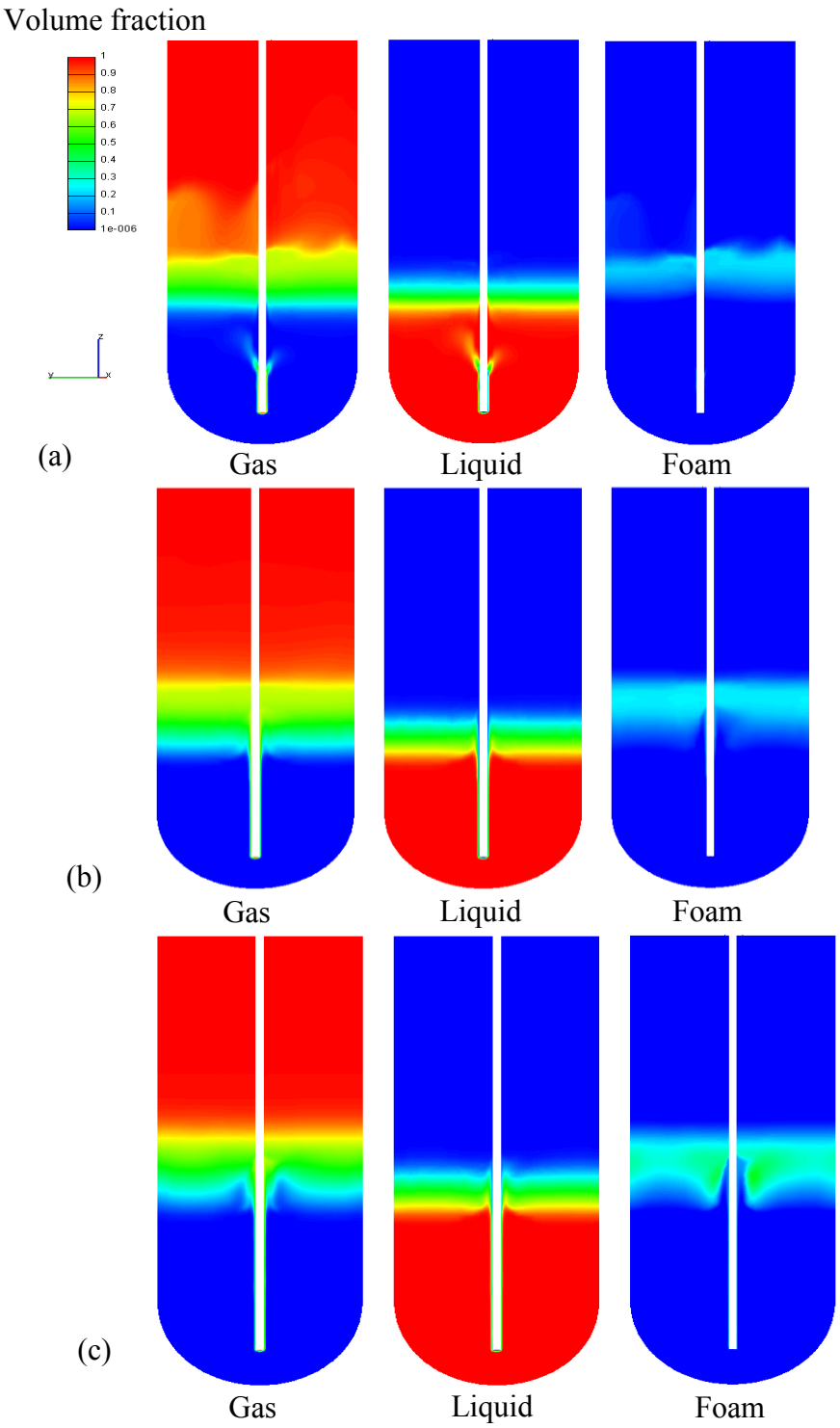

Figure 5.4. Slag foam formation with time at 1773K for 3pct FeO content at U_g =*1cm/s*.
(a) t=10s, (b) t=150s, (c) t=250s.

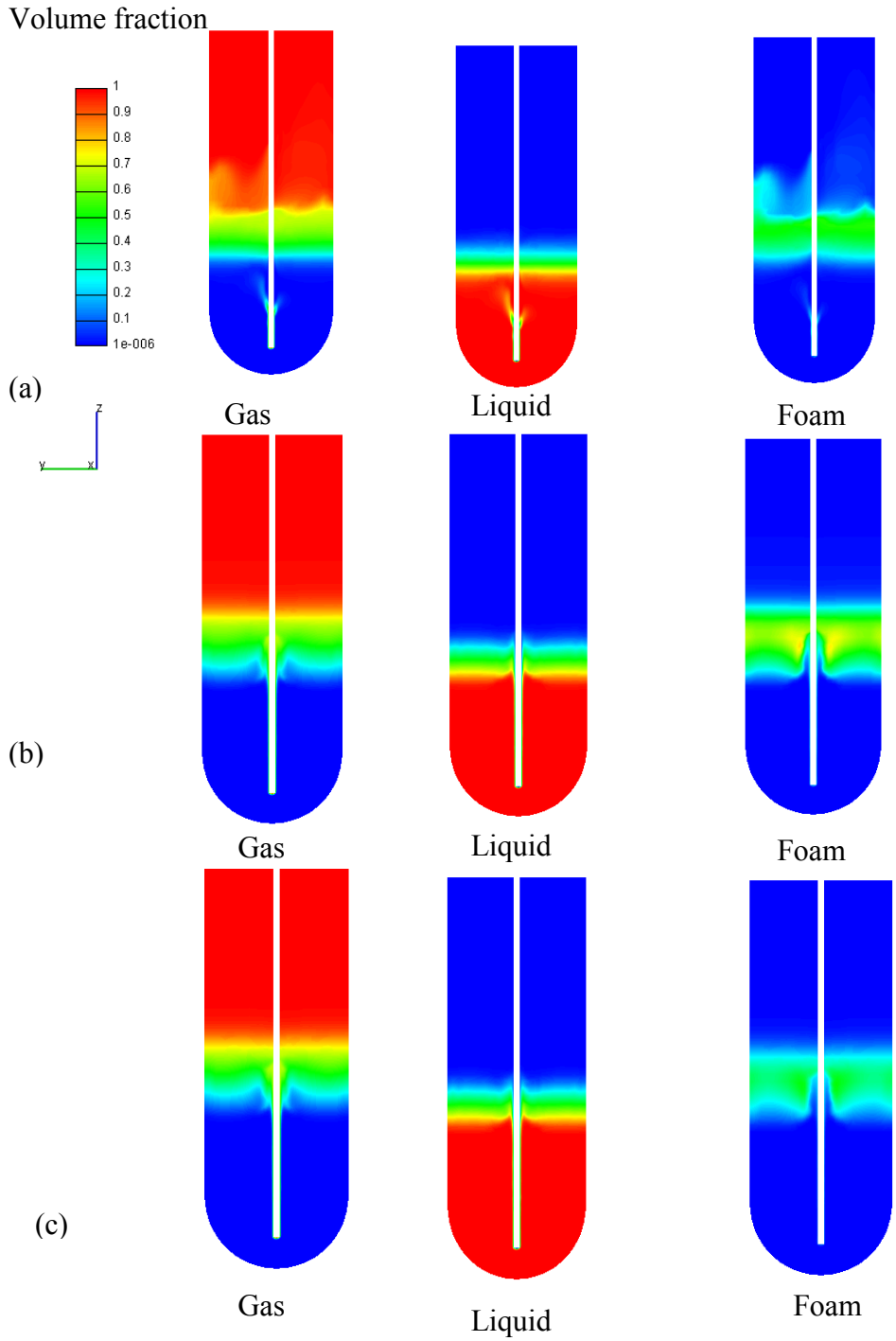

Figure 5.5. Slag foam formation with time at 1773K for 7.5pct FeO content at $U_g = 1cm/s$. (a) t=10s, (b) t=150s, (c) t=250s.

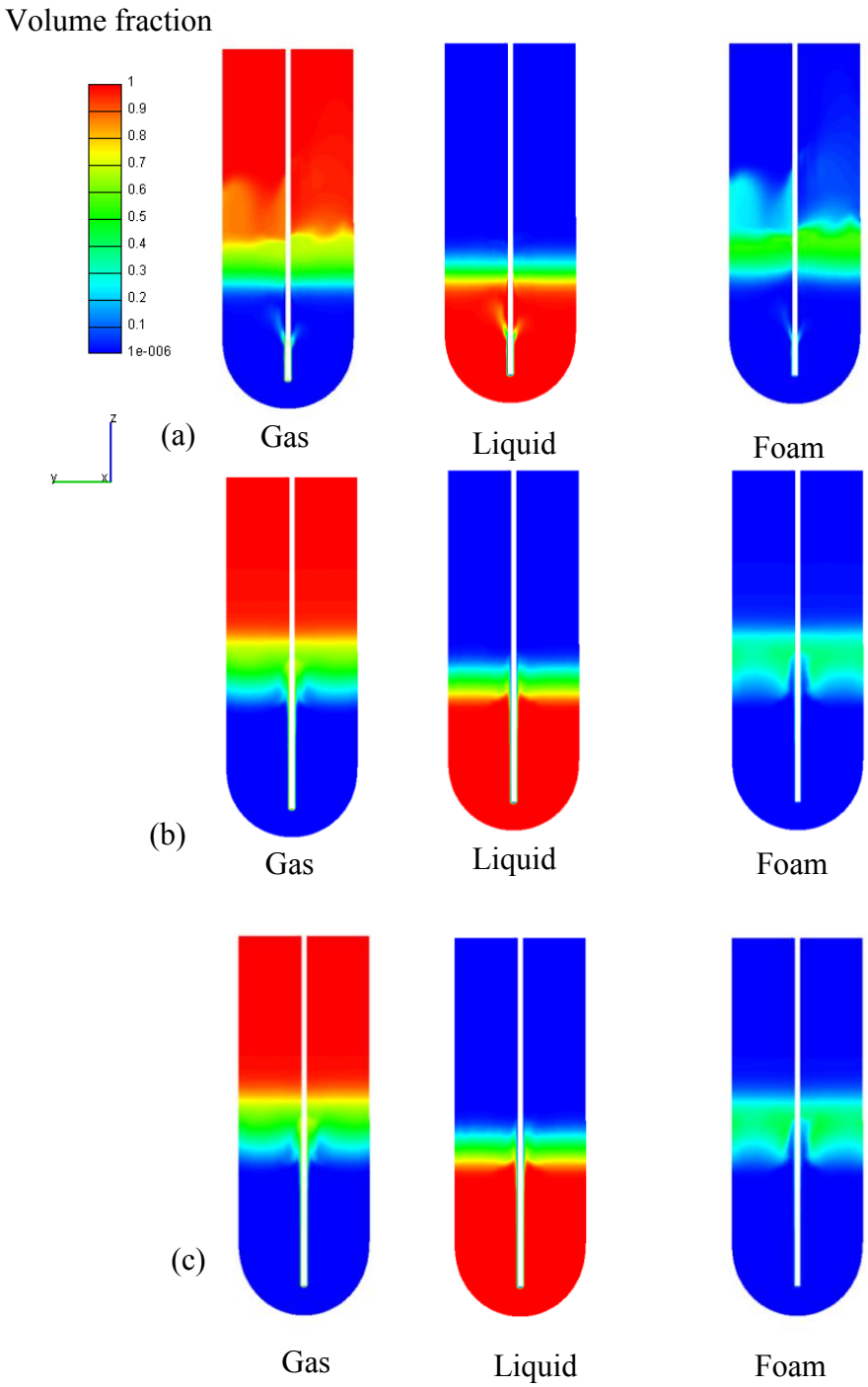

Figure 5.6. Slag foam formation with time at 1773K for 15pct FeO content at $U_g = 1cm/s$. (a) t=10s, (b) t=150s, (c) t=250s.

The predicted surface of the foam was not perfectly horizontal (Figure 5.7) so the foam heights at different position were measured and the average height of foam was considered. The predicted instantaneous foaming heights for $CaO\text{-}SiO_2\text{-}Al_2O_3\text{-}FeO$ are presented as foam volume fraction for superficial gas velocity of 1, 2 and 3cm/s at 250s in Figure 5.7.

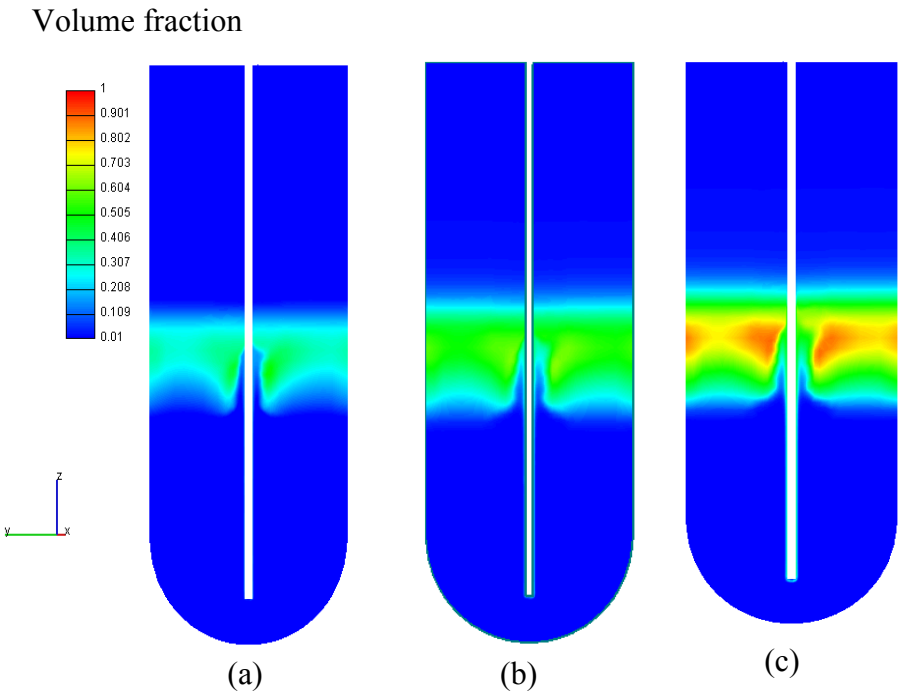

Figure 5.7. Slag foam formation with different superficial gas velocity at 1773K for FeO content 3pct at 250s (a) U_g=1cm/s (b) U_g=2cm/s (c) U_g=1cm/s.

Different superficial gas velocities were employed for the same composition to achieve accurate foaming index. The foaming height of $CaO\text{-}SiO_2\text{-}Al_2O_3\text{-}FeO$ slags as a function of superficial gas velocity is shown in Figure 5.8 along with the data from Jiang and Fruehan (1991). The foaming index was calculated from the slope of the line of the foam height versus superficial gas velocity graph. As expected the foaming height increases with the increase of gas flow rate when the slag composition is the same. The height of slag foam depends on the foam formation due to gas flow and destruction as bubbles burst at the top and the liquid drains. Liquid drainage and bubble bursting depend on the properties of slag. Surfactant stabilizes foam by increasing disjoining pressure and surface viscosity. Coalescence and collapse leads to a local increase in the

surfactant concentration because the absorbed surfactant on the film surface is released into the liquid in the Plateau border channel. The concentration was assumed uniform throughout the foam and liquid (Bhakta and Ruckenstein, 1997). The interfacial tension and surface viscosity also play a role in bursting of bubble at the top. In the present simulation the bursting of bubble was considered to occur due to film rupture caused by drainage. When the gas flow rate is increased the formation of foam is also increased which increases the height of foam and overall volume of foam. The liquid drainage through the Plateau border channel remained same for the same slag composition but the total liquid drainage in the foam increases due to the increases of volume of foam.

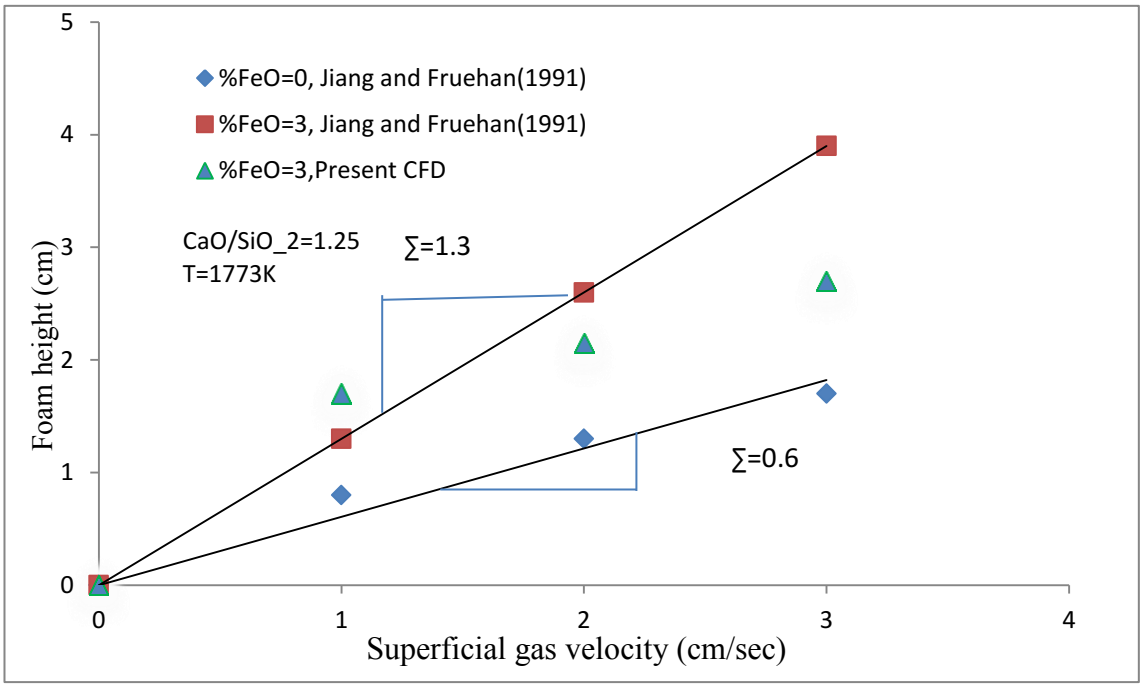

Figure 5.8. Foam heights of slags with different superficial gas velocity at 1773K.

Bubbles bursting at the top remain constant due to constant surface area. For this reason increasing superficial gas velocity causes the increase in foam height when the slag composition is the same. The foaming index of the present CFD model was measured as 1.24 from the slope of the Figure 5.8 for slag with FeO 3pct. The model over predicted the foaming height when the superficial gas velocity was 1cm/sec but under predicted when the superficial gas velocity was 2cm/s and 3cm/s. The formation of slag foam with different FeO content in term of volume fraction is presented in Figure 5.9.

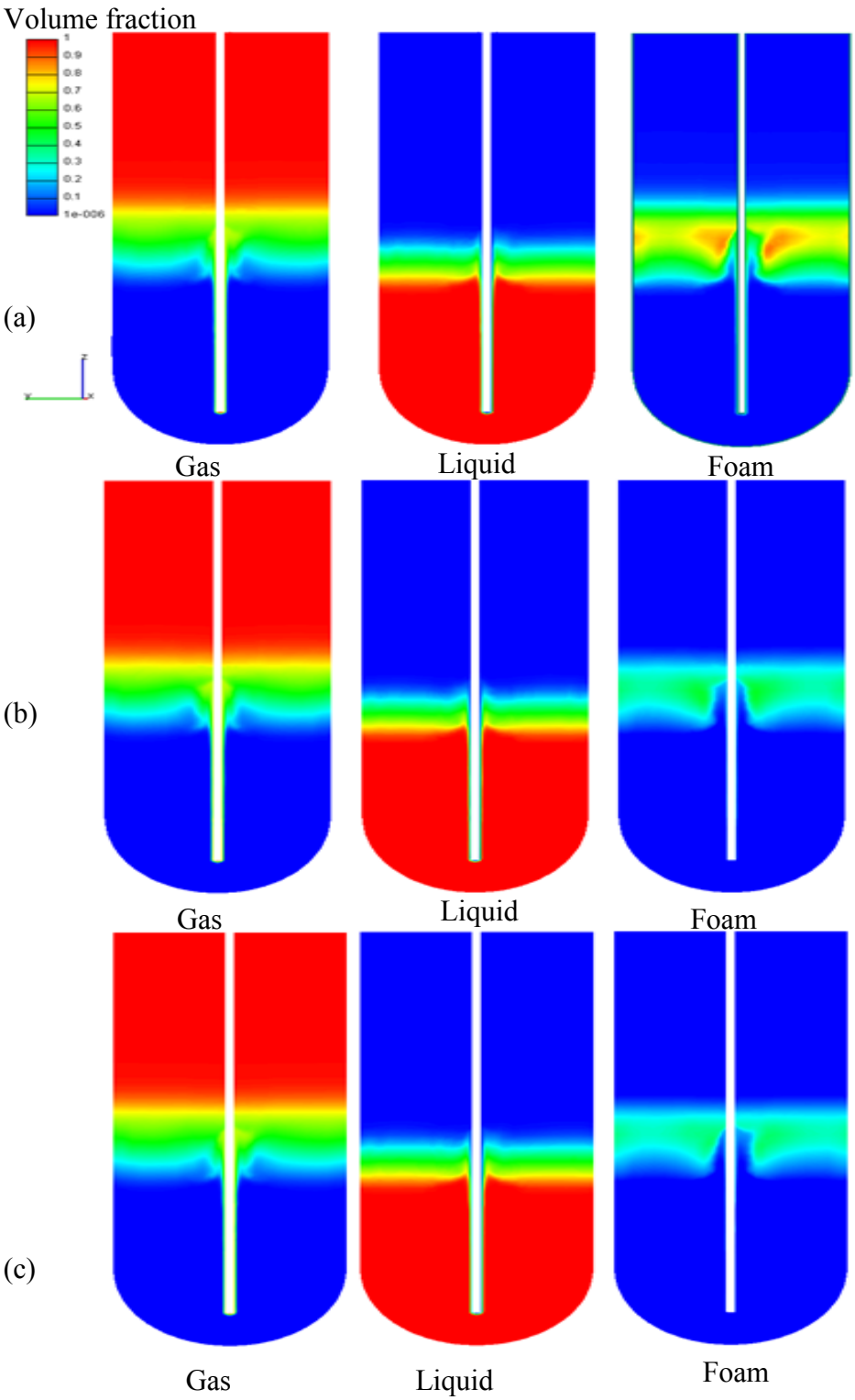

Figure 5.9. Slag foam formation with different FeO content at 1773K at 250s (a) Fe=3pct (b) Fe=7.5pct (c) Fe=15pct.

The average heights of these slag foams were measured and presented in Figure 5.10 as foaming indices. Figure 5.10 shows the foaming index as a function of percentage of FeO in slag. The figure also presents the foaming index determined from the experiment of Jiang and Fruehan (1991) for a slag of CaO-SiO_2-FeO and CaO-SiO_2-Al_2O_3-FeO as well as the predicted data from Ito and Fruehan (1989).

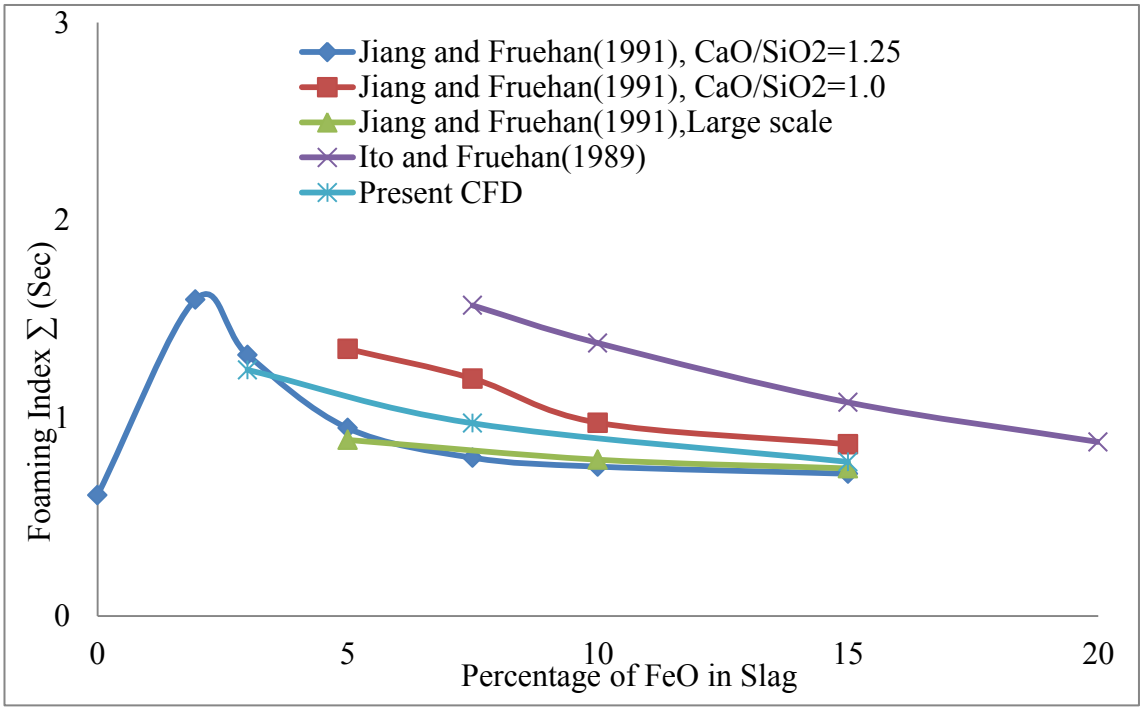

Figure 5.10. Foaming index of slag with different composition at 1773K.

It can be seen from the Figure 5.10 that in all cases the foaming index decreases with increase of FeO (For Jiang and Fruehan (1991) when pct FeO>2). The foaming index increases with viscosity and is inversely proportional to the square root of surface tensionIto and Fruehan (1989). The net result for these slags is that foaming index decreases with increasing the FeO content (Jiang and Fruehan, 1991). Increasing FeO in slag decreases the viscosity and increases surface tension. The above phenomena can be attributed to the fact that increasing FeO in slag decreases the viscosity of the slag (see Table 5.3). The drainage of liquid in foam increases with decreases of viscosity (see Eqn. 4.33). So the height of foam decreases thus decreases the foaming index. The figure also shows that the foaming index of slag with Al_2O_3 is higher than that of slag without Al_2O_3. This is because Al_2O_3 increases the viscosity of the slag (Jiang and

Fruehan, 1991). The increase of viscosity increases the foaming index as described above. The results obtained from the equations of dimensionless numbers derived by Jiang and Fruehan (1991) (Eqns.(5.2)-(5.3)) and that of Ito and Fruehan (1989) (Eqns.(5.4)-(5.5)) are presented in Table 5.4.

Table 5.4. Result of the dimensionless number.

Percentage of FeO	3.0		7.5		15.0	
Dimensionless number	Present CFD	Jiang and Fruehan (1991)	Present CFD	Jiang and Fruehan (1991)	Present CFD	Jiang and Fruehan (1991)
$\prod_1$	9.74	10.18	6.97	5.73	4.85	4.36
$\prod_2$	1436.7	1438.6	2071.55	2065.6	3665.4	3651.0
$\prod_1'$	6.16	6.15	6.746	6.73	7.78	7.77
$\prod_2'$	59.99	62.6	47.06	38.6	37.75	33.90

The logarithmic values of dimensionless numbers are presented in Figure 5.11 and Figure 5.12 for analysis. The least- square regression analysis was performed to derive the equation of the line for the data presented in Figure 5.11 and Figure 5.12.

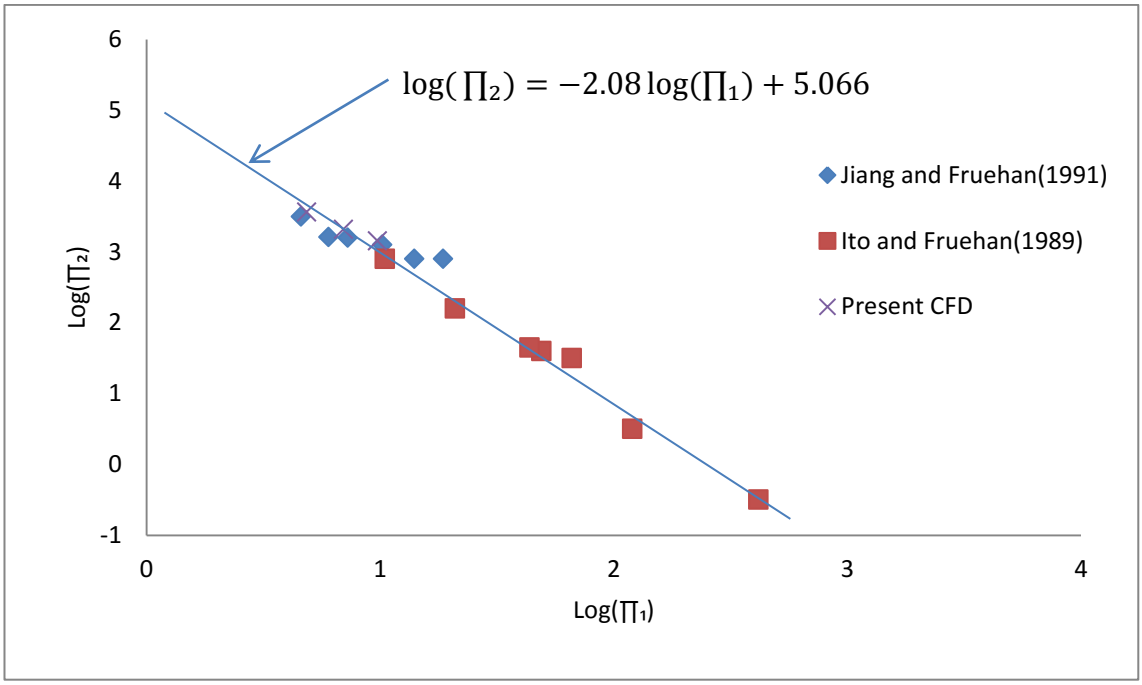

Figure 5.11. Dimensionless analysis of slag foaming phenomena.

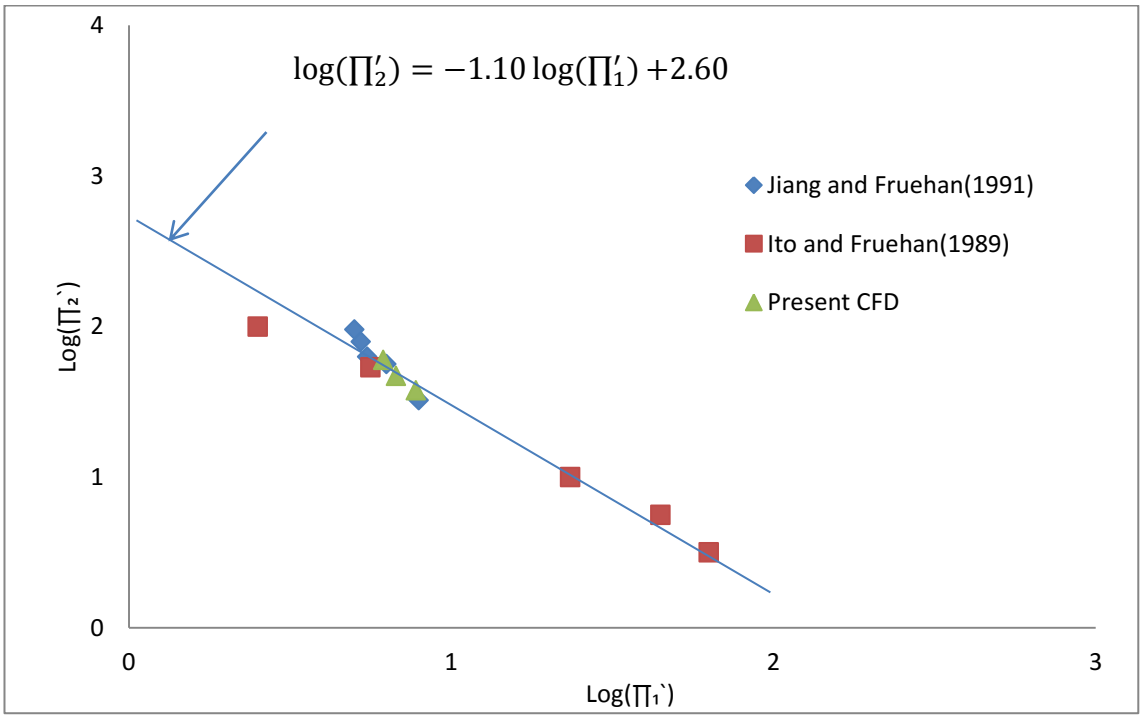

Figure 5.12. Dimensionless analysis of slag foaming phenomena.

The slope of the straight line after least-square regression analysis for Figure 5.10 was found to be -2.08 with intercept equal to 5.066. The equation of the line can be expressed as:

$$\log(\prod_2) = -2.08 \log(\prod_1) + 5.066 \quad (5.6)$$

The slope of the straight line obtained by least-square analysis (Figure 5.11) was -1.10 with intercept equal to 2.60.The equation of the line was found to be:

$$\log(\prod_2') = -1.10 \log(\prod_1') + 2.60 \quad (5.7)$$

Finally the correlation of foaming index with slag properties was obtained from the equation (Eqns. (5.6)-(5.7)) and the equation of dimensionless groups (Eqns. (5.2)-(5.5)). The final equation obtained as:

From Jiang and Fruehan (1991) dimensionless analysis are:

$$\sum = 109 \frac{\mu}{\sqrt{\rho\sigma}} \quad (5.8)$$

And from Ito and Fruehan (1989) dimensionless analysis are:

$$\sum = 127 \frac{\mu}{\sqrt{\rho\sigma}} \quad (5.9)$$

Whilst, there is some objection to the applicability of foaming index (Nexhip et al., 2004, Lin and Guthrie, 1995, Kapilashrami et al., 2006), the foaming index works well for the data set by Ito and Fruehan (1989), so this approach was used in the present study. Further work is required to understand the general applicability of this approach.

The model incorporated the bubble break-up and coalescence with population balance modelling to track the number density of different bubble class. The distribution of bubble class in gas liquid dispersion and foam along the length of the crucible at 300s when FeO=15% is presented in Figure 5.13 and Figure 5.14. In the gas liquid dispersion, not only bubble coalescence is incorporated but also bubble break-up phenomena are considered in the present study. The coalescence causes the increase of upper bubble class whereas the bubble break-up decreases the upper bubble class and increases the lower bubble class in gas liquid dispersion. In foam, bubble coalesces due to the rupture of its film and the liquid drain out through its Plateau border channel. Only the bubble bursting model of Bhakta and Ruckenstein (1997), which accounts for drainage of liquid through Plateau border channel was incorporated in the present study. The bubble coalescence model of Tong et al. (2011), which accounts for bubble film rupture in foam, was incorporated in the present study. The coalescence of bubbles applied in present model causes an increase of upper bubble class in foam. On the other hand, as oppose to gas liquid dispersion, the bursting of bubbles in foam does not increase the lower bubble class in foam. This is because, the bubbles that are bursting in the foam phase are lost from the foam phase and are transformed into liquid and gas phases respectively. Therefore it is not surprising that the number density of upper bubble class in foam is more than that of in gas dispersed in liquid.

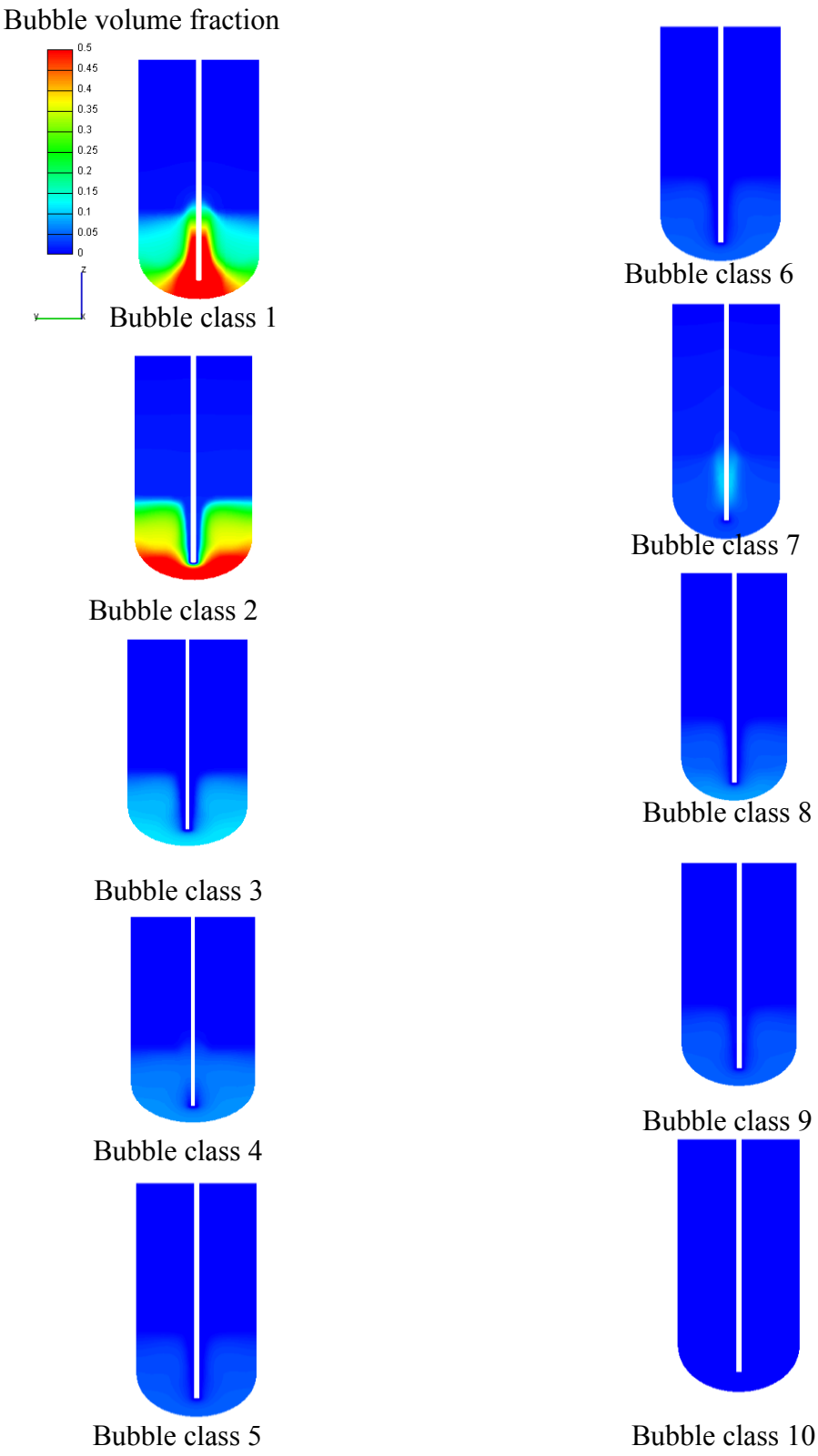

Figure 5.13. Distribution of bubble class in gas liquid dispersion along the length of the crucible at 300s when FeO=15%.

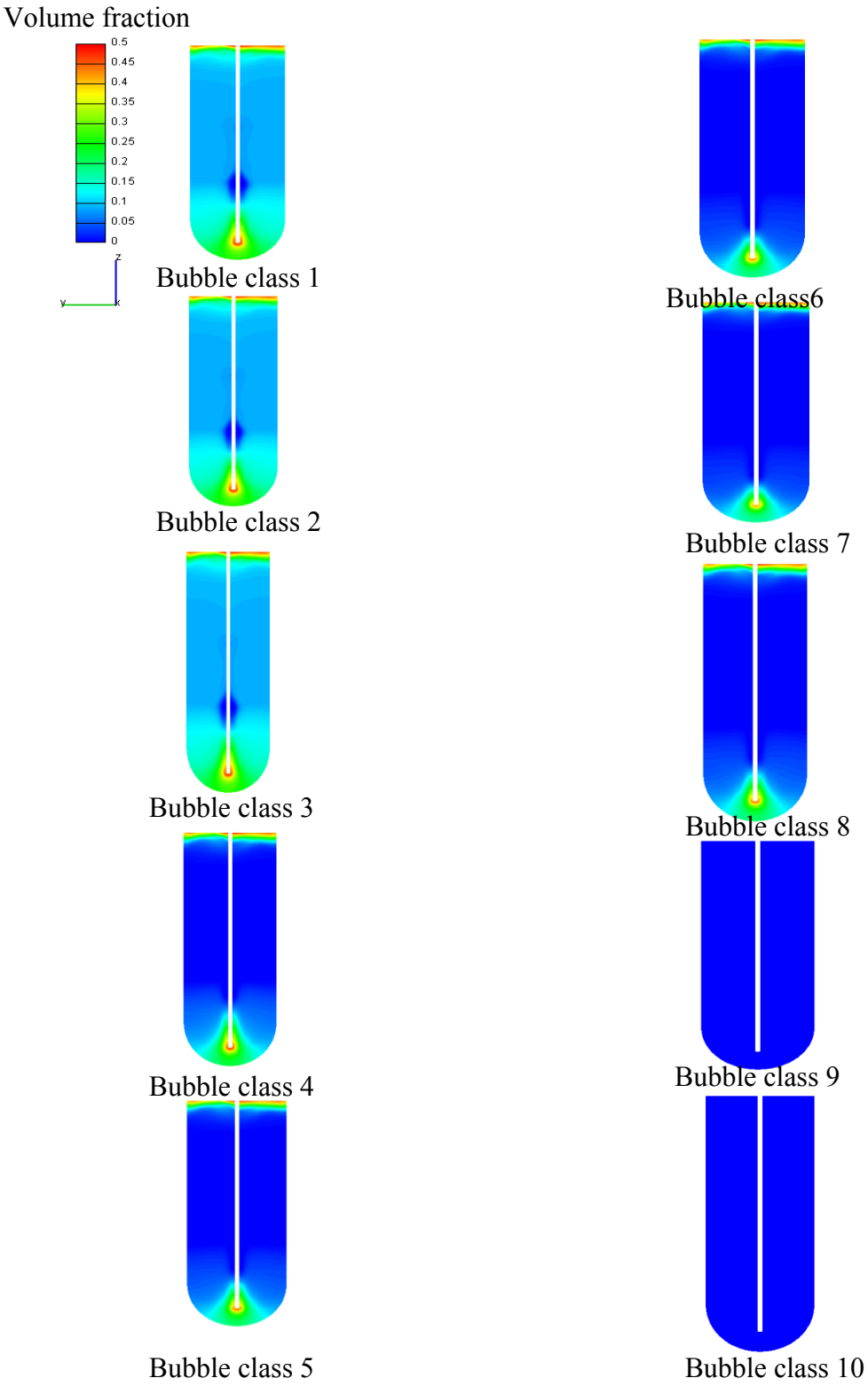

Figure 5.14. Distribution of bubble class in foam along the length of the crucible at 300s when FeO=15%.

As no experimental data for the initial bubble diameter issued from the nozzle were available, the gas was assumed to enter the calculation domain as bubbles of diameter of 0.5mm. With the 0.5mm diameter of bubble assumed to enter into calculation domain from the nozzle, the Sauter mean diameter calculated in the foam are 0.77mm, 0.85mm and 0.95mm when the FeO content is 3, 7.5 and 15 percent respectively. The present model incorporated the bubble break-up and coalescence in liquid and bubble coalescence in foam. The variation of Sauter mean diameter is due to the variation of slag properties caused by the addition of FeO into the slag. The above phenomena can be attributed to the fact that increasing FeO in slag decreases the viscosity of the slag (see Table 5.3). The drainage of liquid in foam increases with the decreases of viscosity (see Eqn. 4.33). The rate of film rupture increases with the increased drainage causing an increase in the number of upper bubble classes and the Sauter mean diameter.

At the beginning of injection of gas, foam starts to form around the nozzle tip in the gas liquid interface when it satisfy the foam formation condition and moves upward along the outer surface of the nozzle then it settle on the top surface of liquid (See Figure 5.4 (a)-Figure 5.6(a)). The free gas also moves upward and escapes into the top gas region in the container where the velocity and turbulent kinetic energy is more than other part of the container (See Figure 5.15(a)- Figure 5.17(a) and Figure 5.18(a)-Figure 5.20(a)). As time elapse the foam height increases (See Figure 5.4(b)-Figure 5.6(b)) which obstructs the quick release of gas into the gas region of the container and therefore the velocity and turbulent kinetic energy is reduced (See Figure 5.15(b)- Figure 5.17(b) and Figure 5.18(b)-Figure 5.20(b)). When the foam height reaches in a steady state condition then the bubble bursting and the free gas from the nozzle starts to escape through foam layer into the gas region of the container (See Figure 5.15(c)- Figure 5.17(c) and Figure 5.18(c)-Figure 5.20(c)).

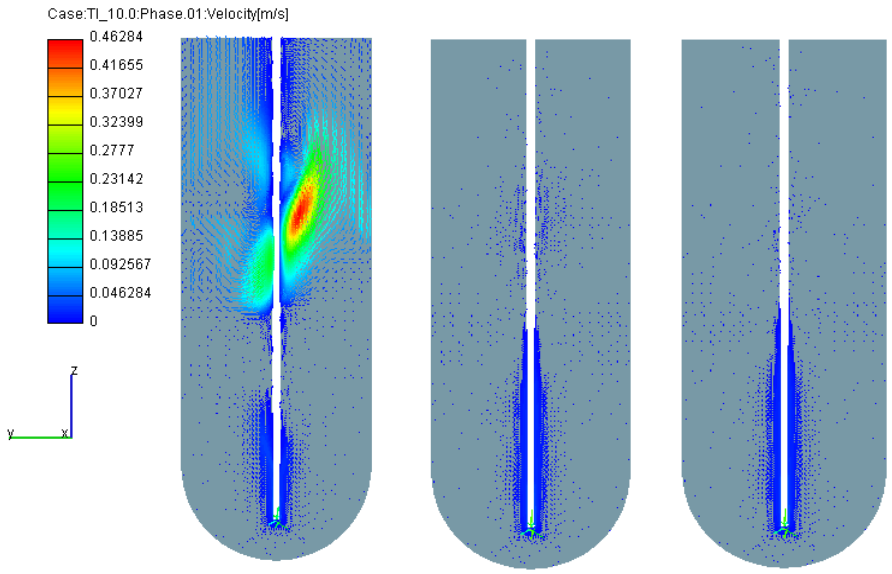

(a) (b) (c)

Figure 5.15. Velocity vector at different time when FeO=3% (a) t=10s, (b)t=150s and (c) t=250s.

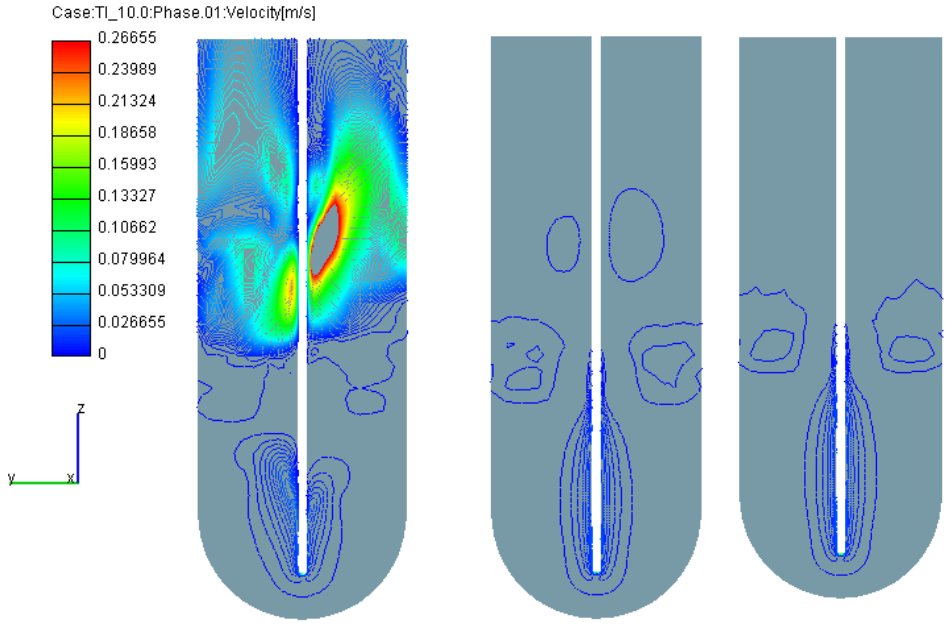

(a) (b) (c)

Figure 5.16. Velocity vector at different time when FeO=7.5% (a) t=10s, (b) t=150s and (c) t=250s.

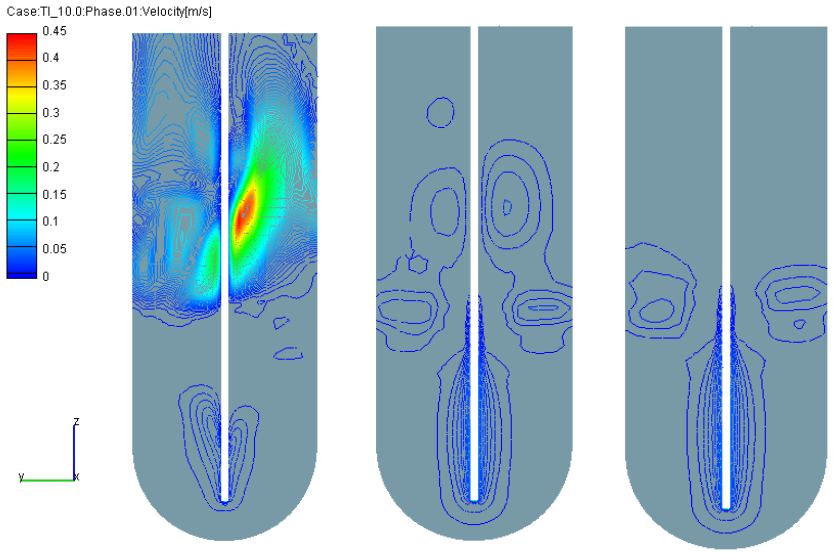

(a) (b) (c)

Figure 5.17. Velocity vector at different time when FeO=15% (a) t=10s, (b) t=150s and (c) t=250s.

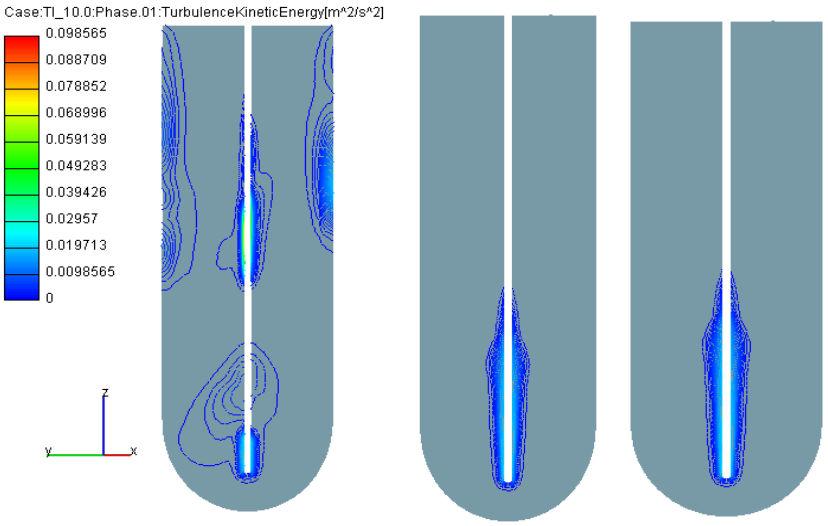

(a) (b) (c)

Figure 5.18. Turbulent kinetic energy at different time when FeO=3% (a) t=10s, (b) t=150s and (c) t=250s.

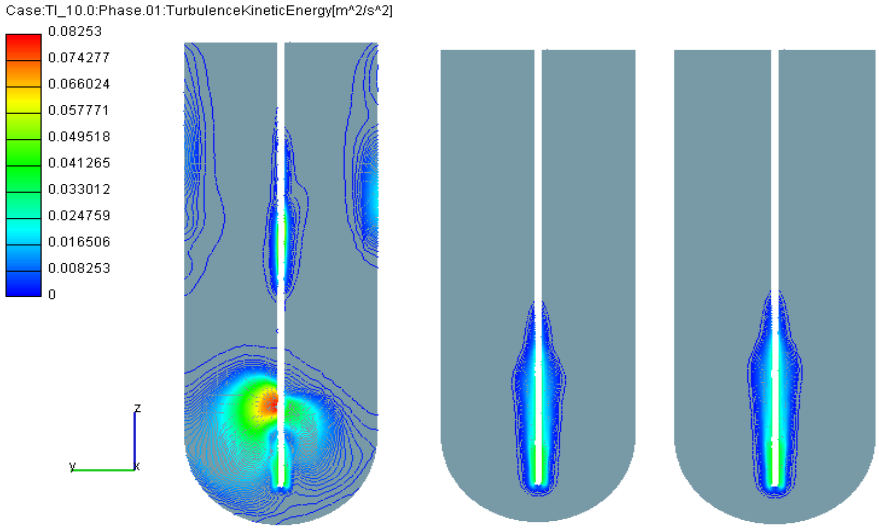

Figure 5.19. Turbulent kinetic energy at different time when FeO=7.5% (a) t=10s, (b) t=150s and (c) t=250s.

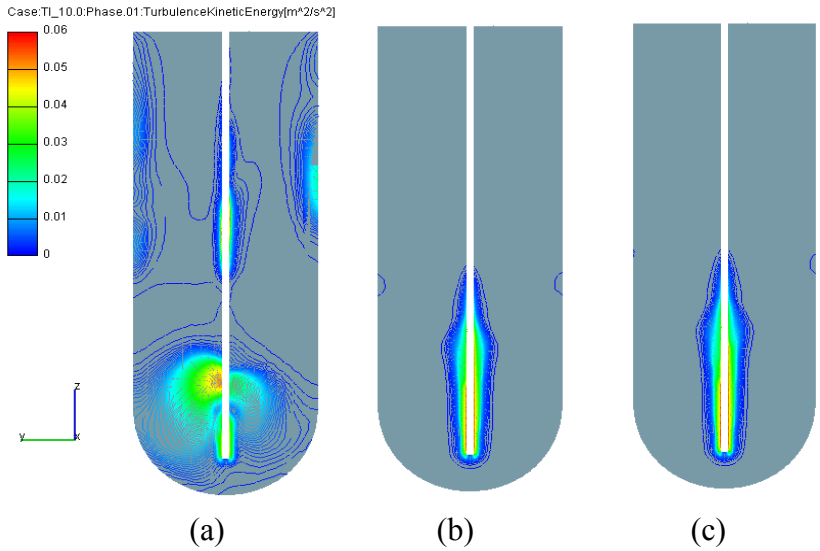

Figure 5.20. Turbulent kinetic energy at different time when FeO=15% (a) t=10s, (b) t=150s and (c) t=250s.

The results of the present CFD model are in reasonably good agreement with the experimental data of Jiang and Fruehan (1991). The present CFD model assumes that the shape of bubbles during the formation of foam is pentagonal dodecahedron but in

reality the bubbles of different shapes exist in the foam. Foams are composed of polyhedral bubbles which differ markedly in shape and size. Even among bubbles having the same volume, there is a variation in the number of faces and the number of edges per face (Bhakta and Ruckenstein, 1997). It is also considered in the present simulation that the cross section of the Plateau border channel does not change with height of foam and the liquid in the lamellae is negligible compared to the Plateau border channel (Narsimhan, 2010). The life of foam depends on the concentration of surface active agent in the foam. The concentration gradient of the surface active agent in the foam is important for the calculation of drainage and film rupture. The coefficient in the equation of frequency of the film failure (eqn.4.9) depends on the fluid viscosity and surface chemistry. The coefficient also includes the hybrid effects of relevant physicochemical properties of the employed surfactant solution on the stability of films (Tong et al., 2011). The effect the coefficient was disregarded in the present study. The results from the present CFD model show that foaming index decreases with increase of FeO content in slag. This phenomenon was attributed to the fact that increasing FeO in slag decreases the viscosity but increases the surface tension. The drainage of liquid in foam increases with the decreases of viscosity resulting in a decrease of foaming index. The results from the CFD model also showed that the foaming index of a slag with Al_2O_3 is higher than that of slag without Al_2O_3. The reason behind this was identified as the increases of viscosity due to addition of Al_2O_3. The Sauter mean diameter is found to increases with increases of FeO content in slag. This was attributed to the fact that the drainage of liquid in foam increases with the decrease of viscosity. The increased drainage leads to increased rate of film rupture and the number of upper bubble class increases thus causing the Sauter mean diameter to increase. Dimensionless analysis was performed based on the model available to correlate the foaming index with the physical properties of the slag. The coefficient of the foaming index was found to be 109 and 127 when the dimensionless groups of Jiang and Fruehan (1991) and Ito and Fruehan (1989) were used respectively. The predicted results from the present study are in reasonably good agreement with the experimental data. The reasons of discrepancies between results of the present CFD model and that of the experimental data were due to the assumptions made and numerical schemes and turbulence model used to avoid the complexity of simulation.

CHAPTER 6

MODELING OF FOAMING IN OXYGEN STEELMAKING CONVERTER

6 Modeling of slag foaming in BOS converter

This chapter presents a numerical simulation on a 3D CFD model of 6 tonne Basic oxygen steel (BOS) converter same as that of the experimental pilot plant model of Millman et al. (2011). The model has been used to predict the foam height, bubble number density of different bubble classes, decarburisation reaction, and velocity of liquid, gas and foam phases with time. The CFD model incorporated the comprehensive approach of foaming which has been proposed and implemented in the aerated liquid and the laboratory scale bath smelting slag presented in Chapter 4 and 5. The Eulerian–Eulerian multiphase flow approach has been used in the modelling of BOS converter. Bubble-bubble interaction, such as bubble breakage and coalescence applied in the modelling of bubble column reactor which is presented in Chapter 3 is also considered in this model. In gas liquid dispersion, bubble break-up due to turbulent collision and bubble coalescence due to combined effect of turbulence and laminar shear were considered in the present CFD model. In foam, bubble coalescence due to film rupture which was applied in the modelling of foaming and presented both in Chapter 4 and Chapter 5 is also considered in this model. A population balance method was used to track the number density of different bubble class. The CFD model used the rectified model of daughter bubble distribution to estimate the fraction of birth and death of bubble due to coalescence and breakage for each bubble class in turbulent dispersed flow. The model of daughter bubble distribution was developed by Hagesaether et al. (2002) and the model has been modified and presented in Chapter 3. A user subroutine has been written using FORTRAN programming language to incorporate bubble break-up and bubble coalescence, decarburisation as well as foaming into the main CFD software. The result of foam and gas and liquid phases was presented in term of volume fraction of phases. The result of number density of different bubble class was presented in term of bubble volume fraction of each bubble class. Sauter mean diameter at different height was evaluated and presented. The results of decarburisation rate and the formation CO gas with time are presented. The result obtained from this CFD model were validated against the result of Millman et al. (2011) pilot plant model and found to be in a reasonable agreement.

6.1 Introduction

In oxygen steelmaking, steel is produced from molten pig iron which contains approximately 3.5–4.5% Carbon with scrap steel through decarburisation using supersonic jet of oxygen. Different type of process is used for the production of low carbon steel from the high carbon containing pig iron. Among the various process currently used for the production of steel, Basic Oxygen Steelmaking (BOS) process is widely used for the production of steel from pig iron. The production of steel from BOS process was 67.1% of the total steel produced in the world using different process in 2008 (Brämming, 2010). In BOS process, a supersonic jet of oxygen is injected into the hot metal in a vessel which is protected by a basic inner liner. Oxygen is either supplied via a top lance on the liquid surface where the process is called top blown or through the bottom tuyers and the process is called bottom blown (Brämming, 2010). A combination of top blown and bottom blown process is also used in steelmaking industry.

The blowing of oxygen into the hot metal oxidizes carbon as well as impurities such as Silicone (Si), Manganese (Mn), Sulphur (S) and Phosphor (P) dissolved in metal. These oxidation reactions are exothermic reactions which produce heat and at the same time the process generates large amount of gas due to reaction of oxygen with carbon. Foam is observed in the process because the generated gas bubble from decarburisation and the free oxygen gas bubble from the blowing combined with liquid. The formation of foam is important for the process because the large interfacial surface area between gas bubble and liquid phases in foam facilitate the reaction in the process. The foam layer resists the heat from escaping and muffles the sound of supersonic jet impinging on the liquid bath. In addition to the above benefit, foam helps to remove the oxide formed during the blowing. Though foam is beneficial for the process excessive foam has detrimental effect on the process. Excessive foam can overflow the vessel which is termed as slopping in BOS. Slopping can reduce production and increase operation cost and sometime can damage the vessel (Nexhip et al., 2004, Jiang and Fruehan, 1991). The formation of foam in oxygen steelmaking has been investigated by many researchers in a laboratory scale model (Kim et al., 2001b). In the laboratory scale, the height of foam is measured and the height is conveniently related with the superficial

gas velocity termed as foaming index (Stadler et al., 2007). Foam is formed by poly-dispersed gas bubbles separated by thin film of liquid. The thin film is joined in a channel called Plateau border channel. The drainage of liquid occurs throught the lamellae and Plateau border channel. The drainage of liquid causes the coalescence and bursting of bubbles in foam. In an oridnary two phase flow considering gas and liquid as working fluid, it is difficult to incorporate these characteristics of foam in CFD model. In addition, the foam is expected to accumulate at the top surface of liquid, but in gas liquid two phase approach, it is not possible to keep the foam at the top surface of liquid because gas diffuses into the gaseous atmosphere above the liquid. The above drawback is eliminated by considering foam as a separate phase made up of gas and liquid.

In multiphase flow, gas bubbles split into smaller bubbles and aggregate to form bigger bubbles due to interaction of bubbles with eddies or bubble-bubble interactions. The number density of different bubble class changes because of the aggregation of bubbles caused by coalescence and disintegration caused by break-up of bubble. Liao and Lucas (2009) presented a different bubble break-up model based on different mechanism. Liao and Lucas (2010) also presented different coalescence model base on different mechanism in their review paper. There are different bubble break-up and coalescence model and mechanisms available in the literature but all models and mechanisms are not significant for all conditions. Therefore, in the present study, bubble break-up due to turbulence and bubble coalescence due to turbulence and laminar shear were considered. The bubble break-up model of Luo and Svendsen (1996) and the coalescence model of Prince and Blanch (1990) are used in the present study. The bubble coalescence model based on film rupture by Tong et al. (2011) has been used in the foam layer for the present study. The population balance modelling, a method used to track the individual entities with time, was used to track the individual bubble class in the process by incorporating birth and death of bubbles due to break-up and coalescence.

Multiphase flow phenomenon such as velocity, mass, and momentum and their interfacial exchanges between phases can be investigated experimentally using different equipment. Multiphase flow phenomena can also be investigated analytically using appropriate equation to describe the flow phenomena. Multiphase flow phenomena can

also be investigated using computer. Computational fluid dynamic (CFD) model, a type of numerical simulation, has been used for many years to investigate the multiphase flow phenomena using computer. The availability of high speed computing machine spurs its application in the modelling of multiphase flow numerically. The CFD model has been used in many fields of engineering including metallurgical process such as oxygen steelmaking involving gas-liquid flow (Alam et al., 2011, Alam et al., 2010a, Alam et al., 2010b, Alam et al., 2012, Huda et al., 2012). Experiment is costly and does not reveal the details in high temperature situation. The alternative is simulation. The present study adopted the numerical technique to investigate this high temperature multiphase flow.

Different approaches such as Euler-Euler approach, Euler-Lagrangian approach, Monte Carlo approaches, discrete bubble model (DBM) or model-free direct numerical simulations (DNS) are used for the simulation of multiphase flow. Among the various techniques, Euler-Euler approach and Euler-Lagrangian approach are commonly used in multiphase flow. In Euler–Lagrangian approach the dispersed phase is divided into particle or bubble and the particles or bubbles are tracked individually whereas in the Euler–Euler approach both the continuous and dispersed phases are considered to be interpenetrating continua and bubbles or particles are introduced as scalar in gas phase (Bannari et al., 2008, Bhole et al., 2008). The time and cost of computation for tracking individual particles or bubbles in Euler–Lagrangian approaches is more than Euler-Euler approach. Therefore, from computational considerations, the Euler–Euler approach is more economical and commonly used (Bhole et al., 2008).

In this study, a thin slice of 3D computational fluid dynamic (CFD) model of 6 tonne BOS converter which is same as that of the pilot plant model of Millman et al. (2011) has been developed. Numerical simulation was carried out based on Euler–Euler approach. The model predicted foam height, bubble number density, decarburisation and multiphase flow phenomena in the process with time. A comprehensive foaming model was incorporated into the model to account for foam formation and destruction. The model incorporated the bubble break-up and bubble coalescence model available in the literature. In the present model ten types of bubble class was considered and their

number density was tracked using population balance modeling. The model incorporated the decarburisation reaction with heat generation in the process.

6.2 Top blowing and convergent divergent nozzle

The application of supersonic pure oxygen jets to oxidize the dissolved impurities in liquid iron led to the invention, in the late 1940s in Austria, of the Linz-Donawitz (LD) process (Deo and Boom, 1993). In oxygen steelmaking, oxygen is blown under approximately 8-10 atmospheric pressure through a convergent divergent (De Laval) nozzle which transforms high pressure energy at the nozzle inlet into kinetic energy (Dogan, 2011). The jet speed at the nozzle exit lies between 2.0 to 2.4 Mach number. Mach number (Ma), named after the Austrian physicist Ernst Mach (1838-1916), is the ratio of the actual velocity of the fluid (or an object in still fluid) to the speed of sound in the same fluid at the same state (Cengel and Cimbala, 2013). The Mach number can be calculated from equation (6.1).

$$Ma = V/c \tag{6.1}$$

Where, V is the velocity of fluid or object and $c = \sqrt{kRT}$ is the velocity of sound. Different flow regions can be found in a convergent-divergent nozzle. The fluid flow regimes in a convergent-divergent nozzle are often described in terms of the flow Mach number. The flow is called sonic when $Ma = 1$, subsonic when $Ma < 1$, supersonic when $Ma > 1$, and hypersonic when $Ma \gg 1$. The exit Mach number of oxygen jet used in the steelmaking processes lies between 2.0 and 2.4. The typical flow regimes in a convergent-divergent nozzle are presented in Figure 6.1.

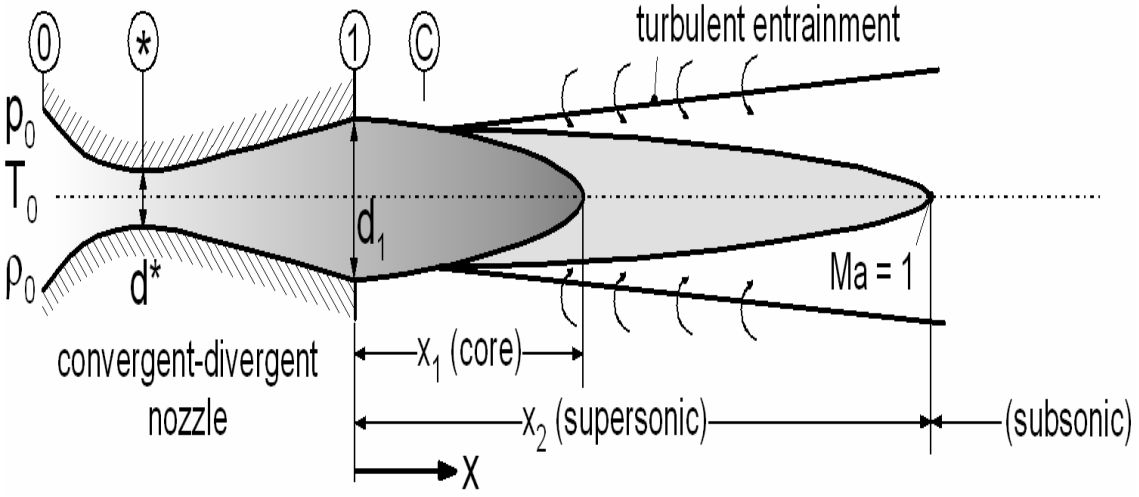

Figure 6.1. Flow regimes in a convergent-divergent nozzle (Odenthal et al., 2006).

The pressure, density and temperature is denoted at upstream as P_0, ρ_0 and T_0, at choke (Throat) as P_*, ρ_* and T_* and at the exit of the nozzle as P, ρ and T. The pressure, density and temperature at any point in the nozzle can be calculated using the following equations.

$$\frac{P}{P_0} = \left(\frac{1}{1+\frac{k-1}{2}Ma^2}\right)^{\frac{k}{k-1}} \tag{6.2}$$

$$\frac{T}{T_0} = \frac{1}{1+\frac{k-1}{2}Ma^2} \tag{6.3}$$

$$\frac{\rho}{\rho_0} = \left(\frac{1}{1+\frac{k-1}{2}Ma^2}\right)^{\frac{1}{k-1}} \tag{6.4}$$

Where, k=1.40 for oxygen, is specific heat ratio. In the pilot plant model, oxygen was blown at a constant flow rate of 17Nm^3/min through a single lance with a throat diameter of 15.5mm with upstream pressure 0.9 MPa. The density of the air at the upstream was calculated using equation (6.5).

$$\rho = \frac{P}{RT} \tag{6.5}$$

Where, R universal gas constant for oxygen R=259.8J/KgK, T temperature and P pressure. The density of the air at the upstream was calculated as 11.82kg/m^3 using equation (5). At the throat the Mach number is Ma=1.0 and for oxygen k=1.4. The values at the throat are calculated as: pressure $P^* = 0.4752$MPa, density $\rho^* = 7.49388$ kg/m^3 and temperature $T^* = 244.9$K. The exit Mach number was calculated from the following equation.

$$\frac{P_e}{P_0} = \left(\frac{1}{1+\frac{k-1}{2}Ma^2}\right)^{\frac{k}{k-1}} \tag{6.6}$$

The exit pressure was assumed to be the atmospheric pressure. Then the Mach number was found to be 2.0. The ratio of the throat area A_t and exit area A_e can be written as:

$$\frac{A_t}{A_e} = \left(\frac{k+1}{2}\right)^{1/k-1}\left\{\left(\frac{k+1}{k-1}\right)\left[\left(\frac{P_e}{P_0}\right)^{2/k} - \left(\frac{P_e}{P_0}\right)^{k+1/k}\right]\right\}^{1/2} \tag{6.7}$$

The ratio of the throat area and exit area was calculated as: $\frac{A_t}{A_e} = 0.5464$ and hence the exit diameter of nozzle was 20.96mm. The supersonic jet issuing from the nozzle has a supersonic core as can be seen in Figure 6.1. The diameter of the supersonic core decreases with the increases of distance from the nozzle exit as shown in Figure 6.1. The diameter of the supersonic core gradually narrow down and the subsonic flow starts where the Mach number is less than 1. The length of the supersonic core varies from three to eight times the nozzle exit diameter in oxygen steelmaking (Deo and Boom, 1993). In the present simulation, the nozzle exit was extended to 24 times the nozzle exit diameter of the nozzle used in the pilot plant model to ensure subsonic flow. The exit diameter was considered as 268mm at a distance 496mm from the original nozzle exit where the Mach number was 0.0322.

6.3 Model geometry and methodology used for BOS converter

The conservation equations for the mass, momentum and energy in Eulerian multiphase flow model and the numerical methods used for the modelling of 6 tonne BOS converter are presented in this section. The equation for the population balance modeling and the closure term of bubble break-up and bubble coalescence used for the present model are

discussed in this section. The detail descriptions of the boundary conditions assigned for the 6 tonne BOS converter is presented in this section. The details of the modelling techniques and its feature are discussed in this section. Meshing procedure of the present model and the methodology used for the numerical simulation is also presented. Initial conditions of the model and the properties of the fluid used for the numerical simulation are also presented in this section.

6.3.1 Model geometry and features

A schematic diagram of the model is shown in Figure 6.2. The internal diameter of the vessel was 1.340m. The length from the bottom of the inner surface to the exit is 2.905m.

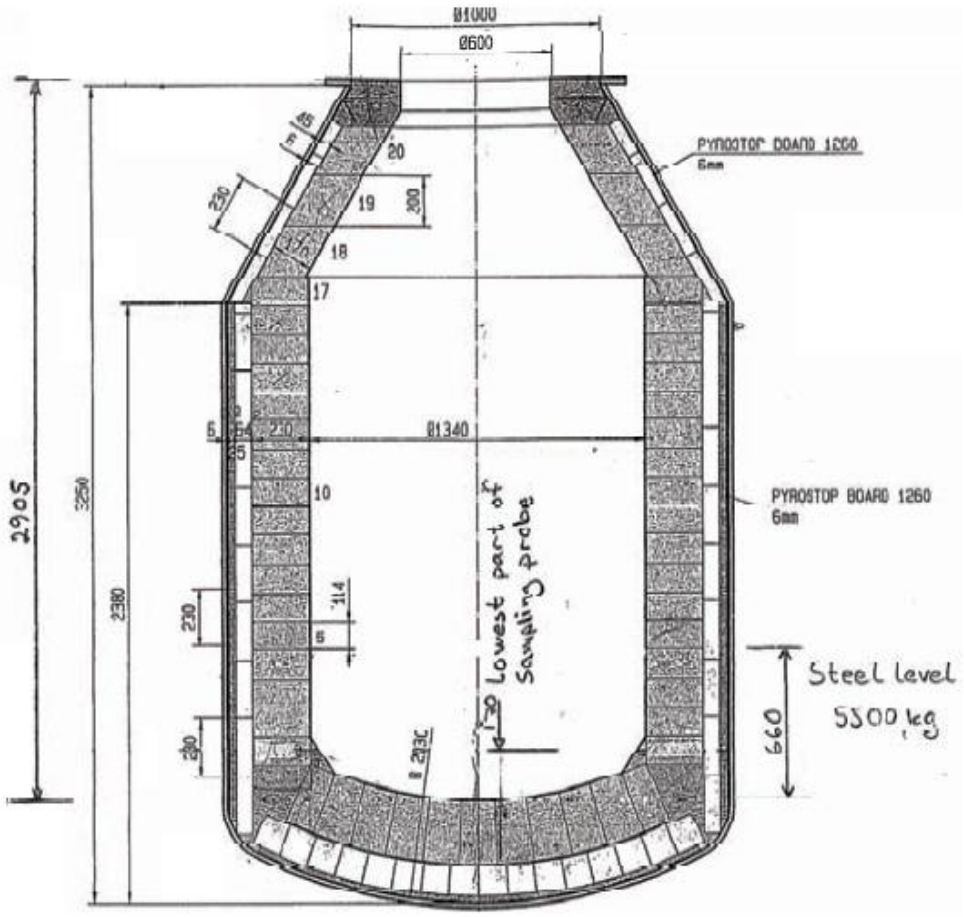

Figure 6.2. Schematic diagram of the 6 tonne BOS converter (Millman, 2011).

A 3D thin slice of the model of has been developed for the simulation to reduce the computational time (Figure 6.3(b)). The surface mesh of the model was generated by the CAD software Rhinoceros 3.0 then the surface mesh was imported in CFD simulation software AVL FIRE 2009.2 to generate volume mesh of the model. The meshing procedure of 3D CAD model was carried out using the Fame Advanced Hybrid meshing technique available in the simulation software. The volumetric mesh of the model was generated with a diameter of D = 1.340m and length Z= 2.905m for the simulation as shown in Figure 6.3. In the simulation the furnace was filled up to L=0.660 m with liquid Fe as shown in red colour in the volumetric mesh in Figure 6.3. In the middle of the vessel a vertical lance was placed with an inner diameter d_i = 15.5 mm. The inlet of the lance was extended based on the jet profile characteristic of lance which is explained in Section 6.2. Then the inlet was specified at a distance of 496mm below from the original tip of the lance. Figure 6.3(b) shows the thin slice of the model.

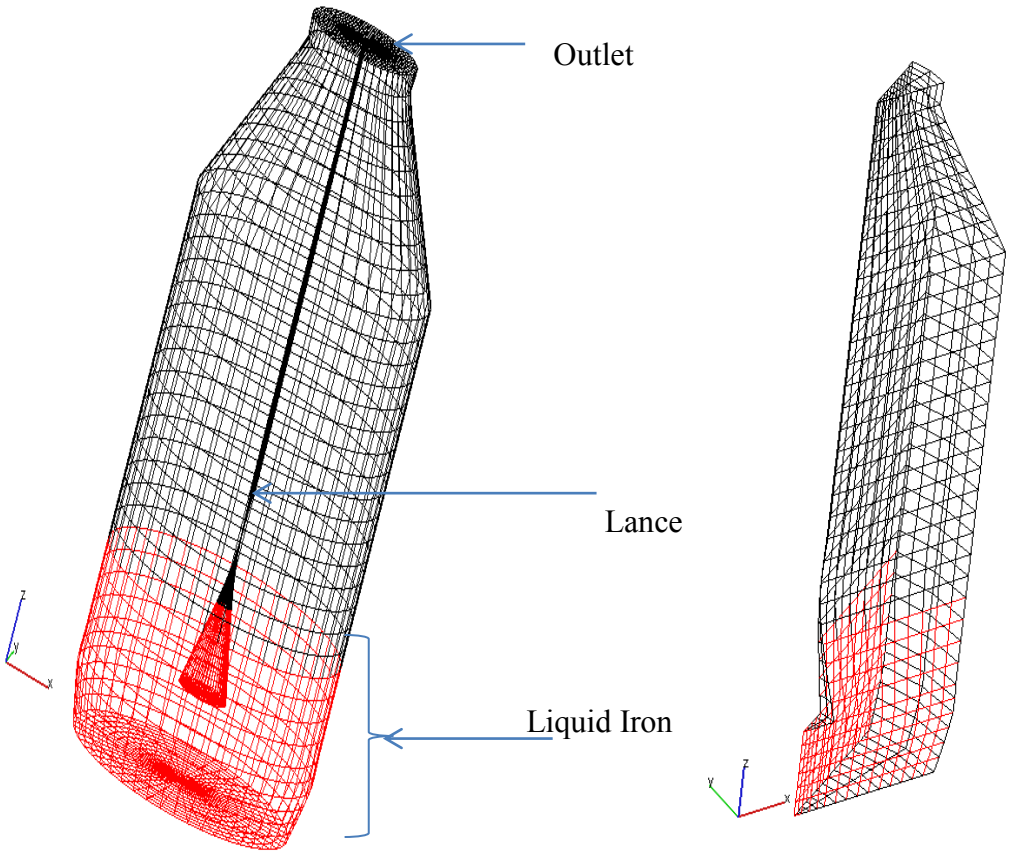

Figure 6.3. Mesh generated for the simulation (a) Full model (b) Thin slice of the model.

Similar to the previous model, bubbles were divided into ten bubble classes where the volume of the upper bubble class was twice the volume of the lower countepart such that $v_i = 2v_{i-1}$. The bubble diameter in the salg are found to be from 1.1mm to 25mm (Kapilashrami et al., 2006, Zhang and Fruehan, 1995). In the present model the minimum diameter of the bubble was considered as 2.5mm and the maximum diameter of the bubble was considered as 20mm. The diameters of the bubble classes considered in this simulation are presented in Table 6.1. Initially the bubbles of the lowest class (class 1) were assumed to enter the calculation domain through the inlet of the nozzle. The simulation was run in an unsteady state with a time step of 10^{-3} second on Intel Xeon Quad Core Z400 Machine with 8.0 GB RAM with processor speed 2.66 GHz.

Table 6.1. Bubble classes used in the simulation.

Bubble class	1	2	3	4	5	6	7	8	9	10
Bubble diameter ($10^{-3}m$)	2.50	3.15	3.97	5.00	6.30	7.94	10.00	12.60	15.87	20.00

The model was developed and simulated by using commercial CFD package AVL FIRE 2009.2. The software is based on finite volume approach which rest on the general conservation principles for properties describing the behaviour of a matter when it interacts with its surrounding. The multiphase flow simulation was carried out with Eulerian-Eulerian frame of reference. There is interaction between phase in term of mass, momentum, and energy. The fluid was considered as incompressible. In this model, an unsteady state multiphase solution for momentum and continuity were used and for turbulence, a standard $k-\varepsilon$ turbulence model was used. A cell centred finite volume approach was used to discretize the governing equations and the resulting discretized equations were solved iteratively using segregated approach. For momentum

and turbulence, first order upwind differencing scheme was used whereas central differencing scheme with second order accuracy was used for the continuity equation.

6.3.2 Boundary conditions assigned in BOS model

The boundary conditions used in the modelling of 6 tonne BOS steel converter are presented below:

6.3.2.1 Inlet

In the pilot plant model of Millman et al. (2011) oxygen enters into the system through the lance tip with supersonic velocity of gas. In the present model the effective radius of the jet was calculated at a distance 496mm below the lance tip based on the upstream flow phenomena. Then the inlet was specified at the extended lance tip. Velocity boundary conditions were applied to match the flow rate of the pilot plant model of Millman et al. (2011). Pure oxygen was injected into the molten metal at a temperature similar to the temperature of liquid metal at initial condition.

6.3.2.2 Outlet

The top surface of the BOS converter was specified as the outlet. The region occupied by the lance tube was excluded from the outlet considered. Static pressure boundary conditions were applied at the outlet.

6.3.2.3 Wall

The wall boundary type for this model is considered as solid wall. A non-slip condition was applied at all walls. The fixed temperature obtained from the pilot plant was assigned for the wall.

6.3.3 Governing equations for the modeling of 6 tonne BOS converter

The present study has considered gas, liquid and foam as separate phases for the purposes of modelling. Bubble classes were introduced as scalar in gas and foam phase. Different regions can be identified in the domain of the model based on the presence of

each of the three phases as shown in Figure 6.4. Liquid is at the bottom of the crucible. Foam remains at the top surface of liquid. The gas is above the top surface of foam. A mixture of gas and liquid (a gas liquid dispersion) remains around the outer surface of nozzle exit. However, due to transient dynamic nature of the three fluid phases in the domain, any phase may exist anywhere at any instant of time. To cater for the transient dynamic situation in the domain, the present model solves all the transport equation for all the three phases throughout the whole domain. The phase may also coexist anytime anywhere in the domain. In this modelling, the bubble break-up and coalescence phenomena are applied in the gas liquid dispersion. The bubble coalescence due to film rupture is applied in the foam phase. The governing equation in Eulerian multiphase flow approach used for the simulation of 6 tonne BOS conveter is presented in the following section. The equation includes the fundamental flow equation such as conservation of mass, momentum and energy. The interfacial exchanges of mass, momentum and energy is also presented. The chemical reaction considered in this model is also discussed. The population balance equation and the equation for the closure term of bubble break-up and bubble coalescence incorporated in the foaming model are also described and presented in the following section.

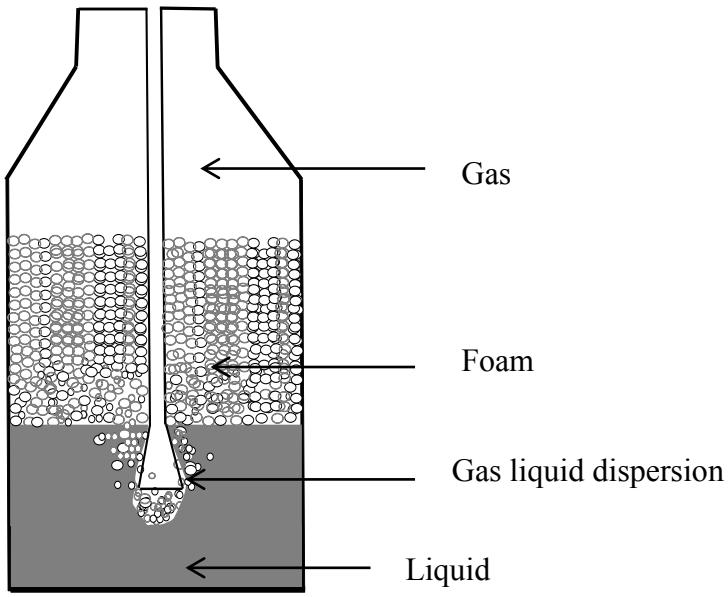

Figure 6.4. Schematic of different regions in the model.

6.3.3.1 Mass conservasation equation

In this model the mass conservation equation for each cell in Eulerian-Eulerian multiphase flow approach was used. The mass conservation equation for each phases was solved. The mass conservation equation (Eqn. 4.1) presented in Chapter 4 was used in this model. The gas, liquid and foam were considered as three separate pahses. The mass transformstion between phases were dealt with the interfacial source term in the mass conservation equation.

6.3.3.1.1 Mass interfacial exchange

There is significant mass exchanges between phases. Gas and liquid is transformed into foam and foam is also transformed into liquid and gas. The dissolved carbon in the liquid phases reacts with oxygen to form CO gas. The transformation of liquid into foam and vice versa are calculated using the euqation (4.2) presented in chapter 4. Similarly the transformation of gas into foam and vice versa were calculated using the equation (4.5) presented in Chapter 4.

6.3.3.2 Momentum conservasation equation

The momentum conservation equation for each phase in Eulerian-Eulerian approach presented in Chapter 3 is also used for the present model. The momentum conservation equation is presented in Chapter 3 at Section 3.2.3.2 (refer to Eqns.3.2-3.5). There is significance momentum transfer between phases and the momentum exchanges was dealt with the interfacial momentum exchanges term in the momentum conservation equation. The momentum interfacial exchange between phases is taken into account and the bubble induced drag force is considered in the present study. The momentum interfacial exchange between bubbles (gas phase) and liquid is modeled by considering interfacial momentum source.

6.3.3.2.1 Momentum interfacial exchange

The momentum interfacial exchange between phases was considered in the present model. The momentum interfacial exchange between phases was dealt with the

momentum exchange source term in the momentum conservation equation presented in Chapter 3 at Section 3.2.3.2.1 (refer to Eqns. 3.6-3.11).

6.3.3.3 Enthalpy conservasation equation

The decarburisation reaction generates heat and the heat is transferred into liquid phase. There is also heat transfer between phases. To cater with the heat transfer and to keep track the tmeperature of phases the enthalpy conservation equation was solved for each phase. The enthalpy conservation equation used can be written as:

$$\frac{\partial(\alpha_k \rho_k h_k)}{\partial t} + \nabla.\alpha_k \rho_k v_k h_k = \nabla.\alpha_k(q_k + q_k^t) + \alpha_k \rho_k q_k + \alpha_k \rho_k f.V_k + \nabla.\alpha_k(\tau_k + \tau_k^t).V_k + \alpha_k \frac{\partial p}{\partial t} + \sum_{l=1,l\neq k}^{N} H_{kl} + h_{kl} \sum_{l=1,l\neq k}^{N} \Gamma_{kl} \quad k = 1 \dots N \tag{6.8}$$

Here, q_k''' is the enthalpy volumteric source, H_{kl} represents the energy interfacial exchnages between phases k and l (gas, liquid and foam). The heat flux q_k can be written as:

$$q_k = \frac{K_k}{C_{p,k}} \nabla h_k \tag{6.9}$$

Here K_k is the phase k thermal conductivity. The turbulent heat flux q_k^t can be calculated as:

$$q_k^t = \frac{\mu_k^t}{\sigma_T} \nabla h_k \tag{6.10}$$

The volumetric enthalpy soruce was calculated from the decarburisation rate of carbon and the heat of reaction of carbon with oxygen. For the present study, the heat of reaction of carbon with oxygen was taken as 4173kJ/mole of carbon.

6.3.3.3.1 Interfacial energy exchnages

The heat generated due to the extohermic reaction of carbon with oxygen is transferred into the liquid by considering the energy exchange at the gas liquid interface. The heat transfer between the gas and liquid was modelled by using the Ranz-Marshall enthalpy

exchnages model. The equation for the enthalpy exchnage used in this model can be written as:

$$H_c = \frac{k_c}{D_b} Nu A_i'''(T_d - T_c) = -H_d \tag{6.11}$$

Where, k_c is the conductivity of continuous phase, D_b is the bubble diameter. The Nusselt number Nu was calculated using the following euqation (Ranz and Marshall, 1952).

$$Nu = 2.0 + 0.6 Re_b^{\frac{1}{2}} Pr^{\frac{1}{3}} \tag{6.12}$$

Where Re_b is the local bubble Reynold number, and Pr is the Prandtl number and interfacial area density A_i''' was calculated using equation (3.8).

6.3.3.4 Chemical reaction

In the present model chemical reaction of dissolve carbon with oxygen was considered. The reactants and products in gas and liquid phases were tracked using the scalar transport equation. The scalar transport equation used in the present model is as follows:

$$\frac{\partial}{\partial t}(\alpha_k \rho_k \phi_{ki}) + \nabla . \alpha_k \rho_k v_k \phi_{ki} = \nabla . \alpha_k \rho_k \mathrm{D_{ki}} \nabla \phi_{ki} + \mathrm{S_{ki}} \tag{6.13}$$

Where α_k is the volume fraction of phase k, $\rho_k$is the density of phase k and $\phi_{ki}$is the scalar fraction of phase k and $\mathrm{S_{ki}}$ is the source of different scalars due to chemical reaction.

The decarburisation rate in each cell of the calculation domain was calculated from the following equation:

$$\frac{dC}{dt} = k \alpha_l v_c \rho_l \left(\emptyset_c - \emptyset_{eq}\right) \tag{6.14}$$

Here k is the rate constant, α_l is the volume fraction of liquid phase in the cell, v_c is the volume of the cell, ρ_l is the density of liquid, $\emptyset_c$ is the carbon fraction in the cell and $\emptyset_{eq}$ is the equilibrium carbon fraction. The equilibrium carbon fraction $\emptyset_{eq}$ is considered as equal to the carbon fraction at the end of the blowing time. The constant k

was estimated from the slope of decarburisation vs time graph of pilot plant data (S1830) (Millman et al., 2011) and was found to be 5.45e-03% carbon/s. The decarburisation follows more complex kinetic equations but in this study used this simple approach to demonstrate the general feasibility of the approach.

6.3.3.5 Population balance modeling

In the modeling of oxygen steelmaking ten types of bubble was considered. The number density of buble class was updated as a consequence of bubble break-up and coalescence in the source term of PBE. The details of the equation is presented in Chapter 3 at Section 3.2.3.3.

6.3.3.6 Bubble break-up modeling and closure term

The bubble break-up due to turbulent bombardment of eddies with the bubble was considered. In the present model binary break-up was considered and the bubble break-up model of Luo and Svendsen (1996) was used. The detail of the model of bubble break-up and the equation for bubble break-up rate is presented in Chapter 3 at Section 3.2.3.5.

6.3.3.7 Bubble coalescence model and closure term in gas liquid dispersion

In the present model bubble coalescence was considered in the gas liquid dispersion. The bubble coalescence model by Prince and Blanch (1990) which is based on the laminar shear collision and turbulent collision is used for the present model. The details of the model and the equation used for the present model to calculate the coalescence rate is presented in Chapter 3 at Section 3.2.3.6.

6.3.3.8 Bubble coalescence model and closure term in foam

In this model the coalescence of bubble in foam due to lamellae rupture was considered. The bubble coalescence model by Tong et al. (2011) was incorporated. The detail model of bubble coalescence in foam due to film rupture is presented in Chapter 4 at Section 4.2.3.6.

6.3.4 Initial conditions of the model and properties of fluids used

In oxygen steelmaking process molten pig iron is charged into the vessel with scrap steel. Then a suersonic jet of oxygen is injected into the molten metal for the oxidation of dissolve carbon. The exothermic reaction of dissolved carbon in liquid metal with pure oxygen injected through the lance produces heat. This generated heat helps melting the scrap and keep the vessel safe from excessive heating. In the pilot plant of Millman et al. (2011), the vessel was initilaly chagred with molten iron and the oxygen was injected into the molten liquid iron for decarburisation. Similarly in the present simulation, the veseel was initially charged with approximately 5.5 tonne of liquid iron at initial temperature 1340°C. The properties of fluid used for the simulation is presented in Table 6.2. The viscosity of iron and gas was calculated at intital temperature of 1340°C. The viscosity of pure oxygen at 1340°C was taken from Cengel and Cimbala (2013) and presented in Table 6.2. The properties of foam was calculated using equations (4.17)-(4.18). The height of the liquid Fe was aproximately 660mm from the bottom. The region above the liquid surface was considered as gas region. Initially there was gas phase at the top and liquid at the bottom of the vessel. The simulation was run for 10 minutes of real time. The simulation was run in an unsteady state with a time step of 1.0e-03 second on Intel Xeon Quad Core Z400 Machine with 8.0 GB RAM with processor speed 2.66 GHz.

Table 6.2. The properties of the fluids used for the modelling of oxygen steelmaking.

Properties	Fe	Oxygen
Density (kg/m^3)	7030	0.233
Viscosity (Ns/m^2)	1.875E-03	6.68E-05

6.3.5 Grid independency test

The grid independency test is important to check the results of the simulation are grid independent. Two different grid of the model was generated with a control volume (number of cells) of 378 (Mesh 1) and 780 (Mesh 2) cells. Simulation was performed on both grid and it has been verified the convergence of the solution in both cases. The time averaged gas velocity at time t=120 second at a height of 0.28m for both mesh is shown in Figure 6.5. The volumetric fraction of gas at time t=120 second at the height of 0.28m for both mesh 1 and mesh 2 is shown in Figure 6.6. The figures show that there are no significant differences in the results. Therefore, for all the subsequent results, the 378 control volumes numerical mesh was used.

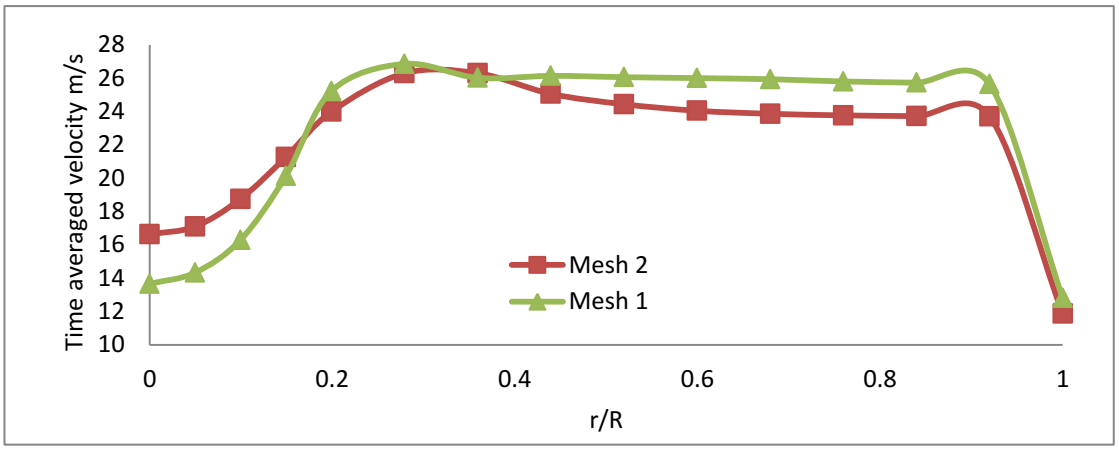

Figure 6.5. Time averaged velocity of gas.

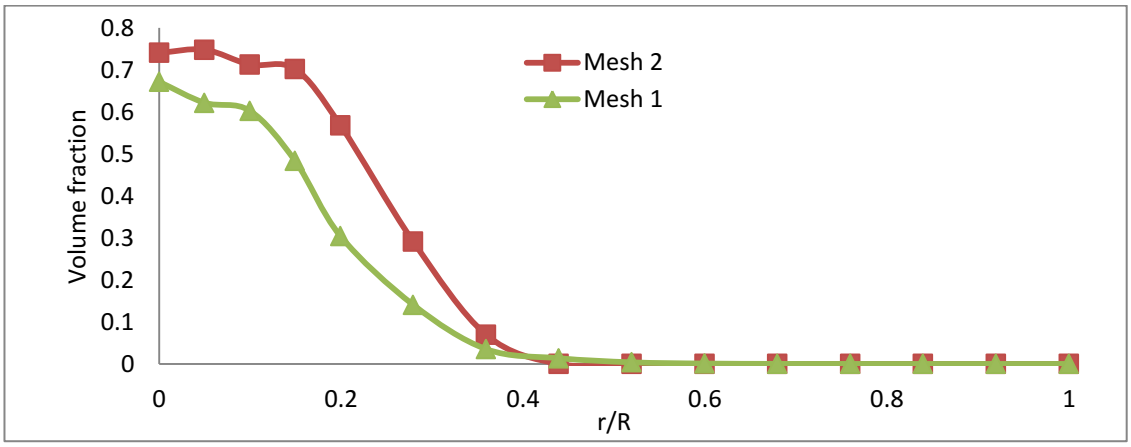

Figure 6.6. Volume fraction of gas.

6.4 Results and discussion

The results from the CFD model are presented in this section. The simulations were carried out in a thin slice of 6 tonne BOS converter with a height of 2.905m and a diameter of 1.340m. Initially the BOS converter was filled with the liquid iron up to 660mm from the bottom and there was gas above the liquid iron. Pure oxygen gas was injected through the extended inlet of the nozzle into the liquid iron. The nozzle was placed at the center of the BOS converter. The results from this model are discussed, analysed and compared with the pilot plant data from Millman et al. (2011).

6.4.1 Foaming height with time

Pure oxygen reacts with dissolve carbon and produce large quantity of gas which combines with liquid to form foam. The excessive gas remains as a free gas in the system or escapes through the top outlet. The instantaneous volume fraction of different phases at different time is presented in Figure 6.7. In Figure 6.7, the volume fraction of gas, liquid and foam with time is shown in 1st, 2nd and third column of the figure respectively. The figure clearly shows the volume fraction of gas, liquid and foam in different regions of the vessel. Figure also shows that the gas remains at the top of the vessel above the foam phases and around the outer surface of nozzle inlet. Liquid phase remains mostly at the bottom of the vessel and foam phases can be seen above the liquid surface in Figure 6.7. The co-existence of gas, liquid and foam can be seen in the interface between foam and liquid (interface between top surface of liquid with the bottom surface of foam). The co-existence of gas, liquid and foam in other regions is also evident. At the initial stage of oxygen injection, the injected gas pushes the liquid and creates a concave shape cavity of gas in front of the inlet nozzle tip. The gas moves upward along the outer surface of the lance. The gas combines with liquid to form foam at the interface of gas and liquid where the condition of foam formation is satisfied. The newly formed foam moves upward and settles at the top surface of the liquid. The excessive gas also moves upward and diffuses into the gas region at the top of the converter then escapes outside through the outlet of the vessel. With the elapse of time the height of the foam sitting on top of the liquid increases which reduces the quick escape of free gas.

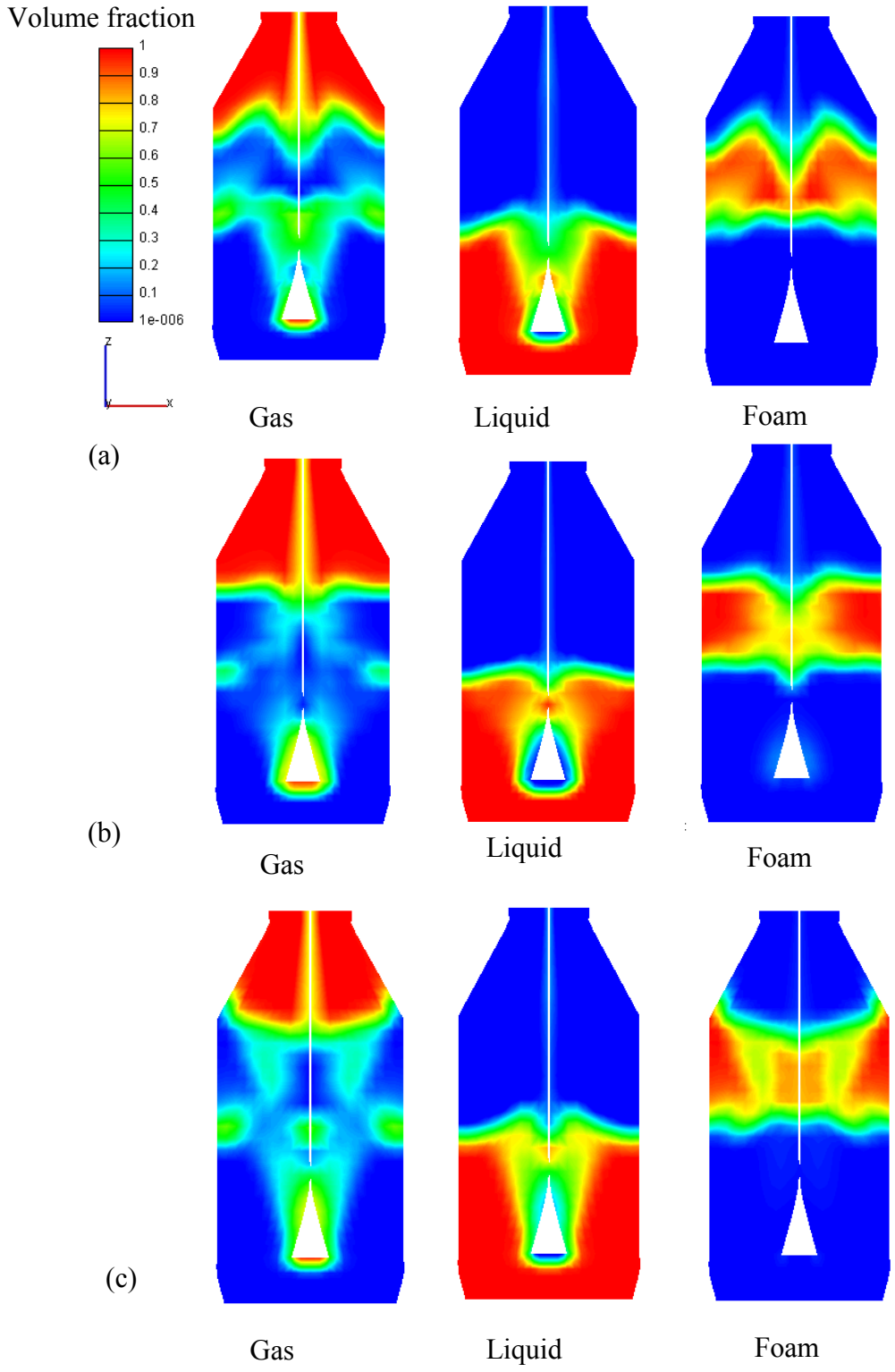

Figure 6.7. Volume fraction of different phases at (a) t=120s, (b) t=300s and (c) t=540s.

When foam is formed at the top, bubble bursting and liquid drainage starts. The height of foam is dynamically balanced by the formation of foam and it's destruction due to liquid drainage and bursting of bubble. When the height of foam increases the release of gas and liquid from foam also increases. The gas and liquid are released from the foam due to liquid drainage through the Plateau border channel and bubble bursting. The volume fraction of gas can be seen inside foam as well as the top surface of foam (Figure 6.7). The height of foam attains a quasi-steady state when the foam formation and foam destruction reaches equilibrium. Due to turbulent nature of fluid flow and the quasi-steady state of foam the height of foam fluctuates and the foam layer is not uniform as can be seen in Figure 6.7.

In the present study, the height of foam was measured as the distance between the top surface of liquid (interface between the top of liquid surface and bottom of foam surface) and the top surface of foam (interface between the top of foam surface and the gas phase above). As the surface of foam is not horizontal so the foam height at three different locations was measured and an average height was taken. The average height of foam at different blowing time is presented in Figure 6.8. The figure shows that the foam height fluctuates but keeps on increasing in first 7 minutes then reaches a quasi-steady state at around 9 minutes. The carbon content in liquid metal is higher at the beginning of blowing; therefore more oxygen reacts with the carbon dissolved in liquid and produces large volume of gas at the beginning of injection. The predicted foaming height is higher than that of the pilot plant data for first 4 minutes. The present CFD model over predicted the foam height during the first 4 minutes of blowing. In steelmaking, reactions such as decarburisation and oxidation of Fe, Si, S, P, and Mn take place. The reaction of Fe, Si, S, P, and Mn with oxygen produces oxides consuming the available oxygen. The decarburisation reaction, which also requires oxygen, has to compete with the above mentioned oxidation reactions for the availability of oxygen. In the present CFD model only the decarburisation reaction is considered so the amount of CO gas produced is more than expected. As the production of gas (CO) is more than expected, the formation of foam and its height is also more than expected. Therefore up to 4 minutes the predicted foaming height is more than the pilot plant data. On the other hand the foaming height in the present CFD model is

lower than the pilot plant data during 5-8 minute. This can be attributed to the fact that with time the amount of carbon in the liquid decrease as can be seen in Figure 6.9.

Decarburisation in the oxygen steelmaking occurs mainly in the bath and emulsion zone. Different mechanisms are used to calculate the decarburisation reaction in various zones. Oxygen from the top blown lance reacts with the dissolved carbon in the impact zone and forms a mixture of CO and CO_2 gases. Subsequently, dissolved carbon also reacts simultaneously with CO_2 at this region and produces CO. The decarburisation reaction in the emulsion phase takes place via FeO reduction. In the emulsion CO reduces FeO at the slag-gas interface and CO_2 reacts with dissolved carbon in the metal-gas interface. It is believed that the decarburisation reaction via FeO reduction is responsible for the majority of decarburisation in oxygen steelmaking, and this reaction is also important to slag foaming and slopping during the process. In the present study, the reaction of carbon with oxygen was considered in the interface between gas and liquid. However in reality, the pure oxygen not only reacts with dissolve carbon in the bulk liquid but also with the carbon in foam. In the foam, the oxidation reaction takes place inside the foam bubble. The oxygen in foam gas bubble reacts with the dissolved carbon in the liquid of lamellae and Plateau border channel. This reaction also produces CO gas and this gas increases the volume of foam due to expansion of foam volume. This reaction between carbon dissolved in liquid phase in foam and FeO in the slag was ignored in the present study.

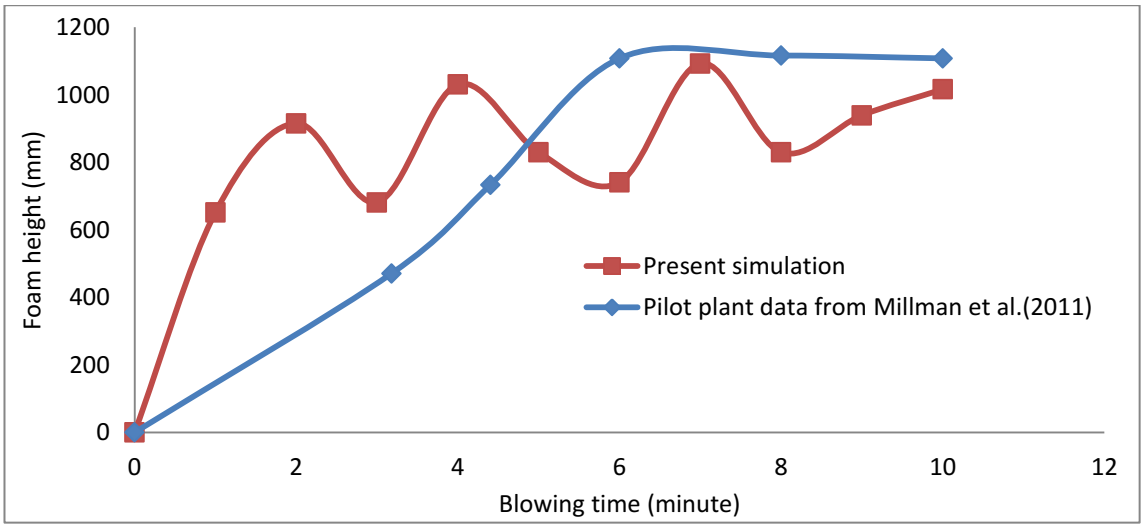

Figure 6.8. Foaming height with different process time.

The foaming height is found to reach in a quasi-steady state around 9-10 minutes. The amount of carbon in the liquid decreases with time as can be seen in Figure 6.9. Therefore the gas production due to reaction of oxygen with carbon also decreases which ultimately decreases the foam formation. After the production of CO from decarburisation is reduced the main gas available for the foam formation foam is O_2 from the inlet nozzle. The loss of foam is due to liquid drainage and bubble bursting. The O_2 gas flow rate from the inlet nozzle is constant and therefore the foam formation attains quasi-steady state in absence of CO production from decarburisation. Thus towards the end of decarburisation the height of foam is much dictated by the flow of gas injected rather than the reaction of dissolved carbon in the liquid with oxygen.

6.4.2 Decarburisation and heat

The purpose of blowing is to remove carbon from the bulk liquid by decarburisation reaction. The blowing oxygen reacts with the dissolved carbon and produce CO gas and the content of carbon in the liquid changes with time. The carbon in the liquid is removed as a CO gas through decarburisation reaction. The CFD model predicted the carbon in the liquid at different time in term of the mass fraction. The mass fraction of carbon in the bulk liquid at different time is presented in Figure 6.9 at a height z=0.28m from the bottom of the vessel. The decarburisation reaction starts at the beginning of the injection and continues until the end of the injection. Initially the mass fraction of carbon in the liquid was 0.045 with time elapses the carbon in the liquid decreases as can be seen in Figure 6.9. The figure shows that the mass fraction of carbon in the liquid is approximately 0.042, 0.021, and 0.018 at 120s, 300s and 600s respectively.

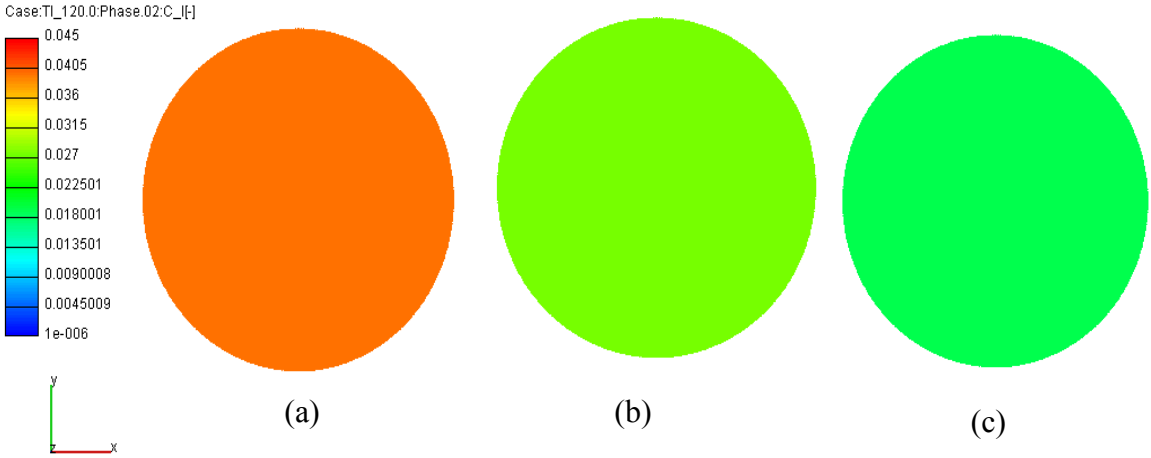

Figure 6.9. Carbon in the liquid at different process time (a) 120s, (b) 360s and (c) 600s.

The percentage of carbon with the time of injection is presented in Figure 6.10. The figure shows that the percentage of carbon in the bulk liquid decreases with time from the start of the injection until the end of injection. Dissolved carbon reacts with oxygen until it is consumed out from the bulk liquid. The Figure 6.10 shows that the decarburisation rate of the present CFD simulation is higher than that of the pilot plant data. In the present CFD simulation, only the reaction of carbon with oxygen is considered and other reactions are ignored. Therefore more carbon reacts with oxygen in the present CFD model and hence the predicted decarburisation rate in this model predicted more than the pilot plant data. In the present CFD model, the reaction was considered as a single step reaction in which dissolved carbon reacts with oxygen and produces carbon monoxide. But in the experiment, the reaction is multi-step and in some cases it produces carbon dioxide and some reverse reactions are also noticed in the system. Carbon dioxide also reacts with dissolve carbon to produce carbon monoxide. These may have contributed to the higher predicted decarburisation rate.

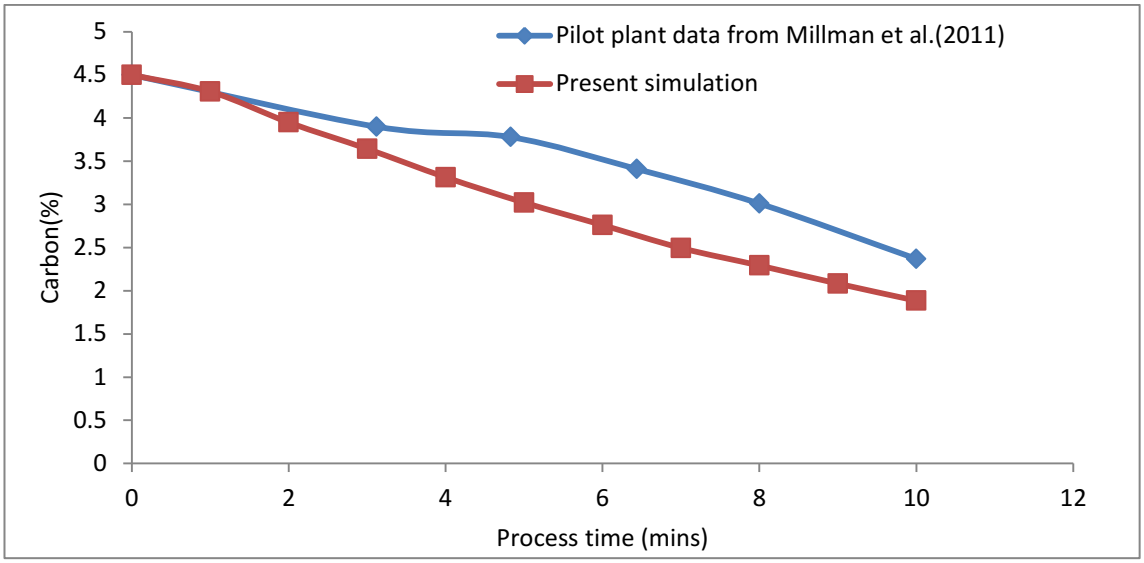

Figure 6.10. Carbon content with different process time.

The predicted temperature contour of the bulk liquid at a height of z=0.28m is presented in Figure 6.11. The figure shows that the temperature of the liquid increases with the increase of process time. In the present CFD model, the heat generation due to the reaction of dissolve carbon in the liquid with oxygen was considered. The decarburisation reaction is an exothermic reaction which produces heat and the heat is transferred into the liquid through the interfacial source term in the energy conservation equation (Eqn. 6.8). The heat gained due to the exothermic reaction increases the temperature of the bulk liquid.

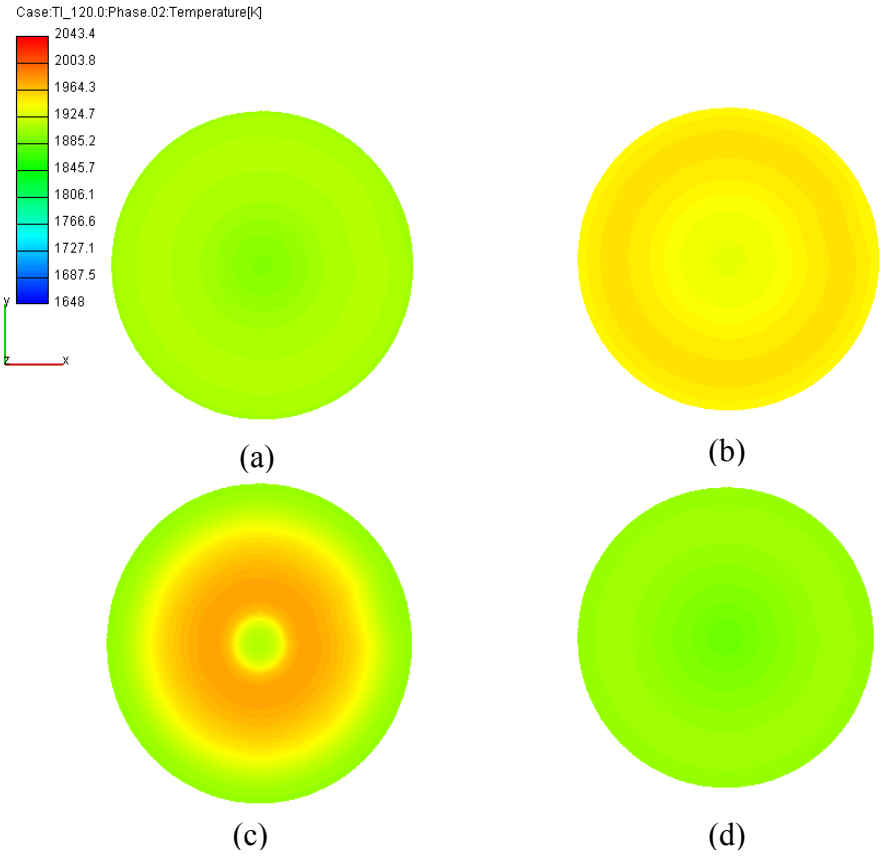

Figure 6.11. Temperature profile of liquid at height of 0.28m (a) 120s, (b) 240s, (c) 420s, and (d) 540s.

The predicted temperature of the bulk liquid along with the pilot plant data from Millman et al. (2011) is presented in Figure 6.12. The figure shows that the temperature of the bulk liquid increases with the increase of process time. The predicted temperature of the bulk liquid is higher than that of the pilot plant data until 8 minutes but after 8 minutes the predicted temperature approaches the pilot plant temperatures. This can be attributed to the over prediction of decarburisation reaction by the present CFD model as already explained. The decarburisation reaction is an exothermic reaction which produces and thus contributes to the increase of bulk liquid temperature. The amount of dissolve carbon in the bulk liquid is higher at the beginning of injection and hence the amount of carbon reacting with oxygen is also higher. Therefore, the amount of heat produced due to the exothermic reaction is higher at the beginning than at the end of the process time. Hence it is not surprising that the predicted temperature of the bulk liquid is higher than the pilot plant data.

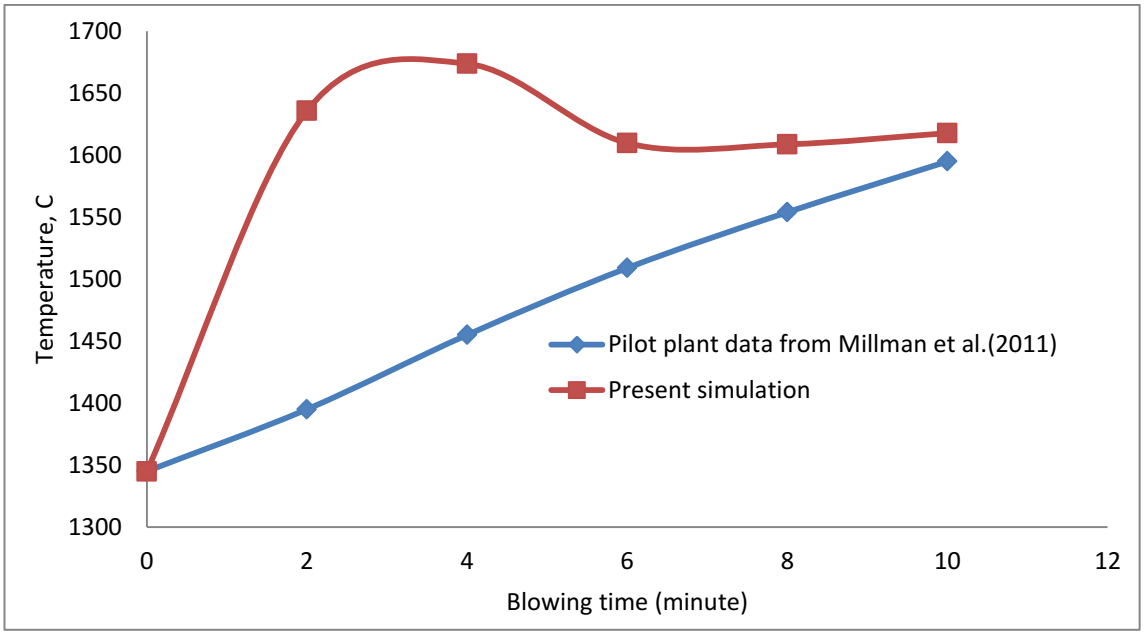

Figure 6.12. Temperature in the liquid at different process time.

The mass fraction of carbon monoxide at different blowing time is presented in Figure 6.13. The figure shows that the carbon monoxide decreases with increases of time. The amount of carbon available in the liquid for decarburisation decreases with time (see Figure 6.9). Therefore, the carbon monoxide produced due to the reaction of carbon with oxygen also decreases. The figure also shows that the carbon monoxide is less around the nozzle exit. The high velocity pure oxygen injected from the nozzle pushes the liquid away and gas region is formed. The CO is more in gas region than other part of the vessel. Carbon monoxide gas moves upward through the liquid. The generated CO passes through the foam layer above the liquid surface and finally exits into the atmosphere through the outlet of the vessel.

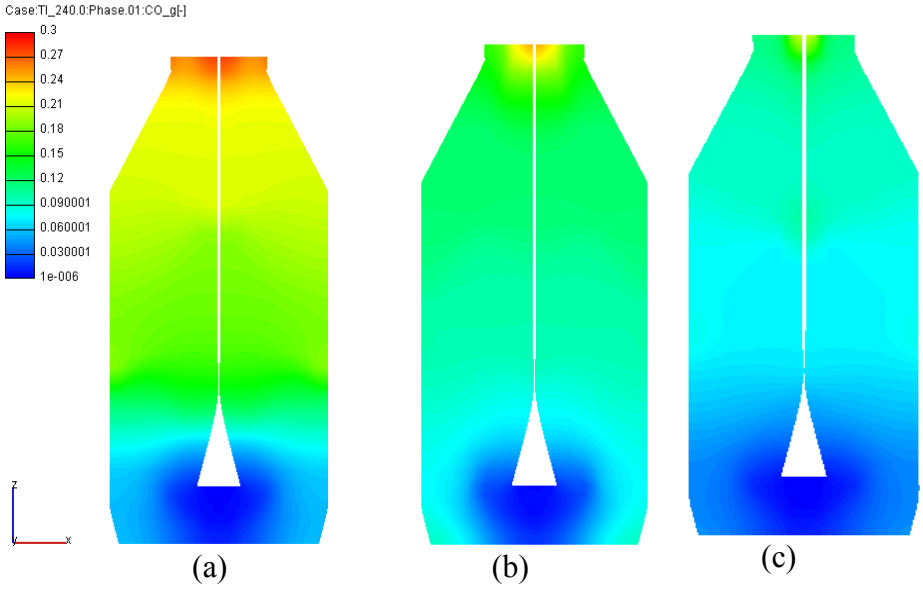

Figure 6.13. Carbon monoxide at different process time (a) 240s, (b) 360s, (c) 600s.

6.4.3 Bubble distribution

The bubble enters into the system through the inlet nozzle. The bubble distribution of different bubble classes in gas liquid dispersion are presented in Figure 6.14. The figure shows that the bubbles are dispersed in the system. Gas bubbles dispersed in liquid due to diffusion and turbulence. When bubble rises from the bottom, the drag force, viscous shear force and the buoyancy acting on the bubble causes it to rise with an oscillating motion (turbulent velocity). This turbulent velocity causes bubbles to collide with each other and radiate away from their centers. Some bubble coalesces while other deflects from each other. The deflection due to collision of bubbles and oscillation motion together with diffusion causes the bubble to disperse from the center. In the present study 10 types of bubble classes were considered. The figures show that the numbers of lower bubble classes are more than the higher bubble classes. In the present study only bubble class 1 was allowed to enter into the calculation domain through the inlet nozzle. The coalescence causes the increase of upper bubble class whereas the bubble break-up decreases the upper bubble class and increases the lower bubble class in gas liquid dispersion. The break up rate of upper bubble classes increases with the increase of their numbers which finally slows down the growth of number density of upper bubble classes.

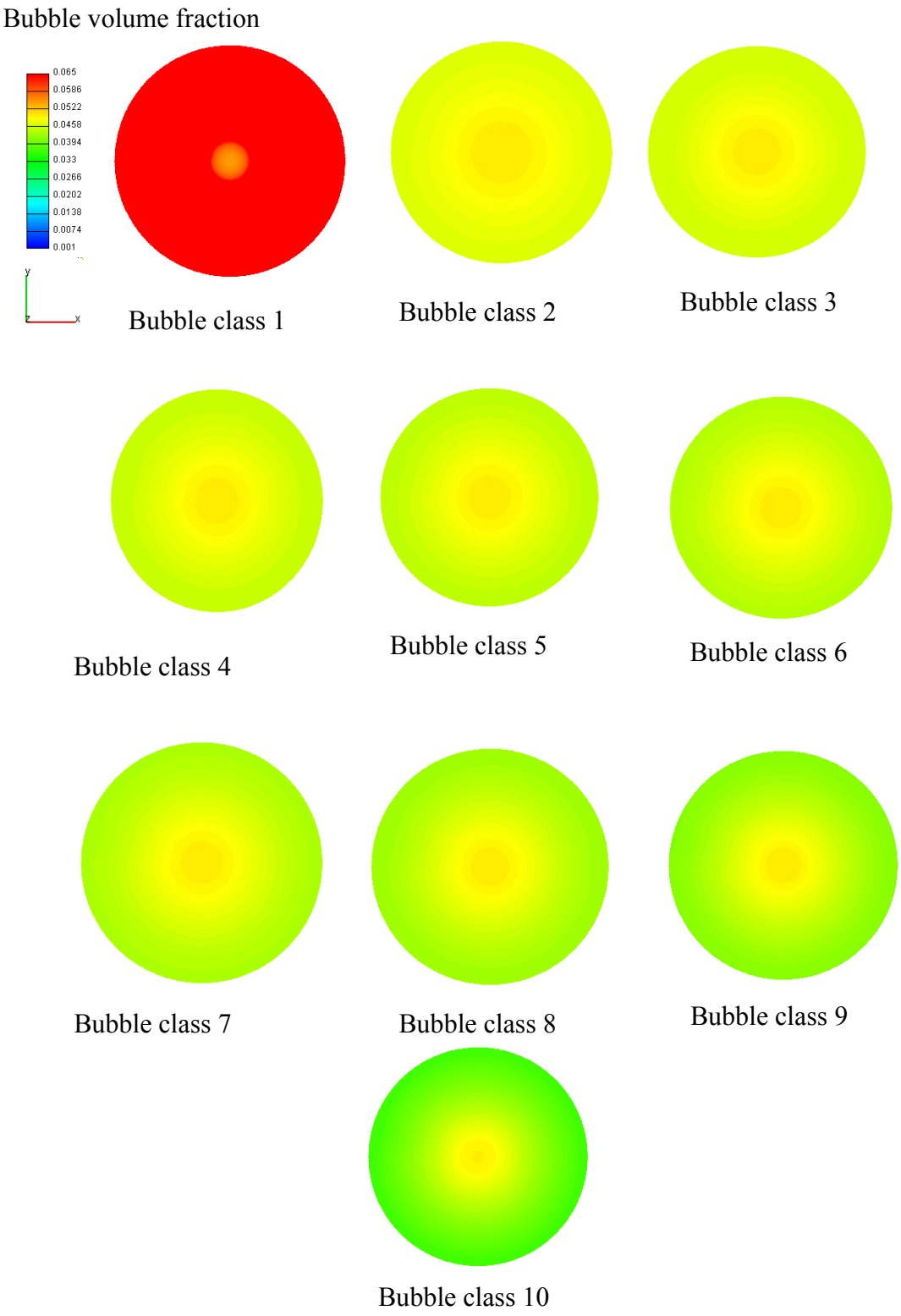

Figure 6.14. Bubble distribution at 0.28m from the bottom at 120s.

6.4.4 Velocity contour of different phases

The velocity contour of different phases at 300s is shown in Figure 6.15. The inlet velocity of gas was approximately 25m/s. The highest gas velocity can be seen around the nozzle exit in Figure 6.15. The velocity of liquid and foam phase are less than the gas as can be seen in the Figure 6.15 (see the value in color bar). The foam and liquid get momentum from the gas phase through the momentum interfacial exchange. The velocity of gas inside foam is less because the foam phase obstructs the gas escape.

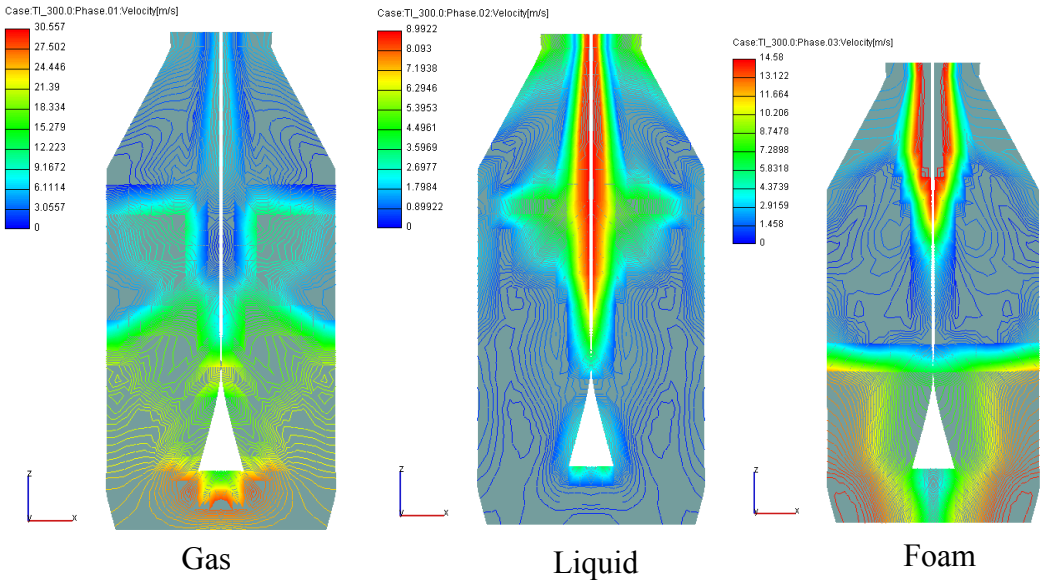

Figure 6.15. Velocity contour of different phases at 300s.

The results from the present CFD model show over prediction of the foaming height at the initial stage. This phenomenon was attributed to the fact that the present CFD model over estimates the decarburisation reaction which results in higher foam formation. In the present CFD simulation, only the reaction of carbon with oxygen is considered, therefore more carbon reacts with oxygen in the initial stage and hence the model over predicted decarburisation. The predicted results from the present study are in reasonably good agreement with the experimental data. The reasons of discrepancies between results of the present CFD model and that of the experimental data were due to the assumptions made and numerical schemes and turbulence model used to avoid the complexity of simulation.

CHAPTER 7

CONCLUSIONS AND RECOMMENDATIONS

7 Conclusions and recommendations

7.1 Conclusions

In the present study different CFD models have been developed and numerical simulation has been carried out to predict different bubble number density, foam height, decarburisation and multiphase flow phenomena. The first three CFD models presented in Chapters 3 to 5 were developed to predict bubble number density and foam height. Then a CFD model of oxygen steelmaking presented in Chapter 6 was developed to predict the bubble number density, foam height and decarburisation reaction with heat generation in the system. A user subroutine was written in FORTRAN programming language to incorporate bubble break-up and coalescence, foaming model and decarburisation into the main program of the software. Based on the results obtained from the CFD models, the concluding remarks for different models are presented as follows:

An anomaly was found in the daughter bubble distribution of population balance model in the open literature which was rectified and used in the modelling of bubble column reactor to predict the bubble number density in the column. A 3D CFD model has been developed which can predict the bubble number density and multiphase flow phenomena. The results from the CFD model have been validated against experimental data available in the open literature and found to conform (Laari and Turunen, 2003, Bhole et al., 2008, Bannari et al., 2008, Laari and Turunen, 2005, Sha et al., 2006).

A new approach of foam which considers foam as a mixture of gas and liquid was proposed and used to predict the foam height. The proposed approach enables us to incorporate liquid drainage and bubble bursting in foam. The proposed approach has been used in the modelling of creaming and formation of foam in aerated liquid and slag foaming on bath smelting slag. The results from the CFD model have been validated against analytical and experimental data available in the literature (Narsimhan, 2010, Jiang and Fruehan, 1991). The model can predict the height of foam, bubble number density and the multiphase flow phenomena with time.

Finally a CFD model of oxygen steelmaking was developed incorporating the modified daughter bubble distribution, new approach of foam and simple approach of the decarburisation reaction. The results from the model have been validated against the pilot plant data available in the open literature. The CFD model can predict the foam height, bubble number density, decarburisation with heat generation and multiphase flow phenomena.

7.2 Recommendations

This section presents few recommendations for future work on the model developed. Incorporation of these recommendations into the model will enhance understanding of the physio-chemical phenomena in the process.

- Different mechanisms and mathematical model for bubble break up and bubble coalescence are available in open literature. The present study has considered the break-up model of Luo and Svendsen (1996) and the coalescence model of Prince and Blanch (1990) in gas liquid dispersion. The coalescence model of Tong et al. (2011) was used in foam. There are also other mathematical model of bubble break-up (Martínez-Bazán et al., 1999a, Wang et al., 2003b, Zhao and Ge, 2007) and coalescence (Lehr et al., 2002, Wu et al., 1998) in the literature which can be incorporated in the future work.
- Decarburisation reactions in the oxygen steelmaking are complex but used simple approach in the present study. The reaction of S, P, Si, Mn and Fe with oxygen can be included in the future work. They play significant role on the properties of foam in the process. The reaction in foam phase can also be included in the future work.
- The slag formation should be included in the future work to understand the slag foaming in the BOF.
- Foam is a highly complex system and all the phenomena of foaming are very difficult to incorporate in a model. The drainage of liquid through lamellae can be incorporated in the future work for better understanding the drainage of liquid. The effect of bubble size on the properties of foam as well as the effect of concentration of each element on the bursting of bubble can be incorporated in the future work.

References

ACRIVOS, A. 1983. The breakup of small drops and bubbles in shear flows. *Annals New York Academy of Sciences***,** 1-11.

AGARWAL, S. 2002. *Efficiency of shear-induced agglomeration of particulate suspensions subjected to bridging flocculation.* West Virginia University.

AKERS, R. J. 1976. *Foams,* London, Academic press.

ALAM, M., IRONS, G., BROOKS, G., FONTANA, A. & NASER, J. 2011. Inclined jetting and splashing in electric Arc furnace steelmaking. *ISIJ International,* 51**,** 1439-1447.

ALAM, M., NASER, J. & BROOKS, G. 2010a. Computational fluid dynamics simulation of supersonic oxygen jet behavior at steelmaking temperature. *Metallurgical and Materials Transactions B: Process Metallurgy and Materials Processing Science,* 41**,** 636-645.

ALAM, M., NASER, J., BROOKS, G. & FONTANA, A. 2010b. Computational fluid dynamics modeling of supersonic coherent jets for electric arc furnace steelmaking process. *Metallurgical and Materials Transactions B: Process Metallurgy and Materials Processing Science,* 41**,** 1354-1367.

ALAM, M., NASER, J., BROOKS, G. & FONTANA, A. 2012. A computational fluid dynamics model of shrouded supersonic jet impingement on a water surface. *ISIJ International,* 52**,** 1026-1035.

ALOPAEUS, V., KOSKINEN, J., KESKINEN, K. I. & MAJANDER, J. 2002. Simulation of the population balances for liquid-liquid systems in a nonideal stirred tank. Part 2-parameter fitting and the use of the multiblock model for dense dispersions. *Chemical Engineering Science,* 57**,** 1815-1825.

ALOPAEUS, V., LAAKKONEN, M. & AITTAMAA, J. 2006. Solution of population balances with breakage and agglomeration by high-order moment-conserving method of classes. *Chemical Engineering Science,* 61**,** 6732-6752.

ANNAPRAGADA, A. & NEILLY, J. 1996. On the modelling of granulation processes: A short note. *Powder Technology,* 89**,** 83-84.

AVL-FIRE 2008. *CFD Solver Manual,* Austria, AVL, Graz,.

BALDYGA, J. & BOURNE, J. R. 1993. Drop breakup and intermittent turbulence. *Journal of Chemical Engineering of Japan,* 26**,** 738-741.

BANNARI, R., KERDOUSS, F., SELMA, B., BANNARI, A. & PROULX, P. 2008. Three-dimensional mathematical modeling of dispersed two-phase flow using class method of population balance in bubble columns. *Computers & Chemical Engineering,* 32**,** 3224-3237.

BHAKTA, A. & RUCKENSTEIN, E. 1997. Decay of standing foams: drainage, coalescence and collapse. *Advances in Colloid and Interface Science,* 70**,** 1-124.

BHOLE, M. R., JOSHI, J. B. & RAMKRISHNA, D. 2008. CFD simulation of bubble columns incorporating population balance modeling. *Chemical Engineering Science,* 63**,** 2267-2282.

BIGGS, C. A., SANDERS, C., SCOTT, A. C., WILLEMSE, A. W., HOFFMAN, A. C., INSTONE, T., SALMAN, A. D. & HOUNSLOW, M. J. 2003. Coupling granule properties and granulation rates in high-shear granulation. *Powder Technology,* 130**,** 162-168.

BIKERMAN, J. J. 1953. *Foams; theory and industrial applications*, Reinhold.

BILICKI, Z. & KESTIN, J. 1987. Transition criteria for two-phase flow patterns in vertical upward flow. *International Journal of Multiphase Flow,* 13**,** 283-294.

BIRK, W., ARVANITIDIS, I., MEDVEDEV, A. & JÖNSSON, P. 2003. Foam level control in a water model of the LD converter process. *Control Engineering Practice,* 11**,** 49-56.

BLUESCOPESTEEL. 2011. Bluescopesteel. Available: http://www.bluescopesteel.com.au/ 2011].

BOKKERS, G. A., LAVERMAN, J. A., ANNALAND, M. V. & KUIPERS, J. A. M. 2006. Modelling of large-scale dense gas-solid bubbling fluidised beds using a novel discrete bubble model. *Chemical Engineering Science,* 61**,** 5590-5602.

BORDEL, S., MATO, R. & VILLAVERDE, S. 2006. Modeling of the evolution with length of bubble size distributions in bubble columns. *Chemical Engineering Science,* 61**,** 3663-3673.

BOUAIFI, M. & ROUSTAN, M. 1998. Bubble size and mass transfer coefficients in dual-impeller agitated reactors. *Canadian Journal of Chemical Engineering,* 76**,** 390-397.

BRÄMMING, M. 2010. *Avoiding Slopping in Top-blown BOS Vessels*.

BRENNEN, C. E. 2005. *Fundamentals of multiphase flow*, Cambridge University Press.

BREWARD, C. J. W. 1999. *The Mathematics of Foam*, University of Oxford. 1999.

BUNNER, B. & TRYGGVASON, G. 1999. Direct numerical simulations of three-dimensional bubbly flows. *Physics of Fluids,* 11**,** 1967-1969.

BUWA, V. V. & RANADE, V. V. 2002. Dynamics of gas-liquid flow in a rectangular bubble column: experiments and single/multi-group CFD simulations. *Chemical Engineering Science,* 57**,** 4715-4736.

CENGEL, Y. & CIMBALA, J. 2013. *Fluid Mechanics Fundamentals and Applications*, McGraw-Hill Education.

CHATZI, E. & LEE, J. M. 1987. Analysis of interactions for liquid-liquid dispersions in agitated vessels. *Industrial and Engineering Chemistry Research,* 26**,** 2263-2267.

CHEN, P., SANYAL, J. & DUDUKOVIC, M. P. 2005. Numerical simulation of bubble columns flows: effect of different breakup and coalescence closures. *Chemical Engineering Science,* 60**,** 1085-1101.

CHESTERS, A. K. 1991. Modelling of coalescence processes in fluid-liquid dispersions. A review of current understanding. *Chemical Engineering Research and Design,* 69**,** 259-227.

COULALOGLOU, C. A. & TAVLARIDES, L. L. 1977. Description of interaction processes in agitated liquid-liquid dispersions. *Chemical Engineering Science,* 32**,** 1289-1297.

CUTHILL, G. K. 1981. *Control of Slopping in Basic Oxygen Steelmaking.* Master of Engineering, McMaster University.

DARELIUS, A., RASMUSON, A., BJÖRN, I. N. & FOLESTAD, S. 2005. High shear wet granulation modelling - A mechanistic approach using population balances. *Powder Technology,* 160**,** 209-218.

DELNOIJ, E., LAMMERS, F. A., KUIPERS, J. A. M. & VAN SWAAIJ, W. P. M. 1997. Dynamic simulation of dispersed gas-liquid two-phase flow using a discrete bubble model. *Chemical Engineering Science,* 52**,** 1429-1458.

DEO, B. & BOOM, R. 1993. *Fundamentals of Steelmaking Metallurgy*, Prentice Hall International, Incorporated.

DIAZ, M. E., IRANZO, A., CUADRA, D., BARBERO, R., MONTES, F. J. & GALAN, M. A. 2008. Numerical simulation of the gas-liquid flow in a laboratory scale bubble column Influence of bubble size distribution and non-drag forces. *Chemical Engineering Journal,* 139**,** 363-379.

DÍAZ, M. E., IRANZO, A., CUADRA, D., BARBERO, R., MONTES, F. J. & GALÁN, M. A. 2008. Numerical simulation of the gas-liquid flow in a laboratory scale bubble column: Influence of bubble size distribution and non-drag forces. *Chemical Engineering Journal,* 139**,** 363-379.

DOGAN, N. 2011. *Mathematical modelling of oxygen steelmaking.* PhD, Swinburne University of Technology.

DRENCKHAN, W. & LANGEVIN, D. 2010. Monodisperse foams in one to three dimensions. *Current Opinion in Colloid & Interface Science,* 15**,** 341-358.

DRUZHININ, O. A. & ELGHOBASHI, S. 1998. Direct numerical simulations of bubble-laden turbulent flows using the two-fluid formulation. *Physics of Fluids,* 10**,** 685-697.

EVESTEDT, M. & MEDVEDEV, A. 2009. Model-based slopping warning in the LD steel converter process. *Journal of Process Control,* 19**,** 1000-1010.

FRIEDLANDER, S. 1977. Smoke, dust and haze. Fundamentals of aerosol behaviour.

FRIEDLANDER, S. K. 2000. *Smoke, Dust and Haze: Fundamentals of Aerosol Behavoir*, Oxford University Press, Incorporated.

FRUEHAN, R. 1998. Overview of steelmaking processes and their development. *The Making, Shaping and Treating of Steel: Steelmaking and Refining volume***,** 2-3.

GERGELY, V. & CLYNE, T. W. 2004. Drainage in standing liquid metal foams: modelling and experimental observations. *Acta Materialia,* 52**,** 3047-3058.

GRASSIA, P., NEETHLING, S. J., CERVANTES, C. & LEE, H. T. 2006. The growth, drainage and bursting of foams. *Colloids and Surfaces A: Physicochemical and Engineering Aspects,* 274**,** 110-124.

GUO, D. C., GU, L. & IRONS, G. A. 2002. Developments in modelling of gas injection and slag foaming. *Applied Mathematical Modelling,* 26**,** 263-280.

GUTHRIE, R. I. L. 2009. A Review of Fluid Flows in Liquid Metal Processing and Casting Operations. *ISIJ International,* 49**,** 1453-1467.

HAGESAETHER, L., JAKOBSEN, H. A. & SVENDSEN, H. F. 2002. A model for turbulent binary breakup of dispersed fluid particles. *Chemical Engineering Science,* 57**,** 3251-3267.

HARA, S., IKUTA, M., KITAMURA, M. & OGINO, M. 1983. *Tetsu-to-Hagane,* 69**,** 1152-1159.

HARA, S. & OGINO, K. 1992. Slag-foaming phenomenon in pyrometallurgical processes. *ISIJ International,* 32**,** 81.

HIBIKI, T., TAKAMASA, T. & ISHII, M. 2001. Interfacial area transport of bubbly flow in a small diameter pipe. *Journal of Nuclear Science and Technology,* 38**,** 614-620.

HINZE, J. O. 1955. Fundamentals of the hydrodynamic mechanism of splitting in dispersion processes. *AIChE Journal,* 1**,** 289-295.

HUDA, N., NASER, J., BROOKS, G., REUTER, M. A. & MATUSEWICZ, R. W. 2012. Computational fluid dynamic modeling of zinc slag fuming process in top-submerged lance smelting furnace. *Metallurgical and Materials Transactions B: Process Metallurgy and Materials Processing Science,* 43**,** 39-55.

HUH, B. G., EUH, D. J., YOON, H. Y., YUN, B. J., SONG, C. H. & CHUNG, C. H. 2006. Mechanistic study for the interfacial area transport phenomena in an air/water flow condition by using fine-size bubble group model. *International Journal of Heat and Mass Transfer,* 49**,** 4033-4042.

HULBURT, H. M. & KATZ, S. 1964. Some problems in particle technology. A statistical mechanical formulation. *Chemical Engineering Science,* 19**,** 555-574.

HUNTER, T. N., PUGH, R. J., FRANKS, G. V. & JAMESON, G. J. 2008. The role of particles in stabilising foams and emulsions. *Advances in Colloid and Interface Science,* 137**,** 57-81.

IRELAND, P. M. 2009. Coalescence in a steady-state rising foam. *Chemical Engineering Science,* 64**,** 4866-4874.

ITO, K. & FRUEHAN, R. J. 1989. Study on the foaming of CaO-SiO2-FeO slags: Part I. Foaming parameters and experimental results. *Metallurgical Transactions B,* 20**,** 509-514.

IVESON, S. M. 2002. Limitations of one-dimensional population balance models of wet granulation processes. *Powder Technology,* 124**,** 219-229.

JIANG, R. & FRUEHAN, R. J. 1991. Slag foaming in bath smelting. *Metallurgical Transactions B,* 22**,** 481-489.

JING, L. & XU, X. 2010. Direct Numerical Simulation of Secondary Breakup of Liquid Drops. *Chinese Journal of Aeronautics,* 23**,** 153-161.

JONES, W. P. & LAUNDER, B. E. 1972. The prediction of laminarization with a two-equation model of turbulence. *International Journal of Heat and Mass Transfer,* 15**,** 301-314.

KALKACH-NAVARRO, S., LAHEY JR, R. T. & DREW, D. A. 1994. Analysis of the bubbly/slug flow regime transition. *Nuclear Engineering and Design,* 151**,** 15-39.

KAM, S. I. 2008. Improved mechanistic foam simulation with foam catastrophe theory. *Colloids and Surfaces A: Physicochemical and Engineering Aspects,* 318**,** 62-77.

KAPILASHRAMI, A., GÖRNERUP, M., SEETHARAMAN, S. & LAHIRI, A. K. 2006. Foaming of slags under dynamic conditions. *Metallurgical and Materials Transactions B,* 37**,** 109-117.

KIM, H. S., MIN, D. J. & PARK, J. H. 2001a. Foaming Behavior of CaO-SiO2-FeO-MgOsatd-X (X=Al2O3,MnO, P2O5, and CaF2) Slags at High Temperatures. *ISIJ Int (Iron Steel Inst Jpn),* 41**,** 317-324.

KIM, H. S., MIN, D. J. & PARK, J. H. 2001b. Foaming Behavior of CaO-SiO2-FeO-MgOsatd-X (X=Al2O3,MnO, P2O5, and CaF2) Slags at High Temperatures. *Iron and steel Institute of Japan International,* 41**,** 317-324.

KITCHENER, J. A. & COOPER, C. F. 1959. Current concepts in the theory of foaming. *Quarterly Reviews, Chemical Society,* 13**,** 71-97.

KOCAMUSTAFAOGULLARI, G. & ISHII, M. 1995. Foundation of the interfacial area transport equation and its closure relations. *International Journal of Heat and Mass Transfer,* 38**,** 481-493.

KOLMOGOROV, A. N. 1949. On the breakage of drops in a turbulent flow. *Doklady Akademii Nauk SSSR,* 66**,** 825–828.

KOMASAWA, I., OTAKE, T. & KAMOJIMA, M. 1980. WAKE BEHAVIOR AND ITS EFFECT ON INTERACTION BETWEEN SPHERICAL-CAP BUBBLES. *Journal of Chemical Engineering of Japan,* 13**,** 103-109.

KOSTOGLOU, M. & KONSTANDOPOULOS, A. G. 2001. Evolution of aggregate size and fractal dimension during Brownian coagulation. *Journal of Aerosol Science,* 32**,** 1399-1420.

KOZAKEVITCH , P. 1969. Foams and emulsions in steelmaking. *Journal of metals***,** 57-68.

KRAYNIK, A. M. & REINELT, D. A. 1996. Linear Elastic Behavior of Dry Soap Foams. *Journal of Colloid and Interface Science,* 181**,** 511-520.

KUMAR, J. 2006. *Numerical Approximations of Population Balance Equations in Particulate Systems*, docupoint-Verlag.

KUMAR, S. & RAMKRISHNA, D. 1996a. On the solution of population balance equations by discretization - I. A fixed pivot technique. *Chemical Engineering Science,* 51**,** 1311-1332.

KUMAR, S. & RAMKRISHNA, D. 1996b. On the solution of population balance equations by discretization - II. A moving pivot technique. *Chemical Engineering Science,* 51**,** 1333-1342.

LAARI, A. & TURUNEN, I. 2005. Prediction of coalescence properties of gas bubbles in a gas-liquid reactor using persistence time measurements. *Chemical Engineering Research & Design,* 83**,** 881-886.

LAARI, A. & TURUNEN, K. 2003. Experimental determination of bubble coalescence and break-up rates in a bubble column reactor. *Canadian Journal of Chemical Engineering,* 81**,** 395-401.

LAHIRI, A. K. & SEETHARAMAN, S. 2002. Foaming behavior of slags. *Metallurgical and Materials Transactions B,* 33**,** 499-502.

LAMB, H. 1932. *Hydrodynamics,* Cambridge, Cambridge University Press.

LAPIN, A. & LÜBBERT, A. 1994. Numerical simulation of the dynamics of two-phase gas-liquid flows in bubble columns. *Chemical Engineering Science,* 49**,** 3661-3674.

LAURIER, L. S. & FRED, W. 1994. Foams: Basic Principles. *Foams: Fundamentals and Applications in the Petroleum Industry.* American Chemical Society.

LEE, C.-H., ERICKSON, L. E. & GLASGOW, L. A. 1987. BUBBLE BREAKUP AND COALESCENCE IN TURBULENT GAS-LIQUID DISPERSIONS. *Chemical Engineering Communications,* 59**,** 65-84.

LEHR, F., MILLIES, M. & MEWES, D. 2002. Bubble-size distributions and flow fields in bubble columns. *Aiche Journal,* 48**,** 2426-2443.

LEONARD, R. A. & LEMLICH, R. 1965. A study of interstitial liquid flow in foam. Part I. Theoretical model and application to foam fractionation. *AIChE Journal,* 11**,** 18-25.

LEVICH, V. G. 1962. *Physicochemical hydrodynamics,* Englewood Cliffs, N.J., Prentice-Hall.

LI, J. & RENARDY, Y. Y. 2000. Shear-induced rupturing of a viscous drop in a Bingham liquid. *Journal of Non-Newtonian Fluid Mechanics,* 95**,** 235-251.

LIAO, Y. & LUCAS, D. 2009. A literature review of theoretical models for drop and bubble breakup in turbulent dispersions. *Chemical Engineering Science,* 64**,** 3389-3406.

LIAO, Y. & LUCAS, D. 2010. A literature review on mechanisms and models for the coalescence process of fluid particles. *Chemical Engineering Science,* 65**,** 2851-2864.

LIN, B. & SUNDARARAJ, U. 2004. Sheet formation during drop deformation and breakup in polyethylene/polycarbonate systems sheared between parallel plates. *Polymer,* 45**,** 7605-7613.

LIN, Y., LEE, K. & MATSOUKAS, T. 2002. Solution of the population balance equation using constant-number Monte Carlo. *Chemical Engineering Science,* 57**,** 2241-2252.

LIN, Z. & GUTHRIE, R. I. L. 1995. Model for slag foaming for the in-bath smelting process. *Iron and Steelmaker (I and SM),* 22**,** 67-73.

LO, S. 1996. Application of MUSIG model to bubbly flows. *AEA Technology*.

LÖHNER, P. R. 2008. *Applied Computational Fluid Dynamics Techniques: An Introduction Based on Finite Element Methods*, Wiley.

LUO, H. & SVENDSEN, H. F. 1996. Theoretical model for drop and bubble breakup in turbulent dispersions. *AIChE Journal,* 42**,** 1225-1233.

MARTÍN-VALDEPEÑAS, J. M., JIMÉNEZ, M. A., BARBERO, R. & MARTÍN-FUERTES, F. 2007. A CFD comparative study of bubble break-up models in a turbulent multiphase jet. *Heat and Mass Transfer,* 43**,** 787-799.

MARTÍN, M., MONTES, F. J. & GALÁN, M. A. 2007. Bubble coalescence at sieve plates: II. Effect of coalescence on mass transfer. Superficial area versus bubble oscillations. *Chemical Engineering Science,* 62**,** 1741-1752.

MARTÍNEZ-BAZÁN, C., MONTAÑÉS, J. L. & LASHERAS, J. C. 1999a. On the breakup of an air bubble injected into a fully developed turbulent flow. Part 1. Breakup frequency. *Journal of Fluid Mechanics,* 401**,** 157-182.

MARTÍNEZ-BAZÁN, C., MONTAÑÉS, J. L. & LASHERAS, J. C. 1999b. On the breakup of an air bubble injected into a fully developed turbulent flow. Part 2. Size PDF of the resulting daughter bubbles. *Journal of Fluid Mechanics,* 401**,** 183-207.

MATSUURA, H. & FRUEHAN, R. J. 2009. Slag Foaming in an Electric Arc Furnace. *ISIJ International,* 49**,** 1530-1535.

MATSUURA, H., MANNING, C. P., FORTES, R. A. F. O. & FRUEHAN, R. J. 2008. Development of a Decarburization and Slag Formation Model for the Electric Arc Furnace. *ISIJ International,* 48**,** 1197-1205.

MILLER, T., JIMENEZ, J., SHARAN, A. & GOLDSTEIN, D. 1998. Oxygen Steelmaking Processes. *The Making Shaping and Treating of Steel,* 11**,** 475-524.

MILLMAN, M. S., OVERBOSCH, A., KAPILASHRAMI, A., MALMBERG, D. & BRÄMMING, M. 2011. Study of refining performance in BOS converter. *Ironmaking & Steelmaking,* 38**,** 499-509.

MILLMAN, M. S. K., A. BRAMMING, M. MALMBERG, D. 2011. Imphos: improving phosphorus refining. Luxembourg: Publications Office of the European Union, 2011.

MOHANARANGAM, K., CHEUNG, S. C. P., TU, J. Y. & CHEN, L. 2009. Numerical simulation of micro-bubble drag reduction using population balance model. *Ocean Engineering,* 36**,** 863-872.

MONTANTE, G., HORN, D. & PAGLIANTI, A. 2008. Gas-liquid flow and bubble size distribution in stirred tanks. *Chemical Engineering Science,* 63**,** 2107-2118.

MORALES, R. D., RUB, EACUTE, N, L. G., OACUTE, PEZ, F., CAMACHO, J. & ROMERO, J. A. 1995. The Slag Foaming Practice in EAF and Its Influence on the Steelmaking Shop Productivity. *ISIJ International,* 35**,** 1054-1062.

MÜLLER-FISCHER, N., TOBLER, P., DRESSLER, M., FISCHER, P. & WINDHAB, E. J. 2008. Single bubble deformation and breakup in simple shear flow. *Experiments in Fluids,* 45**,** 917-926.

NARSIMHAN, G. 2010. Analysis of creaming and formation of foam layer in aerated liquid. *Journal of Colloid and Interface Science,* 345**,** 566-572.

NARSIMHAN, G., GUPTA, J. P. & RAMKRISHNA, D. 1979. A model for transitional breakage probability of droplets in agitated lean liquid-liquid dispersions. *Chemical Engineering Science,* 34**,** 257-265.

NEETHLING, S. J., LEE, H. T. & GRASSIA, P. 2005. The growth, drainage and breakdown of foams. *Colloids and Surfaces A: Physicochemical and Engineering Aspects,* 263**,** 184-196.

NEXHIP, C., SUN, S. & JAHANSHAHI, S. 2004. Physicochemical properties of foaming slags. *International Materials Reviews,* 49**,** 286-298.

ODENTHAL, H.-J., FALKENRECK, U. & SCHLUTER, J. CFD simulation of multiphase melt flows in steelmaking converters. European Conference on Computational Fluid Dynamics, 2006. 121-142.

OLMOS, E., GENTRIC, C., VIAL, C., WILD, G. & MIDOUX, N. 2001. Numerical simulation of multiphase flow in bubble column reactors. Influence of bubble coalescence and break-up. *Chemical Engineering Science,* 56**,** 6359-6365.

OZTURK, B. & FRUEHAN, R. J. 1995. Effect of temperature on slag foaming. *Metallurgical and Materials Transactions B,* 26**,** 1086-1088.

PANJKOVIC, V., TRUELOVE, J. & OSTROVSKI, O. 2002. Analysis of performance of an iron-bath reactor using computational fluid dynamics. *Applied Mathematical Modelling,* 26**,** 203-221.

PAWLAT, J., HAYASHI, N., IHARA, S., SATOH, S., YAMABE, C. & POLLO, I. 2004. Foaming column with a dielectric covered plate-to-metal plate electrode as an oxidants' generator. *Advances in Environmental Research,* 8**,** 351-358.

PILON, L. & VISKANTA, R. 2004. Minimum superficial gas velocity for onset of foaming. *Chemical Engineering and Processing: Process Intensification,* 43**,** 149-160.

PRINCE, M. J. & BLANCH, H. W. 1990. BUBBLE COALESCENCE AND BREAK-UP IN AIR-SPARGED BUBBLE-COLUMNS. *Aiche Journal,* 36**,** 1485-1499.

PUGH, R. J. 1996. Foaming, foam films, antifoaming and defoaming. *Advances in Colloid and Interface Science,* 64**,** 67-142.

QIAN, D., MCLAUGHLIN, J. B., SANKARANARAYANAN, K., SUNDARESAN, S. & KONTOMARIS, K. 2006. Simulation of bubble breakup dynamics in homogeneous turbulance. *Chemical Engineering Communications,* 193**,** 1038-1063.

RAMACHANDRAN, R. & BARTON, P. I. 2010. Effective parameter estimation within a multi-dimensional population balance model framework. *Chemical Engineering Science,* 65**,** 4884-4893.

RAMKRISHNA, D. 2000. *Population Balances: Theory and Applications to Particulate Systems in Engineering*, Elsevier Science.

RANDOLPH, A. D. & LARSON, M. A. 1988. *Theory of particulate processes: analysis and techniques of continuous crystallization*, Academic Press.

RANZ, W. & MARSHALL, W. 1952. Evaporation from drops. *Chem. Eng. Prog,* 48**,** 141-146.

RENARDY, Y. Y. & CRISTINI, V. 2001. Effect of inertia on drop breakup under shear. *Physics of Fluids,* 13**,** 7-13.

RIGOPOULOS, S. 2010. Population balance modelling of polydispersed particles in reactive flows. *Progress in Energy and Combustion Science,* 36**,** 412-443.

ROTH, R. E., JIANG, R. & FRUEHAN, R. J. 1993. Foaming of ladle and BOS-Mn smelting slags. *Transactions of the Iron and Steel Society of AIME,* 14**,** 95-103.

SATTAR, M. A., NASER, J. & BROOKS, G. 2013. Numerical simulation of creaming and foam formation in aerated liquid with population balance modeling. *Chemical Engineering Science,* 94**,** 69-78.

SCHICK, C. 2004. *Mathematical Analysis of Foam Films*, Shaker Verlag GmbH.

SCHLICHTING, H. 1979. Boundary layer theory: Seventh edition.

SEVIK, M. & PARK, S. H. 1972. SPLITTING OF DROPS AND BUBBLES BY TURBULENT FLUID FLOW. *ASME Pap*.

SHA, Z. L., LAARI, A. & TURUNEN, I. 2006. Multi-phase-multi-size-group model for the inclusion of population balances into the CFD simulation of gas-liquid bubbly flows. *Chemical Engineering & Technology,* 29**,** 550-559.

SHINNAR, R. 1961. On the behaviour of liquid dispersions in mixing vessels. *Journal of Fluid Mechanics,* 10**,** 259–275.

SHINNAR, R. & CHURCH, J. M. 1960. Statistical Theories of Turbulence in Predicting Particle Size in Agitated Dispersions. *Industrial & Engineering Chemistry,* 52**,** 253-256.

SMITH, T. R., SCHLEGEL, J. P., HIBIKI, T. & ISHII, M. 2012. Mechanistic modeling of interfacial area transport in large diameter pipes. *International Journal of Multiphase Flow,* 47**,** 1-16.

SOKOLICHIN, A., EIGENBERGER, G., LAPIN, A. & LÜBBERT, A. 1997. Dynamic numerical simulation of gas-liquid two-phase flows: Euler/Euler versus Euler/Lagrange. *Chemical Engineering Science,* 52**,** 611-626.

STADLER, S. A. C., EKSTEEN, J. J. & ALDRICH, C. 2007. An experimental investigation of foaming in acidic, high FexO slags. *Minerals Engineering,* 20**,** 1121-1128.

STEWART, C. W. 1995. Bubble interaction in low-viscosity liquids. *International Journal of Multiphase Flow,* 21**,** 1037-1046.

STROOMER-KATTENBELT, C. 2008. *Modeling and optimization of slopping prevention and batch time reduction in basic oxygen steelmaking.* PhD, University twente.

SWISHER , J. H. & MCCABE, C. L. 1964. *Trans. TMS-AIME,* 230**,** 1665-1675.

TAVLARIDES, L. L. & STAMATOUDIS, M. 1981. The Analysis of Interphase Reactions and Mass Transfer in Liquid-Liquid Dispersions. *In:* THOMAS B. DREW, G. R. C. J. W. H. & THEODORE, V. (eds.) *Advances in Chemical Engineering.* Academic Press.

TAYLOR, G. I. 1934. The formation of emulsions in definable fields of flow. *Procedings of the Royal Society. A* 146**,** 500-523.

TONG, M., COLE, K. & NEETHLING, S. J. 2011. Drainage and stability of 2D foams: Foam behaviour in vertical Hele-Shaw cells. *Colloids and Surfaces A: Physicochemical and Engineering Aspects,* 382**,** 42-49.

TSOURIS, C. & TAVLARIDES, L. L. 1994. Breakage and coalescence models for drops in turbulent dispersions. *AIChE Journal,* 40**,** 395-406.

VARDAR-SUKAN, F. 1998. Foaming: Consequences, prevention and destruction. *Biotechnology Advances,* 16**,** 913-948.

VERBIST, G., WEAIRE, D. & KRAYNIK, A. M. 1996. The foam drainage equation. *J. Phys.: Condens. Matter,* 8**,** 3715–3731.

VERKOEIJEN, D., A. POUW, G., M. H. MEESTERS, G. & SCARLETT, B. 2002. Population balances for particulate processes - A volume approach. *Chemical Engineering Science,* 57**,** 2287-2303.

VERSTEEG, H. H. K. & MALALASEKERA, W. 2007. *An Introduction to Computational Fluid Dynamics: The Finite Volume Method*, Pearson Education Limited.

VYAKARANAM, K. V. & KOKINI, J. L. 2012. Prediction of air bubble dispersion in a viscous fluid in a twin-screw continuous mixer using FEM simulations of dispersive mixing. *Chemical Engineering Science,* 84**,** 303-314.

WALLIS, G. B. 1969. *One-dimensional Two-phase Flow,* New York McGraw-Hill.

WALTER, J. F. & BLANCH, H. W. 1986. Bubble break-up in gas-liquid bioreactors: Break-up in turbulent flows. *The Chemical Engineering Journal,* 32**,** B7-B17.

WANG, T., WANG, J. & JIN, Y. 2003a. A novel theoretical breakup kernel function for bubbles/droplets in a turbulent flow. *Chemical Engineering Science,* 58**,** 4629-4637.

WANG, T., WANG, J. & JIN, Y. 2005. Theoretical prediction of flow regime transition in bubble columns by the population balance model. *Chemical Engineering Science,* 60**,** 6199-6209.

WANG, T. F., WANG, J. F. & JIN, Y. 2003b. A novel theoretical breakup kernel function for bubbles/droplets in a turbulent flow. *Chemical Engineering Science,* 58**,** 4629-4637.

WEAIRE, D. & PHELAN, R. 1994. A counter-example to Kelvin's conjecture on minimal surfaces. *Philosophical Magazine Letters,* 69**,** 107-110.

WEAIRE, D., VAZ, M., TEIXEIRA, P. & FORTES, M. 2007. Instabilities in liquid foams. *Soft Matter,* 3**,** 47-57.

WEAIRE, D. L. & HUTZLER, S. 1999. *The Physics of Foams*, Clarendon Press/Oxford University Press.

WU, Q., KIM, S., ISHII, M. & BEUS, S. G. 1998. One-group interfacial area transport in vertical bubbly flow. *International Journal of Heat and Mass Transfer,* 41**,** 1103-1112.

ZHANG, Y. & FRUEHAN, R. J. 1995. Effect of the bubble size and chemical reactions on slag foaming. *Metallurgical and Materials Transactions B,* 26**,** 803-812.

ZHAO, C. Y., LU, T. J. & HODSON, H. P. 2004. Thermal radiation in ultralight metal foams with open cells. *International Journal of Heat and Mass Transfer,* 47**,** 2927-2939.

ZHAO, H. & GE, W. 2007. A theoretical bubble breakup model for slurry beds or three-phase fluidized beds under high pressure. *Chemical Engineering Science,* 62**,** 109-115.

Appendix A

Table A.1 Bubble class measured in the Y-Z plane (cross section) from the CFD simulation at different height at superficial gas velocity of 0.01m/s.

Height 0										
Time (s)	BC1	BC2	BC3	BC4	BC5	BC6	BC7	BC8	BC9	BC10
500	0.331	0.173	0.131	0.108	0.092	0.077	0.068	0.074	0.223	0.066
510	0.331	0.173	0.131	0.108	0.092	0.077	0.068	0.074	0.223	0.066
520	0.331	0.173	0.131	0.108	0.092	0.077	0.068	0.074	0.223	0.066
530	0.331	0.173	0.131	0.108	0.092	0.077	0.068	0.074	0.223	0.066
540	0.331	0.173	0.131	0.108	0.092	0.077	0.068	0.074	0.223	0.066
550	0.331	0.173	0.131	0.108	0.092	0.077	0.068	0.074	0.223	0.066
560	0.331	0.173	0.131	0.108	0.092	0.077	0.068	0.074	0.223	0.066
570	0.331	0.173	0.131	0.108	0.092	0.077	0.068	0.074	0.223	0.066
580	0.331	0.173	0.131	0.108	0.092	0.077	0.068	0.074	0.223	0.066
590	0.331	0.173	0.131	0.108	0.092	0.077	0.068	0.074	0.223	0.066
600	0.331	0.173	0.131	0.108	0.092	0.077	0.068	0.074	0.223	0.066
Height 0.35										
500	0.000	0.000	0.180	0.161	0.180	0.161	0.140	0.118	0.088	0.038
510	0.000	0.000	0.179	0.157	0.177	0.161	0.142	0.121	0.092	0.040
520	0.000	0.000	0.178	0.153	0.173	0.160	0.144	0.125	0.097	0.042
530	0.000	0.000	0.176	0.148	0.169	0.160	0.145	0.129	0.101	0.044
540	0.000	0.000	0.174	0.144	0.164	0.160	0.147	0.133	0.107	0.047
550	0.000	0.000	0.170	0.140	0.160	0.160	0.149	0.137	0.112	0.049
560	0.000	0.000	0.166	0.135	0.155	0.159	0.151	0.142	0.117	0.052
570	0.000	0.000	0.162	0.131	0.151	0.159	0.153	0.146	0.124	0.055
580	0.000	0.000	0.158	0.126	0.146	0.158	0.156	0.151	0.131	0.058
590	0.000	0.000	0.152	0.122	0.142	0.157	0.159	0.156	0.137	0.062
600	0.000	0.000	0.145	0.118	0.138	0.155	0.162	0.162	0.144	0.065
Height 0.9										
500	0.000	0.000	0.032	0.070	0.409	0.187	0.137	0.101	0.069	0.028
510	0.000	0.000	0.032	0.070	0.408	0.187	0.137	0.102	0.069	0.028
520	0.000	0.000	0.032	0.070	0.407	0.187	0.138	0.103	0.070	0.029
530	0.000	0.000	0.033	0.070	0.406	0.187	0.138	0.103	0.071	0.029
540	0.000	0.000	0.033	0.070	0.405	0.188	0.139	0.104	0.071	0.029
550	0.000	0.000	0.033	0.070	0.404	0.188	0.139	0.105	0.072	0.029
560	0.000	0.000	0.033	0.071	0.403	0.188	0.139	0.105	0.072	0.030
570	0.000	0.000	0.033	0.071	0.403	0.188	0.140	0.105	0.073	0.030
580	0.000	0.000	0.033	0.071	0.402	0.188	0.140	0.106	0.073	0.030
590	0.000	0.000	0.033	0.071	0.402	0.188	0.141	0.106	0.073	0.030

600	0.000	0.000	0.033	0.072	0.401	0.189	0.141	0.107	0.074	0.030
Height 1.65										
500	0.000	0.000	0.030	0.063	0.414	0.184	0.132	0.098	0.066	0.027
510	0.000	0.000	0.030	0.063	0.412	0.184	0.133	0.099	0.067	0.027
520	0.000	0.000	0.030	0.063	0.412	0.184	0.133	0.099	0.067	0.027
530	0.000	0.000	0.030	0.063	0.411	0.184	0.133	0.099	0.068	0.028
540	0.000	0.000	0.030	0.063	0.410	0.184	0.134	0.100	0.068	0.028
550	0.000	0.000	0.030	0.063	0.410	0.184	0.134	0.100	0.068	0.028
560	0.000	0.000	0.030	0.063	0.410	0.184	0.134	0.100	0.069	0.028
570	0.000	0.000	0.030	0.063	0.410	0.184	0.134	0.101	0.069	0.028
580	0.000	0.000	0.030	0.063	0.410	0.184	0.134	0.101	0.069	0.028
590	0.000	0.000	0.030	0.063	0.410	0.184	0.134	0.101	0.069	0.028
600	0.000	0.000	0.030	0.064	0.410	0.184	0.135	0.101	0.069	0.028
Height 2.4										
500	0.000	0.000	0.030	0.063	0.413	0.184	0.132	0.098	0.066	0.027
510	0.000	0.000	0.030	0.063	0.412	0.184	0.133	0.099	0.067	0.027
520	0.000	0.000	0.030	0.063	0.411	0.184	0.133	0.099	0.067	0.027
530	0.000	0.000	0.030	0.063	0.410	0.184	0.133	0.099	0.068	0.028
540	0.000	0.000	0.030	0.063	0.410	0.184	0.133	0.100	0.068	0.028
550	0.000	0.000	0.030	0.063	0.409	0.184	0.134	0.100	0.068	0.028
560	0.000	0.000	0.030	0.063	0.409	0.184	0.134	0.100	0.068	0.028
570	0.000	0.000	0.030	0.063	0.409	0.184	0.134	0.100	0.069	0.028
580	0.000	0.000	0.033	0.063	0.409	0.184	0.134	0.100	0.069	0.028
590	0.000	0.000	0.030	0.063	0.408	0.184	0.134	0.100	0.069	0.028
600	0.000	0.000	0.030	0.063	0.408	0.184	0.134	0.101	0.069	0.028

Table A.2 Bubble class measured in the Y-Z plane (cross section) from the CFD simulation at different height at superficial gas velocity of 0.02m/s.

Height 0										
Time (s)	BC1	BC2	BC3	BC4	BC5	BC6	BC7	BC8	BC9	BC10
500	0.404	0.167	0.124	0.117	0.115	0.099	0.082	0.070	0.115	0.037
510	0.405	0.167	0.124	0.117	0.115	0.099	0.082	0.070	0.115	0.036
520	0.405	0.167	0.124	0.117	0.115	0.099	0.082	0.070	0.114	0.033
530	0.406	0.167	0.124	0.117	0.115	0.099	0.082	0.070	0.114	0.036
540	0.406	0.167	0.124	0.117	0.115	0.099	0.082	0.070	0.114	0.036
550	0.406	0.167	0.124	0.117	0.115	0.099	0.082	0.070	0.114	0.036
560	0.406	0.167	0.124	0.117	0.115	0.099	0.082	0.070	0.114	0.036
570	0.406	0.167	0.124	0.117	0.115	0.099	0.082	0.070	0.114	0.036
580	0.406	0.167	0.124	0.117	0.115	0.099	0.082	0.070	0.114	0.036
590	0.406	0.167	0.124	0.117	0.115	0.099	0.082	0.070	0.115	0.036

600	0.406	0.167	0.124	0.117	0.115	0.099	0.082	0.070	0.115	0.036
Height 0.35										
500	0.005	0.005	0.222	0.384	0.207	0.144	0.108	0.079	0.053	0.022
510	0.005	0.005	0.222	0.384	0.207	0.144	0.108	0.079	0.053	0.022
520	0.005	0.005	0.222	0.384	0.207	0.144	0.108	0.079	0.053	0.022
530	0.005	0.005	0.222	0.384	0.207	0.144	0.108	0.079	0.053	0.022
540	0.005	0.005	0.222	0.385	0.208	0.145	0.108	0.079	0.053	0.022
550	0.005	0.005	0.222	0.385	0.208	0.145	0.108	0.079	0.053	0.022
560	0.005	0.005	0.222	0.385	0.208	0.145	0.108	0.079	0.053	0.022
570	0.005	0.005	0.222	0.385	0.208	0.145	0.108	0.079	0.053	0.022
580	0.005	0.005	0.222	0.385	0.208	0.145	0.108	0.079	0.053	0.022
590	0.005	0.005	0.222	0.385	0.208	0.145	0.108	0.079	0.053	0.022
600	0.005	0.005	0.222	0.385	0.208	0.145	0.108	0.079	0.053	0.022
Height 0.9										
500	0.000	0.000	0.092	0.485	0.215	0.153	0.116	0.087	0.059	0.024
510	0.000	0.000	0.092	0.485	0.215	0.153	0.116	0.087	0.059	0.024
520	0.000	0.000	0.092	0.486	0.215	0.153	0.116	0.087	0.059	0.024
530	0.000	0.000	0.092	0.486	0.215	0.153	0.116	0.087	0.059	0.024
540	0.000	0.000	0.092	0.486	0.215	0.153	0.116	0.087	0.059	0.024
550	0.000	0.000	0.092	0.486	0.215	0.153	0.116	0.087	0.059	0.024
560	0.000	0.000	0.092	0.486	0.215	0.153	0.116	0.087	0.059	0.024
570	0.000	0.000	0.092	0.486	0.215	0.153	0.116	0.087	0.059	0.024
580	0.000	0.000	0.092	0.487	0.215	0.153	0.116	0.087	0.059	0.024
590	0.000	0.000	0.092	0.487	0.215	0.153	0.116	0.087	0.059	0.024
600	0.000	0.000	0.092	0.487	0.215	0.153	0.116	0.087	0.059	0.024
Height 1.65										
500	0.000	0.000	0.086	0.486	0.215	0.155	0.119	0.090	0.062	0.025
510	0.000	0.000	0.086	0.487	0.215	0.155	0.119	0.090	0.062	0.025
520	0.000	0.000	0.086	0.487	0.215	0.155	0.119	0.090	0.062	0.025
530	0.000	0.000	0.086	0.487	0.216	0.155	0.119	0.090	0.062	0.025
540	0.000	0.000	0.086	0.488	0.216	0.155	0.119	0.089	0.061	0.025
550	0.000	0.000	0.086	0.488	0.216	0.155	0.119	0.089	0.061	0.025
560	0.000	0.000	0.086	0.488	0.216	0.155	0.119	0.089	0.061	0.025
570	0.000	0.000	0.086	0.489	0.216	0.155	0.119	0.089	0.061	0.025
580	0.000	0.000	0.086	0.489	0.216	0.155	0.119	0.089	0.061	0.025
590	0.000	0.000	0.086	0.489	0.216	0.155	0.118	0.089	0.061	0.025
600	0.000	0.000	0.086	0.489	0.216	0.155	0.118	0.089	0.061	0.025
Height 2.4										
500	0.000	0.000	0.087	0.485	0.217	0.158	0.123	0.094	0.065	0.027
510	0.000	0.000	0.087	0.486	0.217	0.158	0.122	0.093	0.065	0.027
520	0.000	0.000	0.087	0.487	0.217	0.158	0.122	0.093	0.064	0.026
530	0.000	0.000	0.087	0.488	0.218	0.158	0.122	0.092	0.064	0.026
540	0.000	0.000	0.087	0.488	0.218	0.158	0.122	0.092	0.064	0.026

550	0.000	0.000	0.087	0.489	0.218	0.158	0.121	0.092	0.063	0.026
560	0.000	0.000	0.087	0.490	0.218	0.158	0.121	0.092	0.063	0.026
570	0.000	0.000	0.087	0.490	0.218	0.158	0.121	0.091	0.063	0.026
580	0.000	0.000	0.087	0.491	0.218	0.157	0.121	0.091	0.063	0.026
590	0.000	0.000	0.087	0.491	0.218	0.157	0.121	0.091	0.063	0.026
600	0.000	0.000	0.087	0.491	0.218	0.157	0.121	0.091	0.063	0.026

Table A.3 Bubble class volume fraction measured in the Y-Z plane (cross section) from the CFD simulation at different height at superficial gas velocity of 0.06m/s.

Height 0										
Bubble class	1	2	3	4	5	6	7	8	9	10
Time (s)										
500	0.489	0.103	0.347	0.190	0.118	0.081	0.052	0.032	0.020	0.008
510	0.496	0.116	0.343	0.188	0.117	0.080	0.052	0.032	0.019	0.008
520	0.500	0.116	0.340	0.186	0.116	0.078	0.051	0.031	0.019	0.008
530	0.496	0.117	0.344	0.189	0.117	0.080	0.052	0.032	0.019	0.008
540	0.498	0.118	0.340	0.187	0.117	0.079	0.052	0.031	0.019	0.008
550	0.492	0.114	0.344	0.188	0.117	0.080	0.052	0.032	0.019	0.008
560	0.491	0.114	0.347	0.190	0.119	0.081	0.052	0.032	0.020	0.008
570	0.499	0.117	0.340	0.186	0.116	0.079	0.052	0.031	0.019	0.008
580	0.496	0.116	0.344	0.188	0.118	0.080	0.052	0.032	0.020	0.008
590	0.498	0.107	0.343	0.189	0.118	0.080	0.052	0.032	0.019	0.008
600	0.497	0.116	0.342	0.187	0.117	0.079	0.052	0.032	0.019	0.008
Height 0.35										
500	0.016	0.010	0.634	0.217	0.135	0.097	0.072	0.052	0.035	0.014
510	0.016	0.010	0.634	0.218	0.135	0.097	0.072	0.052	0.035	0.014
520	0.016	0.010	0.635	0.218	0.135	0.097	0.072	0.052	0.035	0.014
530	0.016	0.010	0.635	0.218	0.135	0.097	0.072	0.052	0.035	0.014
540	0.016	0.010	0.635	0.218	0.135	0.097	0.072	0.052	0.035	0.014
550	0.016	0.010	0.636	0.218	0.135	0.097	0.072	0.052	0.035	0.014
560	0.016	0.009	0.636	0.218	0.135	0.097	0.072	0.052	0.035	0.014
570	0.016	0.010	0.636	0.218	0.135	0.097	0.072	0.052	0.035	0.014
580	0.016	0.010	0.627	0.218	0.135	0.097	0.072	0.052	0.035	0.014
590	0.016	0.010	0.637	0.218	0.136	0.975	0.072	0.053	0.035	0.014
600	0.016	0.010	0.637	0.219	0.136	0.098	0.072	0.053	0.035	0.014
Height 1.65										
500	0.000	0.000	0.605	0.198	0.120	0.088	0.068	0.052	0.036	0.015
510	0.000	0.000	0.606	0.199	0.121	0.088	0.068	0.052	0.036	0.015

520	0.000	0.000	0.606	0.199	0.121	0.088	0.068	0.052	0.036	0.015
530	0.000	0.000	0.607	0.199	0.121	0.088	0.068	0.052	0.036	0.015
540	0.000	0.000	0.607	0.199	0.121	0.088	0.068	0.052	0.036	0.015
550	0.000	0.000	0.608	0.199	0.121	0.088	0.068	0.052	0.036	0.015
560	0.000	0.000	0.608	0.199	0.121	0.088	0.068	0.052	0.036	0.015
570	0.000	0.000	0.609	0.199	0.121	0.088	0.068	0.052	0.036	0.015
580	0.000	0.000	0.609	0.200	0.121	0.088	0.068	0.052	0.036	0.015
590	0.000	0.000	0.610	0.200	0.121	0.088	0.068	0.052	0.036	0.015
600	0.000	0.000	0.611	0.200	0.121	0.088	0.068	0.052	0.036	0.015
Height 0.9										
500	0.000	0.000	0.629	0.206	0.125	0.090	0.069	0.052	0.035	0.014
510	0.000	0.000	0.639	0.206	0.125	0.091	0.069	0.052	0.035	0.014
520	0.000	0.000	0.639	0.206	0.125	0.091	0.069	0.052	0.035	0.014
530	0.000	0.000	0.630	0.206	0.125	0.091	0.069	0.519	0.036	0.014
540	0.000	0.000	0.631	0.206	0.125	0.091	0.069	0.052	0.036	0.015
550	0.000	0.000	0.632	0.207	0.125	0.091	0.069	0.052	0.036	0.015
560	0.000	0.000	0.632	0.207	0.125	0.091	0.069	0.052	0.036	0.015
570	0.000	0.000	0.632	0.207	0.125	0.091	0.070	0.052	0.036	0.015
580	0.000	0.000	0.633	0.207	0.125	0.091	0.070	0.052	0.036	0.015
590	0.000	0.000	0.633	0.207	0.125	0.091	0.070	0.052	0.036	0.015
600	0.000	0.000	0.634	0.207	0.126	0.091	0.070	0.052	0.036	0.015
Height 2.4										
500	0.000	0.000	0.587	0.196	0.122	0.092	0.073	0.056	0.040	0.016
510	0.000	0.000	0.588	0.196	0.122	0.091	0.072	0.562	0.039	0.016
520	0.000	0.000	0.589	0.196	0.122	0.091	0.072	0.056	0.039	0.016
530	0.000	0.000	0.590	0.196	0.121	0.091	0.072	0.056	0.039	0.016
540	0.000	0.000	0.591	0.197	0.121	0.091	0.072	0.056	0.039	0.016
550	0.000	0.000	0.592	0.197	0.121	0.091	0.072	0.055	0.039	0.016
560	0.000	0.000	0.593	0.197	0.121	0.091	0.071	0.055	0.039	0.016
570	0.000	0.000	0.593	0.197	0.121	0.090	0.071	0.055	0.038	0.016
580	0.000	0.000	0.594	0.197	0.121	0.090	0.071	0.055	0.038	0.016
590	0.000	0.000	0.595	0.197	0.121	0.090	0.071	0.055	0.038	0.016
600	0.000	0.000	0.596	0.197	0.121	0.090	0.707	0.054	0.038	0.016

Table A.4 Bubble class volume fraction measured in gas and liquid phase at different time when gas fraction was 0.2.

Gas							
Time / Bubble class	180	330	480	510	540	570	600
1	0.548	0.973	0.703	0.706	0.709	0.740	0.799
2	0.251	0.029	0.257	0.248	0.246	0.230	0.192
3	0.131	0.005	0.075	0.072	0.071	0.061	0.043
4	0.069	0.001	0.014	0.015	0.015	0.012	0.008
5	0.031	0.000	0.002	0.002	0.002	0.002	0.001
6	0.010	0.000	0.000	0.000	0.000	0.000	0.000
7	0.002	0.000	0.000	0.000	0.000	0.000	0.000
8	0.000	0.000	0.000	0.000	0.000	0.000	0.000
9	0.000	0.000	0.000	0.000	0.000	0.000	0.000
10	0.000	0.000	0.000	0.000	0.000	0.000	0.000
Foam							
1	0.004	0.134	0.146	0.169	0.187	0.201	0.211
2	0.011	0.087	0.087	0.086	0.086	0.086	0.086
3	0.018	0.086	0.086	0.085	0.084	0.084	0.084
4	0.025	0.085	0.085	0.084	0.083	0.083	0.083
5	0.031	0.085	0.085	0.084	0.083	0.083	0.083
6	0.036	0.085	0.084	0.083	0.083	0.082	0.082
7	0.040	0.084	0.084	0.083	0.082	0.082	0.082
8	0.044	0.085	0.084	0.083	0.083	0.083	0.083
9	0.047	0.087	0.087	0.086	0.085	0.085	0.085
10	0.041	0.097	0.099	0.098	0.098	0.098	0.098

Table A.5 Bubble class volume fraction measured in gas and liquid phase at different time when gas fraction was 0.4.

			Gas				
Time / Bubble class	180	330	480	510	540	570	600
1	0.000	0.057	0.087	0.014	0.149	0.194	0.258
2	0.548	0.973	0.703	0.706	0.709	0.740	0.799
3	0.251	0.029	0.257	0.248	0.246	0.230	0.192
4	0.131	0.005	0.075	0.072	0.071	0.061	0.043
5	0.069	0.001	0.014	0.015	0.015	0.012	0.008
6	0.031	0.000	0.002	0.002	0.002	0.002	0.001
7	0.010	0.000	0.000	0.000	0.000	0.000	0.000
8	0.002	0.000	0.000	0.000	0.000	0.000	0.000
9	0.000	0.000	0.000	0.000	0.000	0.000	0.000
10	0.000	0.000	0.000	0.000	0.000	0.000	0.000
			Foam				
1	0.004	0.134	0.146	0.169	0.187	0.201	0.211
2	0.011	0.087	0.087	0.086	0.086	0.086	0.086
3	0.018	0.086	0.086	0.085	0.084	0.084	0.084
4	0.025	0.085	0.085	0.084	0.083	0.083	0.083
5	0.031	0.085	0.085	0.084	0.083	0.083	0.083
6	0.036	0.085	0.084	0.083	0.083	0.082	0.082
7	0.040	0.084	0.084	0.829	0.082	0.082	0.082
8	0.044	0.085	0.084	0.083	0.083	0.083	0.083
9	0.047	0.087	0.087	0.086	0.085	0.085	0.085
10	0.409	0.097	0.099	0.098	0.098	0.098	0.098

Table A.6 Foam height at different time with iron content 3%.

Velocity	1			2			3		
	Height 1	Height 2	Height 3	Height 1	Height 2	Height 3	Height 1	Height 2	Height 3
Time									
250	1.8	1.8	2.05	2.25	2	2.29	2.7	2.699	2.58
260	1.57	1.57	1.94	2.25	2	2.29	2.7	2.699	2.58
270	1.57	1.79	1.91	2.25	2.036	2.14	2.7	2.699	2.58
280	1.57	1.57	1.91	2.25	2.024	2.1	2.7	2.699	2.58
290	1.8	1.79	1.91	2.25	2.024	2.1	2.699	2.699	2.589
300	1.8	1.79	1.801	2.25	2.024	2.1	2.699	2.7	2.58

Table A.7 Foam height at different time with different iron content.

	%FeO=3			%FeO=7.5			%FeO=15		
	Height 1	Height 2	Height 3	Height 1	Height 2	Height 3	Height 1	Height 2	Height 3
Time (s)									
250	2.25	2	2.29	1.8	1.57	1.8	1.575	1.574	2.026
260	2.25	2	2.29	1.8	1.79	1.8	1.35	1.34	1.57
270	2.25	2.036	2.14	1.8	2.24	2.13	1.57	1.57	1.68
280	2.25	2.024	2.1	2.25	2.03	2.026	1.35	1.57	1.68
290	2.25	2.024	2.1	2.025	2.024	2.026	1.35	1.34	1.91
300	2.25	2.024	2.1	2.025	2.024	1.91	1.57	1.34	1.68

Table A.8 Bubble fraction at 250s in foam with different iron content.

Bubble class	Bubble volume fraction		
	%FeO=3	%FeO=7.5	%FeO=15
1	0.089	0.379	0.368
2	0.079	0.099	0.043
3	0.610	0.033	0.024
4	0.099	0.091	0.003
5	0.039	0.039	0.035
6	0.040	0.035	0.047
7	0.040	0.047	0.035
8	0.040	0.035	0.039
9	0.040	0.049	0.039
10	0.040	0.049	0.440

Table A.9 Bubble fraction at height of 0.28m with time.

Bubble class	Bubble fraction at 120	Bubble fraction at 240	Bubble fraction at 360	Bubble fraction at 480	Bubble fraction at 600
1	0.6905	0.6	0.629	0.5609	0.5057
2	0.01569	0.031008	0.02065	0.0201	0.0256
3	0.01145	0.02777	0.01672	0.01695	0.02237
4	0.01008	0.02612	0.01478	0.01523	0.02067
5	0.00892	0.02467	0.01308	0.0137	0.01918
6	0.0078	0.02316	0.01141	0.01216	0.01769
7	0.00666	0.0215	0.00968	0.01051	0.01608
8	0.00546	0.01961	0.00787	0.00868	0.01429
9	0.00414	0.0173	0.00585	0.006519	0.01213
10	0.0024	0.013111	0.00329	0.00359	0.0085